

Bound states in spectroscopies and dynamics

Dissertation

**with the aim of achieving a doctoral degree
at the Faculty of Mathematics, Informatics and Natural Sciences**

**Department of Physics
of the University of Hamburg**

Roman Rausch

Hamburg, 2016

The following evaluators have recommend the admission of the dissertation:

Evaluators of the dissertation:	Prof. Dr. Michael Potthoff Prof. Dr. Alexander Lichtenstein
Evaluators of the disputation:	Prof. Dr. Michael Potthoff Prof. Dr. Alexander Lichtenstein Prof. Dr. Wilfried Wurth Prof. Dr. Michael Thorwart Prof. Dr. Jochen Liske
Date of the disputation:	September 6, 2017

Kurzfassung

Die vorliegende Arbeit untersucht das Auftreten von gebundenen Zuständen in Spektroskopien und ihre Auswirkungen auf die Realzeitdynamik von stark korrelierten Quantensystemen mit Hilfe der Dichtematrix-Renormierungsgruppe (DMRG) und exakter Diagonalisierung (ED).

Der Hauptfokus betrifft das Verhalten der sogenannten “Dublonen” im Hubbard-Modell, bei denen es sich um gebundene Zustände zweier Elektronen handelt. Das Dublon manifestiert sich in hochaufgelöster CVV-Auger-Elektronenspektroskopie (AES) als ein Satellit im Spektrum. Mit Hilfe der DMRG wird sein Verhalten über alle Füllungen des Hubbard-Modells hinweg nachverfolgt und erklärt. Darüberhinaus wird demonstriert dass ein zweiter Satellit auftaucht, der zu gebundenen Zuständen von vier Elektronen (bzw. zwei Dublonen) korrespondiert, für den der Begriff “Quadruplon” eingeführt wird. Das Quadruplon kann durch Nächste-Nachbarn-Coulomb-Wechselwirkung zusätzlich stabilisiert werden, die zudem weitere gebundene Zustände erzeugt: “Triplonen” (drei Elektronen) und “Dimeronen” (Nächste-Nachbarn-Elektronen). Die Spektren werden auch mit Hilfe des Bethe-Ansatzes analysiert und es werden die Zerfallskanäle des Dublons in Spinonen und Holonen in einer Raumdimension aufgedeckt.

Die Echtzeit-Dynamik und der Zerfall einer lokalen Dublon-Anregung wird untersucht und es wird gezeigt, dass das Dublon bei mittleren Füllungen stabiler wird. Zudem wird gezeigt, dass Zerfallskanäle eine diffusive Komponente zu der Propagation hinzufügen, während eine ballistische Wellenfront erhalten bleibt.

Schließlich wird ein Formalismus für Pump-Probe-Augerspektroskopie entwickelt und mögliche Aufbauten werden diskutiert. Es wird gezeigt, dass die hohe Stabilität des Dublons auf mittleren Zeitskalen bedingt, dass die Spektren keine Abhängigkeit vom Pump-Probe-Delay zeigen und dass entweder eine Modifikation des Aufbaus oder des Modells vonnöten ist. Der letztere Pfad wird verfolgt und es werden Spektren für das dynamische Hubbard-Modell ausgerechnet, wo die Doppelbesetzung an einen bosonischen Freiheitsgrad koppelt. Es wird gezeigt, wie die Parameter der Kopplung zu den Verschiebungen und Intensitäten als Funktion des Delays in den Spektren in Beziehung stehen.

Der sekundäre Fokus liegt in der Untersuchung eines quantenmechanischen oder klassischen Spins als Störstelle auf einem freien oder wechselwirkenden Substrat. Unter anderem wird demonstriert, dass wenn die Wechselwirkung bei Halbfüllung stark genug ist, der Spin nicht vollständig relaxieren kann, d.h. er stellt sich nicht komplett parallel zu einem äußeren Magnetfeld, da die überschüssige Energie vom Substrat nicht aufgenommen werden kann. Dieses Verhalten ist ähnlich zu dem Grund warum das Dublon trotz repulsiver Wechselwirkung gebunden und sehr stabil auf einer mittleren Zeitskala ist.

Abstract

In this work, the appearance of bound states in spectroscopies and their effects on real-time dynamics of strongly correlated quantum systems is investigated with the help of the *density matrix renormalization group* (DMRG) and exact diagonalization (ED).

The main focus surrounds the behaviour of the so-called “doublons” in the Hubbard model, which are repulsively bound states of two electrons. The doublon manifests itself in high-resolution CVV *Auger electron spectroscopy* (AES) in the form of a satellite in the spectrum. Using DMRG, its behaviour is traced and explained through all fillings in the Hubbard model. It is furthermore demonstrated that there appears a second correlation satellite corresponding to bound states of four electrons (or two doublons) which are termed “quadruplons”. The quadruplon can be further stabilized with nearest-neighbour Coulomb interaction which creates even more bound states: “triplons” (three electrons) and “dimerons” (nearest-neighbour electrons). The spectra are also analysed with the help of the Bethe ansatz and decay channels of the doublon into spinons and holons in one spatial dimension are revealed.

The real-time dynamics and decay of a local doublon excitation is investigated and it is shown that the doublon becomes more stable at intermediate fillings and that scattering channels add a diffusive component to its propagation, while a ballistic wavefront remains.

Finally, a formalism for pump-probe Auger spectroscopy is developed and possible setups are discussed. It is shown that due to the high stability of the doublon at the intermediate time scale, the spectra show no dependence on the pump-probe delay and that either a modification of the setup or of the model is necessary. In the latter approach, spectra are calculated for the dynamic Hubbard model, where the double occupancy couples to a bosonic degree of freedom and it is shown how the parameters of the coupling are related to shifts and intensities in the spectra as a function of the delay time.

The secondary focus surrounds the dynamics of a quantum or classical impurity spin coupled to a free or strongly interacting substrate chain. It is demonstrated that for a large enough interaction at half filling, the spin cannot fully relax by aligning itself completely to an external magnetic field because the excess energy cannot be taken up by the substrate. This behaviour is very similar to the reason why the doublon is bound despite repulsive interactions and very stable at an intermediate time scale.

Contents

1. Introduction	1
1.1. The doublon	1
1.2. The two-hole spectral function	4
1.3. Objectives	6
1.4. Bound states in spin dynamics	6
2. Theory	9
2.1. Model	9
2.1.1. The Hubbard model	9
2.1.2. Charge-SU(2) symmetry	10
2.1.3. Extensions	11
2.1.4. Continuous representation of scattering states	12
2.1.5. Coupling to the electromagnetic field	13
2.2. Derivation of the spectroscopic formulae	15
2.2.1. Fermi's golden rule and spectroscopic setups	15
2.2.2. AES and APECS: general	17
2.2.3. AES and APECS: general	18
2.2.4. AES: non-perturbative	19
2.2.5. AES: perturbative	19
2.2.6. APECS: perturbative	22
2.2.7. Spectroscopies in perspective	23
2.2.8. Extra-atomic interferences	26
2.2.9. AES: nonperturbative	27
3. Methods	33
3.1. Exact Diagonalization	33
3.2. The Lanczos algorithm	37
3.2.1. The ground state	37
3.2.2. Time evolution	40
3.3. The Chebyshev expansion technique	42
3.3.1. Spectral functions	42
3.3.2. Multi-dimensional expansion	45
3.3.3. Time evolution	46
3.4. Propagating time-dependent Hamiltonians	47
3.5. Benchmark of the time-propagation algorithms	49
3.6. The Density Matrix Renormalization Group (DMRG)	51
3.6.1. Matrix decompositions: SVD, QR	51
3.6.2. Matrix product states	52
3.6.3. Matrix product operators	54
3.6.4. The ground state in DMRG	57
3.6.5. Entanglement entropy	61
3.6.6. Algorithmic details and caveats	63
3.6.7. Compression of matrix product states	67

3.6.8.	Final DMRG algorithm	68
3.6.9.	Time propagation	69
3.7.	The Bethe Ansatz	77
3.7.1.	The string hypothesis	79
3.7.2.	The thermodynamic Bethe ansatz	80
3.7.3.	Interpreting spectra	83
4.	Spectra	85
4.1.	The two-hole spectral function	85
4.1.1.	Preliminaries	85
4.1.2.	Completely filled band	86
4.1.3.	Partially filled band	88
4.1.4.	Additional points	104
4.2.	Bethe Ansatz analysis of the multi-hole spectra	107
4.2.1.	The full band for various spectroscopies	107
4.2.2.	The band-like part for $n < 2$	108
4.2.3.	The satellites for $n < 2$	110
4.3.	Two dimensions	111
4.3.1.	Ladder geometry	111
5.	Dynamics	117
5.1.	Doublon dynamics	117
5.1.1.	Introduction	117
5.1.2.	Decay	118
5.1.3.	Propagation	121
5.1.4.	Summary	125
5.2.	Spin dynamics	126
5.2.1.	Introduction	126
6.	Pump-probe spectra	143
6.1.	Introduction	143
6.2.	Computational details	143
6.3.	Pump-probe spectra	144
6.4.	The dynamic Hubbard model	145
6.4.1.	Pump-probe AES spectra	148
7.	Summary and outlook	151
Appendix		155
A.	Noninteracting two-hole spectral function	155
B.	Time-dependent perturbation theory	156
B.1.	General	156
B.2.	Time domain	157
B.3.	The Laplace transform	158
B.4.	Laplace domain	159
C.	Orthogonal Polynomial Mapping	160
C.1.	Test case: The Friedrichs-Lee model	162
D.	List of publications and preprints	165

1. Introduction

1.1. The doublon

One of the hallmarks of interacting systems is the emergence of new particles, be it the protons and pentaquarks of high-energy physics or the carbon compounds of chemistry. Solid state physics deals with the interactions of a huge number of electrons (and potentially lattice degrees of freedom as well) and sees its own zoo of particles emerge. There are in fact various concepts of what can be regarded as a particle in a many-body context, like Landau's dressed quasiparticle (*renormalized electrons, polarons*), collective excitations (*phonons, magnons, plasmons*), bound states of electrons or holes (*excitons, Cooper pairs*) or defects related to topological winding numbers (*Skyrmions*). Even though the new particles are usually composites of smaller ones, low-dimensional systems also show the opposite effect: *Spin-charge separation* is the splitting of an electron into an *antiholon* which carries just its charge, and a *spinon* which carries just its spin; and *charge fractionalization* results in entities with a fraction of the elementary charge.

A particle that has received considerable attention over the last years is the *doublon* within the Hubbard model, which falls into the bound state category. What follows is a short pedagogical introduction into the related physics, which will then be expanded throughout this work.

The Hubbard model [[Gutzwiller 1963](#); [Kanamori 1963](#); [Hubbard 1963](#)] describes hopping electrons on a lattice which repel each other whenever they are on the same site. It embodies a system which is conceptually simple, but notoriously difficult to solve, and allows one to study the interplay between Coulomb interaction, kinetic energy, the Pauli principle and lattice structure. With standard notations (see chapter [2.1.1](#) for details), it reads:

$$H = -T \sum_{\langle ij \rangle \sigma} \left(c_{i\sigma}^\dagger c_{j\sigma} + \text{h.c.} \right) + U \sum_i n_{i\uparrow} n_{i\downarrow}. \quad (1.1)$$

There are several limits which are accessible to an analytical solution in order to get an understanding of the emerging physics. One can do perturbation theory in either the hopping or the Coulomb interaction U , provided that one is much smaller than the other. One could neglect the lattice structure and solve a single Hubbard atom (or a small cluster) and try to interpolate the full lattice behaviour from this solution (which was Hubbard's original approach). Lastly, one could limit the amount of electrons to just two, the simplest non-trivial value.

Let us pursue the latter case. For a lattice with L sites, we are dealing with a Hilbert space spanned by the L^2 basis states

$$|ij\rangle := c_{i\downarrow}^\dagger c_{j\uparrow}^\dagger |0\rangle. \quad (1.2)$$

Since this is a simple two-particle problem, it can be solved by just about any method, for instance using the Lippmann-Schwinger equation [[Hecker Denschlag and Daley 2006](#)] or the equation of motion technique for Green's functions [[Nolting 1990](#)]. We can also do it in a very basic textbook

manner by inserting (1.2) into the Schrödinger equation and projecting on an eigenstate $\langle \Psi |$, leading to:

$$-T(C_{i,j-1} + C_{i-1,j} + C_{i,j+1} + C_{i+1,j}) + UC_{ij}\delta_{ij} = EC_{ij}, \quad (1.3)$$

with the overlaps $C_{ij} = \langle \Psi | ij \rangle$. By introducing a centre-of-mass coordinate $R = (R_i + R_j)/2$ and a relative one $r = R_i - R_j$, we can make a separation ansatz [Valiente and Petrosyan 2008; Valiente and Petrosyan 2009; Qin et al. 2014]

$$C_{ij} = e^{iKR}\phi_K(r), \quad (1.4)$$

with a centre-of-mass momentum K and a relative momentum k ; and after inserting obtain the following difference equation:

$$\epsilon(K)[\phi_K(r+1) + \phi_K(r-1)] + U\delta_{r0}\phi_K(r) = E_K\phi_K(r), \quad (1.5)$$

with

$$\epsilon(K) = -2T \cos\left(\frac{K}{2}\right). \quad (1.6)$$

Periodic boundary conditions require $e^{iKL} = 1$, so that K is quantized as $K_n = 2\pi n/L$. Furthermore, $\phi_K(r+L) = e^{\frac{iKL}{2}}\phi_K(r)$, and thus

$$\begin{aligned} \phi_K(-1) &= e^{\frac{-iKL}{2}}\phi_K(L-1), \\ \phi_K(L+1) &= e^{\frac{+iKL}{2}}\phi_K(1). \end{aligned} \quad (1.7)$$

With this, the complexity reduces from L^2 to L and the second-order difference equation (1.5) together with the boundary conditions (1.7) can be easily solved by diagonalizing the corresponding matrix for any value of K_n , and for rather large systems. The resulting eigenstates and eigenenergies E_K can thus be classified according to K and are shown for $L = 100$ in fig. 1.1.

It turns out that there are two kinds of solutions: A continuum of *scattering states* with real values of k where the electrons propagate independently; and *bound states* with an imaginary value of k , which means that the wavefunction decays exponentially with increasing separation of the two electrons. Interestingly, bound states do not only appear for attractive values of the interaction $U < 0$, but also for repulsive $U > 0$ in a symmetric fashion. Their energies lie below and above the energies of two independent particles: $|E| > 2|\epsilon(K)|$. An electron pair in such a *repulsively bound state* remains mostly on the same site and cannot break apart because momentum and kinetic energy have an upper boundary on a lattice¹ – there are simply no states with independent electrons which are fast enough to carry off all of the potential energy imposed by U . Movement is still possible, however, via virtual hopping processes, whereby the pair briefly breaks apart and reassembles again on the neighbouring site, leading to a dispersion as a function of K . This process is suppressed by U and becomes impossible for $U \rightarrow \infty$, where the pair is completely localized. Note also that in one

¹This is meant in a simple lattice model with a cosine dispersion as opposed to particles in a continuum with the dispersion $p^2/2m$. In a real material there will be higher bands, of course, and one would require a sufficiently large band gap to observe the described doublon physics.

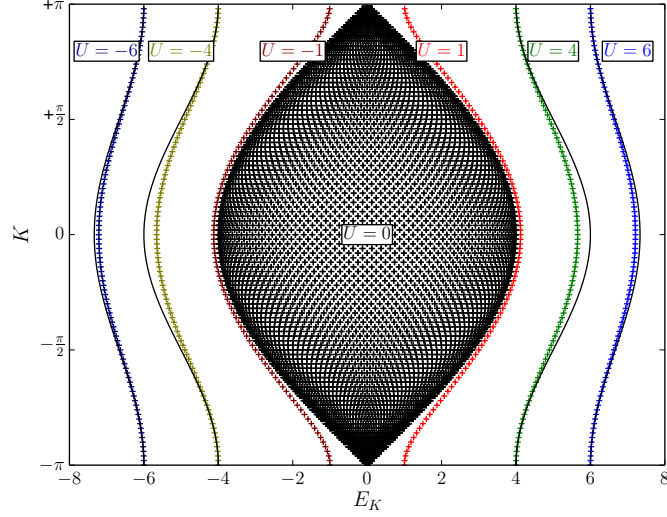


Figure 1.1.: Eigenstates of the $L = 100$ periodic Hubbard chain in the two-particle subspace ($N_{\uparrow} = N_{\downarrow} = 1$), classified according to the centre-of-mass momentum K . For $U \neq 0$ only the bound states with $|E_K| > 2|\epsilon(K)|$ are plotted. The black solid line indicates the free doublon dispersion $\epsilon(K) = J + U + J \cos(K)$ from the effective model (1.9).

spatial dimension, bound states appear for any value of U , but in higher dimensions a critical U_c is required, typically slightly larger than the bandwidth W [Sawatzky and Lenzelink 1980].

These results lead to us to the definition of the *doublon*, created by the operator

$$d_i^{\dagger} := c_{i\downarrow}^{\dagger} c_{i\uparrow}^{\dagger}. \quad (1.8)$$

It is furthermore possible to define an effective doublon model by a Schrieffer-Wolff transformation of the Hubbard Hamiltonian under the assumption of no singly occupied sites and $U/T \gg 1$ (thus entirely neglecting doublon decay) [Rosch et al. 2008; Lenarčič and Prelovšek 2014; Fazekas 1999; Auerbach 2012]²:

$$H_{\text{eff}} = \frac{J}{2} \sum_{\langle ij \rangle} (d_i^{\dagger} d_j + \text{h.c.}) + (J + U) \sum_i n_i^d - J \sum_{\langle ij \rangle} n_i^d n_j^d, \quad (1.9)$$

with $J = 4T^2/U$ and the doublon occupancy number $n_i^d = d_i^{\dagger} d_i$. The doublons in this model are hard-core bosons with the constraint $(d_i^{\dagger})^2 = 0$. Furthermore, it turns out that the interaction between them is *attractive* ($-J < 0$ for $U > 0$) and of moderate strength, only twice the hopping amplitude $J/2$. For our case of a single doublon on an empty lattice, the interaction term vanishes and the remaining single-particle Hamiltonian can be diagonalized via Fourier transformation

$$d_i = \frac{1}{\sqrt{L}} \sum_K d_K \exp(-iKR_i), \quad (1.10)$$

leading to the dispersion relation $\epsilon(K) = J + U + J \cos(K)$. Thus, the delocalized doublon is an eigenstate and we can say that it has infinite lifetime $\tau = \infty$ if regarded as a particle. This dispersion

²Without neglecting singly occupied sites there are in fact many more terms arising after the transformation [Lenarčič and Prelovšek 2014]. These involve hoppings between singly occupied sites, spin-exchange terms and various three-site terms causing a recombination of doublons and holes, all of the order of T^2/U . Neglecting doubly occupied sites rather than singly occupied ones after this general transformation actually leads to the widely known t - J model, which is appropriate below half-filling, while the doublon model is appropriate at almost complete filling. In both cases the *change* of the double occupancy is suppressed with large U .

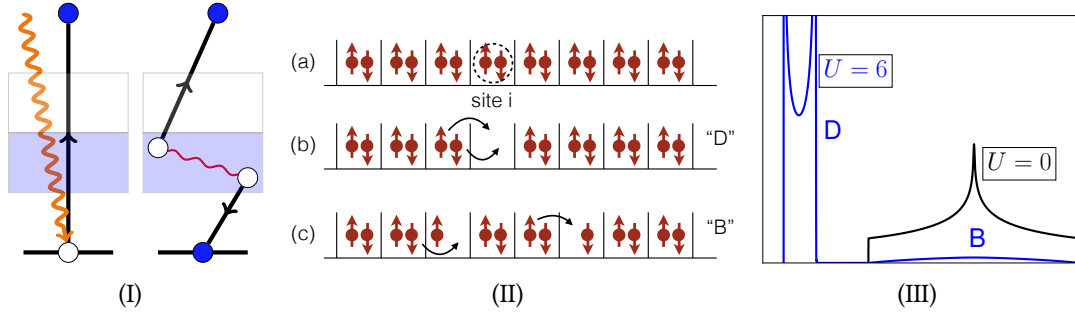


Figure 1.2.: (I) Term diagram of the two steps of Auger electron spectroscopy (AES), emission of the core hole followed by the emission of the Auger electron. (II) Real-space sketch of the processes of the two valence holes in a full band ($n = 2$): (a) initial state, (b) propagation of the bound doublon contributing to the satellite, (c) decay of the doublon and independent propagation of the electron holes contributing to the band-like part. (III) The spectrum for the full band and $U = 6$, with the band-like part (“B”) and the satellite (“D”) indicated; noninteracting case $U = 0$ for comparison.

is compared to the position of the exact eigenstates in fig. 1.1 and one can see that the approximation gets better with increasing U , and becomes quite good when U exceeds the bandwidth $W = 4T$. In fact, the dispersion of the bound state can also be *exactly* reproduced for all U within the Bethe ansatz, which leads to more complicated equations and will be introduced later in chapter 3.7. Note also that the overall hopping sign in (1.9) is positive, for $U > 0$ this leads to an inverted band shape with a maximum at the Γ -point.

The physics of doublons is an implicit driving force of the effects emerging within the Hubbard model. However, with the advent of ultracold atomic lattices, it has become possible to create and observe them in a much more direct fashion. Namely, one can directly prepare one or several doublons $\prod_i d_i^\dagger |0\rangle$ in the middle of the lattice using a trapping potential and then switch it off, letting the system evolve in time, and look at the double occupancy $d(t) = \langle \Psi(t) | n_{i\uparrow} n_{i\downarrow} | \Psi(t) \rangle$. Several predictions of the resulting behaviour have been made [Kajala, Massel, and Törmä 2011; Hofmann and Potthoff 2012; Langer et al. 2012; Boschi et al. 2014].

1.2. The two-hole spectral function

On the other hand, doublons also play a major role in a different kind of experiment, namely high-resolution core-valence (CVV) Auger electron spectroscopy (AES). The setup is as follows: We need a system with localized core states beside a valence band. A high-frequency photon is absorbed by a core electron, allowing it to leave the solid. The resulting core hole is subsequently filled by an electron from the valence band. The energy released by this process is transferred to another electron (the Auger electron) which is also emitted from solid and whose kinetic energy is measured (see fig. 1.2(I)).

One notices that while photoemission is mediated by a one-body term of the type $a_{\mathbf{k},\sigma}^\dagger f_{i\sigma}$ (where f denotes the core electron and a the high-energy scattering state) because classical light is just an external potential for the quantum system, the Auger transition requires a two-body term of the type $a_{\mathbf{k},-\sigma}^\dagger f_{i\sigma}^\dagger c_{i\sigma} c_{i-\sigma}$ and is in essence just Coulomb interaction between particular orbitals.

Assuming that (i) this Coulomb term is weak, (ii) that there are no further interactions between the core and the valence states, as well as (iii) between the high-energy states and the rest of the system; and applying the usual linear-response theory, one arrives at the following Fermi’s golden

rule formula for the AES intensity in terms of a two-hole spectral function (see chapter 2.2 for more details)³:

$$I(\omega) = \sum_n |\langle n | d_{i_0} | 0 \rangle|^2 \delta(\omega - (E_0 - E_n)). \quad (1.11)$$

The core states and the high-energy states drop out and one is simply left with a doublon annihilator $d_{i_0} = c_{i_0\uparrow}c_{i_0\downarrow}$ applied to the ground state $|0\rangle$, while the sum goes over all the eigenstates within the $(N - 2)$ -particle subspace $|n\rangle$. Furthermore, ω corresponds experimentally to the kinetic energy of the Auger electron.

Since the electrons are emitted rather than absorbed in the spectroscopical setup, we now need to think in terms of holes rather than particles, so that an *empty* site will now be called by the name “doublon”. The two-particle case described above is now given by the full band $n = 2$ with two holes, rather than an empty band $n = 0$ with two electrons.

With just the δ -function term, $I(\omega)$ would measure out the positions of eigenenergies of the system. With the addition of the matrix element, these obtain a spectral weight. The weight is large whenever (i) $d_{i_0}|0\rangle$ gives a large contribution, that is when there is a sufficient amount of doubly occupied sites in the ground state; and (ii) whenever the initial state $d_{i_0}|0\rangle$ has substantial overlap with an eigenstate, meaning that the eigenstate has a contribution with a doublon at site i_0 .

The AES spectrum for the $n = 2$ case was first explained by Cini and Sawatzky [Cini 1977; Sawatzky 1977] and is basically given by the K -summation of the eigenenergies in fig. 1.1 with the appropriate weights, see fig. 1.2(III) (later in more detail figs. 4.1(a) and 4.1(b)). That is, one obtains a broad continuum of width $2W = 8T$ termed “band-like part” stemming from the scattering states and a “satellite” stemming from the bound state, whose finite width (given by $J = 4T^2/U$) is due to dispersion. Fig. 1.2(II) shows these elementary processes. Since the satellite is separated by about U from the scattering states, it can be resolved for $U \gtrsim W = 4T$. The band-like part is what one would expect for a non-interacting system described by band theory [Lander 1953]. Not surprisingly, the spectral weight is distributed such that, for large U , most of it is taken by the satellite, while the band-like part is very weak, reflecting the high overlap of the initial state with the bound eigenstates. Thus, unexpectedly from the point of view of band theory, the spectrum looks almost like the spectrum of an atom, with a relatively sharp line only broadened by the doublon dispersion. Realistically, of course, a multiplet is seen [Haak, Sawatzky, and Thomas 1978].

Note that the doublon can decay in two ways: For short times the argument that there is no phase space for final states to transition into under energy conservation is invalid, because there simply is no energy conservation due to the uncertainty principle. On the other hand, for very long times, a doublon excitation can eventually decay in a high-order process involving many intermediate excitations of lower energy. Evidence shows that its lifetime is exponential in the interaction, $\tau \sim \exp(U)$ [Strohmaier et al. 2010]. While this decay process is interesting in the context of the question of thermalization of isolated systems, the short-time decay actually the one which is relevant for spectroscopy. To understand this, note that eq. (1.11) can also be written as a Fourier integral (see chapter 2.2.1 below):

$$I(\omega) = \lim_{t \rightarrow \infty} \frac{1}{2\pi t} \sum_n \left| \int_0^t dt' e^{i\omega t'} \langle n | e^{i(H-E_0)t'} d_{i_0} | 0 \rangle \right|^2. \quad (1.12)$$

The dominant contribution to the integral that produces the broad features in the spectrum comes from short times. The long-time decay should only become visible in the fine-structure at very

³The chemical potential is neglected for the simplicity.

high ω -resolution. Thus, formula (1.12) establishes the connection between the short-time doublon dynamics and Auger electron spectroscopy. Note that it cannot be written as an expectation value of an observable in the state $|\Psi(t)\rangle$ and thus provides information complementary to the dynamics.

While the Auger spectrum of the full band has been understood a long time ago, a reliable extension to intermediate fillings has been missing up to now. A diagrammatic approach has been applied to the almost full band [Cini 1979], by using the hole density as a small parameter, but going to lower fillings constitutes a difficult many-body problem with the additional complication that (1.11) is a *two-particle* Green's function, which is not accessible to every theoretical method.

What can we imagine to happen to a doublon in presence of other doublons and singly occupied sites? In general, we would expect that decay channels should open up, resulting in a finite lifetime and additional broadening. At the same time, the eigenstates of a one-dimensional system are known to consist out of spinon and holon excitations which we expect as the final products of the decay. On the other hand, a neighbouring singly occupied site can actually help the doublon delocalize, as the propagation of the double occupancy to such a site does not cost an energy of U anymore. These two tendencies are thus in competition with each other. Furthermore, the whole picture is additionally complicated by the attractive interaction between doublons in the effective Hamiltonian (1.9).

1.3. Objectives

The conglomerate of the above-mentioned questions connected with the physics of doublons in a many-body environment constitutes the focal point of this thesis. The problem will be approached using the tools of (i) the density-matrix renormalization group (DMRG), which is a way to compress the wavefunction yielding numerically exact results, works especially well in one spatial dimension, and is limited by entanglement growth; (ii) exact diagonalization, which works with the full wavefunction, thus being limited to small Hilbert spaces; and finally (iii) the Bethe ansatz, a method to construct and interpret the excitation energies of the one-dimensional Hubbard model, providing us with invaluable information on what is happening in the system. These methods are described in chapters 3.1, 3.6 and 3.7, respectively. Note that some aspects of the physics are manifestly one-dimensional – as the decay of the doublon into spinons and holons; but others – as the appearance of doublonic bound states as such – are not.

In chapter 4.1, the two-hole spectral function (1.11) will be analysed for all fillings. In chapter 4.2, it will be interpreted with the help of the Bethe ansatz, revealing the decay channels of the doublon in one dimension. In chapter 5.1, the real-time dynamics of the doublon excitation $d_{i_0}|0\rangle$ will be investigated, again for all intermediate fillings. Finally, in chapter 6, the idea of pump-probe setups for Auger spectroscopy will be discussed and proposed. Hereby, the system is pumped into a non-equilibrium state before or during the core-hole decay, with the resulting dynamics providing yet another perspective on the problem.

Publications associated with this work are summarized in appendix D.

1.4. Bound states in spin dynamics

The concepts emerging within the physics of doublons that have been outlined reappear in different contexts as well and are very helpful to understand the underlying physics. For example, typical spintronics applications involve arrays of impurity spins on a metallic substrate which are switched by external magnetic fields. The simplest model to understand the resulting dynamics and relaxation times is the one of a single impurity spin coupled to a one-dimensional chain

$$H = J_{\text{imp-sub}} \mathbf{S} \cdot \mathbf{s}_{i_0} - \mathbf{B} \cdot \mathbf{S} + H_{\text{Hubbard}}, \quad (1.13)$$

where $J_{\text{imp-sub}}$ is the exchange coupling, \mathbf{s}_{i_0} is the spin of the electron at lattice site i_0 and H_{Hubbard} is the previously introduced Hubbard Hamiltonian.

To initiate the dynamics, one can polarize the impurity spin in x-direction ($\mathbf{B} = (B_x, 0, 0)$ with $B_x \rightarrow \infty$) and then suddenly switch the magnetic field in z-direction, $\mathbf{B} = (0, 0, 1)$. The spin will now start to align itself to the field, with the excess energy being carried off by the substrate electrons. The process is completed once the system is locally (around i_0) in its ground state. If the substrate is interacting, one would expect a faster relaxation since scattering processes help to dissipate the energy. However, increasing the Hubbard- U at half filling eventually leads to a reduction of the bandwidth which becomes of the order of $J = 4T^2/U$ and thus much smaller than the magnetic energy. In this case, the magnetic energy cannot efficiently dissipate into the chain and the relaxation of the spin is “frozen” at an intermediate value, very similar to the case of doublons where the double occupancy is frozen at an intermediate value different from the ground-state one (see chapter 5.1 for more details).

Conversely, we can leave the substrate non-interacting ($U = 0$), but increase the value of the product $B_{\text{eff}} = J_{\text{imp-sub}}S$. This is, for example, the case if one increases the spin quantum number S in order to examine the role of quantum spin effects (where $S \rightarrow \infty$ is the classical limit). When B_{eff} exceeds a critical value, two bound states split off symmetrically from the conduction band. (Note that if i_0 is positioned in the middle of the chain, an arbitrarily small perturbation creates a bound state, but if i_0 is at the edge, a critical value is required, similar to the behaviour of a higher-dimensional system.) Since the wavefunction of the bound state is exponentially suppressed in the bulk, the site i_0 effectively decouples from the rest of the chain. This can be observed within DMRG by looking at the corresponding entanglement entropy which becomes small. The dynamics in this case is effectively captured by a two-spin model (\mathbf{S} and \mathbf{s}_{i_0}), with only weak perturbative coupling to the rest of the chain. Once again, the appearance of a bound state inhibits a full relaxation.

Spin dynamics is, however, not the primary focus of this work. Therefore, only the relevant publications are included in chapter 5.2 without any broader discussion (See also appendix D for the references.) The author’s contribution in this collaboration consisted in writing and optimizing the DMRG code and participating in the interpretation of the results.

2. Theory

2.1. Model

2.1.1. The Hubbard model

Throughout this work, we will be dealing with the Hubbard model [[Gutzwiller 1963](#); [Kanamori 1963](#); [Hubbard 1963](#)], given by the Hamiltonian

$$H_{\text{Hub}} = -T \sum_{\langle ij \rangle \sigma} \left(c_{i\sigma}^\dagger c_{j\sigma} + \text{h.c.} \right) + U \sum_i n_{i\uparrow} n_{i\downarrow}, \quad (2.1)$$

where $c_{i\sigma}^\dagger$ is the creation operator of an electron with spin σ in the orbital i , obeying the fermionic anticommutation relations $\{c_\alpha, c_\beta^\dagger\} := c_\alpha c_\beta^\dagger + c_\beta^\dagger c_\alpha = \delta_{\alpha\beta}$ as well as $\{c_\alpha, c_\beta\} = \{c_\alpha^\dagger, c_\beta^\dagger\} = 0$; and $n_{i\sigma} = c_{i\sigma}^\dagger c_{i\sigma}$ is the occupancy operator. The angled bracket signifies that the summation is carried out over nearest-neighbours only (with the convention where each bond is counted once). The parameter U quantifies the local Coulomb interaction between the electrons of the two spin species.

It is a convenient common practice to set the $T = 1$, i.e. to measure all energies in units of T and all times in units of T^{-1} (or \hbar/T , with $\hbar = 1$). This will be done in this work as well, although it is sometimes practical to redundantly keep the T in order to clarify the dimensionality.

Since the hopping does not flip the spin of an electron and the interaction is between the densities only, the total amount of spin-up and spin-down electrons,

$$\hat{N}_\sigma = \sum_i n_{i\sigma}, \quad (2.2)$$

is conserved within the Hubbard model:

$$\left[H, \hat{N}_\sigma \right] = 0. \quad (2.3)$$

We can thus classify the eigenstates accordingly, writing $|n, N_\uparrow, N_\downarrow\rangle$ where the lack of the circumflex signifies the eigenvalue: $\hat{N}_\sigma |n, N_\uparrow, N_\downarrow\rangle = N_\sigma |n, N_\uparrow, N_\downarrow\rangle$. Note that the conservation of N_\uparrow and N_\downarrow implies the conservation of both the total particle number,

$$\hat{N} = \hat{N}_\uparrow + \hat{N}_\downarrow, \quad (2.4)$$

and the total magnetization:

$$S^z = \frac{1}{2} \left(\hat{N}_\uparrow - \hat{N}_\downarrow \right). \quad (2.5)$$

Going further, we can also define the spinflip operators

$$\begin{aligned} S^+ &= \sum_i c_{i\uparrow}^\dagger c_{i\downarrow}, \\ S^- &= \sum_i c_{i\downarrow}^\dagger c_{i\uparrow} \end{aligned} \tag{2.6}$$

along with the x - and y -components of the spin as well:

$$\begin{aligned} S_x &= \frac{1}{2} (S^+ + S^-), \\ S_y &= \frac{1}{2i} (S^+ - S^-), \end{aligned} \tag{2.7}$$

which obey the usual SU(2) algebra $[S^\alpha, S^\beta] = \sum_\gamma \epsilon_{\alpha\beta\gamma} S^\gamma$. The Hubbard Hamiltonian commutes with all of the components of the vector $\mathbf{S} = (S_x, S_y, S_z)$, which constitutes its spin-SU(2) symmetry in addition to the U(1) symmetry $c_\alpha \rightarrow e^{-i\Lambda} c_\alpha$ leading to the conservation of the charge N . Since \mathbf{S}^2 and S^z can be diagonalized simultaneously, we can in principle work in a basis labelled by $|n, N, S, M\rangle$, where $S(S+1)$ is the eigenvalue of \mathbf{S}^2 and M is the eigenvalue of S^z , although this is difficult to achieve in practice.

Note that if an external magnetic field is present, coupling to the z -component of the spin,

$$H_{\text{Hub}+B} = H_{\text{Hub}} - BS^z, \tag{2.8}$$

the Hamiltonian no longer commutes with S_x and S_y , whereby the SU(2) symmetry is broken.

Unless spontaneous symmetry breaking takes place, the ground state for $B = 0$ is a spin singlet with $N_\uparrow = N_\downarrow$, so that we can just write $|n, N\rangle$ without loss of information. The filling $n := N/L$ can be controlled by introducing a chemical potential μ :

$$\mathcal{H} := H_{\text{Hub}} - \mu \hat{N}. \tag{2.9}$$

In presence of B , the ground state is obviously ferromagnetic with $N_\uparrow > N_\downarrow$.

2.1.2. Charge-SU(2) symmetry

Apart from this spin-SU(2) symmetry, the Hubbard model also exhibits a ‘‘hidden’’ charge-SU(2) symmetry [Yang 1989; Zhang 1990]. Namely, introducing the η -operator

$$\eta = \sum_i (-1)^i c_{i\uparrow} c_{i\downarrow}, \tag{2.10}$$

one can easily verify that it is an eigenoperator of H_{Hub} and \hat{N} ¹:

¹The lattice must be bipartite, so that the operator is in fact $\eta = \sum_{i \in A} c_{i\uparrow} c_{i\downarrow} - \sum_{i \in B} c_{i\uparrow} c_{i\downarrow}$, where A and B are the two sublattices.

$$[\eta, H] = U\eta, \quad [\eta, \hat{N}] = 2\eta. \quad (2.11)$$

Comparing (2.10) with the spinflip operators (2.6), it is apparent that η and S^- are related via a spin-asymmetric and staggered particle-hole transformation (“Shiba transformation” [Essler et al. 2005]):

$$U_{\text{sh}}^\dagger c_{i\uparrow} U_{\text{sh}} = (-1)^i c_{i\uparrow}^\dagger. \quad (2.12)$$

This means that we can obtain another charge-SU(2) algebra with a vector \mathbf{T} , sometimes called “isospin”:

$$\begin{aligned} T_x &= \frac{1}{2}(\eta + \eta^\dagger), \\ T_y &= \frac{1}{2i}(\eta - \eta^\dagger), \\ T_z &= \frac{1}{2}(L - \hat{N}). \end{aligned} \quad (2.13)$$

The full Hamiltonian \mathcal{H} only commutes with \mathbf{T} for $\mu = U/2$, which corresponds to half filling $n = 1$. In this case, \mathbf{T} and \mathbf{S} also commute among each other [Essler et al. 2005], altogether giving rise to a charge-U(1) \times spin-SU(2) \times charge-SU(2) symmetry.

Off half filling, it is instructive to decompose \mathcal{H} into

$$\mathcal{H} = \mathcal{H}_0 - (U - 2\mu)T_z + \text{const}, \quad (2.14)$$

where $\mathcal{H}_0 = H - (U/2)\hat{N}$ is the charge-SU(2)-symmetric part ($[\mathbf{T}, \mathcal{H}_0] = 0$), and where the second term now looks just like a homogeneous field coupling to the z -component of \mathbf{T} . This field explicitly breaks the charge-SU(2) symmetry and thus isospin-polarizes the ground state. We still have $[\mathbf{T}^2, \mathcal{H}] = 0$ and $[T_z, \mathcal{H}] = 0$ (but $[\eta, \mathcal{H}] \neq 0$), so that the eigenstates can be characterized by the isospin quantum numbers (T, M_T) corresponding to (\mathbf{T}^2, T_z) . For fillings above half filling, we have $\mu > U/2$, and the field term leads to a state with the isospin pointing into the negative- z direction, i.e., $M_T = -T$. The converse is true below half filling.

An intuitive way to think about isospin is that it pertains to empty and doubly occupied sites in the same way the usual spin operators pertain to singly occupied sites with either an up or down electron. Above half filling we necessarily have more doubly occupied sites than empty ones in the same way we have more spin-up sites than spin-down ones in the presence of an external magnetic field.

2.1.3. Extensions

One often extends the Hubbard model to include the Coulomb interaction between nearest neighbours as well [Jeckelmann 2002]:

$$H_{\text{ext}} = H_{\text{Hub}} + V \sum_{\langle ij \rangle \sigma \sigma'} n_{i\sigma} n_{j\sigma'}. \quad (2.15)$$

This will only have marginal relevance in the present work and shall come into play when analysing multiplons in chapter 4.1.

When discussing Auger electron spectroscopy, we will need core states in addition to the valence band. We assume that they are sufficiently localized, so that any hopping to neighbouring lattice sites can be neglected:

$$H_{\text{core}} = E_c \sum_{i\sigma} n_{i\sigma}^f + U_{cc} \sum_i n_{i\uparrow}^f n_{i\downarrow}^f, \quad (2.16)$$

where $E_c < 0$ is the core atomic level and $n_{i\sigma}^f = f_{i\sigma}^\dagger f_{i\sigma}$. One can also include a core-valence interaction of Hubbard type:

$$H_{\text{core-val}} = U_{cv} \sum_{i\sigma\sigma'} n_{i\sigma}^f n_{i\sigma'}^c. \quad (2.17)$$

The electrons emitted during the spectroscopic process go into scattering states, which are non-interacting:

$$H_{\text{scat}} = \frac{1}{L} \sum_{\mathbf{k}\sigma} \epsilon(\mathbf{k}) a_{\mathbf{k}\sigma}^\dagger a_{\mathbf{k}\sigma}. \quad (2.18)$$

Thus, core-level photoemission is mediated by the quadratic term

$$H_{\text{photo}} = \frac{1}{L} \sum_{i\mathbf{k}\sigma} \left(d_{i\mathbf{k}} a_{\mathbf{k}\sigma}^\dagger f_{i\sigma} + h.c. \right), \quad (2.19)$$

where $d_{i\mathbf{k}}$ is the dipole matrix element; while AES is mediated by a quartic Coulomb interaction between the three bands:

$$H_{\text{Auger}} = \frac{1}{L} \sum_{i\mathbf{k}\sigma} \left(U_{i\mathbf{k}}^A f_{i,-\sigma}^\dagger a_{\mathbf{k}\sigma}^\dagger c_{i,-\sigma} c_{i\sigma} + h.c. \right) \quad (2.20)$$

We will follow the usual procedure of setting the matrix element to a constant:

$$U_{i\mathbf{k}}^A \approx U_A = \text{const.} \quad (2.21)$$

2.1.4. Continuous representation of scattering states

For the practical calculations it is in fact quite helpful to switch to a continuous notation of the scattering states in the following fashion:

$$H_{\text{scat}} = \int d\epsilon \rho(\epsilon) \epsilon a_\sigma^\dagger(\epsilon) a_\sigma(\epsilon), \quad (2.22)$$

where

$$a_\sigma^\dagger(\epsilon) = \frac{1}{\rho(\epsilon)} \frac{1}{L} \sum_{\mathbf{k}} \delta(\epsilon - \epsilon(\mathbf{k})) a_{\mathbf{k}\sigma}^\dagger \quad (2.23)$$

now creates a particle with energy ϵ and

$$\rho(\epsilon) := \frac{1}{L} \sum_{\mathbf{k}} \delta(\epsilon - \epsilon(\mathbf{k})) \quad (2.24)$$

is the density of the scattering states, which we will later assume as being constant. The anticommutation relation for the a -operators reads as follows:

$$\{a(\epsilon), a^\dagger(\epsilon')\} = \frac{1}{\rho(\epsilon)} \delta(\epsilon - \epsilon'). \quad (2.25)$$

Clearly, when going from a description with a wavevector \mathbf{k} to the energy ϵ , some information is lost, since contributions on the same energy shell $\epsilon(\mathbf{k})$ are not distinguished. But this is information we will not need anyway, as long as we deal with energy-resolved spectra, and not momentum-resolved ones. For instance, if $\langle n_{\mathbf{k}} \rangle$ is only a function of $\epsilon(\mathbf{k})$, we can sum up over this energy shell and present the result as a function of $\epsilon = \epsilon(\mathbf{k})$. Thus, we obtain the same result as we would when using the $a(\epsilon)$ -operators in the first place:

$$\langle n(\epsilon) \rangle = \frac{1}{\rho(\epsilon)} \frac{1}{L} \sum_{\mathbf{k}} \langle n_{\mathbf{k}} \rangle \delta(\epsilon - \epsilon(\mathbf{k})). \quad (2.26)$$

2.1.5. Coupling to the electromagnetic field

In first quantization, the coupling of a system of particles with equal charges q and equal masses m to a classical electromagnetic field described by the vector potential $\mathbf{A}(\mathbf{r}, t)$ is given by the following Hamiltonian:

$$H = \sum_{i=1}^{N_{\text{el}}} \frac{1}{2m} (\mathbf{p}_i - \mathbf{A}(\mathbf{r}, t))^2 + V(\{\mathbf{r}_i\}) + H_{\text{rad}}, \quad (2.27)$$

where the term H_{rad} is the Hamilton function of the field itself. Since we assume that the back-action of the system on the field is negligible, it does not play an important role here. The equations of motion derived from (2.27) are the Lorentz force for the particles and a wave equation for \mathbf{A} . The scalar potential $\phi(\mathbf{r})$ does not appear explicitly, since its equation of motion (the Poisson equation) can be solved independently and yields the Coulomb interaction between the electrons, which can be absorbed into the potential $V(\{\mathbf{r}_i\})$.

Unless the wavelength of the radiation is too small, a reasonable approximation is that $\mathbf{A}(\mathbf{r}, t)$ does not vary much within the spatial extent of the system, so that the vector potential only depends on time. This is known as the ‘‘dipole approximation’’:

$$\mathbf{A}(\mathbf{r}, t) \approx \mathbf{A}(t). \quad (2.28)$$

The Hamiltonian (2.27) is difficult to represent in second quantization for a lattice model. However, it turns out that as long as the dipole approximation is valid, the interaction can be rewritten by using a time-dependent gauge transformation [Savasta and Girlanda 1995; Scully and Zubairy 1997; Rzązewski and Boyd 2004]. In order for the Schrödinger equation to remain invariant under such a transformation, it must have the following form, as is easy to check by inspection:

$$\begin{aligned} |\Psi'(t)\rangle &= U^\dagger(t) |\Psi(t)\rangle, \\ H'(t) &= U^\dagger(t) H(t) U(t) - iU^\dagger(t) \dot{U}(t). \end{aligned} \quad (2.29)$$

Let us now choose

$$U(t) := e^{iq\mathbf{A}(t) \sum_{i=1}^{N_{\text{el}}} \mathbf{r}_i}. \quad (2.30)$$

Using the identity

$$e^X Y e^{-X} = \sum_m \frac{1}{m!} [X, Y]_m \quad (2.31)$$

specifically for the canonical commutation relation $[\mathbf{r}, \mathbf{p}] = i$, one can show that it holds in general that

$$e^{-if(\mathbf{r})} g(\mathbf{r}, \mathbf{p}) e^{if(\mathbf{r})} = g(\mathbf{r}, \mathbf{p} + \nabla f(\mathbf{r})), \quad (2.32)$$

where f and g are arbitrary functions of the position and momentum. This means that the momentum shift in the Hamiltonian is cancelled by the transformation:

$$H'_0 = U^\dagger(t) H(t) U(t) = \sum_{i=1}^{N_{\text{el}}} \frac{1}{2m} \mathbf{p}_i^2 + V(\{\mathbf{r}_i\}). \quad (2.33)$$

However, a new interaction term arises from the time derivative of $U(t)$:

$$H_d = -iU^\dagger(t) \dot{U}(t) = q\dot{\mathbf{A}}(t) \sum_{i=1}^{N_{\text{el}}} \mathbf{r}_i = -\mathbf{E}(t) \sum_{i=1}^{N_{\text{el}}} q\mathbf{r}_i = -\mathbf{E}(t) \sum_{i=1}^{N_{\text{el}}} \mathbf{d}_i, \quad (2.34)$$

where $\mathbf{d}_i = q\mathbf{r}_i$ is the dipole moment of the i -th electron and $\mathbf{E}(t) = -\dot{\mathbf{A}}(t)$ is the electric field.

Now it is straightforward to bring the new Hamiltonian $H' = H'_0 + V + H_d$ into a lattice form in second quantization. Let us furthermore specify the problem to a one-dimensional chain or a ring. Working in cylindrical coordinates (r, ϕ, z) , we want a spatially constant electric field in ϕ -direction (in x -direction in the case of a chain):

$$\mathbf{E}(t) = \mathcal{E}(t) \mathbf{e}_{\phi,x} = -\frac{\partial A(t)}{\partial t} \mathbf{e}_{\phi,x}. \quad (2.35)$$

With this, the Hamiltonian reads:

$$H' = H'_0 + V + H_d = -T \sum_{j\sigma} \left(c_{j+1,\sigma}^\dagger c_{j\sigma} + \text{h.c.} \right) + V + \mathcal{E}(t) \sum_j j n_j. \quad (2.36)$$

We now perform the inverse rotation of (2.30) in second quantization, given by [Eckardt 2016]:

$$U(t) = e^{-iqA(t) \sum_j j n_j}. \quad (2.37)$$

It is easy to see that the dipole term is canceled: $-iU^\dagger(t)\dot{U}(t) = -H_d$. Using once more (2.31), now with $[c_i, n_j] = c_i\delta_{ij}$, it is straightforward to show that

$$U^\dagger(t)c_jU(t) = e^{-iqA(t)j}c_j, \quad (2.38)$$

so that the interaction with the field is shifted to the hopping term:

$$H_0 = U^\dagger(t)H'_0U(t) = -T \sum_{j\sigma} \left(e^{iqA(t)}c_{j+1,\sigma}^\dagger c_{j\sigma} + e^{-iqA(t)}c_{j,\sigma}^\dagger c_{j+1,\sigma} \right). \quad (2.39)$$

Thus, electrons hopping the forward direction receive a phase $e^{iqA(t)}$, those hopping backward $e^{-iqA(t)}$. This is known as the ‘‘Peierls substitution’’. All terms which are local or can be written in terms of the occupancy operator n_j (and are contained in V) are unaffected by the transformation.

Note that while the two gauges should give identical results if the model is solved exactly, this is no longer the case when approximations are applied, so that the one or the other may prove to be much better.

2.2. Derivation of the spectroscopic formulae

2.2.1. Fermi’s golden rule and spectroscopic setups

Let us at first establish Fermi’s golden rule in a very general approach. At first, we need a basic division of the problem into a system H_{sys} described by some model and high-energy scattering states H_{scat} into which the electrons are emitted. Let us proceed to work in the convenient continuous-energy formalism of eq. (2.22). Furthermore, we have a term V , which is the only one that couples H_{sys} and H_{scat} , thereby driving the transition:

$$H = H_{\text{sys}} + H_{\text{scat}} + V = H_0 + V. \quad (2.40)$$

The result of first-order perturbation theory in V results in the following expression for the wavefunction, with a correction term linear in V (see appendix B):

$$|\Psi(t)\rangle = e^{-iH_0t}|\Psi(0)\rangle - ie^{-iH_0t} \int_0^t dt' e^{iH_0t'} V e^{-iH_0t'} |\Psi(0)\rangle. \quad (2.41)$$

We assume that the coupling V has the general form where some transition operator of the system T leads to a hopping into the high-energy state $a^\dagger(\epsilon)$ with some coupling strength λ , which is assumed to be independent of the system parameters and the scattering state energy. Hence:

$$V = \lambda A^\dagger T + \text{h.c.}, \quad (2.42)$$

where

$$A^\dagger = \int d\epsilon \rho(\epsilon) a^\dagger(\epsilon). \quad (2.43)$$

Since H_{sys} and H_{scat} are uncoupled in H_0 (this has been taken care of by the first-order perturbation theory in V), the eigenstates of H_0 are given by product states $|n, \epsilon\rangle \equiv |\epsilon\rangle_{\text{scat}} |n\rangle_{\text{sys}} = a^\dagger(\epsilon) |0\rangle_{\text{scat}} |n\rangle_{\text{sys}}$, so that $H_0 |n, \epsilon\rangle = (E_n + \epsilon) |n, \epsilon\rangle$.

Finally, the measured spectrum is just given by tracing out the unobserved system degrees of freedom from the overlap with the wavefunction:

$$I(\epsilon, t) = \sum_n |\langle n, \epsilon | \Psi(t) \rangle|^2 = \sum_n \left| \langle n, 0 | a(\epsilon) e^{-iHt} \int_0^t dt' e^{iHt'} \int d\epsilon' \rho(\epsilon') a^\dagger(\epsilon') T e^{-iHt'} |0, 0\rangle \right|^2. \quad (2.44)$$

Since the scattering states are empty in the initial state, $a(\epsilon) |0\rangle_{\text{scat}} |0\rangle_{\text{sys}} = 0$, we can commute the a -operators past each other, letting them cancel and picking up a phase of ϵ in the exponential. Finally, the time integral can be carried out:

$$\begin{aligned} I(\epsilon, t) &= \sum_n \left| \langle n | \int_0^t dt' e^{i(\epsilon + E_n - E_0)t'} T |0\rangle \right|^2 \\ &= \sum_n |\langle n | T |0\rangle|^2 \left| \frac{e^{i(\epsilon + E_n - E_0)t} - 1}{\epsilon + E_n - E_0} \right|^2 \\ &= \sum_n |\langle n | T |0\rangle|^2 \frac{2 - 2 \cos[(\epsilon + E_n - E_0)t]}{(\epsilon + E_n - E_0)^2} \\ &= \sum_n |\langle n | T |0\rangle|^2 \left(\frac{\sin[(\epsilon + E_n - E_0)t/2]}{(\epsilon + E_n - E_0)/2} \right)^2 \end{aligned} \quad (2.45)$$

Using the relation $\left(\frac{\sin(xt/2)}{x/2}\right)^2 \stackrel{t \rightarrow \infty}{\approx} \pi t \delta(x/2) = 2\pi t \delta(x)$, we see that the transition probability grows linearly for large times. This is expected, since we basically never stop driving the transition induced by V . However, the ratio $j(\epsilon) := \lim_{t \rightarrow \infty} I(\epsilon, t)/t$ does not diverge and can be interpreted as a steady-state current in the detector resulting from a steady beam of incident photons [Freericks, Krishnamurthy, and Pruschke 2009]:

$$j(\epsilon) = 2\pi \sum_n |\langle n | T |0\rangle|^2 \delta(\epsilon + E_n - E_0). \quad (2.46)$$

It is easy to check that, up to constant prefactor, the same result is obtained for a time-dependent transition operator which is harmonic in time, $V(t) = V_0 \cos(\Omega t)$, corresponding to a continuous laser beam, and for a frequency Ω which is high enough, so that only the resonant term $\Omega - \Delta E$ contributes, while the highly oscillating one with $\Omega + \Delta E$ can be neglected (*rotating wave approximation*). As an additional change, energies are then trivially shifted by Ω .

A different spectroscopic setup is given by a pulse, where $V(t) = V_0 \cos(\Omega t) \exp(-(t - t_0)^2/2\sigma_t^2)$ is now damped by a Gaussian. This means that $I(\epsilon, t)$ does not diverge anymore, but approaches a saturated value. In this case, the total intensity $I(\epsilon) = \lim_{t \rightarrow \infty} I(\epsilon, t)$ is the quantity to look at. It will be more or less smeared out depending on the temporal duration of the pulse σ_t due to the uncertainty principle.

One could also follow the spectra as a function of time, without performing the limit $t \rightarrow \infty$. However, this just gives the somewhat trivial rise of energy conservation and sharpening of the

spectral features. Although a temporal resolution is introduced in pump-probe experiments, it is not due to measuring $I(\epsilon, t)$ as function of both variables, but rather due to having two pulses with a delay Δt hitting the system and still propagating the wavefunction to infinity, thereby obtaining a spectrum for each pump-probe delay: $I(\epsilon, \Delta t) = \lim_{t \rightarrow \infty} I_{\Delta t}(\epsilon, t)$.

2.2.2. AES and APECS: general

In this chapter, the formulae for the *Auger electron spectroscopy* (AES) and *Auger-photoelectron coincidence spectroscopy* (APECS) will be derived. The former has already been described in the introduction, the latter just corresponds to the setup where the kinetic energy of the photoelectron ϵ_p is measured in coincidence with the Auger electron ϵ_A , producing two-dimensional data. Obviously, the AES spectrum follows from the APECS spectrum just by integrating over ϵ_p ². The derivation will be attempted as general as possible, so as to cover both the pump-probe case and the time-homogeneous (equilibrium) limit.

The Hamiltonian we are working with has the following general shape:

$$H = H_0 + V_c + V_p = H_c + V_p. \quad (2.47)$$

As before, $H_0 = H_{\text{sys}} + H_{\text{scat}}$. In the pump-probe case, H_0 and V_p have explicit time dependencies for the pump and the probe pulses, respectively:

$$\begin{aligned} H_0 &= H_0(t), \\ V_p &= V_p(t). \end{aligned} \quad (2.48)$$

V_c is the Coloumb term driving the transition, given by:

$$V_c = U_A \sum_{i\sigma} \int \rho(\epsilon) d\epsilon a_{-\sigma}^\dagger(\epsilon) f_{i,\sigma}^\dagger c_{i\sigma} c_{i,-\sigma} + \text{h.c.} \quad (2.49)$$

Note that the core levels are always all filled in the ground state, so that we have $V_c |\Psi(0)\rangle = 0$, meaning that there can be no Coloumb transition to scattering states without previous photoemission. Furthermore, since both the scattering states (and in certain limits also the core states) will be eliminated by commutation as was done in the derivation of Fermi's golden rule above, it is useful to define the following three-body and two-body transition operators for the AES/APECS case:

$$\begin{aligned} V_c^{(3)} &:= U_A \sum_{i\sigma} f_{i,\sigma}^\dagger c_{i\sigma} c_{i,-\sigma}, \\ V_c^{(2)} &:= U_A \sum_{i\sigma} c_{i\sigma} c_{i,-\sigma}. \end{aligned} \quad (2.50)$$

$V_c^{(3)}$ appears in after the elimination of the scattering states, $V_c^{(2)}$ in the case of vanishing core-valence interaction after the elimination of the core states.

V_p is dipole term driving the initial photoemission, given by:

²One can also do the converse case and integrate over ϵ_A to obtain the core-level photoemission spectrum shaken up by Auger recombinations.

$$V_p(t) = s(t) d_0 \sum_{i\sigma} \int \rho(\epsilon) d\epsilon a_{i\sigma}^\dagger(\epsilon) f_{i\sigma}. \quad (2.51)$$

Here, $s(t)$ is the dimensionless envelope function of the pump pulse inducing the photoemission, usually an oscillating term damped by a Gaussian.

As before, elimination of the core states in the AES/APECS case will lead to the following reduced operator:

$$V_p^{(1)}(t) = s(t) d_0 \sum_{i\sigma} f_{i\sigma}. \quad (2.52)$$

Of course, the dipole matrix element is in general dependent on all the orbitals, but it is common practice to set it to a constant: $d_i(\epsilon) \approx d_0 = \text{const}$.

It will always be assumed that the Auger electron and the photoelectron are distinguishable particles due to the separation of their momenta and energies ($\mathbf{k}_A \neq \mathbf{k}_p$) and that they do not interact. Energy exchange between the two (“postcollision interaction”) can be of importance as well, leading to the effect of “chirping” [Schütte et al. 2012], but is not the focus of this work.

Let us start with the first-order time-dependent perturbation theory in V_p by expanding the full propagator (see appendix B for a detailed derivation):

$$|\Psi(t)\rangle \approx U_c(t, 0) |\Psi(0)\rangle - i \int_0^t dt' U_c(t, t') V_p(t') U_c(t', 0) |\Psi(0)\rangle. \quad (2.53)$$

Here, the time evolution operator $U_c(t, t')$ describes the dynamics with the Hamiltonian H_c including the transition Coulomb term. Without explicit time dependence, it is just given by

$$U_c(t, t_0) = e^{-iH_c(t-t_0)}. \quad (2.54)$$

Let us also introduce a shorthand notation for the wavefunction propagated to t following the application of V_p at t' using the subscript p :

$$|\Psi_p(t')\rangle = U_c(t, t') V_p^{(1)} U_0(t', 0) |\Psi(0)\rangle. \quad (2.55)$$

In the time-homogeneous case, the application of $U_0(t', 0)$ just gives a factor of $e^{-iE_0 t'}$, of course.

2.2.3. AES and APECS: general

For the overlap of $|\Psi(t)\rangle$ (eq. (2.53)) with an eigenstate we obtain:

$$\langle n, \epsilon_A, \epsilon_p | \Psi(t) \rangle = -i \int_0^t dt' s(t') \langle n, \epsilon_A | \Psi_p(t') \rangle e^{-i\epsilon_p(t-t')}. \quad (2.56)$$

The APECS spectrum results by taking the modulus squared and tracing over the system, using $\sum_n |n\rangle\langle n| = \mathbb{1}_{\text{sys}}$:

$$\begin{aligned}
I_{\text{APECS}}(\epsilon_A, \epsilon_p, t) &= \sum_n \left| \langle n, \epsilon_A, \epsilon_p | \Psi(t) \rangle \right|^2 \\
&= \int_0^t dt' \int_0^{t'} dt'' s(t') s(t'') \langle \Psi_p(t'') | \epsilon_A \rangle \langle \epsilon_A | \Psi_p(t') \rangle e^{i\epsilon_p(t'-t'')}.
\end{aligned} \tag{2.57}$$

This formula can be used as the starting point for further approximations.

2.2.4. AES: non-perturbative

The AES spectrum is obtained from the APECS one simply by integrating out the photoelectron energies:

$$I_{\text{AES}}(\epsilon_A, t) = \int d\epsilon_p \rho(\epsilon_p) I_{\text{APECS}}(\epsilon_A, \epsilon_p, t). \tag{2.58}$$

Assuming a constant density of the scattering states, $\rho(\epsilon_p) \approx \rho_p^{(0)} = \text{const}$, the integral over the exponential function just gives $2\pi\rho_p^{(0)}\delta(t' - t'')$. Taking the limit $t \rightarrow \infty$, we thus get:

$$I_{\text{AES}}(\epsilon_A) = 2\pi\rho_p^{(0)} \int_0^\infty dt' s^2(t') \left| \langle \epsilon_A | \Psi_p(t') \rangle \right|^2 = 2\pi\rho_p^{(0)} \int_0^\infty dt' s^2(t') \langle \Psi_p(t') | n(\epsilon_A) | \Psi_p(t') \rangle, \tag{2.59}$$

with $n(\epsilon_A) = a^\dagger(\epsilon_A) a(\epsilon_A)$.

This is a one-step AES formula³, which is still non-perturbative in the Auger term V_c and is also valid for the pump-probe case. It has a very intuitive form: The occupancy number of the scattering states at a given energy $n(\epsilon_A)$ is evaluated in the time-dependent wavefunction $|\Psi_p(t')\rangle$ and integrated, sampled by the pump pulse envelope $s(t')$.

2.2.5. AES: perturbative

We can now apply perturbation theory in the Auger term V_c as well, by expanding the propagator $U_c(t, t')$:

$$U_c(t, t') \approx U_0(t, t') - i \int_{t'}^t dt'' U_0(t, t'') V_c U_0(t'', t'). \tag{2.60}$$

The Auger spectrum becomes:

³“One-step” means that whole process from core-hole production to Auger auto-ionization is treated as one chain of time propagations. A two-step approach would start with an existing core hole and the valence band in its ground state. This is exact if the valence band is completely full or there is no interaction between the core and the valence states. Otherwise it is an approximation which assumes that the valence band relaxes faster than the core hole lifetime.

$$I_{\text{AES}}(\epsilon_A, t) = 2\pi\rho_p^{(0)} \int_0^t dt' s^2(t') \int_{t'}^t dt'' \int_{t'}^t dt''' \langle \Psi(0) | U_0(0, t') V_p^{(1)\dagger} U_0(t', t'') V_c^\dagger U_0(t'', t) | \epsilon_A \rangle \times \\ \times \langle \epsilon_A | U_0(t, t''') V_c U_0(t''', t') V_p^{(1)} U_0(t', 0) | \Psi(0) \rangle. \quad (2.61)$$

Since $|\epsilon_A\rangle$ is an eigenstate of H_{scat} and the system is now completely decoupled from the scattering states due to the application of perturbation theory, we can apply time propagation to the $|\epsilon_A\rangle$ states, giving $U_0(t, t_0) |\epsilon_A\rangle = e^{-i\epsilon_A(t-t_0)} |\epsilon_A\rangle$, after which none of the a/a^\dagger -operators appear in the exponentials. The remaining ones are in the V_c -terms and can be commuted out using $a_{\sigma'}(\epsilon'_A) a_{\sigma}^\dagger(\epsilon_A) |0\rangle = 1/\rho(\epsilon_A) \delta(\epsilon_A - \epsilon'_A) |0\rangle$ to get the reduced $V_c^{(3)}$ introduced above. All of this leads to:

$$I_{\text{AES}}(\epsilon_A, t) = 2\pi\rho_p^{(0)} \int_0^t dt' s^2(t') \int_{t'}^t dt'' \int_{t'}^t dt''' e^{-i\epsilon_A(t''-t''')} \times \\ \times \langle \Psi(0) | U_0(0, t') V_p^{(1)\dagger} U_0(t', t'') V_c^{(3)\dagger} U_0(t'', t''') V_c^{(3)} U_0(t''', t') V_p^{(1)} U_0(t', 0) | \Psi(0) \rangle. \quad (2.62)$$

The scattering states are now completely eliminated and all time propagations pertain to the system alone. This expression is as far as one can go in the general pump-probe case. A comparison with (2.59) shows that it is actually not necessarily easier than the non-perturbative one, as the elimination of the scattering states is bought with an integration over three times instead of one, and the corresponding propagations in between, even though the Hilbert space dimension is now reduced.

For the time-homogeneous case $H_0 \neq H_0(t)$, the time evolution operator becomes $U_0(t, t_0) = U_0(t - t_0) = e^{-iH_0(t-t_0)}$, so that we can substitute $t_1 = t'' - t'$, $t_2 = t''' - t'$:

$$I_{\text{AES}}(\epsilon_A, t) = 2\pi\rho_p^{(0)} \int_0^t dt' s^2(t') \int_0^{t-t'} dt_1 \int_0^{t-t'} dt_2 e^{-i\epsilon_A(t_1-t_2)} \times \\ \times \langle \Psi(0) | V_p^{(1)\dagger} U_0^\dagger(-t_1) V_c^{(3)\dagger} U_0(t_1 - t_2) V_c^{(3)} U_0(t_2) V_p^{(1)} | \Psi(0) \rangle. \quad (2.63)$$

However, the divergences due to the application of the perturbation theory are now, with it having been applied two times, more difficult to deal with. In particular, the equations do not really simplify if we just set the pulse envelope to a continuous beam, $s(t) = 1$, because the upper limit of the integrals over t_1 and t_2 is $t - t'$ and the t' -integral does not go away. They do simplify, however, if we assume a finite pulse duration, so that $s(t)$ is constant up to a time $t_p \ll t$. Then the limits can be set to t and the t' -integral just gives a global factor of t_p ⁴. We obtain:

$$I_{\text{AES}}(\epsilon_A, t) = 2\pi\rho_p^{(0)} t_p \int_0^t dt_1 \int_0^t dt_2 e^{-i\epsilon_A(t_1-t_2)} \times \\ \times \langle \Psi(0) | V_p^{(1)\dagger} U_0^\dagger(-t_1) V_c^{(3)\dagger} U_0(t_1 - t_2) V_c^{(3)} U_0(t_2) V_p^{(1)} | \Psi(0) \rangle. \quad (2.64)$$

⁴The duration can also be made infinitely small, so that $s(t) = \delta(t)$ (even though this is somewhat problematic in terms of unit dimensions), which instantaneously creates a core hole at $t = 0$.

Abbreviating

$$|\Psi_{cp}(t)\rangle = e^{iH_0t}V_c^{(3)}e^{-iH_0t}V_p^{(1)}|\Psi(0)\rangle, \quad (2.65)$$

the result can also be written compactly

$$I_{\text{AES}}(\epsilon_A, t) = 2\pi\rho_p^{(0)}t_p \int_0^t dt_1 \int_0^{t_1} dt_2 \langle \Psi_{cp}(t_1) | \Psi_{cp}(t_2) \rangle e^{-i\epsilon_A(t_1-t_2)}. \quad (2.66)$$

The propagated state in eq. (2.65) can be pre-calculated and saved at the intermediate points, which allows for an efficient evaluation. Formula (2.66) was first derived by Gunnarsson and Schönhammer [Gunnarsson and Schönhammer 1980].

The result can also be rewritten in the energy domain. Here, in order to avoid divergences, it is helpful to introduce a finite core hole lifetime. This means that the Hamiltonian after the core hole excitation obtains an imaginary part: $H_0 \rightarrow H_0 - i\Gamma$, with $\Gamma > 0$. This may seem ad hoc at first, but can actually be rigorously derived in the case of the full band (see chapter 2.2.9). An approximation is, however, that Γ is a real number in all circumstances, whereas it would become an operator away from the full band in an exact calculation [Gunnarsson and Schönhammer 1980] (see chapter 2.2.9). Inserting resolutions of unity in terms of eigenstates, we can carry out the integrals. The exponentials now neatly vanish at the upper limit due to the finite Γ . Physically this means that the Auger process will be over at some point, the core hole having been filled. One obtains:

$$\begin{aligned} I_{\text{AES}}(\epsilon_A) &= 2\pi\rho_p^{(0)}t_p \sum_{mnl} \frac{\langle 0|V_p^{(1)\dagger}|l\rangle\langle l|V_p^{(3)\dagger}|m\rangle\langle m|V_p^{(3)}|n\rangle\langle n|V_p^{(1)}|0\rangle}{(\epsilon_A - i\Gamma - E_l + E_m)(\epsilon_A + i\Gamma - E_n + E_m)} \\ &= 2\pi\rho_p^{(0)}t_p \sum_m \left| \sum_n \frac{\langle m|V_c^{(3)}|n\rangle\langle n|V_p^{(1)}|0\rangle}{\epsilon_A + i\Gamma - E_n + E_m} \right|^2. \end{aligned} \quad (2.67)$$

If $V_p^{(1)}|\Psi(0)\rangle$ is an eigenstate of the system, we can simplify things further starting from (2.66). This is the case when there is no interaction between the core and valence states or when the band is completely filled. In this case, $HV_p^{(1)}|\Psi(0)\rangle = (E_0^{(N)} + (2L-1)E_c)V_p^{(1)}|\Psi(0)\rangle$ due to one missing core hole (cf. eq. 2.16⁵), where $E_0^{(N)}$ is the ground state energy of the N -particle valence band only. Applying the time evolution to this state and carrying out the time integral, one obtains:

$$\begin{aligned} I_{\text{AES}}(\epsilon_A, t) &= 2\pi\rho_p^{(0)}t_p \int_0^t dt_1 \int_0^{t_1} dt_2 \langle \Psi(0) | V_c^{(2)\dagger} e^{-i(\epsilon_A + H - E_0^{(N)} - (2L-1)E_c)(t_1-t_2)} V_c^{(2)} | \Psi(0) \rangle \\ &= 2\pi\rho_p^{(0)}t_p \sum_n |\langle n | V_c^{(2)} | \Psi(0) \rangle|^2 \frac{2 - 2 \cos\left([\epsilon_A + E_0^{(N-2)} - E_0^{(N)} + E_c]t\right)}{\left(\epsilon_A + E_0^{(N-2)} - E_0^{(N)} + E_c\right)^2}. \end{aligned} \quad (2.68)$$

And then in the usual manner as was done to derive Fermi's golden rule:

⁵The Coulomb repulsion between the core electrons U_{cc} only gives a trivial shift and will be ignored.

$$j_{\text{AES}}(\epsilon_A) = \lim_{t \rightarrow \infty} \frac{I_{\text{AES}}(\epsilon_A, t)}{t} = 4\pi^2 \rho_p^{(0)} t_p \sum_n |\langle n | V_c^{(2)} | \Psi(0) \rangle|^2 \delta(\epsilon_A + E_n^{(N-2)} - E_0^{(N)} + E_c). \quad (2.69)$$

2.2.6. APECS: perturbative

Applying the same perturbation expansion (2.60) to the more general APECS case (2.57), we obtain the following expression:

$$\begin{aligned} I_{\text{APECS}}(\epsilon_p, \epsilon_A, t) &= \int_0^t dt' \int_0^t dt'' \int_{t'}^t d\tau' \int_{t''}^t d\tau'' s(t') s(t'') e^{i\epsilon_p(t'-t'')} \times \\ &\times \langle \Psi(0) | U_0(0, t'') V_p^{(1)\dagger} U_0(t'', \tau'') V_c^\dagger U_0(\tau'', t) | \epsilon_A \rangle \\ &\times \langle \epsilon_A | U_0(t, \tau') V_c U_0(\tau', t') V_p^{(1)} U_0(t', 0) | \Psi(0) \rangle. \end{aligned} \quad (2.70)$$

We go to the time-homogeneous limit by substituting $t_1 = \tau'' - t''$ and $t_2 = \tau' - t'$, setting $s(t) \equiv 1$ up to $t_p \ll t$ as before, and pulling $|\epsilon_A\rangle$ past the time-evolution:

$$\begin{aligned} I_{\text{APECS}}(\epsilon_p, \epsilon_A, t) &= \int_0^{t_p} dt' \int_0^{t_p} dt'' \int_0^t dt_1 \int_0^t dt_2 e^{-i(E_0^{(N)} - \epsilon_p)(t'-t'')} e^{-i\epsilon_A(t_1 - t_2 + t'' - t')} \\ &\langle \Psi(0) | V_p^{(1)\dagger} U_0^\dagger(t_1) V_c^{(3)\dagger} U_0(t_1 - t_2 + t'' - t') V_c^{(3)} U_0(t_2) V_p^{(1)} | \Psi(0) \rangle. \end{aligned} \quad (2.71)$$

Using (2.65), this can be rewritten as:

$$\begin{aligned} I_{\text{APECS}}(\epsilon_p, \epsilon_A, t) &= \int_0^{t_p} dt' \int_0^{t_p} dt'' \int_0^t dt_1 \int_0^t dt_2 e^{-i(E_0^{(N)} - \epsilon_p)(t'-t'')} e^{-i\epsilon_A(t_1 - t_2 + t'' - t')} \times \\ &\times \langle \Psi_{cp}(t_1) | U_0(t'' - t') | \Psi_{cp}(t_2) \rangle. \end{aligned} \quad (2.72)$$

The integrals over t' and t'' can now be carried out to obtain:

$$\begin{aligned} I_{\text{APECS}}(\epsilon_p, \epsilon_A, t) &= \int_0^t dt_1 \int_0^t dt_2 e^{-i\epsilon_A(t_1 - t_2)} \langle \Psi_{cp}(t_1) | \Psi_{cp}(t_2) \rangle \times \\ &\times \frac{2 - 2 \cos\left([\epsilon_A + \epsilon_p + E_n^{(N-2)} - E_0^{(N)}]t\right)}{\left(\epsilon_A + \epsilon_p + E_n^{(N-2)} - E_0^{(N)}\right)^2}. \end{aligned} \quad (2.73)$$

For the coincidence setup, we cannot assume a too short duration of the photoemission pulse t_p , since it would trivialize the results, eliminating the dependence on ϵ_p . An infinite t_p , on the other

hand, leads to problems with integral limits. We thus have to assume it to be finite, but large: t_p^{-1} should be much larger than the energy difference in the cosine term. Then we can still approximate it by a delta function:

$$\begin{aligned}
I_{\text{APECS}}(\epsilon_p, \epsilon_A) &\approx 2\pi t_p \int_0^\infty dt_1 \int_0^\infty dt_2 e^{-i\epsilon_A(t_1-t_2)} \langle \Psi_{cp}(t_1) | \Psi_{cp}(t_2) \rangle \delta(\epsilon_A + \epsilon_p + E_n^{(N-2)} - E_0^{(N)}) \\
&= 2\pi t_p \int_0^\infty dt_1 \int_0^\infty dt_2 e^{-i\epsilon_A(t_1-t_2)} \langle \Psi_{cp}(t_1) | \delta(\epsilon_A + \epsilon_p + H_0 - E_0^{(N)}) | \Psi_{cp}(t_2) \rangle.
\end{aligned} \tag{2.74}$$

This is now in a mixed real-time and energy representation. We can also switch to an energy-only representation by inserting resolutions of unity in terms of eigenstates, as well as the core hole lifetime as before, obtaining:

$$I_{\text{APECS}}(\epsilon_p, \epsilon_A) = 2\pi t_p \sum_m \left| \sum_n \frac{\langle m | V_c^{(3)} | n \rangle \langle n | V_p^{(1)} | 0 \rangle}{\epsilon_A + i\Gamma - E_n + E_m} \right|^2 \delta(\epsilon_A + \epsilon_p + E_n^{(N-2)} - E_0^{(N)}). \tag{2.75}$$

Obviously, the only difference to AES is the presence of the δ -function ensuring energy conservation between the initial and the final state, resulting from the long duration of the pump pulse. An integration over ϵ_p recovers the previous AES formula (2.67).

The numerical evaluation of both formulas is straightforward: In eq. (2.74), $|\Psi_{cp}(t)\rangle$ needs to be propagated and stored at all points of the discretized integral. The delta function can be evaluated using Chebyshev polynomials (see chapter 3.3) with various $|\Psi_{cp}(t)\rangle$ as initial and final states. Eq. (2.75) can be evaluated using a three-dimensional Chebyshev expansion once the modulus square is expanded, which is a much more costly procedure, as the former approach involves two rather than three propagations/iterations.

2.2.7. Spectroscopies in perspective

While this work focuses on AES, there are several other spectroscopic setups that are very similar and can be treated within the same formalism. In this chapter, an overview and a classification is presented. The setups can be classified according to the order of perturbation theory, the number of Green's function arguments and the amount of independently measured frequencies. Table 2.1 shows an overview of the mathematical details, while fig. 2.1 displays the involved physical processes.

Photoemission (PES) This is by far the most well-known and widely implemented spectroscopy. An electron is emitted from the solid (this can be the valence band or a core level) due to the photoelectric effect and its kinetic energy distribution is measured [Schaich and Ashcroft 1970; Almladh 1985]. The light sources used in the experiment are weak enough as to justify first-order perturbation theory (Fermi's golden rule). Without interaction, this probes the density of occupied states in the valence band.

spectroscopy	PT order	GF args	#freq.	T_1	T_2	non-interact.
PES	1	1	1	$c_{i\sigma}/f_{i\sigma}$		ρ_{occ}
IPES	1	1	1	$c_{i\sigma}^\dagger$		ρ_{unocc}
AES (no CV interaction)	1	1	1	$c_{i\uparrow}c_{i\downarrow}$		$\rho_{\text{occ}} * \rho_{\text{occ}}$
AES (with CV interaction)	1	3	1	$f_{i\sigma}$	$f_{i\sigma}^\dagger c_{i\sigma} c_{i,-\sigma}$	
APS	1	1	1	$c_{i\downarrow}^\dagger c_{i\uparrow}^\dagger$		$\rho_{\text{unocc}} * \rho_{\text{unocc}}$
APECS	1	3	2	$f_{i\sigma}$	$f_{i\sigma}^\dagger c_{i\sigma} c_{i,-\sigma}$	
XAS	1	1	1	$c_{i\sigma}^\dagger f_{i\sigma}$		$\sim \rho_{\text{unocc}}$
DPS	1	3	2	$c_{i\sigma}$	$c_{j\sigma'}$	
RIXS	2	3	1	$c_{i\sigma}^\dagger f_{i\sigma}$	T_1^\dagger	$\sim \rho_{\text{occ}} * \rho_{\text{unocc}}$

Table 2.1.: A classification of various spectroscopies according to the order of perturbation theory, the number of energy summations or time integrations (Green’s function arguments), the amount of frequencies, the involved operators (see eqs. (2.77) and (2.78)) and the noninteracting limits.

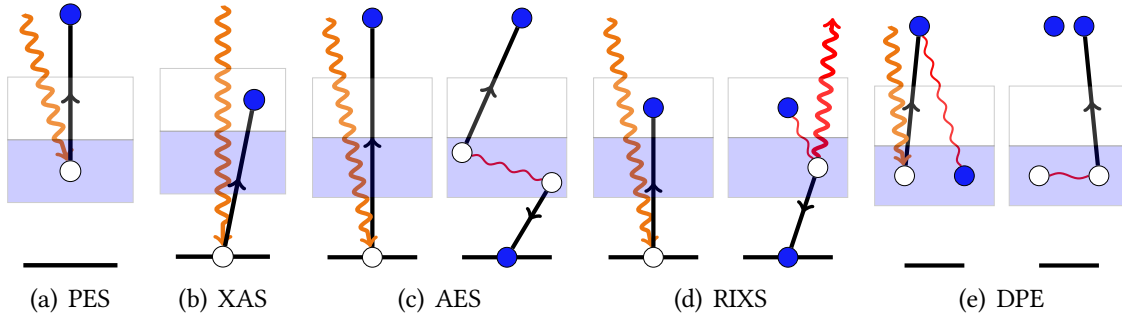


Figure 2.1.: An overview of selected spectroscopies: (a) In photoemission spectroscopy (PES), an incident photon leads to the emission of an electron from the valence band. (b) In x-ray absorption spectroscopy (XAS), an electron is excited into the unoccupied valence band. (c) In Auger electron spectroscopy (AES), a core electron is emitted. The resulting core hole is filled by another electron from the valence band. The energy released from this process is transferred to the Auger electron which is emitted and detected. (d) In resonant inelastic x-ray scattering (RIXS), the first step is identical to XAS. The resulting core hole is filled by another electron and the energy is released in an emission of second photon which is detected. (e) In double photoemission (DPE), an electron is emitted from the valence band and “drags” another electron with it due to Coulomb interaction. The electrons are analysed in two detectors.

Inverse photoemission (IPES) This is the time-inverse process of photoemission: An electron at a given kinetic energy falls into the valence band, releasing its energy as a photon [Smith 1988]. Without interaction, this probes the density of unoccupied states.

Appearance potential spectroscopy (APS) This is the time-inverse counterpart to AES: An electron at a given kinetic energy falls into the valence band and the kinetic energy is used to excite a core electron into the valence band as well [Potthoff et al. 1993a; Potthoff et al. 1993b; Potthoff et al. 1994]. One ends up with two more electrons rather than two holes in the final state. Without interaction, this measures the self-convolution of the density of unoccupied states.

X-ray absorption spectroscopy (XAS) In this setup, a core electron is excited as well, but the photon energy is tuned such that it goes into the valence band. This is similar to inverse photoemission with the difference that the electron is drawn from the core states rather than from an external source. This means there is a core potential as well and bound excitonic states are possible [Haverkort, Zwierzycki, and Andersen 2012]. Without interaction, this in principle also probes the unoccupied states, but one has to consider that there can be various core states with different degeneracies.

Double photoemission (DPE) In this setup, an incident photon is absorbed by the system, but leads to the emission of *two* electrons, whose kinetic energies are measured in coincidence, similar to APECS [Berakdar 1998; Pavlyukh, Schüler, and Berakdar 2015; Riessen et al. 2010; Pavlyukh, Schüler, and Berakdar 2015]. One would think that this requires second-order perturbation theory, since the light field is just an external potential and can only shift a single electron in first order. However, experimentally, the light intensity can be lowered so far that the integrated spectral weight is proportional to it (in our notation $\propto |d_0|^2$), proving that this is still a first-order process. Thus, the emission of the second electron must be due to a Coulomb interaction term similar to the Auger process. However, since no core levels are involved, it ought to be an interaction between three scattering states and a valence-band state:

$$V_c = U_D \sum_{i\sigma\sigma'} \prod_{\alpha=1}^3 \left(\int \rho(\epsilon) d\epsilon_\alpha \right) a_\sigma^\dagger(\epsilon_1) a_{\sigma'}^\dagger(\epsilon_2) a_{\sigma'}(\epsilon_3) c_{i\sigma} + \text{h.c.} \quad (2.76)$$

Resonant inelastic x-ray scattering (RIXS) This technique has become very popular over the last years. As in XAS, a core electron is excited into the unoccupied part of the valence band and the resulting core hole can be filled by any other electron from the valence band. This leads to the emission of a second photon whose energy is measured and may be different from the incident one. Because two photons are involved, this method requires second-order perturbation theory, translating experimentally to intense light sources (synchrotrons). RIXS can be used as a probe of magnetic excitations since the spin of the intermediate core hole can be flipped due to spin-orbit interaction. It will thus be filled by an electron of opposite spin compared to the excited one. In a limiting case, the RIXS spectrum is just given by the dynamical spin structure factor. However, the general expression is the “Kramers-Heisenberg formula”, which is just the result of second-order time-dependent perturbation theory, one order beyond Fermi’s golden rule:

$$I(\omega_1, \omega_2) = \sum_m \left| \sum_n \frac{\langle m|T_2|n\rangle \langle n|T_1|0\rangle}{\omega_1 + E_0 - E_n} \right|^2 \delta(\omega_1 - \omega_2 + E_0 - E_m), \quad (2.77)$$

where ω_1 is the fixed frequency of the incident photon and ω_2 is the measured frequency of the emitted photon.

One can see that this expression is mostly identical to the APECS case (2.75), which instead results from the application of first-order perturbation theory two times. Note, however, that ω_1 is fixed in RIXS, so that only ω_2 is a active variable. If the modulus square is expanded, one obtains a sum over three energies instead of one in Fermi's golden rule

$$I(\omega) = \sum_n |\langle n|T|0\rangle|^2 \delta(\omega - E_0 + E_n), \quad (2.78)$$

making an exact calculation more difficult.

2.2.8. Extra-atomic interferences

Let us take a closer look at expression (2.69) for the Auger current. Inserting the transition operator $V_c^{(2)}$, one obtains:

$$\begin{aligned} j_{\text{AES}}(\epsilon_A) &\propto |U_A|^2 \sum_n |\langle n | \sum_{i\sigma} c_{i\sigma} c_{i,-\sigma} | 0 \rangle|^2 \delta(\epsilon_A + E_n^{(N-2)} - E_0^{(N)} + E_c) \\ &= |U_A|^2 \sum_n \sum_{ii'\sigma\sigma'} \langle 0 | c_{i'\sigma'}^\dagger c_{i\sigma}^\dagger | n \rangle \langle n | c_{i\sigma} c_{i,-\sigma} | 0 \rangle \delta(\epsilon_A + E_0^{(N-2)} - E_n^{(N)} + E_c). \end{aligned} \quad (2.79)$$

Note that we have created a coherent superposition of doublons, since the sum over i is within the modulus square brackets. However, since the orbital-dependence of the Coulomb matrix element has been neglected, one may question whether this will be the right coherent combination. To this end, let us go back to step (2.58), where the integral over all photoelectron energies is taken. If we switch back from a continuous representation of scattering states to discrete momenta, what has to be calculated there has the following form:

$$\frac{1}{L} \sum_{\mathbf{k}_p} d_{i\mathbf{k}_p} d_{i'\mathbf{k}_p}^* f(\epsilon(\mathbf{k}_p)), \quad (2.80)$$

where the remaining dependencies have been absorbed into the function $f(\epsilon(\mathbf{k}_p))$. Let us now evaluate this sum as best as possible with reasonable assumptions. First off, it stands to reason that the dipole matrix element is local in real space:

$$d_{ij} = d_0 \delta_{ij}. \quad (2.81)$$

Its partial Fourier transform therefore becomes

$$d_{i\mathbf{k}_p} = \frac{1}{L} \sum_j d_{ij} e^{-i\mathbf{k}_p \mathbf{R}_j} = d_0 e^{-i\mathbf{k}_p \mathbf{R}_i} \quad (2.82)$$

Plugging this into eq. (2.80), one has to calculate:

$$\frac{1}{L} \sum_{\mathbf{k}_p} e^{-i\mathbf{k}_p \mathbf{R}_{ii'}} f(\epsilon(\mathbf{k}_p)) = \int d\epsilon_p \rho_{ii'}(\epsilon_p) f(\epsilon_p) \quad (2.83)$$

where $\rho_{ii'}(\epsilon_p)$ is the *lattice density of states* of the photoelectrons

$$\rho_{ii'}(\epsilon_p) = \frac{1}{L} \sum_{\mathbf{k}_p} \delta(\epsilon_p - \epsilon(\mathbf{k}_p)) e^{-i\mathbf{k}_p \mathbf{R}_{ii'}}, \quad (2.84)$$

and $\mathbf{R}_{ii'} = \mathbf{R}_i - \mathbf{R}_{i'}$. We can evaluate it for free electrons $\epsilon_p = \mathbf{k}_p^2/2m$:

$$\begin{aligned} \rho_{ii'}(\epsilon_p) &= \frac{1}{L} \frac{V}{(2\pi)^3} \int_0^\infty dk_p k_p^2 \int_{-1}^{+1} d \cos \theta \delta\left(\epsilon_p - \frac{k^2}{2m}\right) e^{-ik_p R_{ii'} \cos \theta} \\ &= \frac{1}{L} \frac{V}{(2\pi)^3} \int_0^\infty dk_p k_p^2 \delta\left(\epsilon_p - \frac{k_p^2}{2m}\right) \frac{2 \sin(k_p R_{ii'})}{k_p R_{ii'}} \\ &= \frac{1}{L} \frac{V}{(2\pi)^3} \frac{1}{2\sqrt{2m\epsilon_p}} \int_0^\infty dk_p k_p^2 (\delta(k_p - \sqrt{2m\epsilon_p}) + \delta(k_p + \sqrt{2m\epsilon_p})) \frac{2 \sin(k_p R_{ii'})}{k_p R_{ii'}} \\ &= 2\sqrt{2m\epsilon_p} \frac{\sin(k_p R_{ii'})}{k_p R_{ii'}} \\ &= \frac{1}{2\pi} \rho(\epsilon_p) \frac{\sin(k_p R_{ii'})}{k_p R_{ii'}}, \end{aligned} \quad (2.85)$$

where $\rho(\epsilon_p)$ is the usual density of states for free particles:

$$\rho(\epsilon_p) = \frac{1}{L} \sum_{\mathbf{k}_p} \delta(\epsilon_p - \epsilon(\mathbf{k}_p)) = 4\pi \sqrt{2m\epsilon_p}. \quad (2.86)$$

One observes that $\rho_{ii'}(\epsilon_p)$ is peaked at $R_{ii'} = 0$. The nearest neighbours give little contribution if it holds for the lattice spacing that $a \gg k_p^{-1}$, that is if the photoelectron momentum is sufficiently high. Hence $\rho_{ii'}(\epsilon_p) \sim \rho(\epsilon_p) \delta_{ii'}$. This means that extra-atomic contributions interfere destructively, which has consequences for the Auger term, as well: The double sum over the orbitals in eq. (2.79) reduces to a single sum, which in turn gives the same contribution for each site due to translational invariance, and thus a factor of L , while the spin summation gives a factor of 2:

$$j_{\text{AES}}(\epsilon_A) \propto 2L |U_A|^2 \sum_n |\langle n | c_{i\uparrow} c_{i\downarrow} | 0 \rangle|^2 \delta\left(\epsilon_A + E_n^{(N-2)} - E_0^{(N)} + E_c\right). \quad (2.87)$$

For more details and further issues regarding interference effects, see [Abraham-Ibrahim et al. 1978](#).

2.2.9. AES: nonperturbative

Let us investigate what happens if we try to treat the Auger term nonperturbatively. This is more conveniently done in the Laplace space and the resulting expression can be exactly evaluated for the full band. Thus, keeping V_p perturbatively, but treating V_c to all orders, the Auger intensity can be expressed in the following fashion (see eq. (B.29)):

$$I(\epsilon_A, \epsilon_p, t) = \sum_n \left| \frac{1}{2\pi i} \int_C dz e^{-izt} \int_{-\infty}^{+\infty} d\tilde{\omega} s(\tilde{\omega}) \frac{1}{z - \omega - E_0^{(N)}} G_n(\epsilon_A, \epsilon_p, z) \right|^2, \quad (2.88)$$

where C is the Bromwich integral on a line parallel to the real axis above all singularities of the integrand. The quantity G which naturally appears in the calculation is very similar to a Green's function, but involves the overlap with an excited state:

$$G_n(\epsilon_A, \epsilon_p, z) = \langle n, \epsilon_A, \epsilon_p | \hat{G}(z) V_p | \Psi(0) \rangle, \quad (2.89)$$

where the operator \hat{G} is given by the perturbation series

$$\hat{G}(z) = \frac{1}{z - H_0 - V_c} = \frac{1}{z - H_0} + \frac{1}{z - H_0} V_c \frac{1}{z - H_0} + \frac{1}{z - H_0} V_c \frac{1}{z - H_0} V_c \frac{1}{z - H_0} + \dots \quad (2.90)$$

As before, we can pull the operator $a_{\sigma_p}^\dagger(\epsilon_p)$ past the resolvents and let it cancel with the bra state $\langle 0 | a_{\sigma_p}(\epsilon_p)$. Remember that we assume the photoelectron and the Auger electron as distinguishable, so that the latter states remain unaffected. Pulling the operator past $\hat{G}(z)$ just shifts the argument by ϵ_p and we need to replace V_p by $V_p^{(1)}$:

$$G_n(\epsilon_A, \epsilon_p, z) = \langle n, \epsilon_A | \hat{G}(z - \epsilon_p) V_p^{(1)} | \Psi(0) \rangle. \quad (2.91)$$

Let us now decompose the Auger term into a term V_c^- which creates the outgoing electron, reducing the amount of particles in the system by one; and a term V_c^+ which lets the Auger electron recombine:

$$\begin{aligned} V_c &= U_A \sum_{i\sigma_A} \int \rho(\epsilon_A) d\epsilon_A \left(f_{i\sigma_A}^\dagger a_{-\sigma_A}^\dagger(\epsilon_A) c_{i\sigma_A} c_{i,-\sigma_A} + \text{h.c.} \right) \\ &\equiv V_c^- + V_c^+ \\ &= V_c^- + (V_c^-)^\dagger = (V_c^+)^\dagger + V_c^+ \end{aligned} \quad (2.92)$$

Since there is only one core hole due to perturbation theory in V_p , there can only be at most one Auger electron at a time. Thus, the identity operator can be written in the following fashion:

$$\mathbb{1} = \sum_l |n\rangle \langle n|_{(N-1)} \otimes |0\rangle \langle 0| + \sum_n \int \rho(\epsilon_A) d\epsilon_A |n\rangle \langle n|_{(N-2)} \otimes |\epsilon_A\rangle \langle \epsilon_A|. \quad (2.93)$$

Note that N now refers to both the valence band and the core states. The Auger term mediates between these two subspaces:

$$\begin{aligned} V_c^- |n(N-2), \epsilon_A\rangle &= 0 \\ V_c^- |n(N-1), 0\rangle &= \int \rho(\epsilon_A) d\epsilon_A |\epsilon_A\rangle V_c^{(3)-} |n(N-1)\rangle \\ V_c^+ |n(N-1), 0\rangle &= 0 \\ V_c^+ |n(N-2), \epsilon_A\rangle &= |0\rangle V_c^{(3)+} |n(N-2)\rangle \end{aligned} \quad (2.94)$$

The nonzero matrix elements are hence:

$$\begin{aligned}
\langle n(N-2), \epsilon_A | V_c^- | m(N-1), 0 \rangle &= \langle n(N-2) | V_-^{(3)} | m(N-1) \rangle \\
\langle n(N-1), 0 | V_c^+ | m(N-2), \epsilon_A \rangle &= \langle n(N-1) | V_+^{(3)} | m(N-2) \rangle \\
&= \langle m(N-2) | V_-^{(3)} | n(N-1) \rangle^*
\end{aligned} \tag{2.95}$$

Inserting the identity operator $\mathbb{1}$ after the first application of V_c on the left (note that the zeroth order without any Auger term $V_c^{(3)}$ vanishes), as well as before $V_p^{(1)} | \Psi(0) \rangle$ on the right of eq. (2.91) gives:

$$\begin{aligned}
G_n(\epsilon_a, \epsilon_p, z) &= \frac{1}{z - \epsilon_p - \epsilon_A - E_n^{(N-2)}} \sum_{lm} \langle n(N-2) | V_c^{(3)} | l(N-1) \rangle \times \\
&\quad \times R_{lm}(z - \epsilon_p) \langle m(N-1) | V_p^{(1)} | \Psi(0) \rangle.
\end{aligned} \tag{2.96}$$

The kernel $R_{lm}(z)$ can only contain pairwise products of V_c^+ and V_c^- to get a nonzero matrix element:

$$\begin{aligned}
R_{lm}(z) &= \langle l(N-1) | \left(\frac{1}{z - \epsilon_p - H_0} + \frac{1}{z - \epsilon_p - H_0} V_c^+ \frac{1}{z - \epsilon_p - H_0} V_c^- \frac{1}{z - \epsilon_p - H_0} + \dots \right) | m(N-1) \rangle \\
&= \frac{1}{z - \epsilon_p - E_l^{(N-1)}} \left(\delta_{lm} + \frac{\Sigma_{lm}(z)}{z - E_m^{(N-1)}} + \sum_r \frac{\Sigma_{lr}(z)}{z - E_r^{(N-1)}} \frac{\Sigma_{rm}(z)}{z - E_m^{(N-1)}} + \dots \right) \\
&= \frac{1}{z - \epsilon_p - E_l^{(N-1)}} (\mathbb{1} + \mathbf{O}(z) + \mathbf{O}^2(z) + \mathbf{O}^3(z) + \dots)_{lm} \\
&= \frac{1}{z - \epsilon_p - E_l^{(N-1)}} ((\mathbb{1} - \mathbf{O}(z))^{-1})_{lm},
\end{aligned} \tag{2.97}$$

with the geometric sum over powers of the operator

$$(\mathbf{O}(z))_{lm} = \frac{\Sigma_{lm}(z)}{z - \epsilon_p - E_m^{(N-1)}}, \tag{2.98}$$

where a self-energy-like quantity Σ_{lm} appears, which describes the process of an Auger emission, propagation of the system in the $(N-2)$ -particle subspace, followed by an Auger recombination (where the Auger electron falls back into the valence band and the core hole is recreated), all evaluated within two eigenstates:

$$\begin{aligned}
\Sigma_{lm}(z) &= \langle l(N-1) | V_c^+ \frac{1}{z - \epsilon_p - H_0} V_c^- | m(N-1) \rangle \\
&= \sum_r \int \rho(\epsilon_A) d\epsilon_A \frac{\langle l(N-1) | V_+^{(3)} | r(N-2) \rangle \langle r(N-2) | V_-^{(3)} | m(N-1) \rangle}{z - \epsilon_p - \epsilon_A - E_r^{(N-2)}} \\
&= \sum_r \sum_{i\sigma_A i'\sigma'_A} \langle l(N-1) | c_{i',-\sigma'_A}^\dagger c_{i\sigma_A}^\dagger f_{i'\sigma'_A} | r(N-2) \rangle \langle r(N-2) | f_{i\sigma_A}^\dagger c_{i\sigma_A} c_{i,-\sigma_A} | m(N-1) \rangle \times \\
&\quad \times |U_A|^2 \int d\epsilon_A \frac{\rho(\epsilon_A)}{z - \epsilon_p - \epsilon_A - E_r^{(N-2)}}.
\end{aligned} \tag{2.99}$$

Supposing that the density of states is approximately constant, $\rho_A(E) \approx \rho_A^0$, one obtains for the last term near the real axis, for $z = \omega \pm i0^+$:

$$|U_A|^2 \int d\epsilon_A \frac{\rho(\epsilon_A)}{\omega \pm i0^+ - \epsilon_p - \epsilon_A - E_r^{(N-2)}} \approx \mp i\pi \rho_A^0 |U_A|^2. \quad (2.100)$$

The self-energy is then frequency-independent and purely imaginary:

$$\Sigma_{lm}(\omega \pm i0^+) = \mp i\Gamma_{lm}. \quad (2.101)$$

For an initially fully occupied valence band Σ_{lm} loses its dependence on the eigenstate indices. The eigenstates in the $(N-1)$ -subspace just consist out of a core hole at some lattice site i_0 with a spin σ_p and can be labelled accordingly: $|i_0, \sigma_p\rangle = f_{i_0\sigma_p}|0\rangle$. However, because of translational invariance and the fact the valence band is full and looks the same, this is just the same state and Auger recombination always brings the system back to it. We can hence drop the indices l and m and use $E^{(N-1)}$ for the energy of this state:

$$\begin{aligned} \Sigma(\omega \pm i0^+) &= \mp i\pi \rho_A^0 |U_A|^2 \sum_r |\langle r(N-2) | \sum_{i\sigma_A} f_{i,\sigma_A}^\dagger c_{i\sigma_A} c_{i,-\sigma_A} f_{i_0\sigma_p} |0\rangle|^2 \\ &= \mp i\pi \rho_A^0 |U_A|^2 \sum_r |\langle r(N-2) | c_{i_0\sigma_p} c_{i_0,-\sigma_p} |0\rangle|^2 \\ &\equiv \mp i\Gamma. \end{aligned} \quad (2.102)$$

The kernel reduces to:

$$R(\omega \pm i0^+) = \frac{1}{\omega - \epsilon_p - E^{(N-1)} \pm i\Gamma}. \quad (2.103)$$

Finally, one obtains the result:

$$\begin{aligned} G_n(\epsilon_A, \epsilon_p, \omega \pm i0^+) &= U_A d_0 \langle n(N-2) | \sum_i c_{i\sigma_p} c_{i,-\sigma_p} |0(N)\rangle \times \\ &\times \frac{1}{\omega \pm i0^+ - \epsilon_p - \epsilon_A - E_n^{(N-2)}} \cdot \frac{1}{\omega - \epsilon_p - E^{(N-1)} \pm i\Gamma}. \end{aligned} \quad (2.104)$$

This means that the only difference to the perturbative case is the addition of a finite imaginary part to the eigenenergies in the propagation after the photoexcitation: $\epsilon_p + E^{(N-1)} \rightarrow \epsilon_p + E^{(N-1)} - i\Gamma$ (for the retarded case $\omega + i0^+$). The calculation is not fully complete, of course: One has to insert (2.104) back into (2.88), perform a partial fraction decomposition $\frac{1}{z-A} \frac{1}{z-B} = \frac{1}{A-B} \left(\frac{1}{z-A} - \frac{1}{z-B} \right)$ and calculate the Laplace back transform exploiting the fact that a Hermitian operator has all of its poles (discrete spectrum) or branch cuts (continuous spectrum) on the real axis. Having done that, after a lengthy computation (which is left out here), expression (2.66) with a finite Γ is eventually recovered.

The inverse of Γ can be interpreted as the core hole lifetime. One can see that it lives longer for (1) weak coupling to the continuum U_A , (2) few available states for the decay (small ρ_A^0), (3) a smaller overlap of the two-hole state with the eigenstates of the system.

In spectroscopical calculations, it is common practice to include such a finite Γ as a parameter,

termed “optical potential” [[Gunnarsson and Schönhammer 1980](#)]. It is then approximated to be just a number, whereas the exact formulae (2.97) and (2.99) produce a frequency-dependent operator. Since its calculation requires a matrix inversion on the whole Hilbert space, it is clearly not feasible for reasonably-sized systems.

3. Methods

3.1. Exact Diagonalization

“Exact Diagonalization”¹ (ED) is a somewhat unfortunate term which refers to solving quantum lattice models numerically exactly. Ground states can be obtained by the Lanczos algorithm (see chapter 3.2); for dynamical correlation functions and time-propagations with a time-independent Hamiltonian $H \neq H(t)$ one can employ a modified form of the Lanczos algorithm or the Chebyshev expansion (see chapter 3.3); for a generic time-propagation with a time-dependent Hamiltonian $H(t)$ one can pair the latter methods with the *commutator-free exponential time-propagation* algorithm (CFET, see chapter 3.4). Neither of the methods actually involves a diagonalization of H , they rather reduce the problem to matrix-vector multiplications of the Hamiltonian with the wavefunction in the full basis. Whenever diagonalization is performed, it is usually called “full diagonalization”.

It is well-known that the Hilbert space of a quantum system grows exponentially with the system size L^d . This can be immediately deduced from the fact that the entropy is on the one hand an extensive quantity, $S \sim L^d$; and at the same time is related to the amount of microstates via the Boltzmann relation $S \sim \ln \dim \mathcal{H}$, so that $\dim \mathcal{H} \sim e^{L^d}$. This means that the ED method is limited to small system sizes: For the one-dimensional Hubbard model with N_\uparrow spin-up particles and N_\downarrow spin-down particles we have $\dim \mathcal{H} = \binom{L}{N_\uparrow} \cdot \binom{L}{N_\downarrow}$. The greatest resource consumption occurs at half filling $N_\uparrow = N_\downarrow = \frac{L}{2}$, where for $L = 16$, the Hilbert space exceeds $165.6 \cdot 10^6$ and the required memory to store a single state reaches about 1.23 GB, so that the calculations become severely limited by current hardware rather quickly. It is even more costly to store the Hamiltonian; luckily it is a sparse matrix due to the tight-binding nature of the hopping. Its memory consumption can be quantified by introducing the amount of non-zeros per row or column α . For the Hubbard model we have $\alpha \sim 6 - 11$ in $d = 1$ and up to $\alpha \sim 20$ in $d = 2$ (when hermiticity is also exploited). There are more entries in two dimensions because of more hopping options. In other words, the Hamiltonian roughly takes up the memory of $O(10)$ states. Its storage can actually be avoided altogether, at the expense of some calculation time (see below).

The first step is to define a basis to work with. Since we are working with fermions, the numbering of the orbitals is important to impose the correct anticommutation relations. In the case of ED, the following order is convenient:

$$|n_{1\uparrow} \dots n_{L\uparrow} n_{1\downarrow} \dots n_{L\downarrow}\rangle := \left(c_{1\uparrow}^\dagger\right)^{n_{1\uparrow}} \dots \left(c_{L\uparrow}^\dagger\right)^{n_{L\uparrow}} \left(c_{1\downarrow}^\dagger\right)^{n_{1\downarrow}} \dots \left(c_{L\downarrow}^\dagger\right)^{n_{L\downarrow}} |0\rangle. \quad (3.1)$$

This means that one puts all the spin-up creation operators before all the spin-down ones. Because each orbital can only be occupied by either zero or one fermion, we can use bitsets to encode the state numerically, which does not require much memory. Moreover, the chosen order and the fact that the hopping preserves spin permits one to build up the Hilbert spaces for each spin orientation independently and then combine them into the full model. Thus, we can first set up the basis for spinless fermions (a common short term for fermions of the same spin orientation) by

¹In the atomic and molecular community, this is equivalent to “full configuration interaction”.

$$|n_1 n_2 \dots n_L\rangle := \left(c_1^\dagger\right)^{n_1} \dots \left(c_L^\dagger\right)^{n_L} |0\rangle. \quad (3.2)$$

It is of course convenient for the basis to have a sort order of some kind, so that one can find a given state efficiently. A natural choice is found by realizing that a bitset of occupation numbers like 0101011 defines a binary number, so that the basis states can simply be sorted according to that very value. However, one should avoid a naive conversion into decimals, since the values will become rather large. Instead, noticing that this ordering is equal to the colexicographical (or ‘‘colex’’) order of all subsets of $\binom{L}{N}$, one can make use of a well-known recursive combinatorial algorithm to create these subsets in just a few lines of code [[Ruskey 2003](#)].

The next step is to set up the Hamiltonian in matrix form (or, more generally, also the operators c_i and c_i^\dagger). To do that, one simply loops through the basis and applies the creation or annihilation operator by flipping the corresponding bit. This gives a new state which one can find in the sorted target basis using bisection (so that the total effort scales as $N \log N$). The result will then be either $+1$ or -1 . For c_i , this depends on whether there is an even or odd amount of fermions (set bits) between the first and the i -th site, since it requires that many transpositions to move the operator to the right place in (3.2). For a hopping term $c_i^\dagger c_j$, one only needs to count the amount of set bits between i and j , since the other ones cancel out.

Having set up the hopping matrices \underline{T}_\uparrow and \underline{T}_\downarrow , the Hubbard Hamiltonian is found via

$$\begin{aligned} \underline{H} &= \underline{T}_\uparrow \otimes \mathbb{1}_\downarrow + \mathbb{1}_\uparrow \otimes \underline{T}_\downarrow + \underline{U} \\ &= \underline{T}_\uparrow \oplus \underline{T}_\downarrow + \underline{U}, \end{aligned} \quad (3.3)$$

where $\mathbb{1}_\sigma$ is the unity operator on the Hilbert space with the spin orientation σ , and \underline{U} is a diagonal matrix where each entry on row and column i is given by the amount of set bits in the state i on the full Hilbert space times the Coulomb interaction U . The tensor products appearing in the above relation can be implemented as Kronecker products for the given matrices. This means that the mapping from the state indices of the spin subspaces i_\uparrow and i_\downarrow to the index i on the full Hilbert space is achieved via

$$i = i_\downarrow + \dim \mathcal{H}_\downarrow \cdot i_\uparrow. \quad (3.4)$$

Vice versa, given i , one obtains $i_\downarrow = i \bmod \mathcal{H}_\downarrow$ and $i_\uparrow = i \operatorname{div} \mathcal{H}_\downarrow$ where the latter represents integer division, i.e. division without remainder. This is of course just a special case of a mapping of r indices $i_1 \dots i_r$, each having its own range $n_1 \dots n_r$ to a super-index i given by:

$$\begin{aligned} i &= i_r + n_r (i_{r-1} + n_{r-1} (\dots (i_2 + n_2 i_1) \dots)) \\ &= i_r + i_{r-1} n_r + i_{r-2} n_r n_{r-1} + \dots + i_1 n_r n_{r-1} \dots n_2, \end{aligned} \quad (3.5)$$

which is very useful in numerous applications. The reverse mapping is found via successive mod and div operations. Note that if all the ranges are equal, $n_1 = n_2 = \dots n_r =: n$, this is simply the representation of the number i in base n where each i_r is the corresponding digit; otherwise we are dealing with a so-called mixed-radix representation.

Since \underline{T}_σ is a Hermitian matrix, it is sufficient to store only the upper or lower triangle. The Kronecker product preserves this property, so that \underline{H} will also be upper or lower triangular. The action

of the matrix elements in the other triangle is then taken into account during the matrix-vector multiplication itself.

In the case of the Peierls substitution (see chapter 2.1.5), however, the hopping becomes complex and direction-dependent. It has the form $e^{iA(t)}$ for hopping processes from left to right through the one-dimensional chain, and $e^{-iA(t)}$ for hopping processes in the reverse direction. In this case, the corresponding directional hopping matrices $\underline{T}_\sigma^>$ and $\underline{T}_\sigma^<$ are not necessarily equivalent to the upper and lower triangles of the full hopping matrix. However, it still holds that $\underline{T}_\sigma^< = (\underline{T}_\sigma^>)^T$. The Hamiltonian can then be written in the following fashion:

$$\begin{aligned} \underline{H} &= (e^{+iA(t)}\underline{T}_\uparrow^> + e^{-iA(t)}\underline{T}_\uparrow^<) \otimes \mathbb{1}_\downarrow + \mathbb{1}_\uparrow \otimes (e^{+iA(t)}\underline{T}_\downarrow^> + e^{-iA(t)}\underline{T}_\downarrow^<) + \underline{U} \\ &= e^{+iA(t)}\underline{T}^> + e^{-iA(t)}(\underline{T}^>)^T + \underline{U}, \end{aligned} \quad (3.6)$$

where $\underline{T}^> = \underline{T}_\uparrow^> \oplus \underline{T}_\downarrow^>$. In this case, it is always convenient to store just the real matrix $\underline{T}^>$ and only recalculate the phase $e^{iA(t)}$. A matrix-vector multiplication then involves the application of $\underline{T}^>$ with the phase factor $e^{iA(t)}$, its transpose with the conjugate phase factor, and finally the diagonal matrix \underline{U} , all in succession.

In order to preserve working memory, one can store the Hamiltonian on the hard drive or avoid storing it altogether and instead use a function which calculates the result of its application to a given basis state. However, in order to maintain some compromised efficiency, one can also exploit the tensor-product structure of the Hubbard model. A look at eq. (3.3) reveals that rather than calculating the tensor product explicitly, we can just calculate \underline{T}_\uparrow and \underline{T}_\downarrow . These subspaces do not actually require much memory (compare again the case $L = 16$ and $N_\uparrow = N_\downarrow = 8$, equivalent to $\dim\mathcal{H}_\sigma = 12870$, thus merely 100 kilobytes!). The full Hamiltonian matrix contains \underline{T}_\uparrow and \underline{T}_\downarrow as block matrices, we just need to find the right block in the vector we want to apply the Hamiltonian to. Thus, the problem boils down to the memory-efficient calculation of

$$\mathbf{v}' = \mathbb{1}_l \otimes \underline{H} \otimes \mathbb{1}_r \cdot \mathbf{v}, \quad (3.7)$$

for a given matrix \underline{H} , a given vector \mathbf{v} and given left and right sizes N_l and N_r of the identity matrices $\mathbb{1}_l$ and $\mathbb{1}_r$, respectively. A tested algorithm which achieves that is the so-called *shuffle algorithm* [Czekster et al. 2007; Fernandes, Plateau, and Stewart 1998]; it is presented in alg. 1.

Of course, it does not have to be executed if $N_r = 1$, as the resulting matrix will simply consist out of blocks of \underline{H} on the diagonal, so that \underline{H} can be applied to the appropriate segments of the vector \mathbf{v} , and can thus be even trivially parallelized. However, no such simple form appears in the case of $N_l = 1$ because the Kronecker product is not commutative. Still, a relationship between the two exists in the form of [Davio 1981]

$$\underline{H} \otimes \mathbb{1}_r = \underline{S}_{N_r, N} \cdot (\mathbb{1}_l \otimes \underline{H}) \cdot \underline{S}_{N, N_r}. \quad (3.8)$$

Here, $\underline{S}_{a,b}$ is an $(ab) \times (ab)$ permutation matrix, called the *perfect shuffle*, and \underline{H} is assumed to be $N \times N$. A similar relation exists for the case of two identity matrices:

$$\mathbb{1}_l \otimes \underline{H} \otimes \mathbb{1}_r = \underline{S}_{N_r, N_l N} \cdot (\mathbb{1}_{lr} \otimes \underline{H}) \cdot \underline{S}_{N_l N, N_r} \quad (3.9)$$

where $\mathbb{1}_{lr}$ is of dimension $N_l N_r$ identity matrix.

Algorithm 1 Pot-Sh⁺ algorithm

```
1: procedure POTSHPLUS(diml, dimH, dimr, H, Vin, Vout) ▷ Calculates
    $V_{out} \leftarrow \mathbb{1}_{diml \times diml} \otimes H_{dimH \times dimH} \otimes \mathbb{1}_{dimr \times dimr} \cdot V_{in}$  in a memory-efficient way
2:    $V_{out} \leftarrow V_{in}$ 
3:    $base \leftarrow 0$ 
4:    $jump \leftarrow dimH * dimr$ 
5:   for  $block = 0, 1, \dots, diml - 1$  do
6:     for  $offset = 0, 1, \dots, dimr - 1$  do
7:        $index \leftarrow base + offset$ 
8:       allocate  $V_{tmp}$  of size  $dimH$ 
9:       for  $h = 0, 1, \dots, dimH - 1$  do
10:         $V_{tmp}[h] \leftarrow V_{out}[index]$ 
11:         $index \leftarrow index + dimr$ 
12:        $V_{tmp} \leftarrow H * V_{tmp}$ 
13:        $index \leftarrow base + offset$ 
14:       for  $h = 0, 1, \dots, dimH - 1$  do
15:         $V_{out}[index] \leftarrow V_{tmp}[h]$ 
16:         $index \leftarrow index + dimr$ 
17:        $base \leftarrow base + jump$ 
```

Let us delve very briefly into the question of how to calculate the perfect shuffle $S_{a,b}$ without bringing up too many number-theoretical details. In the case of $a = b$ (which means $\dim \mathcal{H}_\uparrow = \dim \mathcal{H}_\downarrow$, i.e. half filling), an efficient algorithm has been recently developed by Yang et al., exploiting the fact that each permutation can be written as a product of two involutions² [Yang et al. 2013]. For our needs, this boils down to alg. 2, called *revswap*. Note that the loop body just reverses the last two digits of i in binary representation, obtaining j and converts this result into a decimal representation. This defines the indices to be swapped.

Algorithm 2 revSwap2 algorithm

```
1: procedure REVSWAP(k, Vinout) ▷ Calculates the perfect shuffle  $S_{k,k}$  for a vector with  $N = k^2$ 
   rows.
2:    $N \leftarrow rows(Vinout)$ 
3:   for  $i = 1, 2, \dots, N - 2$  do
4:      $r \leftarrow i$ 
5:      $ultimate \leftarrow r \bmod k$ 
6:      $r \leftarrow r \operatorname{div} k$ 
7:      $penultimate \leftarrow r \operatorname{div} k$ 
8:      $j \leftarrow i + ultimate * (k - 1) + penultimate * (1 - k)$ 
9:     if  $i < j$  then
10:       $Vinout(i) := Vinout(j)$ 
```

However, for $a \neq b$ calculating the perfect shuffle is much more costly, involving the calculation of the greatest common divisor of two numbers. Even though this can be done rather efficiently by Euler's algorithm, this method has performed very poorly in practice due to the sheer amount of operations involved when the Hilbert space dimension is high; and could not outperform the shuffle algorithm. Thus, in the calculations performed in this work, the shuffle algorithm was used when the Hilbert space exceeded a certain size, except at half filling, where the in-place revswap was used.

²An involution is a self-inverse mapping.

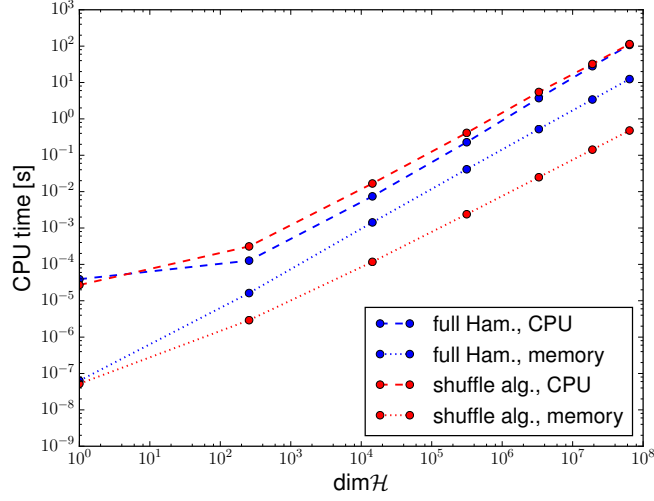


Figure 3.1.: Comparison of the CPU time in seconds needed for a matrix-vector multiplication (averaged over 10 MVMs, dashed lines) and the memory consumption of the Hamiltonian in gigabytes (dotted lines) as a function of the Hilbert space dimension for the two approaches: When the full Hamiltonian is constructed (blue) and when only the spin subspaces are constructed and the shuffle algorithm is used (red).

All in all, the memory can be managed dynamically in the following fashion: If the Hilbert space does not exceed a threshold value (10^7 was set in this work), the full Hamiltonian is constructed. Otherwise, only the spin subspaces and the interaction part \underline{U} from eq. (3.3) are constructed fully and the shuffle of revswap algorithms are used for matrix-vector multiplications. The memory consumption of the subspaces can be neglected, while \underline{U} takes as much memory as one vector from the Hilbert space.

A benchmark of the two approaches is shown in fig. 3.1, where the matrix-vector multiplication time and the memory consumption of the Hamiltonian are measured for an $L = 4 \times 4$ Hubbard model with varying filling, thereby varying the Hilbert space dimension. It turns out that the shuffle algorithm performs only slightly worse, and for the largest Hilbert spaces just as well, probably due to the denser Hamiltonian as compared to $d = 1$. On the other hand, the memory consumption is smaller by a factor of up to 26.

3.2. The Lanczos algorithm

3.2.1. The ground state

If we seek to minimize the ground-state energy functional of a quantum system described by the wavefunction $|\Psi\rangle$,

$$E[\Psi] = \frac{\langle \Psi | H | \Psi \rangle}{\langle \Psi | \Psi \rangle}, \quad (3.10)$$

we can do so by first defining a gradient vector as the derivative with respect to $\langle \Psi |$:

$$\frac{\delta E[\Psi]}{\delta \langle \Psi |} = \frac{H|\Psi\rangle - E[\Psi]|\Psi\rangle}{\langle \Psi | \Psi \rangle} = |\Psi_{\text{grad}}\rangle. \quad (3.11)$$

An initial guess for $|\Psi\rangle$ will be improved if we go in the direction of steepest descent, i.e. $E[\Psi - \alpha\Psi_{\text{grad}}] < E[\Psi]$ for an $\alpha > 0$ which needs to be determined. To do so, it is helpful to form an orthogonal basis $|u\rangle_0, |u\rangle_1$ from the vectors $|\Psi\rangle$ and $|\Psi_{\text{grad}}\rangle$. A look at eq. (3.11) reveals that the space spanned by them is equal to the space spanned by $|\Psi\rangle$ and $H|\Psi\rangle$: $\text{span}(|\Psi\rangle, |\Psi_{\text{grad}}\rangle) = \text{span}(|\Psi\rangle, H|\Psi\rangle)$. Using this orthogonal basis, a general vector $|u\rangle$ can be written as:

$$|u\rangle = \cos\theta|u_0\rangle + \sin\theta|u_1\rangle. \quad (3.12)$$

A minimization with respect to θ leads to the improved guess

$$|\Psi\rangle_{\min} = \cos\theta_{\min}|u_0\rangle + \sin\theta_{\min}|u_1\rangle \quad (3.13)$$

and implicitly defines the abovementioned α . The procedure can now be repeated with $|\Psi\rangle_{\min}$ as the starting guess. Seeing however, that the minimization with respect to θ is of negligible numerical cost (it is equivalent to finding the lowest eigenvalue in the two-dimensional space $\text{span}(|\Psi\rangle, H|\Psi\rangle)$), we can do even better than that and work on a much larger space, the Krylov space of dimension N (typically $N \lesssim 100$):

$$\mathcal{K}_N[u_0, H] := \text{span}(|u_0\rangle, H|u_0\rangle, H^2|u_0\rangle, \dots, H^{N-1}|u_0\rangle). \quad (3.14)$$

It turns out that the orthogonal basis for this space can be constructed iteratively and is no more costly than in the case of two vectors. We can start by orthogonalizing $H|u_0\rangle$ and $|u_0\rangle$, leading to:

$$|\tilde{u}_1\rangle = H|u_0\rangle - a_0|u_0\rangle, \quad (3.15)$$

where $a_0 = \langle u_0|H|u_0\rangle$. The tilde in $|\tilde{u}_1\rangle$ indicates that this vector is not normalized yet. We obtain the first Lanczos vector $|u_1\rangle$ by normalizing it:

$$|u_1\rangle = \frac{1}{b_1}|\tilde{u}_1\rangle, \quad (3.16)$$

with $b_1^2 = \langle \tilde{u}_1|\tilde{u}_1\rangle$. At the n -th step we orthogonalize $|\tilde{u}_n\rangle$ to all the previous vectors:

$$|\tilde{u}_n\rangle = H|u_n\rangle - \sum_{i=0}^n \langle u_i|H|u_n\rangle|u_i\rangle. \quad (3.17)$$

Exploiting this relationship for $|u_0\rangle \dots |u_{n-1}\rangle$ and the fact that these vectors have already been made orthonormal, one sees that the above sum reduces to:

$$\sum_{i=0}^n \langle u_i|H|u_n\rangle|u_i\rangle = a_n|u_n\rangle + b_n|u_{n-1}\rangle, \quad (3.18)$$

with

$$a_n = \langle u_n|H|u_n\rangle, \quad b_n^2 = \langle \tilde{u}_n|\tilde{u}_n\rangle \quad (3.19)$$

and

$$|u_n\rangle = \frac{1}{b_n}|\tilde{u}_n\rangle. \quad (3.20)$$

Thus, we arrive at the central relation of the Lanczos algorithm, the three-term recurrence relation:

$$b_{n+1}|u_{n+1}\rangle = H|u_n\rangle - b_n|u_{n-1}\rangle - a_n|u_n\rangle, \quad (3.21)$$

from which one can see that obtaining an additional Lanczos vector requires one matrix-vector multiplication, not counting the orthogonalizations. These multiplications are the most costly part of the algorithm and can be taken as a measure of the numerical effort. Eq. (3.21) also shows that the Hamiltonian in the Krylov space $H^\mathcal{K}$ (with $(H^\mathcal{K})_{ij} = \langle u_i|H|u_j\rangle$) is given by a tridiagonal matrix:

$$\underline{H}^\mathcal{K} = \begin{pmatrix} a_0 & b_1 & 0 & \dots & 0 & 0 \\ b_1 & a_1 & b_2 & \dots & 0 & 0 \\ 0 & b_2 & a_3 & \dots & 0 & 0 \\ \vdots & \vdots & \ddots & \ddots & \ddots & \vdots \\ 0 & 0 & 0 & \dots & a_{N-2} & b_{N-1} \\ 0 & 0 & 0 & \dots & b_{N-1} & a_{N-1} \end{pmatrix}. \quad (3.22)$$

Since N is small, the calculation of its eigenvalues $E_n^\mathcal{K}$ is of negligible cost. In particular, the lowest energy is an approximation to the ground-state energy on the full Hilbert space:

$$E_0 \approx E_0^\mathcal{K}. \quad (3.23)$$

If we write $\psi_{n,k}^\mathcal{K}$ for k -th component of the n -th eigenvector of the Krylov space, the approximation to the ground state on the full Hilbert space $|\Psi_0\rangle$ can be written as a linear combination of the Lanczos vectors in the following way:

$$|\Psi_0\rangle \approx \sum_{k=0}^{N-1} \psi_{0,k}^\mathcal{K} |u_k\rangle. \quad (3.24)$$

In terms of memory management, we can set up the Lanczos algorithm in two ways:

- *Time-efficient setup*: In this case, we store the whole Lanczos basis, so that the calculation of the ground state (3.24) comes at no additional cost (in terms of matrix-vector multiplications).
- *Memory-efficient setup*: In this case, we store only the three vectors of the recursion relation (3.21), but have to regenerate the Lanczos basis when calculating the state (3.24).

There is also a choice when it comes to the Krylov space management:

- *Continuing setup*: We can start with $N = 2$ and add more and more Lanczos vectors to the basis, diagonalizing $H^\mathcal{K}$ with each new one, until convergence is reached. The disadvantage is that the Krylov space can grow in a somewhat uncontrolled fashion in tough cases, which can in particular lead to memory problems in the time-efficient setup.
- *Restarting setup*: We fix N and generate the basis of the Krylov space for this value. If convergence is not reached, we restart the procedure with the obtained guess for $|\Psi_0\rangle$. The disadvantage is that one will do more iterations than necessary if convergence is already reached for some $N_0 < N$.

Of course, it is possible to combine the two approaches by diagonalizing $H^{\mathcal{K}}$ at each step to check the convergence, but restart after a given N to preserve memory.

Furthermore, there are additional caveats to consider:

- In the implementation one should immediately orthogonalize a given vector \tilde{u}_n , otherwise the norm of each vector will approximately grow by a factor of $\|H\|$ and result in overflow.
- If the vectors $H^n|u_0\rangle$ are not all linearly independent, orthogonalization will result in a vanishing vector, i.e. there will be some N_0 for which $b_{N_0} = 0$ (or very small numerically). At this point, the iteration has to quit.
- A well-known problem is the loss of orthogonality in the Lanczos vectors due to finite-precision arithmetics. To remedy that, one can perform a full Gram-Schmidt reorthogonalization which may increase the numerical costs significantly. Alternative algorithms using a partial reorthogonalization of selected vectors only, which still ensure numerical stability, have been developed in the 1980s (Grcar 1981; Simon 1984).
- Instead of selecting the lowest energy, we can also select the highest one and obtain an approximation for the highest energy on the full Hilbert space as well. This is required for the Chebyshev expansion method (see chapter 3.3).
- If the Hamiltonian is real, then the ground state can be gauged to be real as well, and only real arithmetic is required. However, when applying this method to time evolution (see chapter 3.2.2), complex arithmetic is required. Thus, a generic template implementation in C++ is of advantage.

The Lanczos algorithm is a very generic one, it only needs to know basic linear algebra operations: matrix-vector multiplications, vector additions and multiplications with a scalar, as well as scalar products. The latter induces a norm and one has to be able to normalize a vector. Finally, an implementation of swapping two vectors in memory is recommended. This perfectly lends itself to a very generic implementation in C++, where the same Lanczos solver class can be used to handle both exact states (see chapter 3.1) and matrix product objects (see chapter 3.6) using template parameters, provided that the above operations are defined.

3.2.2. Time evolution

The Lanczos algorithm can also be used for time propagation. To see that, let us first introduce the matrix V of size $\dim \mathcal{H} \times N$, which has the Lanczos vectors as columns:

$$\underline{V} = (\mathbf{u}_0, \mathbf{u}_1 \dots \mathbf{u}_{N-1}). \quad (3.25)$$

Using V , the Hamiltonian in the Krylov space can be written as

$$H^{\mathcal{K}} = V^\dagger H V \quad (3.26)$$

From the orthonormality of the Lanczos vectors one has:

$$V^\dagger V = \mathbb{1}_{N \times N}, \quad (3.27)$$

but since $N \ll \dim \mathcal{H}$,

$$VV^\dagger = P \quad (3.28)$$

is the projector on the Krylov space rather than $\mathbb{1}_{\dim \mathcal{H} \times \dim \mathcal{H}}$. When projected onto the Krylov space, the Hamiltonian acts in the following way:

$$PHP = VV^\dagger HVV^\dagger = VH^\mathcal{K}V^\dagger. \quad (3.29)$$

In the time evolution of a state, we are interested in:

$$|\Psi(t + \delta t)\rangle = e^{-iH\delta t}|\Psi(t)\rangle. \quad (3.30)$$

We note that for a small time step δt , the Taylor series of $e^{-H\delta t}$ is nothing but the Krylov space. This means that we can find an N so that replacing $H \rightarrow PHP$ in the above equation has a very small error and immediately obtain:

$$|\Psi(t + \delta t)\rangle \approx Ve^{-H^\mathcal{K}\delta t}V^\dagger|\Psi(t)\rangle. \quad (3.31)$$

The numerical recipe is thus straightforward:

1. Use $|\Psi(t)\rangle$ as the starting vector for the Lanczos recursion, yielding $H^\mathcal{K}$ and the projected state $|v(t)\rangle = V^\dagger|\Psi(t)\rangle$. Since $|\Psi(t)\rangle/\|\Psi(t)\|$ is the first vector of the Lanczos basis, this projection is just given by $\mathbf{v}^T(t) = (\|\Psi(t)\|, 0, \dots, 0)$.
2. Perform the time evolution in the Krylov space exactly, by diagonalizing $H^\mathcal{K} = U^\dagger\Lambda U$, obtaining the time-evolved projected state $v(t + \delta t) = U^\dagger e^{-i\Lambda\delta t}U|v(t)\rangle$, where Λ is the diagonal matrix of the eigenvalues of $H^\mathcal{K}$.
3. Project the resulting state out again by multiplying with V from the left; in other words $|\Psi(t + \delta t)\rangle \approx \sum_{k=0}^{N-1} v_k(t + \delta t)|u_k\rangle$.

As with the ground state calculation, the Krylov space size N is a measure of the cost of the algorithm, as one needs to perform a matrix-vector multiplication at each step. An optimal choice is obtained from the following a posteriori error bound ([Lubich 2008](#)):

$$\text{dist} = \|Ve^{-iH^\mathcal{K}\delta t}V^\dagger|\Psi(t)\rangle - e^{-iH\delta t}|\Psi(t)\rangle\| \leq (H^\mathcal{K})_{N+1,N} \int_0^{\delta t} dt' \left| \left(e^{-iH^\mathcal{K}t'} \right) \right|. \quad (3.32)$$

Approximating the integral crudely using the Simpson rule, one obtains:

$$\text{dist} \leq (H^\mathcal{K})_{N+1,N} \left(\frac{2}{3} \left| \left(e^{-iH^\mathcal{K}\delta t/2} \right)_{N,1} \right|^2 + \frac{1}{6} \left| \left(e^{-iH^\mathcal{K}\delta t} \right)_{N,1} \right|^2 \right) \delta t. \quad (3.33)$$

Thus, one can add more and more Lanczos vectors until the distance falls below a given tolerance. As before, the cost of diagonalizing the Krylov space Hamiltonian after adding a Lanczos vector is negligible.

Note that the Lanczos algorithm for the ground state is recovered if we perform an imaginary-time evolution with $e^{-H\delta\tau}$ instead of $e^{-iH\delta t}$ and set the imaginary time step $\delta\tau$ to infinity ($\tau = \infty$ is equivalent to $T = 0$, and thus the ground state). In this case, all eigenvectors but the lowest one in

$e^{-H^K \delta\tau}$ give a negligible contribution and the τ -evolution is equivalent to simply replacing $v(\delta\tau)$ by the lowest-energy eigenvector.

See also chapter 3.5 for a benchmark of the Lanczos time evolution with the Chebyshev algorithm, which is described in chapter 3.3.3.

3.3. The Chebyshev expansion technique

3.3.1. Spectral functions

One is often dealing with problems of calculating functions of a single continuous variable (either the frequency $g(\omega)$, the time $g(t)$ or the inverse temperature $g(\beta)$), where either a trace over the whole Hamiltonian H , or equivalently, a sum over all of its eigenvalues E_n is needed. Examples include the partition function

$$Z(\beta) = \text{Tr} e^{-\beta H} = \sum_n e^{-\beta E_n}, \quad (3.34)$$

the density of states

$$\rho(\omega) = -\frac{1}{\pi} \text{Tr} \text{Im} \frac{1}{\omega + i0^+ - H} = \sum_n \delta(\omega - E_n), \quad (3.35)$$

spectral functions in the Lehmann representation

$$\langle\langle A^\dagger; A \rangle\rangle(\omega) = -\frac{1}{\pi} \text{Tr} \text{Im} \frac{A|0\rangle\langle 0|A^\dagger}{\omega + i0^+ - E_0 + H} = \sum_n |\langle n|A|0\rangle|^2 \delta(\omega - E_0 + E_n), \quad (3.36)$$

or the time evolution of a state

$$|\Psi(t)\rangle = e^{-iHt} |\Psi(0)\rangle = \sum_n \langle n|\Psi(0)\rangle e^{-iE_n t} |n\rangle. \quad (3.37)$$

Let us focus on the spectral function first, and then on time evolution in the next section. A possible approach is to evaluate the desired $g(x)$ on the Krylov space, i.e. approximate it by a fixed amount of polynomials M . In principle, we could use the monomial basis x^k :

$$g(x) \approx \sum_{k=0}^{M-1} \mu_k^{\text{mon}} x^k, \quad -1 < x < 1. \quad (3.38)$$

Because the polynomials have to converge, one has to use rescaled frequencies $-1 < x < 1$:

$$\begin{aligned} x &:= (\omega - b) / a, \\ \tilde{H} &:= (H - b) / a, \\ a &:= (E_{\max} - E_{\min}) / (2 - \epsilon), \\ b &:= (E_{\max} + E_{\min}) / 2, \end{aligned} \quad (3.39)$$

with $\epsilon \ll 1$, which serves as a safety padding to avoid touching the edges; and with E_{\min} , E_{\max} signifying the lowest and highest eigenenergy, respectively.

The task is now to calculate the moments μ_k^{mon} . In theory, one could use a Taylor expansion, but it only gives good results for small x and is very poor at the edge of the convergence radius $|x| \rightarrow 1$. Instead, we can profit from the know-how of approximation theory, accumulated over the last two centuries. It turns out that Chebyshev polynomials are a better, and in fact an almost optimal choice: They deviate the least from zero among all polynomials, so that the error is evenly spread across the whole interval.

In general, orthogonal polynomials can be defined either via a recursion relation or via an orthogonality relation involving a weight function. For Chebyshev polynomials, the former reads:

$$T_n(x) = 2xT_n(x) - T_{n-1}(x), \quad (3.40)$$

with the initial conditions $T_0(x) = 1$, $T_1(x) = x$. The weight function is given by $w(x) = 1/\pi\sqrt{1-x^2}$ and the orthogonality relation is

$$\int_{-1}^1 dx \frac{1}{\pi\sqrt{1-x^2}} T_m(x) T_n(x) = \frac{1}{2} (1 + \delta_{m0}) \delta_{mn}. \quad (3.41)$$

In fact, there is also an explicit form

$$T_n(x) = \cos(n \arccos(x)), \quad (3.42)$$

but it is not very stable to evaluate numerically for large n compared to (3.40).

Thus, the Chebyshev expansion of a function $g(x)$ becomes:

$$(A) \quad g(x) = \mu_0 + 2 \sum_{n=1}^{\infty} \mu_n T_n(x), \quad (3.43)$$

with the coefficients given by a projection onto the basis of Chebyshev polynomials (which can be easily verified using (3.41)):

$$(A) \quad \mu_n = \int_{-1}^1 dx \frac{1}{\pi\sqrt{1-x^2}} T_n(x) g(x). \quad (3.44)$$

One recognizes that this is in fact completely analogous to a Fourier expansion (where $\exp(ik_n x)$ rather than $T_n(x)$ forms a natural basis for periodic functions). However, the square root in the above formula becomes problematic to evaluate if T_n is a function of the Hamiltonian. In such a case, we can just redefine the expansion in the following way:

$$(B) \quad g(x) = \frac{1}{\pi\sqrt{1-x^2}} \left(\mu_0 + 2 \sum_{n=1}^{\infty} \mu_n T_n(x) \right), \quad (3.45)$$

which amounts to expanding $g(x) w^{-1}(x)$ rather than just $g(x)$. The corresponding moments are now:

$$(B) \quad \mu_n = \int_{-1}^1 dx g(x) T_n(x). \quad (3.46)$$

The downside of using the expansion (3.45) is that the resolution now becomes somewhat uneven, as the edges of the interval gain more weight.

The next step is to limit the infinite sum to a finite amount of coefficients, which leads to the *kernel polynomial approximation* [Silver and Röder 1994; Wang 1994; Silver and Röder 1997; Weiße and Fehske 2008; Weiße et al. 2006]:

$$g(x) \approx g_{\text{KPM}}(x) = \frac{1}{\pi\sqrt{1-x^2}} \left(d_0\mu_0 + 2 \sum_{n=1}^{M-1} d_n\mu_n T_n(x) \right). \quad (3.47)$$

Note that the right-hand side is a polynomial of degree $M-1$, thus a change of basis into the original ansatz with monomials (3.38) is in principle possible. The additional coefficients d_n are required to damp Gibbs oscillations which arise near points where the function is not differentiable. The Gibbs phenomenon is a direct result of the truncation of the infinite series and also well-known from the Fourier series expansion. It has relevance for physical applications, since a spectral function is a sum of delta peaks, at the edges of which Gibbs oscillations would otherwise appear. One can make several choices for the damping, which is equivalent to convolutions with different kernels, thereby broadening the δ -peaks in different ways. The most relevant are [Weiße and Fehske 2008; Weiße et al. 2006]:

$$\begin{aligned} d_n^{\text{Jackson}} &= \left[(M-n+1) \cos k_n + \sin k_n \tan^{-1} k_1 \right] / (N+1), \quad k_n = n \frac{\pi}{N+1}, \\ d_n^{\text{Lorentz}} &= \sinh \left[\lambda (1 - n/N) \right] / \sinh \lambda, \quad \lambda \in \mathbb{R}. \end{aligned} \quad (3.48)$$

The Jackson damping produces δ -peaks broadened as Gaussians, the Lorentz damping as somewhat wider Lorentzians.

In order to calculate the spectral function (3.36), let us introduce an unshifted “operator density of states”:

$$\rho_A(x) = \sum_n |\langle n|A|0\rangle|^2 \delta(x - E_n). \quad (3.49)$$

The Chebyshev moments for $\rho_A(x)$ are obtained via:

$$\begin{aligned} \mu_k[\rho_A] &= \int_{-1}^1 dx T_k(x) \rho_A(x) \\ &= \int_{-1}^1 dx T_k(x) \sum_n |\langle n|A|0\rangle|^2 \delta(x - E_n) \\ &= \sum_n T_k(E_n) \langle 0|A^\dagger|n\rangle \langle n|A|0\rangle \\ &= \sum_n \langle 0|A^\dagger T_k(\tilde{H})|n\rangle \langle n|A|0\rangle \\ &= \langle 0|A^\dagger T_k(\tilde{H}) A|0\rangle. \end{aligned} \quad (3.50)$$

Because of the symmetry relation (following from (3.42))

$$T_n(-x) = (-1)^n T_n(x), \quad (3.51)$$

using $(-1)^n \mu_n$ instead of μ_n mirrors the delta function to $\delta(-x - E_n) = \delta(x + E_n)$. Back-scaling and shifting then gives the original δ -peak:

$$\delta(\omega - E_0 + E_n) = \frac{1}{|a|} \delta(x + E_n + 2b - E_0) = \frac{1}{|a|} \delta(x + E_n + E_{\min} + E_{\max} - E_0). \quad (3.52)$$

The whole algorithm for the evaluation of (3.36) thus looks like that:

1. Calculate the ground state $|0\rangle$, its energy E_0 , as well as the maximal and minimal energies E_{\max} , E_{\min} in the appropriate subspace using the Lanczos method (chapter 3.2). This requires up to three runs and can be parallelized.
2. Use the energies to rescale the Hamiltonian according to (3.39).
3. Apply the operator A to $|0\rangle$ and save the state (can be applied in place).
4. Calculate $|T_k\rangle := T_k(\tilde{H})A|0\rangle$ using the recursion relation (3.40). At each recursion step, the result can be projected on $\langle 0|A^\dagger$ in order to obtain μ_n according to (3.50).
5. The spectral function can now be evaluated at each point x by carrying out the summation (3.45) and scaled back to ω using (3.52). This can be also done very efficiently for an array of ω -points at once using the cosine transform [Weiße and Fehske 2008; Weiße et al. 2006]. In this work, this was implemented using the FFTW library [Frigo and Johnson 1998].

Finally, one should mention the helpful relations

$$\begin{aligned} T_{2k}(x) &= 2T_k(x)T_k(x) - T_0(x), \\ T_{2k+1}(x) &= 2T_{k+1}(x)T_k(x) - T_1(x). \end{aligned} \quad (3.53)$$

Exploiting them, we get:

$$\begin{aligned} \mu_{2k} &= 2\langle T_k|T_k\rangle - \mu_0, \\ \mu_{2k+1} &= 2\langle T_{k+1}|T_k\rangle - \mu_1, \end{aligned} \quad (3.54)$$

thereby obtaining $2M$ moments for a given iteration depth M . This is very helpful when working with exact states. However, experience has shown that when using the Chebyshev expansion in combination with matrix-product states, this leads to larger numerical errors and is hence only employed with exact states.

3.3.2. Multi-dimensional expansion

When applying the filter technique in order to analyse the spectral function in chapter 4.1.3, we will be faced with the calculation of a two-dimensional expansion (4.24), whose Lehmann representation is given by

$$\rho_{AB}(x, y) = \sum_{mn} \langle 0|A^\dagger|n\rangle \langle m|B|n\rangle \langle n|A|0\rangle \delta(x - x_n) \delta(y - x_m). \quad (3.55)$$

We can apply the Chebyshev expansion by simply expanding the x - and y -direction independently in a tensor-product fashion:

$$\rho_{AB}(x, y) = \sum_{k=0}^M \sum_{l=0}^M \frac{\mu_{kl} h_{kl} d_k d_l}{\pi^2 \sqrt{(1-x^2)(1-y^2)}} T_k(x) T_l(y), \quad (3.56)$$

where the factor h_{kl} takes care of the fact that the zeroth coefficient has to be halved:

$$h_{kl} = \frac{2}{1 + \delta_{k,0}} \frac{2}{1 + \delta_{l,0}}. \quad (3.57)$$

The moments now constitute a matrix and are found to be:

$$\mu_{kl} = \langle 0 | A^\dagger T_l(\tilde{H}) B T_k(\tilde{H}) A | 0 \rangle. \quad (3.58)$$

The matrix is obviously symmetric:

$$\mu_{kl} = \mu_{lk}. \quad (3.59)$$

Eq. (3.58) is best evaluated with enough space to store all the vectors of the outer iteration $|T_k\rangle = T_k(\tilde{H}) A | 0 \rangle$, so that the rest is obtained using matrix-vector multiplications with B , followed by scalar products. If the whole two-dimensional spectrum is required, it can be most efficiently evaluated using the two-dimensional cosine transform of the moment matrix. Once more, the FFTW library can be used [Frigo and Johnson 1998].

3.3.3. Time evolution

In order to calculate the time evolution of a state, we can make use of the better expansion (3.43), writing [Tal-Ezer and Kosloff 1984; Lubich 2008; Weiße and Fehske 2008; Weiße et al. 2006]:

$$|\Psi(t)\rangle = e^{-i(a\tilde{H}+b)t} |\Psi(0)\rangle \approx e^{-ibt} \left(\mu_0 + 2 \sum_{k=1}^{M-1} T_k(\tilde{H}) \right) |\Psi(0)\rangle =: P_M |\Psi(0)\rangle. \quad (3.60)$$

The moments can now be calculated analytically:

$$\mu_k = \int_{-1}^1 dx \frac{1}{\pi \sqrt{1-x^2}} T_k(x) e^{-iaxt} = (-i)^k \mathcal{J}_k(at), \quad (3.61)$$

where $\mathcal{J}_k(at)$ denotes the k -th Bessel function of the first kind. It decays rather quickly for $k > at$, so that only few additional iterations are required after this condition has been fulfilled at some iteration depth k . A detailed error analysis yields the following expression for the distance to the exact state [Lubich 2008]:

$$\text{dist} = \|P_M |\Psi(0)\rangle - e^{-iHt} |\Psi(0)\rangle\| \leq 4 \left(e^{1 - \left(\frac{at}{2k}\right)^2} \frac{at}{2k} \right)^k, \quad k \geq at, \quad (3.62)$$

thus a scaling which is even faster than exponential.

We can also look at the algorithm in the following way: In order to propagate over the whole interval t , the Chebyshev iteration effectively chooses steps of the order of $\delta t \sim 1/a2/(E_{\max} - E_{\min})$, so that the complexity depends on the full bandwidth of the spectrum; or is linear in t for a given bandwidth.

Overall, eq. (3.61) allows us to pre-calculate the coefficients of the expansion (stopping when they become sufficiently small), thereby assessing the effort required to carry out the timestep (3.60) a priori. The downside is that a rescaling of the Hamiltonian requires additional Lanczos runs, which is not practical if the Hamiltonian $H = H(t)$ depends on time explicitly, so that the spectrum grows and shrinks in time. In the latter case, a combination of the Magnus expansion technique paired with the Lanczos time propagation (where the polynomial is not fixed a priori, but implicitly changes at each timestep) is more appropriate, see chapter 3.4.

3.4. Propagating time-dependent Hamiltonians

The time-independent Schrödinger equation $i\partial_t|\Psi\rangle = H|\Psi\rangle$ can be immediately solved by exponentiation $|\Psi(t)\rangle = U(t)|\Psi(0)\rangle = \exp(-iHt)|\Psi(0)\rangle$, so that the problem of time-propagation reduces to the evaluation of a matrix exponential. If the Hamiltonian is time-dependent, but commutes with itself at different times, a solution in terms of an exponential can still be obtained by an integrating factor:

$$U(t) = \exp\left[-i\int_0^t dt' H(t')\right], \quad [H(t), H(t')] = 0. \quad (3.63)$$

This form can still be preserved in the general case by introducing a time-ordering operator \mathcal{T} ,

$$U(t) = \mathcal{T} \exp\left[-i\int_0^t dt' H(t')\right], \quad [H(t), H(t')] \neq 0, \quad (3.64)$$

however, this is not very practical in terms of a numerical implementation. Instead, let us first consider the simple case where the Hamiltonian has a time dependence with two plateaus:

$$H(t) = \begin{cases} B, & 0 \leq t \leq 1, \\ A, & 1 < t \leq 2, \end{cases} \quad (3.65)$$

with $[A, B] \neq 0$. Then, the solution at $t = 2$ is given by $U(t=2) = \exp(-iA)\exp(-iB)$ and can be written in terms of a single exponential $U(t=2) = \exp(-iC)$ with the help of the well-known Baker-Campbell-Hausdorff (BCH) formula:

$$C = A + B + \frac{1}{2}[A, B] + \frac{1}{12}([A, [A, B]] + [[A, B], B]) \pm \dots \quad (3.66)$$

Now we can think of a general time-dependence as being composed out of many non-commuting, but piecewise constant Hamiltonians, with the time evolution operator being given by the corresponding matrix exponential. A natural question is to ask whether there is a continuous generalization of the BCH formula, which gives this continuous application of matrix exponential in terms of one effective exponential:

$$U(t) = \exp[-i\Omega(t)] = \exp\left[-i\sum_{k=0}^{\infty}\Omega_k(t)\right], \quad [H(t), H(t')] \neq 0. \quad (3.67)$$

Such a generalization has been indeed found by Magnus [Magnus 1954; Blanes et al. 2009]. The first coefficients of the Magnus series are given as follows, with an apparent analogy to the BCH formula:

$$\begin{aligned} \Omega_0(t) &= \int_0^t dt' H(t') \\ \Omega_1(t) &= \frac{1}{2} \int_0^t dt' \int_0^t dt'' [H(t'), H(t'')] \\ \Omega_2(t) &= \frac{1}{6} \int_0^t dt' \int_0^t dt'' \int_0^t dt''' ([H(t'), [H(t''), H(t''')]] + [H(t'''), [H(t''), H(t')]]) \\ &\dots \end{aligned} \quad (3.68)$$

Even after the integrals in the above formula are approximated by a discrete weighted sum, $\int dt f(t) = \sum_i w_i f(t_i)$, using e.g. Gauss-Legendre integration, we are left with an expression of the type $U(\delta t) = \exp(-iH_{\text{eff}}\delta t)$ for a step δt , where H_{eff} contains unwieldy commutators which cannot be numerically evaluated with any reasonable cost. The idea behind the *commutator-free exponential time-propagation method* (CFET) is now to make use of the BCH formula in reverse to write the time evolution operator as a product of exponentials in such a fashion that the first terms of the Magnus series are reproduced:

$$U(\delta t) = \exp[-i\Omega(\delta t)] \approx \exp(-iH_{\text{eff}}\delta t) \approx \prod_{n=1}^{N_{\text{exp}}} \exp(-iH_{n,\text{eff}}\delta t). \quad (3.69)$$

Apart from the amount of integration points, the accuracy is controlled by the amount of exponentials N_{exp} . The simplest CFET with $N_{\text{exp}} = 1$ is a second-order method given by

$$H_{1,\text{CFET}21} = \sum_i w_i H(t_i). \quad (3.70)$$

This is what one would naively set using a small timestep and neglecting all commutators. However, Alvermann and Fehske have found a fourth-order approximation with just $N_{\text{exp}} = 2$ [Alvermann and Fehske 2011; Alvermann, Fehske, and Littlewood 2012]:

$$H_{n,\text{CFET}42} = \sum_{m=1}^2 g_{nm} H(x_m \delta t), \quad (3.71)$$

where the coefficients g_{nm} can be arranged in a matrix:

$$\underline{g} = \begin{pmatrix} g_- & g_+ \\ g_+ & g_- \end{pmatrix} \quad (3.72)$$

with $g_{\pm} = \frac{3 \pm 2\sqrt{3}}{12}$, while the steps are given by $x_{1/2} = \frac{1}{2} \mp \frac{\sqrt{3}}{6}$. Alvermann, Fehske and Littlewood also give a fourth-order method with three exponentials and a smaller error prefactor:

$$H_{n,\text{CFET43}} = \sum_{m=1}^3 g_{nm} H(x_m \delta t), \quad (3.73)$$

with the coefficient matrix now being given by

$$\underline{g} = \begin{pmatrix} \frac{37}{240} - \frac{10}{87} \sqrt{\frac{5}{3}} & -\frac{1}{30} & \frac{37}{240} + \frac{10}{87} \sqrt{\frac{5}{3}} \\ -\frac{11}{360} & \frac{23}{45} & -\frac{11}{360} \\ \frac{37}{240} + \frac{10}{87} \sqrt{\frac{5}{3}} & -\frac{1}{30} & \frac{37}{240} - \frac{10}{87} \sqrt{\frac{5}{3}} \end{pmatrix}, \quad (3.74)$$

while the steps are $x_{1/3} = \frac{1}{2} \mp \sqrt{\frac{3}{20}}$, $x_2 = \frac{1}{2}$.

Of course, whenever the time-dependence of the Hamiltonian can be separated out as $H(t) = H_0 + f(t)V$, one can pre-sum the values of the time-dependent function to obtain effective Hamiltonians of the type $H_{n,\text{eff}}(\delta t) = H_0 + [\sum_m g_{nm} f(x_m \delta t)]V$.

3.5. Benchmark of the time-propagation algorithms

Let us now make a performance benchmark of the available time evolution algorithms. Fig. 3.2(a) shows a comparison of the Chebyshev and the Lanczos algorithms (chapters 3.3.3 and 3.2.2, respectively) for a Hamiltonian that does not depend on time. A Hubbard model with $L = 6$, $N_\uparrow = N_\downarrow = 3$ and $U = 6$ is taken, whose Hilbert space is still small enough to be diagonalized. A random state from the Hilbert space is then propagated to $t = 20$ using various fixed recursion depths M in the Chebyshev case and fixed Krylov space dimensions N in the Lanczos case. As a measure of error, the distance to the exactly propagated state is calculated using the uniform norm, given by:

$$\|\Psi\|_\infty = \lim_{p \rightarrow \infty} \left(\sum_i |\Psi_i|^p \right)^{1/p} = \max_i |\Psi_i|. \quad (3.75)$$

As a measure of effort, the amount of matrix-vector multiplications (MVMs) is taken, which is essentially equal to N and M , respectively.

One observes that the error remains fairly large, of the order of $O(10^{-1})$ during the first $O(10^2)$ iterations for both methods (note that $at = (E_{\max} - E_{\min})/2 \cdot t = 220$ in the Chebyshev case), until it suddenly drops hyperexponentially and is only limited to $O(10^{-11})$ due to finite-accuracy arithmetics. The Lanczos algorithm appears to perform better, requiring fewer MVMs to reach the same accuracy. However, this is only possible if the whole Krylov space basis can be stored. The other curves in fig. 3.2(a) show the case where only $N = 30, 40, 50$ basis states can be stored and it turns out that the algorithm performs much worse. For the Chebyshev expansion, one always needs to store only 3 states during the recursion relation.

To test the validity of the distance estimates (3.62) and (3.33), the algorithms are run in an adaptive mode, stopping the iterations when a given tolerance is reached, which is varied between 10^{-3} and 10^{-15} . The results are displayed as dots in fig. 3.2(a). One observes that the estimates are very conservative, the real error is in fact much smaller, especially in the Chebyshev case, though again limited by the finite-precision arithmetics to $O(10^{-11})$.

Finally, let us test the case of a time-dependent Hamiltonian $H = H(t)$. Fig. 3.2(b) compares the various variants of the CFET algorithm, where an adaptive Lanczos solver is used as a driver

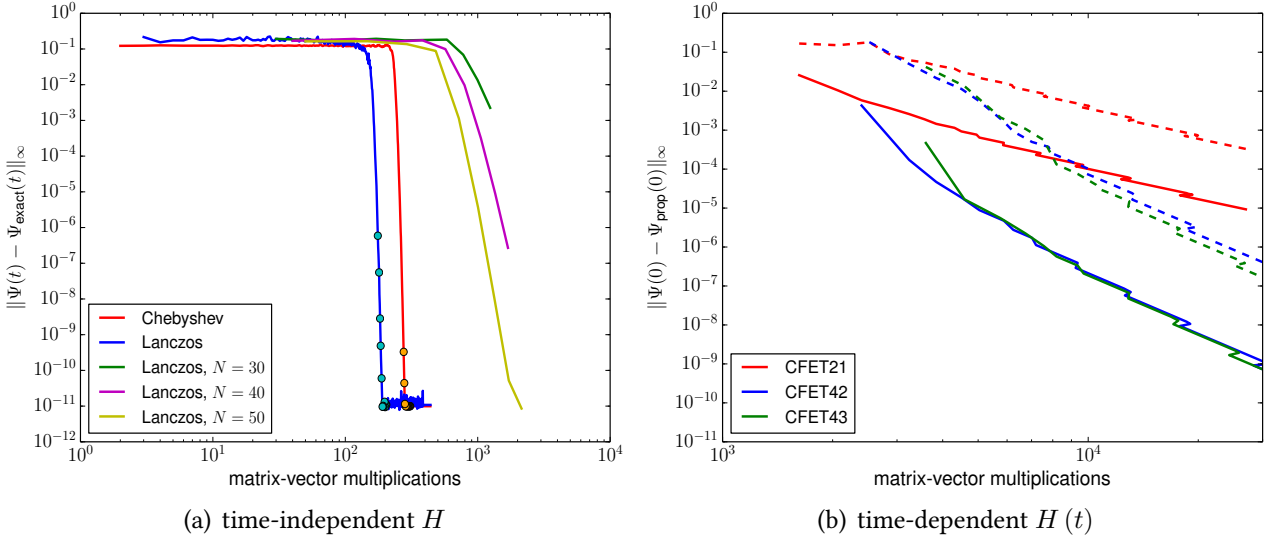


Figure 3.2.: (a) Distance between the numerically propagated state and the exact one (obtained by diagonalization) using the uniform norm (3.75) as a function of matrix-vector multiplications. Parameters: Hubbard model with $L = 6$, $N_{\uparrow} = N_{\downarrow} = 3$, $U = 6$, the initial state is random, the propagation time is $t = 20$. The blue curve uses the Lanczos algorithm and stores as many Krylov states as needed, the other Lanczos curves use a Krylov space dimension N as indicated and reset after a given timestep. The dots indicate the algorithms in an adaptive mode where the tolerance is varied between 10^{-15} and 10^{-3} using eqs. (3.62) and (3.33).

(b) Distance between a forth-and-back propagated state and the initial state as a function of matrix-vector-multiplications. Parameters: Hubbard model as in (a) with the addition of an external electric field $\mathcal{E}(t) = \mathcal{E}_0 \cos(\Omega t)$ ($\mathcal{E}_0 = 1$), described by the Peierls substitution, the propagation is until $t = 10$ (followed by a backward propagation). Various CFET setups are used in combination with the Lanczos algorithm. The solid lines are for $\Omega = 1$, the dotted lines for $\Omega = 10$.

to compute the matrix exponentials. The same model is taken, but with an external electric field $\mathcal{E}(t) = \mathcal{E}_0 \cos(\Omega t)$, with $\mathcal{E}_0 = 1$ and $\Omega = 1$ (slow dynamics), $\Omega = 10$ (fast dynamics). Instead of a cumbersome calculation of the exact time evolution in this case, the following approach is used: The state is propagated to $t = 10$ and then back in time to $t = 0$ using twice the amount of timesteps. Since one has to get back the initial state, the distance between the propagated and the initial state is taken as the error. The doubling of the timesteps on the back propagation is necessary to ensure that the right time dependence has been sampled.

One observes that both CFET43 and CFET42 show a significant improvement as compared to the simple CFET21 (which is equivalent to treat $H(t)$ as constant during a timestep), but they do not differ much among each other, so that a further optimization does not seem to be possible. Not very surprisingly, the fast dynamics with $\Omega = 10$ shows a larger error, but the relative relation of the algorithms remains the same.

3.6. The Density Matrix Renormalization Group (DMRG)

3.6.1. Matrix decompositions: SVD, QR

The singular value decomposition (SVD) is a decomposition of a matrix M into a product of three other matrices,

$$M = USV^\dagger, \quad (3.76)$$

where U and V have the properties $U^\dagger U = \mathbb{1}$ and $V^\dagger V = \mathbb{1}$, while S is diagonal ($S_{ij} = s_i \delta_{ij}$) and contains the singular values s_i in decreasing order. This decomposition works even if M is non-quadratic $N_r \times N_c$. The amount of singular values then goes as far as $\min(N_r, N_c)$. Hence it follows that if M is tall and skinny ($N_r \geq N_c$), then V^\dagger is quadratic and thereby unitary. Similarly, if M is short and fat ($N_c \geq N_r$), then U is quadratic and thereby unitary.

One should note the relation of the SVD to diagonalization. Decomposing the product MM^\dagger , we find

$$MM^\dagger = USV^\dagger V S U^\dagger = US^2 U^\dagger. \quad (3.77)$$

One recognizes that this is simply the diagonalization of MM^\dagger (which is hermitian by construction) and it follows that the eigenvalues of MM^\dagger are equal to the squares of the singular values of M .

The SVD can be used a tool for compression: For instance, given a grey-scale digital picture, we can interpret it as a matrix with entries ranging between 0 and 255, representing each pixel. Applying the SVD to it, one will notice that whenever there is sufficient structure contained within the picture, the singular values will decrease and can be truncated, but will all remain of the same order of magnitude whenever if the picture only contains white noise. Assuming for simplicity that the original picture is quadratic $N \times N$, we can take the first χ dominant singular values and then only need to store of the order of χN numbers rather than N^2 , a noticeable gain for $\chi \ll N$.

Mathematically, the truncated SVD appears in the problem of low-rank approximation. If we seek to approximate a matrix by another of smaller rank, i.e. $\min \|M - M'\|^2$ with $\text{rank}(M') < \text{rank}(M)$ using the Frobenius norm $\|M\|^2 = \sum_{ij} |M_{ij}|^2$, then M' is found by the same procedure of truncated SVD as described above.

This compression property of the SVD lies at the heart of DMRG, which is essentially an elaborate framework to compress the wavefunction and work with it efficiently.

Another helpful tool is the QR-decomposition, given by

$$M = QR, \quad (3.78)$$

where Q has the property $Q^\dagger Q = \mathbb{1}$. The relation to SVD is quite obvious: $U = Q$ and $SV^\dagger = R$. The QR-decomposition does not reveal the singular values, thus no truncation can be carried out, but it is slightly cheaper and therefore preferable whenever no truncation is desired in the first place. In a similar fashion we can define an RQ-decomposition,

$$M = RQ, \quad (3.79)$$

now related to the SVD via $US = R$ and $V^\dagger = Q$. It can be found by observing that

$$M^\dagger = \tilde{Q}\tilde{R} = (RQ)^\dagger = Q^\dagger R^\dagger, \quad (3.80)$$

so that $R = \tilde{R}^\dagger$ and $Q = \tilde{Q}^\dagger$. Thus, to find the RQ-decomposition of M , one needs to apply the QR-decomposition to M^\dagger and take the adjoint of the result again.

3.6.2. Matrix product states

The many-body wavefunction is normally expressed as a sum over Fock states, with each Fock state being given by a set of occupancy numbers. However, a more natural basis for DMRG is the basis of local states, which will be denoted by $|\sigma_l\rangle$, where l enumerates the lattice site. The local bases for the most commonly investigated solid state models look as follows (with the site index dropped assuming homogeneity):

Heisenberg model	$\{ \uparrow\rangle, \downarrow\rangle\}$
t-J model	$\{ 0\rangle, \uparrow\rangle = c_\uparrow^\dagger 0\rangle, \downarrow\rangle = c_\downarrow^\dagger 0\rangle\}$
Hubbard model	$\{ 0\rangle, \uparrow\rangle, \downarrow\rangle, c_\uparrow^\dagger c_\downarrow^\dagger 0\rangle = \uparrow\downarrow\rangle\}$
Kondo model	$\{ \sigma\rangle_{\text{Heisenberg}} \otimes \sigma\rangle_{\text{Hubbard}}\}$

Let us assume for simplicity that the system is a homogeneous chain of length L with open boundary conditions. Then we can define a site-independent local dimension D (2, 3, 4 and 8 respectively for the models above), so that the Hilbert space size is D^L . The wavefunction in the local basis reads:

$$|\Psi\rangle = \sum_{\sigma_1 \dots \sigma_L} c_{\sigma_1 \dots \sigma_L} |\sigma_1\rangle \dots |\sigma_L\rangle. \quad (3.81)$$

The next step is to think of the D^L coefficients $c_{\sigma_1 \dots \sigma_L}$ which appear in the formula above as a tensor of rank L . It can be reshaped into a $D \times D^{L-1}$ matrix by bijectively mapping of all the indices but the first onto a superindex. We can denote this by using parentheses: $c_{\sigma_1 \dots \sigma_L} \rightarrow c_{\sigma_1(\sigma_2 \dots \sigma_L)}$. We can then apply the SVD to this matrix, obtaining:

$$c_{\sigma_1(\sigma_2 \dots \sigma_L)} = \sum_i U_{\sigma_1 i} S_{ii} V_{i(\sigma_2 \dots \sigma_L)}^\dagger. \quad (3.82)$$

Now we reshape the indices of U , introduce a dummy index 1, and define the following A -tensor:

$$A_{1i}^{\sigma_1} := U_{\sigma_1 i}. \quad (3.83)$$

If no truncation is carried out, then we are dealing with a $1 \times D$ matrix for each σ_1 .

In the next step, we take the remainder of the tensor $c_{i\sigma_2 \dots \sigma_L} := S_{ii} V_{i(\sigma_2 \dots \sigma_L)}^\dagger$ and reshape it into a matrix by mapping the first two indices onto rows and the rest onto columns: $c_{i\sigma_2 \dots \sigma_L} \rightarrow c_{(i\sigma_2)\sigma_3 \dots \sigma_L}$. Applying the SVD once more, we obtain:

$$c_{(i\sigma_2)\sigma_3 \dots \sigma_L} = \sum_j U_{(i\sigma_2)j} S_{jj} V_{j\sigma_3 \dots \sigma_L}^\dagger \quad (3.84)$$

and can now define the next A -tensor:

$$A_{ij}^{\sigma_2} := U_{(i\sigma_2)j}. \quad (3.85)$$

The index j runs over the minimum of the rows and columns of $c_{(i\sigma_2)\sigma_3 \dots \sigma_L}$, in this case D^2 , so that the new A -tensor is now a $D \times D^2$ matrix for each σ_2 .

Continuing this procedure iteratively until the end of the chain is reached, we obtain the wavefunction as a matrix product state:

$$|\Psi\rangle = \sum_{\sigma_1 \dots \sigma_L} \underline{A}^{\sigma_1} \underline{A}^{\sigma_2} \dots \underline{A}^{\sigma_L} |\sigma_1\rangle \dots |\sigma_L\rangle. \quad (3.86)$$

This is exact since no truncation has been carried out. Therefore, the matrix dimensions increase exponentially towards the middle of the chain and then decrease again until they reach $D \times 1$ at the last site.

Since the A -tensors were chosen as the reshaped U -matrices of the SVD, the following orthogonality relation ("left-orthogonality") follows from the $U^\dagger U = \mathbb{1}$ property of the latter:

$$\sum_{\sigma_l} (\underline{A}^{\sigma_l})^\dagger \underline{A}^{\sigma_l} = \mathbb{1}. \quad (3.87)$$

Alternatively, we can apply the chain of SVDs to the c -tensor from the right, keeping V^\dagger in every step. In this case we obtain

$$|\Psi\rangle = \sum_{\sigma_1 \dots \sigma_L} \underline{B}^{\sigma_1} \underline{B}^{\sigma_2} \dots \underline{B}^{\sigma_L} |\sigma_1\rangle \dots |\sigma_L\rangle, \quad (3.88)$$

where the B -tensors now fulfill the following relation ("right-orthogonality"):

$$\sum_{\sigma_l} \underline{B}^{\sigma_l} (\underline{B}^{\sigma_l})^\dagger = \mathbb{1}. \quad (3.89)$$

A mixed representation is also possible, by applying the SVD both from the left and right. We may choose to go to the site l from the left and to $l + 1$ from the right, then the singular values will be placed on the bond between these sites:

$$|\Psi\rangle = \sum_{\sigma_1 \dots \sigma_L} \underline{A}^{\sigma_1} \dots \underline{A}^{\sigma_l} \underline{S}^{l,l+1} \underline{B}^{\sigma_{l+1}} \dots \underline{B}^{\sigma_L} |\sigma_1\rangle \dots |\sigma_L\rangle. \quad (3.90)$$

By contracting $\underline{S}^{l,l+1}$ with the preceding A -tensor or the following B -tensor, the result will be non-orthogonal. We can denote this by the letter M , so for example:

$$|\Psi\rangle = \sum_{\sigma_1 \dots \sigma_L} \underline{A}^{\sigma_1} \dots \underline{A}^{\sigma_{l-1}} \underline{M}^{\sigma_l} \underline{B}^{\sigma_{l+1}} \dots \underline{B}^{\sigma_L} |\sigma_1\rangle \dots |\sigma_L\rangle. \quad (3.91)$$

This representation actually happens to be the most practical. The site l , which has been selected in this fashion, is often called *orthogonality centre*, but to me the term *pivot* seems more appropriate: In the DMRG algorithm, one will seek to modify the tensor at this site, while keeping the rest constant. The term *pivot* is already established for algorithms which proceed in this manner, e.g. Gaussian elimination [Press 2007].

The procedure of moving the pivot left and right through the chain by applying the SVD (or QR) is called *sweeping* and is an essential part of improving the efficiency of the algorithm.

3.6.3. Matrix product operators

In order to apply operators to the wavefunction in matrix product form, we also need to represent them as matrix product operators (MPOs). So, by analogy, we seek the representation of the Hamiltonian in the following form:

$$H = \sum_{\sigma\sigma'} \underline{W}^{\sigma'_1\sigma_1} \underline{W}^{\sigma'_2\sigma_2} \dots \underline{W}^{\sigma'_L\sigma_L} |\sigma'\rangle \langle \sigma|, \quad (3.92)$$

where the vector notation indicates the set of local bases: $\sigma = \{\sigma_1 \dots \sigma_L\}$. For a tight-binding Hamiltonian of the type

$$H = \sum_l \left(X_l Y_{l+1}^\dagger + Y_{l+1} X_l^\dagger \right) + \sum_l Z_l \quad (3.93)$$

such a representation can be constructed explicitly by introducing a generator, which is a matrix of operators:

$$\underline{G}^{(l)} = \begin{pmatrix} \mathbb{1} & 0 & 0 & 0 \\ X_l & 0 & 0 & 0 \\ X_l^\dagger & 0 & 0 & 0 \\ Z_l & Y_l^\dagger & Y_l & \mathbb{1} \end{pmatrix}, \quad l = 2, \dots, L-1. \quad (3.94)$$

At the first site, we set it to the last row of the matrix above, on the last site to the first column:

$$\begin{aligned} G_{1i}^{(1)} &= G_{4i}, \\ G_{i1}^{(L)} &= G_{i1}. \end{aligned} \quad (3.95)$$

The W -matrices in (3.92) are now found to be:

$$\underline{W}_{ij}^{\sigma'_i \sigma_i} = \langle \sigma'_i | G_{ij}^{(l)} | \sigma_i \rangle. \quad (3.96)$$

This can be verified by multiplying out the product in (3.92), which gives the Hamiltonian (3.93).

Thus, unlike matrix product states, the MPO representation of a tight-binding Hamiltonian is exact due to the fact that only neighbouring sites are related, so that the bond dimension is

$$\chi_{\text{MPO}} = 2 + N_{\text{nn}}, \quad (3.97)$$

where N_{nn} is the amount of the nearest-neighbour terms. In a similar fashion, an MPS becomes an exact representation of a state with finite correlation length, such as the AKLT state with $\chi = 2$ [Affleck et al. 1987; Schollwöck 2011].

However, the MPO representation is not unique: For example, the nearest-neighbour Coloumb interaction term in the Hubbard model (see chapter 2.1.3) contains four operator pairs if written

$$V \sum_{\langle ij \rangle} (n_{i\uparrow} n_{j\uparrow} + n_{i\uparrow} n_{j\downarrow} + n_{i\downarrow} n_{j\uparrow} + n_{i\downarrow} n_{j\downarrow}), \quad (3.98)$$

but by an obvious reordering of the summation

$$V \sum_{\langle ij \rangle} (n_{i\uparrow} + n_{i\downarrow}) (n_{j\uparrow} + n_{j\downarrow}) = V \sum_{\langle ij \rangle} n_i n_j \quad (3.99)$$

it contains only one.

One should further note that by flipping the bra vector to a ket in (3.92), an MPO acquires an MPS form with the local basis given by $|\sigma_i\rangle \otimes |\sigma_i\rangle$, so that all algorithms, including the compression via truncating the singular values can be applied:

$$H = \sum_{\sigma' \sigma} \underline{W}^{(\sigma'_1 \sigma_1)} \underline{W}^{(\sigma'_2 \sigma_2)} \dots \underline{W}^{(\sigma'_L \sigma_L)} |\sigma' \sigma\rangle. \quad (3.100)$$

However, while the bond dimension may shrink, the sparsity of the matrices is lost, effectively resulting in more entries than before, so that this procedure is of little advantage in practice. It can, however, be used to find compact representations of long-range Hamiltonians [Fröwis, Nebendahl, and Dür 2010] or to compress an operator when performing time-evolution in the Heisenberg picture [Hartmann et al. 2009].

For DMRG, it is advantageous to calculate and store H^2 as well, which is helpful to quantify the error of the ground state (see 3.6.4). One can easily check that the generator for this is just the tensor (or Kronecker) product $\underline{G}^{(l)} \otimes \underline{G}^{(l)}$. As sparsity is preserved in this case, the numerical costs of handling H^2 in this fashion are usually still acceptable, unless the local dimension gets too large.

For the Hubbard model, the generator contains the operators for the two spin polarizations in the local basis, which are given by

$$c_{\uparrow} = \begin{pmatrix} 0 & 1 & 0 & 0 \\ 0 & 0 & 0 & 0 \\ 0 & 0 & 0 & 1 \\ 0 & 0 & 0 & 0 \end{pmatrix} \quad (3.101)$$

and

$$\underline{c}_\downarrow = \begin{pmatrix} 0 & 0 & 1 & 0 \\ 0 & 0 & 0 & -1 \\ 0 & 0 & 0 & 0 \\ 0 & 0 & 0 & 0 \end{pmatrix}. \quad (3.102)$$

From here we have $\underline{n}_\sigma = (\underline{c}_\sigma)^\dagger \underline{c}_\sigma$ and all the other necessary operators.

Note that the above matrices take care of the fermionic minus sign in the local basis only, but there is an additional non-local contribution. To account for it, it is helpful to define the following convention for the order of operators in the basis states:

$$|n_1 n_2 \dots n_L\rangle := \prod_{i=1}^L \left(c_{i\uparrow}^\dagger \right)^{n_{i\uparrow}} \left(c_{i\downarrow}^\dagger \right)^{n_{i\downarrow}} |0\rangle. \quad (3.103)$$

Thus, unlike what had been done for exact states (see eq. (3.2)), we now group all local operators rather than all operators with the same spin.

To sort an operator acting on site j into this list, one has to pull it past all the sites $i < j$, each giving a fermionic phase factor f_i :

$$c_{j\sigma} = \left(\prod_{i<j} f_i \right) c_{j\sigma}^{\text{loc}}. \quad (3.104)$$

The phase factor is -1 if there is another electron and $+1$ if the site is empty. This can be represented by the occupancy number operators in the following fashion:

$$f_i = (1 - 2n_{i\uparrow}) (1 - 2n_{i\downarrow}). \quad (3.105)$$

In matrix form each f_i is given by:

$$\underline{f} = (1 - 2\underline{n}_\uparrow) (1 - 2\underline{n}_\downarrow) = \begin{pmatrix} 1 & 0 & 0 & 0 \\ 0 & -1 & 0 & 0 \\ 0 & 0 & -1 & 0 \\ 0 & 0 & 0 & 1 \end{pmatrix}. \quad (3.106)$$

This is in principle just the Jordan-Wigner transformation [Jordan and Wigner 1993; Dolfi et al. 2014]. One has of course that $f_i^2 = \mathbb{1}$. Due to this property, the fermionic phase cancels in a tight-binding hopping term, leaving only the contribution between sites:

$$c_{i+1,\sigma}^\dagger c_{i\sigma} = \left(c_{i+1,\sigma}^{\text{loc}} \right)^\dagger f_i c_{i\sigma}^{\text{loc}}. \quad (3.107)$$

In this way, we obtain the MPO generator for the extended Hubbard model:

$$\underline{G}_{\text{Hubbard}} = \begin{pmatrix} \mathbb{1} & 0 & 0 & 0 & 0 & 0 & 0 \\ \underline{c}_{\uparrow}^{\dagger} & 0 & 0 & 0 & 0 & 0 & 0 \\ \underline{c}_{\downarrow}^{\dagger} & 0 & 0 & 0 & 0 & 0 & 0 \\ \underline{c}_{\uparrow} & 0 & 0 & 0 & 0 & 0 & 0 \\ \underline{c}_{\downarrow} & 0 & 0 & 0 & 0 & 0 & 0 \\ \underline{n} & 0 & 0 & 0 & 0 & 0 & 0 \\ U\underline{d} & -\underline{f}\underline{c}_{\uparrow} & -\underline{f}\underline{c}_{\downarrow} & +\underline{f}\underline{c}_{\uparrow}^{\dagger} & +\underline{f}\underline{c}_{\downarrow}^{\dagger} & V\underline{n} & \mathbb{1} \end{pmatrix}, \quad (3.108)$$

with $\underline{d} = \underline{n}_{\uparrow}\underline{n}_{\downarrow}$. The minus sign in the last row is due to the overall negative hopping $-t = -1$ (necessary to produce a minimum of the band dispersion at the Γ -point), while the flipped sign is due to an additional commutation in order to preserve hermiticity: $-tc_{i\sigma}^{\dagger}c_{i+1,\sigma} + tc_{i\sigma}c_{i+1,\sigma}^{\dagger} = -t(c_{i\sigma}^{\dagger}c_{i+1,\sigma} + h.c.)$.

This explicit construction to obtain an MPO can also be extended to next-nearest neighbour Hamiltonians of the type

$$H = \sum_l \left(X_l Y_{l+2}^{\dagger} + Y_{l+2} X_l^{\dagger} \right). \quad (3.109)$$

A possible generator now looks like this:

$$G^{(l)} = \begin{pmatrix} \mathbb{1} & 0 & 0 & 0 & 0 & 0 \\ X_l & 0 & 0 & 0 & 0 & 0 \\ X_l^{\dagger} & 0 & 0 & 0 & 0 & 0 \\ 0 & \mathbb{1} & 0 & 0 & 0 & 0 \\ 0 & 0 & \mathbb{1} & 0 & 0 & 0 \\ 0 & 0 & 0 & Y_l^{\dagger} & Y_l & \mathbb{1} \end{pmatrix}. \quad (3.110)$$

The difference to the tight-binding case is the appearance of the "transfer" block near the left lower corner. This means that the MPO bond dimension now grows by two for each next-nearest neighbour operator pair N_{nmn} :

$$\chi_{\text{MPO}} = 2 + N_{nn} + 2N_{nmn}. \quad (3.111)$$

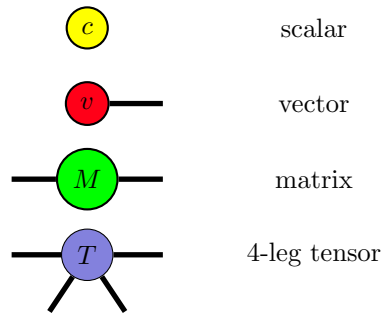
Very recently, a method of calculating MPOs from local operators has been suggested which adds them up and uses an optimized compression algorithm which preserves the sparsity of the involved matrices [Hubig, McCulloch, and Schollwöck 2017]. This is a promising step of evolution, altogether removing the need for generators tailored to the problem.

3.6.4. The ground state in DMRG

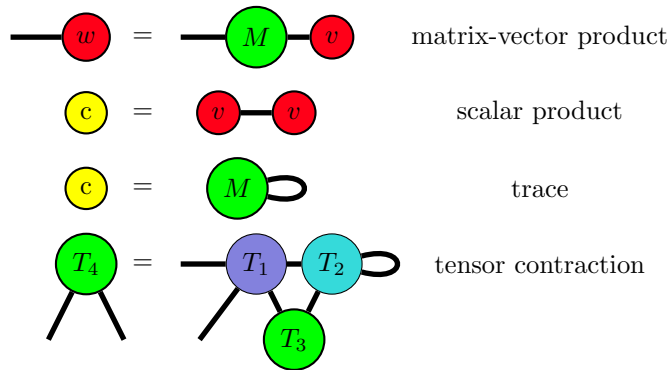
We have defined an MPS as a decomposition of the exact wavefunction which can be compressed by truncating the singular values occurring in the SVD decomposition. In practice, the exact wavefunction is of course unknown, so that we need to work backwards: Setting a threshold for maximum amount of singular values χ , we can start with a random MPS and try to work toward the ground state by interpreting the matrix entries as variational parameters and applying the Ritz principle:

$$\min \left(\langle \Psi | H | \Psi \rangle - \lambda \langle \Psi | \Psi \rangle \right) \quad (3.112)$$

with a Lagrange parameter λ . This defines a simple tensor contraction and it is helpful to represent it in graphical form. By letting closed shapes denote tensors and outgoing legs their indices in the following way:

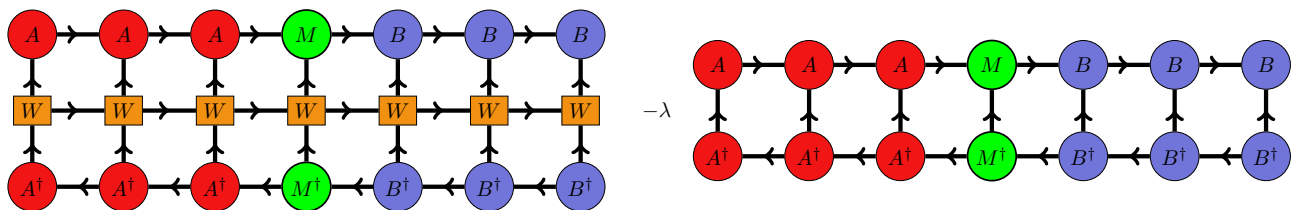


we can represent basic linear algebra operations as well as arbitrary pair contractions by identifying the legs:

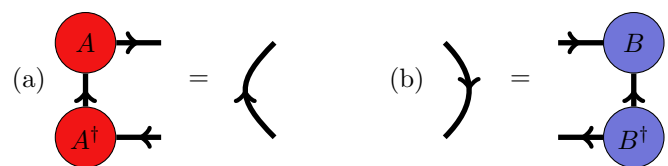


This is in fact a simplified version of the Penrose graphical notation from high-energy physics [Jorgensen 2006].

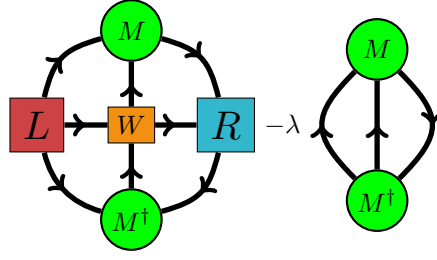
The functional in eq. (3.112) can then be represented in the following form, where we use the mixed-orthogonal form (3.91) of the MPS (the significance of the arrows is explained in 3.6.6):



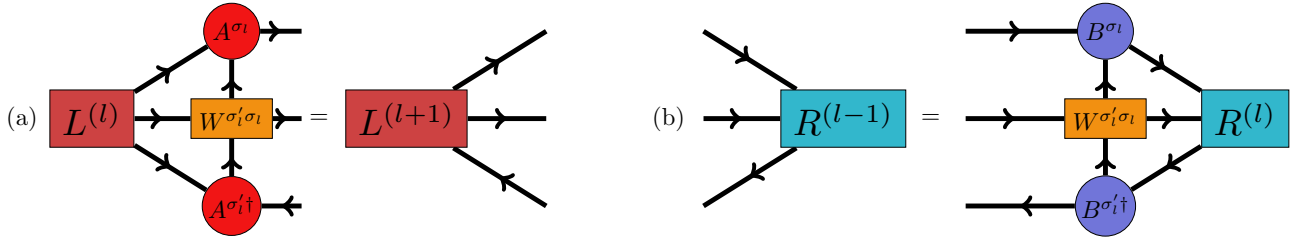
We are now facing the problem that the amount of free parameters is too large to minimize at once, and this is where the sweeping procedure comes in. At first, we note that the orthogonality constraints (3.87) and (3.89) can be represented in the following graphical form:



That is, such contractions simplify to a simple line (the identity). Next, we can contract all the tensors to the left and right of the pivot site, leading to:



The resulting three-leg tensors L and R can be interpreted as the left and right environment of the given pivot site l . The graphical notation already suggests how they can be obtained efficiently, namely by contracting iteratively from left to right or from right to left:



We can translate this back into index language, but in order not to overburden the notation, let us slightly regroup the indices in the following fashion:

$$W_{a_l b_l}^{\sigma'_i \sigma_i} \rightarrow W_{\sigma' \sigma ab}^{(l)} \quad (3.113)$$

and analogously for the other tensors. The iterative procedure now reads:

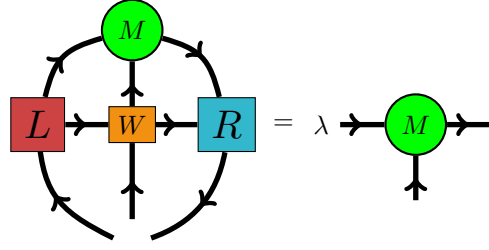
$$\begin{aligned} L_{bi'i}^{(l)} &= \sum_{ajj'} W_{\sigma' \sigma ab}^{(l-1)} \cdot \left(M_{\sigma' j' i' i}^{(l-1)} \right)^* \cdot L_{a j' j}^{(l-1)} \cdot M_{\sigma j i}^{(l-1)}, \\ R_{aii'}^{(l)} &= \sum_{bjj'} W_{\sigma' \sigma ab}^{(l+1)} \cdot M_{\sigma i j}^{(l+1)} \cdot R_{b j j'}^{(l+1)} \cdot \left(M_{\sigma' i' j' j'}^{(l+1)} \right)^*. \end{aligned} \quad (3.114)$$

We can interpret the last two indices of $L_{ijk}^{(l)}$ and $R_{ijk}^{(l)}$ as rows and columns of a matrix, so that the above equations can also be written in terms of matrix-matrix multiplications:

$$\begin{aligned} \underline{L}_b^{(l)} &= \sum_a W_{\sigma' \sigma ab}^{(l-1)} \cdot \left(\underline{M}_{\sigma'}^{(l-1)} \right)^\dagger \cdot \underline{L}_a^{(l-1)} \cdot \underline{M}_\sigma^{(l-1)}, \\ \underline{R}_a^{(l)} &= \sum_b W_{\sigma' \sigma ab}^{(l+1)} \cdot \underline{M}_\sigma^{(l+1)} \cdot \underline{R}_b^{(l+1)} \cdot \left(\underline{M}_{\sigma'}^{(l+1)} \right)^\dagger. \end{aligned} \quad (3.115)$$

In this way, we have obtained a form which can be efficiently implemented by falling back to linear algebra libraries.

Now, instead of optimizing all the parameters of the wavefunction at once, we can optimize one site at a time by taking the derivative with respect to $\left(\underline{M}_{\sigma'}^{(l)} \right)^\dagger$. Graphically, this results in:



In index notation, it becomes:

$$\sum_{ab} \sum_{i'j'\sigma'} W_{\sigma'\sigma ab}^{(l)} \cdot L_{aii'}^{(l)} \cdot R_{bjj'}^{(l)} \cdot M_{\sigma'i'j'}^{(l)} = \lambda M_{\sigma ij}^{(l)}. \quad (3.116)$$

And once more, we convert it into a matrix notation for the actual implementation:

$$\sum_{ab} W_{\sigma'\sigma ab}^{(l)} \cdot \underline{L}_a^{(l)} \cdot \underline{M}_{\sigma'}^{(l)} \cdot \underline{R}_b^{(l)} = \lambda \underline{M}_{\sigma}^{(l)}. \quad (3.117)$$

This equation is easily recognized as an eigenvalue problem for the following effective single-site Hamiltonian:

$$H_{(ij\sigma)(i'j'\sigma')}^{(l)} = \sum_{ab} W_{\sigma'\sigma ab}^{(l)} \cdot L_{aii'}^{(l)} \cdot R_{bjj'}^{(l)}. \quad (3.118)$$

Reshaping all the indices of $M_{\sigma ij}^{(l)}$ into a common vector index,

$$(\mathbf{M}^{(l)})_{(\sigma ij)} = M_{\sigma ij}^{(l)}, \quad (3.119)$$

we can simply write:

$$\underline{H}^{(l)} \cdot \mathbf{M}^{(l)} = \lambda \mathbf{M}^{(l)}. \quad (3.120)$$

Finally, a simple DMRG algorithm for the ground state is set up as follows:

Preliminary DMRG algorithm

1. Create an MPO representation of the Hamiltonian. Set a cutoff matrix dimension χ and create a random MPS of length L , i.e. a two-dimensional $L \times D$ array of matrices $\underline{M}_{\sigma}^{(l)}$ for each lattice site l and local basis vector $|\sigma_l\rangle$. Also allocate vectors of matrices $\underline{L}^{(l)}$ and $\underline{R}^{(l)}$, both of size L . Set $\underline{L}^{(1)} = \underline{R}^{(L)} = 1$ (of size 1×1) as the initial condition.
2. Left-orthogonalize the MPS by sweeping from right to left using the QR decomposition. While doing so, create the right environments $R^{(l)}$ for each site after each sweep step. This moves the pivot to $l = 1$.
3. Solve the eigenvalue problem (3.120) using the Lanczos algorithm, obtaining a new ground state energy E_0 . Use the existing tensor $M_{\sigma ij}^{(1)}$ as the initial guess. Replace $M_{\sigma ij}^{(1)}$ by the ground state solution obtained from this algorithm. Sweep to the right by decomposing the newly obtained $M_{\sigma ij}^{(1)}$ using QR, updating $M_{\sigma ij}^{(2)}$ and $L^{(2)}$. This moves the pivot to $l = 2$.

4. Continue in this fashion until each $M_{\sigma_{ij}}^{(l)}$ has been updated once. This concludes a half-sweep. Check whether the ground state energy E_0 has changed significantly during the procedure and repeat half-sweeps from right to left, followed by those from left to right until convergence.
5. Finally, ensure that the result does not depend on the cutoff χ by performing a second calculation with a larger χ ; or choose it large enough from experience.

While this algorithm will perform reasonably well for simple problems like the ground state energy of a Heisenberg chain, there are many more things to improve for an application to tougher fermionic problems (with a larger local dimension D and more entanglement entropy), which will be discussed in detail in sections 3.6.6 and 3.6.8.

3.6.5. Entanglement entropy

Let us now take a brief look at the question of why and when DMRG works and how good it is. To this end, we need to obtain its relation to reduced density matrices, from which the name itself is derived.

A common procedure is to take a system of interest, described by a wavefunction $|\Psi\rangle$ and integrate out a part of it in order to find an effective description of the remainder, in whose behaviour one is interested. It will be an open system, and thus should be properly described by a density matrix rather than a pure state. In our case, we take the chain and divide it into two blocks A and B . The reduced density matrix of block A reads:

$$\rho_A = \text{Tr}_B |\Psi\rangle\langle\Psi|. \quad (3.121)$$

Introducing the basis of the left block as $|i\rangle_A$ and the basis of the right block as $|j\rangle_B$, the wavefunction can be written as

$$|\Psi\rangle = \sum_{ij} \Sigma_{ij} |i\rangle_A |j\rangle_B. \quad (3.122)$$

Using this basis, the trace over B in (3.121) can now be easily carried out, giving

$$\rho_A = \sum_{ii'} \Sigma_{ij} \Sigma_{i'j}^* |i\rangle_A \langle i'|_A, \quad (3.123)$$

or, by stripping off the basis vectors and using a matrix notation,

$$\underline{\rho}_A = \underline{\Sigma} \underline{\Sigma}^\dagger. \quad (3.124)$$

On the other hand, we can also abuse the SVD one more time to carry out a decomposition of the matrix Σ_{ij} , leading to:

$$\begin{aligned} |\Psi\rangle &= \sum_{ij} \sum_a U_{ia} S_{aa} (V^\dagger)_{aj} |i\rangle_A |j\rangle_B \\ &= \sum_a \left(\sum_i U_{ia} |i\rangle_A \right) S_{aa} \left(\sum_j (V^\dagger)_{aj} |j\rangle_B \right) \\ &=: \sum_a S_{aa} |a\rangle_A |a\rangle_B. \end{aligned} \quad (3.125)$$

Such a representation is called *Schmidt decomposition*. In this case, U and V^\dagger define basis transformations of the bases of A and B respectively, such that the entanglement between the two subsystems becomes evident: If there is only one non-zero singular value, the two subsystems form a product state and are not entangled at all, and the more singular values are of significant size, the stronger the entanglement. Notably, the a -summation in the above equation is limited by $\min(\dim\mathcal{H}_A, \dim\mathcal{H}_B)$, so that a small system cannot couple to more states than it contains itself.

Comparing (3.125) to the MPS representation (3.90), we can see that they are identical if we set $|a\rangle_A = \sum_{\sigma_1 \dots \sigma_l} \underline{A}^{\sigma_1} \dots \underline{A}^{\sigma_l} |\sigma_1 \dots \sigma_l\rangle$, so that the first l sites of the chain form the subsystem A , while the rest forms B . Thus, DMRG can be thought of as a successive Schmidt decomposition at different points and a truncation of the singular values is possible whenever the two subsystems are weakly entangled.

Comparing (3.124) with the SVD property (3.77), one can also read off that the singular values of the Schmidt decomposition are equivalent to the eigenvalues of the reduced density matrix.

A convenient measure of the strength of the entanglement between the two subsystems is the *entanglement entropy* S . It can be defined in an intuitive fashion using the reduced density matrix in the same way the von Neumann entropy is defined in statistical mechanics:

$$S_{AB} = -\text{Tr}\rho_A \ln \rho_A. \quad (3.126)$$

As such, it is dependent on the position of the cut in the chain. Within DMRG, S is directly accessible via

$$S_{AB} = -\sum_a s_a^2 \ln s_a^2. \quad (3.127)$$

For a product state, $S = 0$ holds. Apart from that, S is expected to be maximal for a bipartition of the chain into two equal parts, as long as the system is homogeneous. Therefore, this is the quantity we shall focus on, suppressing the subscripts. This is also where the MPS will have the largest bond dimension, with $S \sim \ln \chi$ (cf. $S = k_B \ln \Omega$ from statistical mechanics). This relation can also be inverted to read $\chi \sim \exp S$ and we may ask ourselves how large χ needs to be to faithfully represent the state.

In statistical mechanics, the entropy is an extensive quantity, which is why the Hilbert space grows exponentially. For quantum ground states, however, the scaling with L is more favourable. The general result from conformal field theory is that gapped systems obey an area law, meaning that $S \sim L^{d-1}$ [Schollwöck 2005]. Intuitively, we can achieve a bipartition in $d = 1$ by cutting just one bond, while doing the same in $d = 2$ requires cutting the order of L bonds. As long as entanglement is short-ranged, the two subsystems can be thought of as only being entangled via this boundary. In $d = 1$ this means that $S = \text{const}$ and thus the wavefunction can be represented by an MPS of fixed bond dimension no matter the system size. However, with periodic boundary conditions, we need to cut two bonds and expect to get twice the entanglement entropy of open ones. While the bond dimension χ_{PBC} is still constant, with this estimate one gets that $\chi_{PBC} = \chi_{OBC}^2$. This shows that DMRG calculations with periodic boundary conditions are much more costly and are therefore avoided as much as possible.

Most of the interesting quantum systems are not actually gapped. In this case, S acquires a logarithmic term: $S \sim \ln L$ in $d = 1$. This means that χ grows as a power law and no arbitrarily large system sizes can be worked with. However, the achieved system sizes are still large enough to display thermodynamic limit behaviour: for spins (e.g. XXZ or transverse Ising model) typically $L \sim 10^3$, for fermions (e.g. Hubbard model or Kondo impurity model) typically $L \sim 10^2$. For the

former $S \sim 0.5 - 1.5$, for the latter $S \sim 1.5 - 3$. Apart from that the local dimension $D = 2$ of spin systems makes all calculations numerically cheaper.

For dynamical problems, the entanglement entropy also grows in time. This is quite obvious physically, as a perturbation will spread to neighbouring sites and create more entanglement. If we think algorithmically, time propagation is a sequence of applications of the Hamiltonian to a state and subsequent additions of states. Neither operation preserves the bond dimension: Since matrix product states dwell on the truncated Hilbert space, they do not form a vector space. The exact application of an MPO involves a tensor product and leads to an MPS with $\chi = \chi_{MPO} \cdot \chi_{MPS}$, while the exact sum of two MPS involves a direct sum of the matrices and leads to an MPS with $\chi = \chi_1 + \chi_2$.

Again, general considerations within conformal field theory lead to the prediction that $S \sim \ln t$ for a local perturbation, which is the case when calculating spectral functions or quenching impurities. In this case, a light cone propagates from the point of perturbation and S increases according to a power law. The achievable system sizes are about half of what is possible in equilibrium. The MPS can be typically propagated until the perturbation hits the edge of the chain at which point the first and last site become entangled. Calculations are easier when the perturbation is applied to the edge site, as only half of the sites get entangled at each timestep. In the case of a global parameter quench, the entanglement grows as $S \sim t^v$, so that χ increases exponentially with the prefactor v . We can now think of light cones originating at every site, leading to a much faster and stronger entanglement [Calabrese and Cardy 2005]. In this case, only few inverse hoppings can be achieved. Another general result is that entanglement grows faster for nonintegrable systems. In this case, the time scale can be very limited even for local perturbations [Prosen and Žnidarič 2007; Muth, Unanyan, and Fleischhauer 2011].

Lastly, it should be noted that the scaling of the entanglement has opened up new physical venues with an active field of what is now termed *entanglement spectroscopy*. For example in $d = 2$, one finds $S \sim \alpha L - \gamma$ where γ is a constant offset which depends on the topological state of the system. However, these developments are only tangential to the present work. See Regnault (2017) for a recent review.

3.6.6. Algorithmic details and caveats

Abelian symmetries

Just as the Hamiltonian in an exact basis becomes block-diagonal in presence of conserved quantities, a similar property emerges for matrix product states as well, although it is considerably harder to enforce algorithmically. Let us assume we have an additive conserved quantity $\hat{Q} = \sum_{l=1}^L \hat{q}_l$ with $[H, \hat{Q}] = 0$. We can then choose a basis of local eigenstates of \hat{Q} . The first thing to notice is that the left and right states of the MPS (see (3.122)) become eigenstates of \hat{Q} as well:

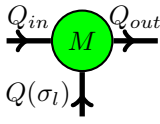
$$\begin{aligned}\hat{Q}|i\rangle_A &= Q_{iA}|i\rangle_A, \\ \hat{Q}|j\rangle_B &= Q_{jB}|j\rangle_B.\end{aligned}\tag{3.128}$$

With this, the local tensors are only non-zero if the following condition is respected:

$$M_{ij}^{\sigma_l} \begin{cases} \neq 0 & \text{if } Q_{iA} + Q(\sigma_l) = Q_{jA} \\ & \text{and } Q_{iA} + Q_{jB} = Q_{\text{tot}} \text{ can be fulfilled,} \\ = 0 & \text{else,} \end{cases}\tag{3.129}$$

where Q_{tot} is the desired quantum number of the state (e.g. a fixed particle number or magnetization). Hence, \underline{M}^{σ_l} obtains a block structure. This result can be straightforwardly generalized to tuples of quantum numbers resulting from different $U(1)$ symmetries: $\hat{Q} = \{\hat{Q}^{(1)}, \hat{Q}^{(2)}, \dots\}$.

As a visualization of Abelian symmetries in the diagrammatic representation, we can assign arrows to all contraction lines and count incoming lines with a plus sign, outgoing lines with a minus sign:



$$Q_{in} + Q(\sigma_l) - Q_{out} = 0$$

This is reminiscent of Kirchhoff's rules for currents in circuits. As boundary conditions, we need to assume that there is a vacuum state flowing into the first site and the value Q_{tot} flowing out of the last site. To demonstrate the block structure of an MPS with Abelian symmetries, fig. 3.3 shows an $L = 6$ Hubbard chain with $Q = \{N_{\uparrow}, N_{\downarrow}\}$ and $Q_{\text{tot}} = \{3, 3\}$ (half filling).

In the numerical implementation, instead of a simple matrix for each value of σ_l , the encoding of \underline{M}^{σ_l} now requires an object of higher complexity, let's call it *biped* for its amount of legs (the physical index σ_l is treated separately): It needs to contain a vector of block matrices and two corresponding vectors of quantum numbers, incoming and outgoing³. The quantum numbers themselves are generally tuples, as we have seen, and can be added and subtracted entry-wise. This kind of problem lends itself nicely to an object-oriented implementation in C++ using generic containers. Note that we also have the reverse problem of finding a particular block matrix from a given pair of quantum numbers. It needs to be solved efficiently lest the overhead kills any performance gains, and can actually be done so by endowing the *biped* class with a dictionary, which translates quantum number pairs back into vector indices. If one provides a hash function for the quantum number pairs, such a dictionary search will work in constant time.

Finally, every operation one had with normal matrices has to be generalized for the *biped* object: Addition must be performed block-wise, unmatching block matrix sizes must not appear. Multiplication $M_1 \cdot M_2$ is performed only for those blocks where the outgoing indices of M_1 match the incoming indices of M_2 . The resulting block then has the incoming index of M_1 and the outgoing index of M_2 .

Another operation which needs to be generalized is sweeping. The reshaping of indices $M_{ij}^{\sigma} \rightarrow M_{(\sigma_l)j}$ during a right-sweep shows that this can be done for all outgoing indices of M_{ij}^{σ} , since the outgoing leg j is not touched. Of course, the reverse case is true for a left-sweep. This means that one needs to loop over all distinct outgoing indices, concatenate the corresponding block matrices, perform the SVD (or QR), unconcatenate the updated U -matrix to update the blocks at site l and multiply the SV^{\dagger} part onto the block matrix with the incoming index at the site $l + 1$ which matches the sum rule. The sweep to the left follows analogously.

Having a *biped* class is not enough, however, since the DMRG algorithm also requires the environment tensors $L_{a_i i' i}^{(l)}$ and $R_{a_j j' j}^{(l)}$ which have three legs; and possibly larger tensors as well. Hence, the above class needs to be further generalized to a *multipede* with an arbitrary amount of legs. A vector of block matrices now becomes a multi-array and we need some kind of convention of how to refer to the additional legs, all of which can be incoming or outgoing.

Thus one can see that while the enforcement of Abelian symmetries is straightforward conceptually, a numerical implementation requires a lot of effort and actually constitutes the main part of a working DMRG code.

³One of the two is actually redundant due to the sum rule, but keeping it is helpful to preserve the sanity of the programmer.

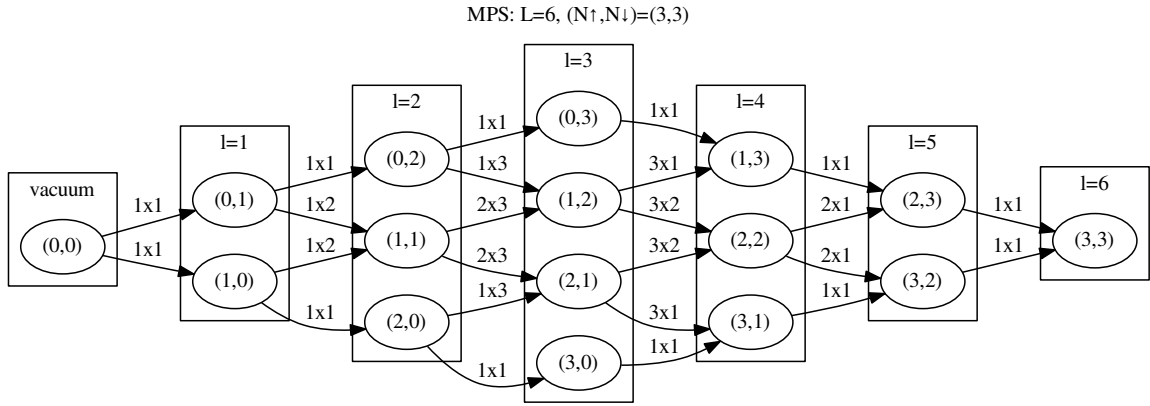


Figure 3.3.: Graph representation of the subspaces of the Hubbard model with $L = 6$ sites at half filling. The values in brackets represent tuples of the good quantum numbers $(N_{\uparrow}, N_{\downarrow})$, the values on the arrows indicate the matrix dimensions, which are the exact values for this small problem.

Fluctuations

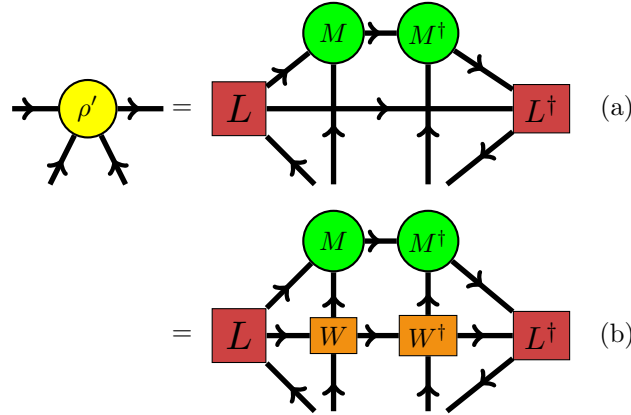
While the implementation of Abelian symmetries leads to a significant increase in numerical efficiency, it also produces two additional problems: First, the bond dimension χ is now obtained as the maximal sum of rows or columns of all block matrices, but it is not clear a priori how large the block matrices have to be, a simple uniform distribution of χ onto the blocks will surely be suboptimal. Second, the algorithm becomes prone to being stuck in a local minimum because of the reduced parameter space during optimization. However, both problems can be solved simultaneously, as described in the following.

Two-site algorithm The simple solution is to modify the algorithm into being two-site, that is instead of optimizing \underline{M}^{σ_l} , one optimizes the contraction of two tensors $\tilde{\underline{M}}^{(\sigma_l \sigma_{l+1})} = \underline{M}^{\sigma_l} \underline{M}^{\sigma_{l+1}}$ with the corresponding effective Hamiltonian, but then still moves the pivot site only by one. In this way, the parameter space is somewhat enlarged, and the block matrix rows and columns can grow dynamically during countergoing half-sweeps. This is a very robust procedure which also works in the presence of non-Abelian symmetries, as well as when compressing an MPS (see 3.6.7).

Density matrix perturbation Another method going back to White [White 2005] is to perform sweeping by diagonalizing the density matrix, $\underline{\rho}_{\sigma_l \sigma'_l} = \underline{M}^{\sigma_l} \underline{M}^{\sigma'_l \dagger}$ on the right-sweep and $\underline{\rho}_{\sigma_l \sigma'_l} = \underline{M}^{\sigma'_l \dagger} \underline{M}^{\sigma_l}$ on the left-sweep. This is identical to the SVD by virtue of (3.77). The idea is now to add a controlled fluctuation term to the density matrix, $\underline{\rho} \rightarrow \underline{\rho} + \alpha \underline{\rho}'$ with a small mixing parameter α . The fluctuation leads to a dynamic increase in matrix size and moves the algorithm out of a local minimum, but if it is completely random, the algorithm will be drawn away from the fixpoint. We thus need fluctuations which are directed towards it. The solution comes from realizing that the power method, where one iterates $|\Psi\rangle_{n+1} = (1 - \alpha H) |\Psi\rangle_n$ converges to the ground state (this serves as a kind of simplified Lanczos algorithm). One thus basically needs a multiplication of the current wavefunction with the Hamiltonian:

$$\underline{\rho}' = \text{Tr}_R (H (\underline{\rho} \otimes \mathbb{1}) H^\dagger) \quad (\text{right-sweep}). \quad (3.130)$$

The exact evaluation of this formula becomes too laborious and is in fact not needed. One can use a number of approximations instead, for example [Schwabe 2015]:



or in formulaic notation:

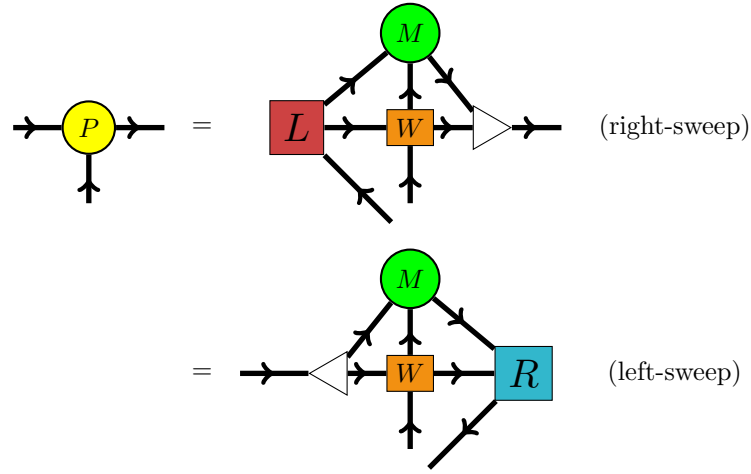
$$\begin{aligned} (a) \quad \underline{\rho}'_{\sigma_l \sigma'_l} &= \sum_a \underline{L}_a^{(l-1)} \rho^{\sigma_l \sigma'_l} \left(\underline{L}_a^{(l-1)} \right)^\dagger, \\ (b) \quad \underline{\rho}'_{\sigma_l \sigma'_l} &= \sum_a \sum_{\sigma''_l \sigma'''_l} W_{ab}^{\sigma_l \sigma''_l} \underline{L}_a^{(l-1)} \rho^{\sigma''_l \sigma'''_l} \left(\underline{L}_a^{(l-1)} \right)^\dagger \left(W_{ab}^{\sigma'_l \sigma'''_l} \right)^*. \end{aligned} \quad (3.131)$$

The formulae for the left-sweep follow analogously. In practice, α should be slowly decreased to zero as the ground state converges. Unfortunately, due to the construction of the density matrix, the algorithm will now perform significantly slower.

Enriched SVD Recently, another technique has been suggested that outperforms the density matrix perturbation in every way [Hubig et al. 2015]. The idea is to expand the pivot tensor in the direction opposite to the concatenation during sweeping, thereby increasing the basis for the ground state search. To preserve the MPS form, the neighbouring tensor has to be enlarged as well and filled with zeros:

$$\begin{aligned} \underline{M}^{\sigma_l} &\rightarrow \left[\begin{array}{cc} \underline{M}^{\sigma_l} & \underline{P}^{\sigma_l} \end{array} \right], & \underline{B}^{\sigma_{l+1}} &\rightarrow \left[\begin{array}{c} \underline{B}^{\sigma_{l+1}} \\ 0 \end{array} \right] \quad (\text{right-sweep}), \\ \underline{M}^{\sigma_l} &\rightarrow \left[\begin{array}{c} \underline{M}^{\sigma_l} \\ \underline{P}^{\sigma_l} \end{array} \right], & \underline{A}^{\sigma_{l-1}} &\rightarrow \left[\begin{array}{cc} \underline{A}^{\sigma_{l-1}} & 0 \end{array} \right] \quad (\text{left-sweep}). \end{aligned} \quad (3.132)$$

In order to compute the perturbation \underline{P}^{σ_l} , Hubig et al. suggest the following contractions:



or in formulaic notation:

$$\begin{aligned}
 \underline{P}_{i(jb)}^{\sigma_l} &= \alpha \sum_{\sigma'_l} W_{ab}^{\sigma_l \sigma'_l} \left(\underline{L}_a^{(l-1)} \underline{M}^{\sigma'_l} \right)_{ij} \quad (\text{right-sweep}), \\
 \underline{P}_{(ia)j}^{\sigma_l} &= \alpha \sum_{\sigma'_l} W_{ab}^{\sigma_l \sigma'_l} \left(\underline{M}^{\sigma'_l} \underline{R}_b^{(l+1)} \right)_{ij} \quad (\text{left-sweep}).
 \end{aligned} \tag{3.133}$$

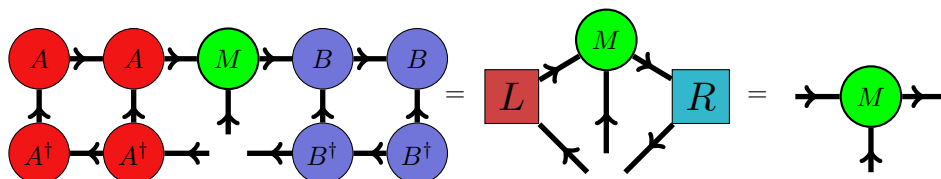
As a heuristic motivation, one sees here a similar partial multiplication with the Hamiltonian $\langle \Psi | H | \Psi \rangle$ as in the case of the density matrix perturbation. However, in contrast to the latter, the contraction itself is cheaper to obtain and one does not need to construct the full expensive density matrix either. Furthermore, this technique is found to require less sweeps to reach the ground state, overall leading to a significant increase in efficiency. Finally, the mixing parameter α does not have to be small or taken to zero, as the additional states will be simply ignored by the ground state algorithm once one is sufficiently converged. This removes the need for fine-tuning a protocol of setting α to zero, as is required in the density matrix perturbation method.

3.6.7. Compression of matrix product states

When working with MPS, and in particular during time evolution, one is often faced with a problem of compressing an MPS to minimize the bond dimension, or in other words to find a $|\phi\rangle$, such that

$$\left\| |\phi\rangle - |\Psi\rangle \right\|^2 = \langle \phi | \phi \rangle + \langle \Psi | \Psi \rangle - \langle \phi | \Psi \rangle - \langle \Psi | \phi \rangle < \epsilon \tag{3.134}$$

for a given $|\Psi\rangle$ (not necessarily normalized) and a tolerance ϵ . Since this problem is very similar to the ground state minimization, one can proceed in a similar fashion. Writing down the overlap in the mixed orthogonalization, taking the derivative with respect to $(\underline{M}^{\sigma_l})^\dagger$ (which only appears in $\langle \phi |$) and contracting the tensors to form the left and right environment of the site l , one obtains:



This means that compared to running a Lanczos algorithm with an effective Hamiltonian, as was done to find the ground state, one can simply update \underline{M}^{σ_l} as the above contraction before continuing to sweep. Due to this relation, we have that $\langle \phi | \Psi \rangle = \langle \phi | \phi \rangle$, so that the calculation of the tolerance comes very cheaply:

$$\epsilon = \langle \Psi | \Psi \rangle - \langle \phi | \phi \rangle = \langle \Psi | \Psi \rangle - \sum_{\sigma_l} \text{Tr} (\underline{M}^{\sigma_l \dagger} \underline{M}^{\sigma_l}). \quad (3.135)$$

The whole procedure obviously generalizes to the case where $|\Psi\rangle$ is a product with an operator, $O|\Psi\rangle$. For that, calculating the tolerance requires the contraction $\langle \Psi | O^\dagger O | \Psi \rangle$ instead of $\langle \Psi | \Psi \rangle$. In this way, the application of an MPO to an MPS can be implemented efficiently.

An important special case is polynomial iteration, where one has to minimize

$$\| |\phi\rangle - \alpha H |\Psi_1\rangle - \beta |\Psi_2\rangle \|^2 = \epsilon. \quad (3.136)$$

For Chebyshev polynomials, $\alpha = 2$ and $\beta = -1$ (cf. eq. 3.40). Naively, one would perform this in two steps, which is unnecessary and leads to avoidable errors.

Instead, one can set up two environments, one with the overlap $\langle \phi_1 | H | \Psi_1 \rangle$ and one with $\langle \phi_2 | \Psi_2 \rangle$. Then, $|\phi_1\rangle$ and $|\phi_2\rangle$ are optimized at the same pivot site and the addition $\underline{M}^{\sigma_l} = \alpha \underline{M}_1^{\sigma_l} + \beta \underline{M}_2^{\sigma_l}$, resulting in the pivot tensor of $|\phi\rangle$, can be performed blockwise. For the error one obtains in the case of real states:

$$\epsilon = \beta^2 \langle \Psi_2 | \Psi_2 \rangle + \alpha^2 \langle \Psi_1 | H^2 | \Psi_1 \rangle + 2\alpha\beta \langle \Psi_2 | H | \Psi_1 \rangle - \langle \phi | \phi \rangle. \quad (3.137)$$

Note that in a compression problem we know the wavefunction which we want to approximate exactly (we just want to prevent it from growing uncontrollably), so that the tolerance ϵ is known exactly as well, and the whole procedure is well-controlled.

With regard to the bond dimension, it stands to reason to start with a state $|\phi\rangle$ which has the same block dimensions as $|\Psi\rangle$. If the given error tolerance cannot be achieved, it means that the bond dimension of $|\phi\rangle$ has to be increased. To do that dynamically and adaptively, one can shift to a two-site algorithm (as described in 3.6.6) for a single half-sweep. In practice, doing such an enlargement every four ordinary half-sweeps has been found to be optimal.

3.6.8. Final DMRG algorithm

This chapter mentions a couple of crucial details which are necessary for an efficient DMRG algorithm to be able to handle fermionic problems, such as has been implemented as part of this work.

- As the first step, one fixes a total quantum number Q_{tot} , e.g. the amount of particles or magnetization, and creates an MPS with the respective block arrays, incoming/outgoing indices and dictionaries. When working with symmetries, one can effectively only fix the maximal bond dimension of a single block χ^{sub} , while the total maximal bond dimension emerges from χ^{sub} and the amount of blocks. As the initial value, $\chi^{\text{sub}} = 1$ works just fine.
- While the algorithm runs, the enriched SVD technique (3.6.6) is used with $\alpha = 10^{-2}$ (which does not need to be changed during the run), allowing the state to grow adaptively, so that an optimal χ is achieved at the end. If the problem is prone to converge in a local minimum, one might need to increase α up to $\alpha = 10^1$.

- All singular values which are smaller than a tolerance ϵ_{SVD} are cut (the value $\epsilon_{SVD} = 10^{-7}$ has proven adequate), but not more than a given integer N_{sv} (with an initially small $N_{sv} = 4$, for example). This has the effect that the state has time to pre-converge at a smaller bond dimension and χ is prevented from growing too fast. If the sum of all truncated singular values exceeds ϵ_{svd} after a sweep, N_{sv} can be slowly taken up (specifically in the code: by 10%, though at least by 1).
- As the main error tolerance, one uses the change in the energy density $\epsilon_{\text{energy},n} = |E_{0,n} - E_{0,n-1}|/L$ after the n -th half-sweep. As an additional tolerance of the quality of the state, one can use the variance $\epsilon_{\text{state},n} = |\langle E_{0,n}|H^2|E_{0,n}\rangle - E_{0,n}^2|/L$. It is normally not costly to compute and store H^2 , making the contraction $\langle H^2 \rangle$ rather fast (not more than a few percent of the half-sweep time). Otherwise one can also perform the full contraction with $H \cdot H$ each time. If this is also too costly, the quality of the state can also be assessed by checking the change in the overlap $\epsilon_{\text{state},n} = |1 - \langle E_{0,n}|E_{0,n-1}\rangle|$, but looking only at changes has the danger of getting stuck in a local minimum without noticing it. Typically, requiring $\epsilon_{\text{energy},n} < 10^{-7}$ and $\epsilon_{\text{state},n} < 10^{-6}$ is necessary to achieve a well-converged solution.

3.6.9. Time propagation

Splitting integrators

Before discussing specific time propagation algorithms for DMRG, it is helpful to familiarize oneself with splitting integration methods. Apart from the fact that many physical problems naturally lend themselves to such techniques, they also exhibit some desirable structure-preserving properties, like unitarity (preservation of the norm), symplecticity (preservation of the phase space volume) and reversibility.

Let us assume that we have a first-order ordinary differential equation where we can split the right-hand side in such a fashion that the equation would be integrable by a known method if only one of the terms was present:

$$\dot{x} = f(x) = A(x) + B(x), \quad (3.138)$$

with the integration rules φ_h^A and φ_h^B for a small timestep h , so that:

$$\begin{aligned} x(h) &= \varphi_h^A(x_0), & B &= 0, \\ x(h) &= \varphi_h^B(x_0), & A &= 0. \end{aligned} \quad (3.139)$$

This type of problem is quite common. For instance, it appears in a classical Hamiltonian system with $x = (q, p)$, where we can split off the kinetic and potential energies: $H(p, q) = T(p) + V(q)$, so that $T(p)$ can be trivially integrated over q , while $V(q)$ can be trivially integrated over p .

We can now introduce an integration rule for the full problem by composing the two integrators, thus obtaining a first-order integrator⁴:

$$\chi_h = \varphi_h^B \circ \varphi_h^A. \quad (3.140)$$

Of course, one can just as well compose the individual integrators in the reverse order with the same error, which is called the "adjoint integrator":

⁴By convention, an integrator is called n -th order if it is correct up to $O(h^{n+1})$.

$$\chi_h^* = \varphi_h^B \circ \varphi_h^A. \quad (3.141)$$

By composing more integrators, we can choose the timesteps in such a fashion that the error scaling goes down even more. A popular choice is the following symmetric second-order integrator [Lubich 2008; McLachlan 1995; Blanes, Casas, and Murua 2008]

$$S_h^{(2)} = \varphi_{h/2}^A \circ \varphi_h^B \circ \varphi_{h/2}^A = \chi_{h/2}^* \circ \chi_{h/2}. \quad (3.142)$$

It is called *leapfrog*, *Störmer–Verlet method* or *Strang splitting*, depending on the field of application.

A likewise popular choice is the following fourth-order and three-stage method, which means that it is composed out of three $S^{(2)}$ integrators [Lubich 2008; McLachlan 1995; Blanes, Casas, and Murua 2008]:

$$S_h^{(4,3)} = S_{\alpha h}^{(2)} \circ S_{\beta h}^{(2)} \circ S_{\alpha h}^{(2)}, \quad \alpha = \frac{1}{2 - 2^{1/3}} \approx 1.351, \quad \beta = 1 - 2\alpha \approx -0.702. \quad (3.143)$$

One notices that the timestep becomes negative, a property one cannot get rid of at higher orders [Blanes et al. 2009].

We could also seek a cheaper two-stage integrator:

$$S_h^{(4,2)} = S_{h/2}^{(2)} \circ S_{h/2}^{(2)}, \quad (3.144)$$

but an error analysis shows that it is still of second order, albeit with a smaller prefactor [McLachlan 1995].

The precision can be pushed further, formulae for up to eighth order have been derived [McLachlan 1995]. However, they are only necessary if one attempts a propagation to extremely long times, where the timestep error becomes noticeable. The precision is obviously bought by more function evaluations at each timestep. For quantum systems, only modest time scales can be achieved due to other reasons (as finite-size effects or entanglement growth), so that the above formulae are more than enough to achieve sufficient accuracy. In addition, a peculiarity of DMRG consists in the fact that each application of an MPO to the state (which plays the role of a function evaluation) is error-prone in itself due to truncation, so that avoiding higher integration orders actually leads to an *improvement* in accuracy for short to medium times.

Time-evolving block decimation (TEBD)

The Suzuki-Trotter method, for historical reasons also called *time-evolving block decimation* (TEBD), is a method imported into the DMRG world from Monte Carlo simulations and has been the working horse for dynamic problems for many years. The key idea is to realize that a tight-binding Hamiltonian can be split into two commuting parts for even and odd bonds:

$$\begin{aligned} H &= \sum_{i=1}^{L-1} h_{i,i+1} = H_o + H_e, \\ H_o &= h_{12} + h_{34} + \dots + h_{L-1,L}, \\ H_e &= h_{23} + h_{45} + \dots + h_{L-2,L-1}, \end{aligned} \quad (3.145)$$

with

$$[H_e, H_o] = 0, \quad (3.146)$$

where we have assumed the chain length to be even.

The splitting integration method can now be applied due to the fact that all the bond terms in H_e and H_o also commute with each other:

$$[h_{i,i+1}, h_{i+2,i+3}] = 0 \quad \text{etc.}, \quad (3.147)$$

so that the subsequent splitting

$$e^{-iH_o t} = e^{-ih_{12}t} e^{-ih_{34}t} \dots e^{-ih_{L-1,L}t} \quad (3.148)$$

involves no approximation. The above expression just contains propagations with two-site Hamiltonians. The solution can be obtained by fully diagonalizing them and applying the SVD to the result in order to maintain an MPO form [Schollwöck 2011]. Note that this destroys the sparsity of the original Hamiltonian, the result consists out of dense $1 \times D^2$ and $D^2 \times 1$ matrices.

Thus, we obtain a second-order integrator with the leapfrog algorithm (3.142):

$$e^{-iH\delta t} = e^{-iH_o\delta t/2} e^{-iH_e\delta t} e^{-iH_o\delta t/2} + O(\delta t^3) \quad (3.149)$$

and similarly a fourth-order algorithm with eq. (3.143). At the application of each exponential, the state must be truncated.

An obvious disadvantage of the TEBD method is that it is limited to tight-binding systems. But even setting that aside, it seems very un-DMRG-like: It would be nicer if we could propagate the state itself with local updates as we did in the ground state calculation rather than dealing with the dense time evolution operator. A method which does exactly that is presented in the following.

Time-dependent variational principle (TDVP)

The time-dependent variational principle was first introduced by Dirac [Dirac 1930]. Essentially, it generalizes the Ritz variational principle to the time-dependent Schrödinger equation. A solution of

$$\frac{\partial}{\partial t} \psi(t) = -iH\psi(t) \quad (3.150)$$

is now sought to be restricted to a variational submanifold \mathcal{S} at all times. Let us assume that at $t = 0$, we have found a solution $u(0)$ which is in \mathcal{S} . The state will leave that manifold if we attempt to solve the equation exactly, so what we are interested in is an approximate solution from the manifold $u(t) \in \mathcal{S}$ rather than the exact $\psi(t)$.

We can find $u(t)$ by imposing the condition that $\frac{\partial u}{\partial t}$ should lie in the tangent space to \mathcal{S} at u , denoted by $\mathcal{T}_u \mathcal{S}$. In other words, we choose $\frac{\partial u}{\partial t}$ as the w for which $\|w + iHu\|^2$ is minimal. In yet other words this is equivalent to choosing $\frac{\partial u}{\partial t}$ as the orthogonal projection of iHu onto the tangent space [Lubich 2008]. We can introduce a projection operator to denote this:

$$\frac{\partial u}{\partial t} = P_{\tau_u} S H u(t). \quad (3.151)$$

In DMRG, the wavefunction is parametrized as a matrix product state using the tensors $M_{ij}^{\sigma_l}$. Each entry is a variational parameter, so that a general variation looks like this:

$$\delta|\Psi[M]\rangle = \sum_l \sum_{\{ij\sigma_l\}} \delta M_{ij}^{\sigma_l} \frac{\partial}{\partial M_{ij}^{\sigma_l}} |\Psi[M]\rangle. \quad (3.152)$$

Let us rewrite that expression exploiting the mixed-orthogonal form:

$$\begin{aligned} |\Theta[C]\rangle &= \sum_l \sum_{\{\sigma_l\}} \underline{A}^{\sigma_1} \dots \underline{A}^{\sigma_{l-1}} \underline{C}^{\sigma_l} \underline{B}^{\sigma_{l+1}} \dots \underline{B}^{\sigma_L} |\sigma_1 \dots \sigma_l \dots \sigma_L\rangle \\ &=: \sum_l \sum_{\{ij\sigma_l\}} C_{ij}^{\sigma_l} |a_i^{[1:l-1]}\rangle |\sigma_l\rangle |b_j^{[l+1:L]}\rangle. \end{aligned} \quad (3.153)$$

$|\Theta[C]\rangle$ is now the most general variation of an MPS. However, not all the linearly independent choices for C produce linearly independent tangent vectors, so that an additional restriction has to be imposed. Haegeman et al. have proposed the following [Haegeman et al. 2011; Haegeman et al. 2016]:

$$\sum_{\sigma_l} (\underline{A}^{\sigma_l})^\dagger \underline{C}^{\sigma_l} = 0 \quad \forall l = 1, \dots, L-1, \quad (3.154)$$

which we accept here without proof. We thus need to calculate

$$\min_C \left\| |\Theta[C, A]\rangle + iH|\Psi[A(t)]\rangle \right\|^2, \quad (3.155)$$

with the restriction (3.154) in order to fix C . In order to facilitate readability, we can consider a general vector $|\Xi\rangle$:

$$\min_C \left\| |\Theta[C]\rangle - |\Xi\rangle \right\|^2 = \min_C (\langle\Theta|\Theta\rangle - \langle\Theta|\Xi\rangle - \langle\Xi|\Theta\rangle). \quad (3.156)$$

This becomes:

$$\min_C \sum_l \sum_{\sigma_l} (\underline{C}^{\sigma_l} \underline{C}^{\sigma_l \dagger} - \underline{C}^{\sigma_l} \underline{F}^{\sigma_l \dagger} - \underline{F}^{\sigma_l} \underline{C}^{\sigma_l \dagger}), \quad (3.157)$$

where the matrix elements of \underline{F}^{σ_l} are given by:

$$F_{ij}^{\sigma_l} = \langle a_i^{[1:l-1]} \sigma_l b_j^{[l+1:L]} | \Xi \rangle. \quad (3.158)$$

A quick look shows that \underline{C}^{σ_l} must be essentially equal to \underline{F}^{σ_l} , but since we also need to take care of the restriction (3.154), the solution is given by:

$$\underline{C}^{\sigma_l} = \sum_{\sigma'_l} \left(\delta_{\sigma_l \sigma'_l} - \underline{A}^{\sigma_l} \left(\underline{A}^{\sigma'_l} \right)^\dagger \right) \underline{F}^{\sigma'_l}. \quad (3.159)$$

One can check that eq. (3.154) is fulfilled by inspection. Plugging this back into eq. (3.153) we obtain

$$|\Theta[C]\rangle = P_{\mathcal{T}_{\Psi[M]}\mathcal{S}}|\Xi\rangle, \quad (3.160)$$

with the projection operator onto the tangent space we were looking for:

$$P_{\mathcal{T}_{\Psi[M]}\mathcal{S}} = \sum_l P_A^{[1:l-1]} \otimes \mathbf{1}_l \otimes P_B^{[l+1:L]} - \sum_l P_A^{[1:l]} \otimes P_B^{[l+1:L]}, \quad (3.161)$$

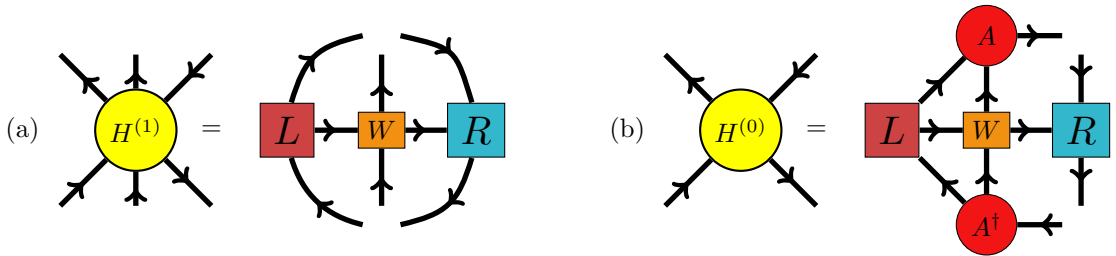
where we have defined

$$\begin{aligned} P_A^{[1:n]} &= \sum_i |a_i^{[1:l]}\rangle \langle a_i^{[1:l]}|, \\ P_B^{[l+1:L]} &= \sum_i |b_i^{[l+1:L]}\rangle \langle b_i^{[l+1:L]}|. \end{aligned} \quad (3.162)$$

Hence, the TDVP differential equation becomes:

$$\begin{aligned} \frac{\partial}{\partial t} |\Psi[M]\rangle &= -i P_{\mathcal{T}_{\Psi[M]}\mathcal{S}} H |\Psi[M]\rangle \\ &= -i \left(\sum_l H_l^{(1)} - \sum_l H_l^{(0)} \right) |\Psi[M]\rangle. \end{aligned} \quad (3.163)$$

Here, $H_l^{(1)}$ is the same effective one-site Hamiltonian which also appears in the ground state algorithm, while $H_l^{(0)}$ is an effective zero-site Hamiltonian acting between bonds:



With the matrix-vector notation introduced in (3.120), the first term can be integrated exactly by calculating

$$\mathbf{M}_l(t) = e^{-i\underline{H}_l^{(1)}t} \mathbf{M}_l(0), \quad (3.164)$$

using the Lanczos time propagation method (see chapter 3.2.2) and performing a half-sweep through the chain once. Writing $\underline{M}^{\sigma_l} = \underline{A}^{\sigma_l} \underline{\Gamma}^{\sigma_l}$ for the SVD decomposition of the pivot tensor and using the same matrix-vector notation, the second term can be integrated by calculating

$$\Gamma_l(t) = e^{+i\mathbb{H}_l^{(0)}t}\Gamma_l(0) \quad (3.165)$$

and doing a half-sweep as well. Note that in the latter case, we are curiously dealing with a propagation backwards in time.

We can now join the two integrators to obtain a first-order integrator of the full problem according to (3.140) by first applying (3.164), SVD-decomposing the result, applying (3.165), multiplying $\underline{\Gamma}^{\sigma_l}(t)$ onto the next site and continuing until a half-sweep is completed. The adjoint of this is simply given by a half-sweep in the other direction. Thus, by composing the integrator with its adjoint and half the timestep according to the leapfrog formula (3.142), we obtain a second-order algorithm with one full sweep.

While the whole point of the time-dependent variational principle is to approximate the state on a given manifold for all times, we know that this is not possible for matrix product states, as the bond dimension grows in time, so that it is necessary to move to a different manifold with a higher bond dimension and more variational parameters. It stands to reason to modify the TDVP algorithm to be a two-site algorithm, as it was done in 3.6.6 and 3.6.7 [Haegeman et al. 2016]. Everything generalizes straightforwardly and instead of $H^{(1)}$ and $H^{(0)}$, we now need the two- and one-site Hamiltonians, respectively: $H^{(2)}$ and $H^{(1)}$.

Performance benchmark

When propagating matrix product states, there is an additional source of error due to the compression of the wavefunction at each timestep, which is absent when working with exact states. It is intermingled with the usual timestep error: A larger timestep leads to fewer compressions, but the wavefunction will deteriorate for long times. However, in order to reduce the error at long times, small timesteps are necessary. This means that one needs to strike a compromise.

In the following, the two above-mentioned algorithms are tested out by calculating the dynamical spin-spin susceptibility

$$\Pi_{ij}(t-t') = -i\theta(t-t') \langle [\mathbf{S}_i(t), \mathbf{S}_j(t')] \rangle \quad (3.166)$$

for the Hubbard model. It was used in a side-project to this work in order to investigate the dynamics of a classical magnetic impurity on a correlated substrate [Sayad, Rausch, and Potthoff 2016a] (see chapters 1.4 and 5.2). When treating the impurity-substrate coupling in perturbation theory, one can derive an integro-differential equation of motion for the classical spin, which contains a memory kernel given by $\Pi_{ij}(t-t')$. Exploiting rotational symmetry in the spin space and placing the impurity on the edge of a one-dimensional chain ($i = j = 1$), one only needs to calculate $\Pi_{11}^{zz}(t-t')$. With some straightforward manipulations, the latter can be brought into the following numerically convenient form:

$$\Pi_{11}^{zz}(t-t') = \theta(t-t') 2\text{Im} \left(e^{iE_0(t-t')} \langle E_0 | S_1^z e^{-iH(t-t')} S_1^z | E_0 \rangle \right). \quad (3.167)$$

During the time propagation, the energy as well as the norm of the wavefunction have to be conserved, but numerical truncation will lead to a deterioration. One can take the relative deviation from the initial value as a measure of error:

$$\delta E := \left| \frac{\langle \Psi(t) | H | \Psi(t) \rangle - \langle \Psi(0^+) | H | \Psi(0^+) \rangle}{\langle \Psi(0^+) | H | \Psi(0^+) \rangle} \right|, \quad (3.168)$$

where the state at time $t = 0^+$ is taken to be $|\Psi(0^+)\rangle = S_1^z|E_0\rangle$.

We compare the second-order TEBD algorithm (3.149) with the second-order two-site TDVP algorithm. As the error tolerance for TEBD, we fix the compression tolerance at the application of each exponential, $\epsilon = \left\| |\phi\rangle_n - \exp(-iH_{e/o}t) |\phi\rangle_{n-1} \right\|^2$. As the error tolerance for TDVP, we fix the singular value truncation threshold. It should be noted that the two are not the same, making a direct comparison difficult. Yet, a value of 10^{-7} according to both definitions leads to such large bond dimensions that the problem becomes barely computable, in this sense the two are at least roughly comparable. We can therefore vary ϵ between 10^{-4} and 10^{-6} .

The timestep should be smaller than the typical timescale of the system (equal to 1 in our units), but it is desirable to keep it as large as possible. The upper two panels of fig. 3.4 show the errors for fixed $\delta t = 0.2$ and different compression tolerances ϵ . One observes that the error is fairly large for TEBD and cannot be reduced further with a smaller value of ϵ , which means that the Trotter error resulting from the non-commutativity of the bonds $[H_e, H_o] \neq 0$ dominates and can only be brought down by reducing the timestep. In other words, TEBD cannot handle large timesteps, unless one puts in more effort and goes beyond second order. On the other hand, the TDVP error is much smaller overall and monotonously decreases with the compression tolerance.

The next two panels of fig. 3.4 show the error at a fixed compression tolerance $\epsilon = 10^{-5}$ for different timesteps. For TEBD, one observes that it goes down at first, as expected, but then deteriorates again due to the many compression steps in the algorithm. A further reduction of the error at this point also requires a reduction of ϵ . On the other hand, the TDVP error again decreases monotonously and is actually not too sensitive to the size of the timestep.

Finally, we can also compare the calculated results with the exact ones for $U = 0$, where the solution follows from the diagonalization of the hopping matrix for open boundary conditions:

$$\begin{aligned} c_l(t) &= \sqrt{\frac{2}{L+1}} \sum_{k=1}^L \sin\left(\frac{\pi kl}{L+1}\right) c_k(t) \\ &= \sqrt{\frac{2}{L+1}} \sum_{k=1}^L \sin\left(\frac{\pi kl}{L+1}\right) e^{2i \cos\left(\frac{\pi k}{L+1}\right)t} c_k(0). \end{aligned} \quad (3.169)$$

This a non-trivial case for DMRG, as there is still entanglement and the wavefunction needs to be compressed. Apart from δE , the (absolute⁵) deviation from the exact result

$$\delta\Pi := \left| \Pi_{11,\text{ex.}}^{zz}(t) - \Pi_{11,\text{num.}}^{zz}(t) \right| \quad (3.170)$$

is plotted as a dashed line in the lower four panels of fig. 3.4. The maximal error during the whole propagation time are indicated by the horizontal lines.

One observes that the TEBD error is rather large even at short times and becomes even larger at long times. On the other hand, the TDVP error shows approximately the same rate of deterioration as δE , albeit now non-monotonically in time, and is also relatively insensitive to the magnitude of the timestep at fixed ϵ .

Summarizing, we can conclude that TDVP outperforms TEBD by being able to handle large timesteps and showing stricter, monotonic error scalings. As an optimal choice of parameters, compromising between small errors and efficiency, one can take $\delta t = 0.2$ and $\epsilon = 10^{-5}$.

⁵Since $\Pi_{11}^{zz}(t-t')$ can become small and go through zero, we take the absolute deviation rather than the relative one.

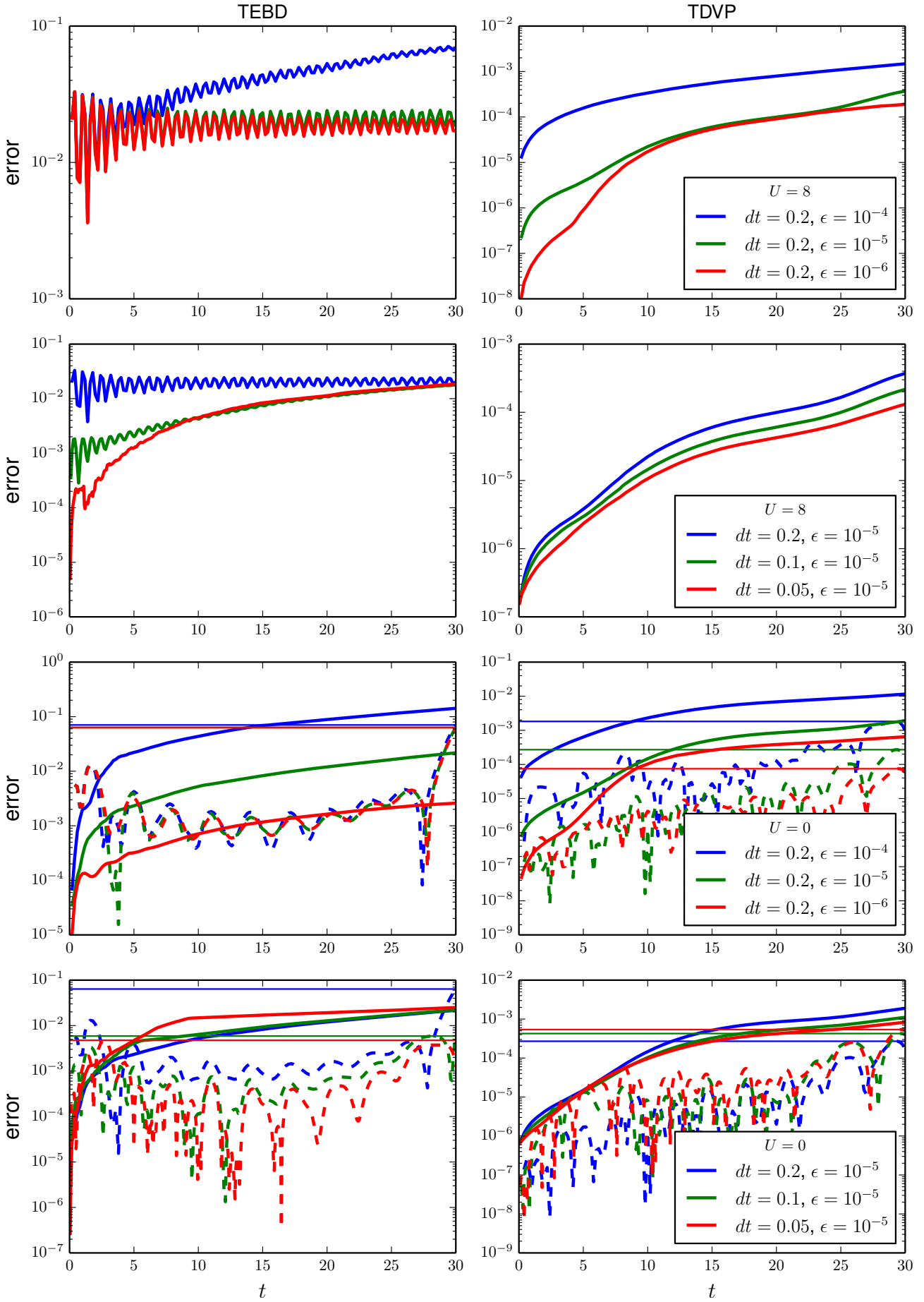


Figure 3.4.: Error of the dynamical spin-spin susceptibility $\Pi_{11}^{zz}(t)$ calculated by TEBD (left column) and TDVP (right column) for an $L = 30$ Hubbard chain at half filling, given by the relative change in energy (3.168) (solid line) for $U = 8$ and by the deviation from the exact value (3.170) (dashed line) for $U = 0$. Horizontal lines indicate the maximal error.

3.7. The Bethe Ansatz

The *Bethe ansatz* is a framework to analytically construct and interpret the eigenstates of interacting one-dimensional quantum systems [Essler et al. 2005; Sólyom 2010; Schulz 1993; Deguchi et al. 2000].

Commonly investigated models, such as the Heisenberg/XXZ or the Hubbard chain, are integrable in one dimension, i.e. they exhibit a macroscopic amount of conserved quantities. In these cases, the eigenstates can be constructed using the Bethe ansatz. However, handling the resulting wavefunctions is very costly in practice, the calculation of matrix elements scales like $N!$, thus much worse even than the e^N scaling when numerically working in the exact basis. Furthermore, the Bethe ansatz fails to produce a solution for nonintegrable systems such as the extended Hubbard model. Still, it has been used successfully to interpret features in the one-particle Green's function of the 1D Hubbard model (spinon and holon modes) and it stands to reason to attempt to do the same for the two-particle case.

The Bethe ansatz wavefunction is a plane-wave ansatz in first quantization:

$$\Psi_{\sigma_1 \dots \sigma_N}(x_1 \dots x_N) = \sum_P (-1)^P A_{\sigma_{Q(1)} \dots \sigma_{Q(N)}}(P, Q) e^{i \sum_j k_{P(j)} x_j}. \quad (3.171)$$

Here, the permutation Q has to be determined such that the coordinates of the N electrons are ordered from left to right in the chain $x_{Q(1)} < x_{Q(2)} < \dots < x_{Q(N)}$. The sum runs over all permutations of N elements. Plugging this into the Schrödinger equation and imposing periodic boundary conditions to determine the amplitudes A , one eventually arrives at the Lieb-Wu equations [Lieb and Wu 1968]:

$$e^{ik_j L} = \prod_{\alpha=1}^{N_\downarrow} \frac{\lambda_\alpha - \sin k_j - iU/4}{\lambda_\alpha - \sin k_j + iU/4}, \quad j = 1 \dots N \quad (3.172)$$

$$\prod_{\alpha=1}^{N_\downarrow} \frac{\lambda_\alpha - \sin k_j - iU/4}{\lambda_\alpha - \sin k_j + iU/4} = \prod_{\beta=1, \beta \neq \alpha}^{N_\downarrow} \frac{\lambda_\alpha - \lambda_\beta - iU/2}{\lambda_\alpha - \lambda_\beta + iU/2}, \quad \alpha, \beta = 1, \dots, N_\downarrow$$

These equations are valid at and below half filling, $n \leq 1$ and for $N_\downarrow \leq N/2$. No generality is lost due to the symmetries of the model. The presence of two equations already signals the separation of the spin and charge degrees of freedom. Hereby, k_j is wavenumber associated with the charge, while λ_α is called *spin rapidity*⁶ and is associated with the spin. In fact, neglecting the $\sin k_j$ term in the second equation and rescaling the rapidities by $U/2$ leads to the Bethe ansatz solution of the Heisenberg model.

The energy of the eigenstate is given by the wavenumbers only:

⁶Interestingly, there is an analogy with the more well-known rapidity for relativistic particles: The latter is given by $\Lambda = \operatorname{arctanh}(v/c)$, with which the momentum and energy can be parametrized via $p = m \sinh \Lambda$ and $E = m \cosh \Lambda$ (so that $E^2 - p^2 = m^2$ with $c = 1$). For the half-filled one-dimensional Hubbard model, the spinon momentum and energy are given by explicit integrals with $\sin x\Lambda$ and $\cos x\Lambda$ in the integrands, respectively.

Furthermore, it is possible to obtain a relativistic dispersion by taking the continuum limit $a \rightarrow 0$, $T \rightarrow \infty$, $aT = \text{const}$ and the scaling limit $U \rightarrow 0$, $\Delta(U) = \text{const}$, where a is the lattice constant, T is the hopping amplitude and $\Delta(U)$ is the energy gap. Then spinons behave like massless relativistic particles and holons like massive ones with the mass given by $\Delta(U)$. The model becomes a relativistic field theory, so that it is possible to calculate correlation functions as well [Essler et al. 2005; Melzer 1995; Woynarovich 1996].

$$E = -2t \sum_j \cos k_j. \quad (3.173)$$

Note that k_j and λ_α are in general complex, meaning that the imaginary parts of k_j have to cancel out in the above expression.

By taking the logarithm of the above equations, we can cast them into a different form:

$$\begin{aligned} Lk_j &= 2\pi I_j + \sum_\beta \theta(2 \sin k_j - 2\lambda_\beta), \\ \sum_j \theta(2 \sin k_j - 2\lambda_\alpha) &= 2\pi J_\alpha - \sum_\beta \theta(\lambda_\alpha - \lambda_\beta), \end{aligned} \quad (3.174)$$

with

$$\theta(x) = -2 \arctan\left(\frac{2x}{U}\right). \quad (3.175)$$

Here, I_j and J_α appear due to the multivaluedness of the complex logarithm. They can be interpreted as quantum numbers and are restricted to the following values:

$$-\frac{L}{2} < I_j \leq \frac{L}{2}, \quad |J_\alpha| \leq \frac{N - N_\downarrow + 1}{2}. \quad (3.176)$$

Furthermore:

$$I_j \text{ is } \begin{cases} \text{integer} & \text{if } N_\downarrow \text{ is even,} \\ \text{half-odd integer} & \text{if } N_\downarrow \text{ is odd,} \end{cases} \quad (3.177)$$

$$J_\alpha \text{ is } \begin{cases} \text{integer} & \text{if } N - N_\downarrow \text{ is odd,} \\ \text{half-odd integer} & \text{if } N - N_\downarrow \text{ is even.} \end{cases} \quad (3.178)$$

For each distinct set of the Bethe quantum numbers $\{I_j\}$, $\{J_\alpha\}$, the equations (3.174) need to be solved to obtain the corresponding k_j and λ_α . The ground state is given by the set with the lowest energy and the excited states can be constructed either by removing or changing a particular value from this distribution $|\{I_j\}, \{J_\alpha\}\rangle_{\text{gs}}$.

It should be noted that the procedure does not yield all the eigenstates of the Hubbard model yet, but just the highest-weight states with respect to the spin and charge SU(2) symmetries:

$$\begin{aligned} \eta |\{I_j\}, \{J_\alpha\}\rangle &= 0, \\ S^+ |\{I_j\}, \{J_\alpha\}\rangle &= 0. \end{aligned} \quad (3.179)$$

To obtain the complete set of eigenstates, one has to apply the lowering operators:

$$(S^-)^m (\eta^\dagger)^n |\{I_j\}, \{J_\alpha\}\rangle = 0. \quad (3.180)$$

The solution of (3.174) can be in principle obtained using Newton's method in the complex plane. It turns out, however, that the basin of attraction of many solutions is fairly small, while being large for unphysical solutions with coincident roots which would violate the Pauli exclusion principle [Avdeev and Dörfel 1987]. This means that a very good initial guess needs to be inserted. Luckily, the equations can be massaged even further to obtain something more stable.

3.7.1. The string hypothesis

In the so-called *string hypothesis* [Takahashi 1971] one surmises that bound state solutions of the Bethe ansatz equations in the thermodynamic limit form vertical "strings" in the complex plane, meaning that the corresponding roots share the same imaginary part.

An explicit calculation is quite instructive in the case of the doublon problem, i.e. $N = 2$, $N_{\downarrow} = 1$. There are two k 's and since their imaginary parts must cancel each other out, we can make the ansatz $k_{\pm} = k \pm i\xi$ with $\xi > 0$ and $k \in \mathbb{R}$. The Lieb-Wu equation (3.172) for k_- becomes:

$$e^{ik_-L} = \frac{\lambda - \sin k_- - iU/4}{\lambda - \sin k_- + iU/4}. \quad (3.181)$$

The left-hand side diverges for $L \rightarrow \infty$, meaning that in this limit, we need to have a matching divergence on the right-hand side:

$$\sin k_- = \lambda + \frac{iU}{4}. \quad (3.182)$$

The second equation can be written as

$$1 = \frac{\lambda - \sin k_+ - iU/4}{\lambda - \sin k_+ + iU/4} \cdot \frac{\lambda - \sin k_- - iU/4}{\lambda - \sin k_- + iU/4}. \quad (3.183)$$

One notices that the denominator in the second factor diverges in face of (3.182), so that it has to be compensated by the numerator:

$$\sin k_+ = \lambda - \frac{iU}{4}. \quad (3.184)$$

Adding (3.182) and (3.184), one recognizes that λ must be real, so that $\sin k_+$, $\sin k_-$ and λ all lie on a vertical string. The (unnormalized) wavefunction becomes:

$$\Psi(x_1, x_2) = e^{ik(x_1+x_2)} e^{-\xi|x_1-x_2|}. \quad (3.185)$$

Due to the exponential drop with increasing separation of the electrons, this is now recognized as a bound-state solution, which we had already obtained in chapter 1.1 with more conventional means. In the Bethe ansatz jargon, the bound state is called a " k - Λ string".

The string hypothesis generalizes this type of solutions, so that the BA equations can then be recast into a form which only involves the real parts and barycentres of the strings, leading to purely real equations.

3.7.2. The thermodynamic Bethe ansatz

Since the string hypothesis is valid for $L \rightarrow \infty$, this limit needs to be carried out for the Bethe ansatz equations, so that one obtains the *thermodynamic Bethe ansatz* (TBA). It was first applied by Yang and Yang to the Bose gas with a δ -interaction [Yang and Yang 1969]. By recognizing that the spacing between the BA roots scales like $k_{j+1} - k_j \sim 1/L$, one can introduce a “root density” $\rho(k)$ by way of

$$n = \frac{1}{L} \sum_{j=1}^N 1 = \sum_{j=1}^N \rho(k_j) \Delta k_j \rightarrow \int_{-Q}^Q dk \rho(k). \quad (3.186)$$

It satisfies the following integral equation:

$$\rho(k) = \frac{1}{2\pi} + \int_{-Q}^Q dk' \cos k R(\sin k' - \sin k) \rho(k'). \quad (3.187)$$

Another quantity that needs to be introduced is the “dressed energy” which satisfies another integral equation:

$$\kappa(k) = -2 \cos k - \mu - \frac{U}{2} + \int_{-Q}^Q dk' \cos k' R(\sin k' - \sin k) \kappa(k') \quad (3.188)$$

with the boundary condition

$$\kappa(\pm Q) = 0, \quad (3.189)$$

which just sets the Fermi energy to zero.

The integral kernel in the above expressions contains

$$\begin{aligned} R(x) &= \int_{-\infty}^{\infty} \frac{d\omega}{2\pi} \frac{e^{i\omega x}}{1 + \exp\left(\frac{U|\omega|}{2}\right)} \\ &= \frac{1}{\pi U} \operatorname{Re} \left[\psi \left(1 - \frac{ix}{U} \right) - \psi \left(\frac{1}{2} - \frac{ix}{U} \right) \right]. \end{aligned} \quad (3.190)$$

where ψ is the digamma function $\psi(x) = \frac{d}{dx} \ln \Gamma(x)$, which is tabulated⁷. Note that the above equations are valid for zero temperature, $B = 0$, and make use of the string hypothesis.

The kernel is well-behaved and the equations can be easily solved in the following fashion:

At first, the root of the function $f(Q) := \int_{-Q}^Q dk \rho(k) - n$ must be found, which determines the pseudo-Fermi momentum Q . This can be done by the bisection method, as Q is known to lie in the interval $Q \in [0, \pi]$ with $Q = 0$ for $n = 0$ and $Q = \pi$ for $n = 1$, due to Luttinger’s theorem. Each function evaluation involves solving the Fredholm integral equation (3.187), for which Gauss-Legendre integration with $30 \sim 100$ points is more than sufficient. With the given Q , one proceeds to find the root of eq. (3.189) which fixes μ .

From these formulas we can construct so-called *elementary excitations* via integrals over ρ and κ . Each of these has a dressed momentum and a dressed energy:

⁷“Tabulated” means here that it can be numerically evaluated to arbitrary precision in negligible time.

- holon: $-p^h(k), -\kappa(k)$
- antiholon: $p^h(k), \kappa(k)$
- spinon: $-p^s(\Lambda), -\epsilon^s(\Lambda)$
- k - Λ string of length m ⁸: $p_m^{\text{string}}(\Lambda), \epsilon_m^{\text{string}}(\Lambda)$

The spin rapidity is now a continuous variable and ranges for an unmagnetized band as $\Lambda \in [-\infty, \infty]$. In the case of finite magnetization, a cutoff A has to be determined from $\epsilon^s(\pm A) = 0$ and plays an analogous role to the Fermi vector for spinons⁹. Numerically, one can just choose a value large enough, so that $\epsilon^s(\pm \Lambda_{\text{cutoff}}) < \epsilon_{\text{cutoff}}$ is fulfilled to machine accuracy.

The dressed momentum for both the holon and antiholon is given by

$$p^h(k) = 2\pi \int_0^k dk' \rho(k'). \quad (3.191)$$

However, the holon dwells below the pseudo-Fermi momentum Q , with the restriction $|k| \leq Q$; while the antiholon dwells above it with $|k| > Q$.

The dressed momentum of the spinon is obtained via

$$p^s(\Lambda) = \frac{n\pi}{2} - 2 \int_{-Q}^Q dk \arctan \left[\exp \left(-\frac{2\pi}{U} (\Lambda - \sin k) \right) \right] \rho(k) \quad (3.192)$$

and its dressed energy via

$$\epsilon^s(\Lambda) = \int_{-Q}^Q dk \frac{\cos k}{U} \frac{1}{\cosh \left(\frac{2\pi}{U} (\Lambda - \sin k) \right)} \kappa(k). \quad (3.193)$$

The dressed momentum of the k - Λ string reads:

$$p_m^{\text{string}}(\Lambda) = -2\text{Re} \arcsin \left(\Lambda - \frac{imU}{4} \right) + 2 \int_{-Q}^Q dk \arctan \left(\frac{4(\Lambda - \sin k)}{mU} \right) \rho(k) + \pi(m+1) \quad (3.194)$$

and its dressed energy:

$$\epsilon_m^{\text{string}}(\Lambda) = 4\text{Re} \sqrt{1 - \left(\Lambda - \frac{imU}{4} \right)^2} - 2m\mu - mU + \int_{-Q}^Q dk \frac{mU/4}{(mU/4)^2 + (\sin k - \Lambda)^2} \kappa(k). \quad (3.195)$$

The dispersions of selected excitations are shown in fig. (3.5). Note that because of Luttinger's theorem, the Fermi wave vector is $k_F = n\pi/2$ independent of U . The corresponding Fermi wave vector of the holon (where $\epsilon^h(k_F^h) = 0$) is $k_F^h = \pm n\pi = 2k_F$, also independent of U . The same holds for the antiholon, since the dispersion crosses the Fermi energy continuously. For the spinon we always have $k_F^s = n\pi/2 = k_F$.

⁸By convention, the value m is taken here as the string length, starting with $m = 1$. Another convention is to start counting at 2.

⁹The magnetization is then fixed with the help of a spin root density $\sigma(\Lambda)$ with $\int_{-A}^A d\Lambda \sigma(\Lambda) = n_\downarrow$ analogously to the charge root density $\rho(k)$ in (3.186).

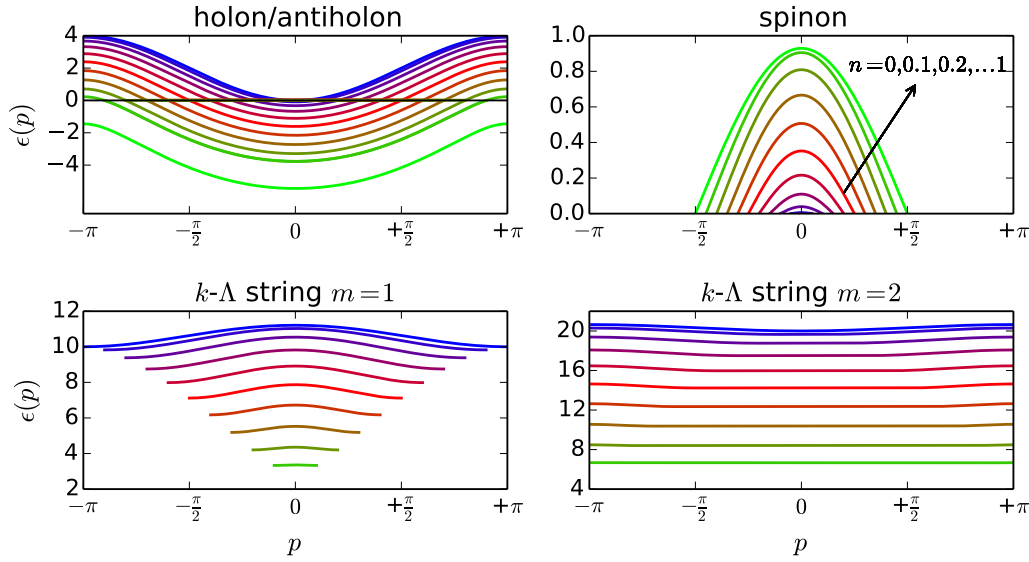


Figure 3.5.: Some of the elementary excitation dispersions of the Bethe ansatz for $U = 6$. The filling increases from $n = 0$ (blue) to $n = 1$ (green) in steps of 0.1. The sign of the holon energies is chosen such that they fall below the Fermi energy $E_F = 0$. Note that there are no string solutions at $n = 1$.

Note that these excitations are qualitatively different from the case $U = 0$ with $\epsilon(k) = -2 \cos(k)$ and $\mu = \epsilon(k_F) = -2 \cos(\pi \frac{n}{2})$. For example, at $n = 1$ the filled band occupies a width of $\Delta E = 2$ in the latter case, but the holon bandwidth is $W_h = 4$ for any value of U and is moreover gapped by

$$\Delta = -2 - \frac{U}{2} + 2 \int_0^\infty dx \frac{\mathcal{J}_1(x)}{x} \frac{e^{-xU/4}}{\cosh(xU/4)}, \quad (3.196)$$

where $\mathcal{J}_1(x)$ is the first Bessel function. This can be qualitatively understood due to the Mott transition at half filling, where the system becomes an antiferromagnet with one electron per site, so that a hole can propagate in this background as a free particle. In $d = 1$, the Mott transition occurs at any finite value of U , although the charge gap is exponentially small for small U , namely $\Delta \propto \sqrt{U} e^{-1/U}$, and becomes $\Delta \propto U$ for large U [Essler et al. 2005; Sólyom 2010]¹⁰.

Each elementary excitation defines an excited state: Holons can be thought of as removing charge, antiholons as adding charge, spinons as adding or removing spin, and k - Λ strings as creating multipionic bound states (which will be discussed in great detail in chapter 4.1). Furthermore, the elementary excitations can be freely combined by adding all possible momenta $p_{\text{tot}} = \sum_\alpha p^\alpha$ (and either reflecting at the Brillouin zone edges whenever the modulus of the result exceeds π , or working in an extended zone) and energies $E_{\text{tot}} = \sum_\alpha \epsilon^\alpha$, thus forming continua.

A caveat should be mentioned: There can be a shift of the momentum by $\pm\pi n$ due to the fact that the corresponding distribution $\{I_j\}$ switches from half-odd integer to integer and consequently a new distribution of the roots, asymmetric around zero. The presence of such a shift has to be considered for each physical excitation. See Essler et al. (2005) for more details.

Some of the excitation continua relevant for this work are shown in fig. 3.6.

Finally, we can also form the derivatives of the dressed excitation energies with respect to the dressed momenta:

¹⁰In the Mott phase, the chemical potential is not well-defined. Eq. (3.196) and fig. 3.5 use the symmetric convention $\mu = E_F = 0$. One can also choose an asymmetric convention $\mu = \mu_- < 0$, where the precise value has to be determined from the Bethe ansatz equations in the usual way.

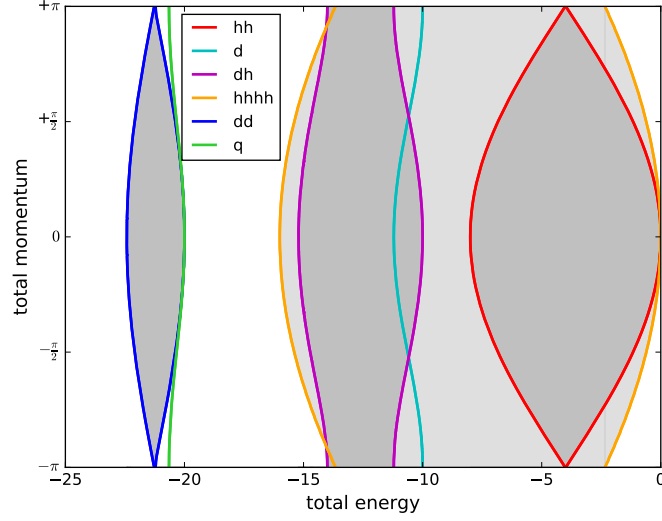


Figure 3.6.: Several excitations of the Hubbard model with $U = 6$ and $n = 2$ in the two-, three- and four-particle subspace obtained from the Bethe ansatz; hh : 2-holon continuum, d : k - Λ string of length 1, dh : string-holon continuum, $hhhh$: 4-holon continuum, dd : 2-string continuum, q : k - Λ string of length 2

$$\begin{aligned}
 v^h(k) &= \frac{\partial \kappa(p^h)}{\partial p^h} = \frac{\kappa'(k)}{p^{h'}(k)}, \\
 v^s(\Lambda) &= \frac{\partial \epsilon^s(p^s)}{\partial p^s} = \frac{\epsilon^{s'}(\Lambda)}{p^{s'}(\Lambda)}.
 \end{aligned}
 \tag{3.197}$$

Close to the Fermi energy, a linearization of the dispersion is possible and one can interpret $v^h(k = Q)$ and $v^s(\Lambda = \infty)$ (for an unmagnetized band) as the charge and spin velocities, respectively.

3.7.3. Interpreting spectra

The Bethe ansatz has been previously applied to interpret the photoemission spectrum of a one-dimensional Hubbard system and evidence for holon and spinon branches has been found experimentally in the one-dimensional compound tetrathiafulvalene tetracyanoquinodimethane (TTF-TCNQ) [Claessen et al. 2002; Claessen, Schäfer, and Sing 2007].

Since an electron consists out of charge and spin, removing it in photoemission equals the excitation of a spinon and holon, so that one expects the support of the one-hole spectral function (see also chapter 4.1.4 below), given by

$$A_{1\text{-hole},\sigma}(\omega) = \sum_n |\langle n, N-1 | c_{i\sigma} | 0, N \rangle|^2 \delta(\omega + \mu - (E_0^{(N)} - E_n^{(N-1)})),
 \tag{3.198}$$

in the (k, ω) -plane to coincide with the spinon-holon continuum with

$$\begin{aligned}
 p^{hs} &= -p^h(k) - p^s(\Lambda) \pm \pi n, \\
 E^{hs} &= -\kappa(k) - \epsilon^s(\Lambda),
 \end{aligned}
 \tag{3.199}$$

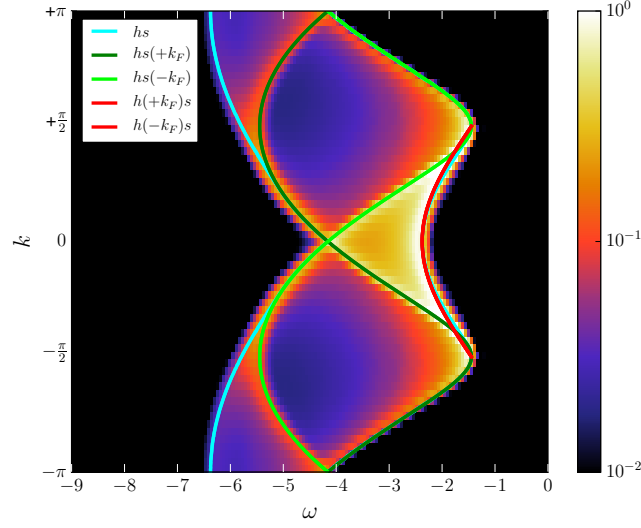


Figure 3.7.: One-hole spectral function of the one-dimensional Hubbard model for $L = 60$, $n = 1$ and $U = 6$, calculated with DMRG. The labels indicate: hs : holon-spinon continuum, $hs(\pm k_F)$: holon dispersion with the spinon pinned to its Fermi momentum, $h(\pm k_F)s$: spinon dispersion with the holon pinned to its Fermi momentum

where $k = p^{hs}$ and $\omega = E^{hs}$.

In a similar fashion, the support of the dynamic spin structure factor (or dynamic susceptibility) $\langle\langle \mathbf{S}_k; \mathbf{S}_k \rangle\rangle(\omega, k)$ should coincide with the spinon-spinon continuum; and the support of the dynamic charge structure factor $\langle\langle n_k; n_k \rangle\rangle(\omega, k)$ with the holon-antiholon continuum. However, in all the cases, spectral weight associated with bound states (identical to string solutions) can appear outside of the continua.

Fig. 3.7 shows the one-hole spectral function at half filling (where no string solutions appear) with overlaid lines highlighting the Bethe ansatz excitations. The boundary of the hs -continuum is drawn as a cyan line. Within this continuum, additional structures can be identified, namely dispersive lines corresponding to either the spinon or the holon pinned to their respective Fermi momenta $\pm k_F^s = \pm\pi/2$ and $\pm k_F^h = \pm\pi$ [Claessen et al. 2002]. The pinned particles have maximal momentum, but zero energy. In the former case this leads to a doubling of the lines due to the shift by $\pi/2$, with the branch at high binding energy being often called “shadow band”. In the latter case there is no doubling because the shift by $\pm\pi$ is exactly compensated by the $\pm\pi n$ term in the sum of momenta (modulo 2π), so that on balance, one obtains the simple spinon dispersion. Note that off half filling the bound doublon appears in the spectrum with a gap given approximately by U , which corresponds to a k - Λ string with $m = 1$ [Benthien 2005].

4. Spectra

4.1. The two-hole spectral function

4.1.1. Preliminaries

Our goal is to compute the local two-particle spectral function, defined as

$$A_2(\omega) = A_{2\text{-hole}}(\omega) + A_{2\text{-particle}}(\omega), \quad (4.1)$$

which consists of the *two-hole* excitation spectrum

$$A_{2\text{-hole}}(\omega) = \sum_n \left| \langle n, N-2 | c_{i\uparrow} c_{i\downarrow} | 0, N \rangle \right|^2 \delta \left(\omega + 2\mu^{(N-1)} - \left(E_0^{(N)} - E_n^{(N-2)} \right) \right), \quad (4.2)$$

with excitation energies $\omega \leq 0$, related to Auger electron spectroscopy; and of the *two-particle* excitation spectrum

$$A_{2\text{-particle}}(\omega) = \sum_n \left| \langle n, N+2 | c_{i\downarrow}^\dagger c_{i\uparrow}^\dagger | 0, N \rangle \right|^2 \delta \left(\omega + 2\mu^{(N+1)} - \left(E_n^{(N+2)} - E_0^{(N)} \right) \right), \quad (4.3)$$

with excitation energies $\omega \geq 0$. While the former is related to Auger electron spectroscopy, the latter is related to the so-called *appearance potential spectroscopy* [Potthoff et al. 2001].

Note that the definition (4.2) slightly differs from the eq. (2.87): In the experimental setup, the kinetic energy ϵ_A of the Auger electron is measured, but in (4.2) one rather measures binding energies (though speaking of the “frequency” ω by convention). The Hamiltonian used is $\mathcal{H} = H - \mu\hat{N}$, where the chemical potential ensures the negativity of ω for $A_{2\text{-hole}}$, corresponding to states below the Fermi level; and the positivity of ω for $A_{2\text{-particle}}$, corresponding to states above the Fermi level.

Since we are working with a finite system, a finite-size variant of μ is needed, which depends on the particle number. It is defined as:

$$\begin{aligned} \mu^{(N-1)} &= (E_0^{(N)} - E_0^{(N-2)})/2, \\ \mu^{(N+1)} &= (E_0^{(N+2)} - E_0^{(N)})/2. \end{aligned} \quad (4.4)$$

Particle-hole symmetry implies that the two-hole spectrum at filling n is related to the two-particle spectrum at filling $2-n$ via

$$A_{2\text{-hole}}(\omega, n) = A_{2\text{-particle}}(-\omega, 2-n). \quad (4.5)$$

It is therefore sufficient to study the two-hole and the two-particle spectrum for fillings at and above half filling: $1 \leq n \leq 2$.

We are also interested in the k -resolved two-hole spectral function, which for periodic boundary conditions is given by:

$$A_{2\text{-hole}}(\omega, k) = \frac{1}{L} \sum_n \left| \langle n, N-2 | \sum_i e^{-ikR_i} c_{i\uparrow} c_{i\downarrow} | 0, N \rangle \right|^2 \delta \left(\omega + 2\mu - \left(E_0^{(N)} - E_n^{(N-2)} \right) \right). \quad (4.6)$$

Exploiting translational symmetry, it is straightforward to show that k -summation yields

$$A_{2\text{-hole}}(\omega) = \frac{1}{L} \sum_k A_{2\text{-hole}}(\omega, k). \quad (4.7)$$

To calculate $A_{2\text{-hole}}(\omega)$, DMRG in combination with the Chebyshev expansion technique is employed (see chapters 3.3.1 and 3.6). The Chebyshev method has an approximately uniform energy resolution δE given by $\delta E \sim \Delta E/M$ where $\Delta E = E_{\max} - E_{\min}$ is the total bandwidth and M is the amount of moments [Weiß et al. 2006; Weiß and Fehske 2008]. In order to be able to compare the spectra for various fillings and parameters, it is therefore sensible to fix δE as a measure of resolution rather than M in all calculations.

4.1.2. Completely filled band

Let us start the discussion of the results by re-establishing the simple case of the completely filled band ($n = 2$) described in the introduction. Some numerical results for $L = 1000$ and periodic boundary conditions are shown in fig. 4.1(a) (k -resolved) and 4.1(b) (k -summed).

The two-hole spectra for different U can be understood as follows: If $U = 0$, one can straightforwardly evaluate eq. (4.2) by Fourier transformation to reciprocal space (see appendix A). This yields

$$A_{2\text{-hole}}^{(0)}(\omega) = \int dx \rho_0(x) \rho_0(\omega + E_0^{(N)} - E_0^{(N-2)} - x), \quad (4.8)$$

where $\rho_0(x) = 1/L \sum_k \delta(x - \varepsilon(k))$ and $\varepsilon(k) = -2 \cos(k)$ (the hopping T is set to 1), i.e., the two-hole spectrum is given by the self-convolution of the non-interacting density of states [Lander 1953]. For $n < 2$ and $U = 0$, one has to take the only the occupied part. The self-convolution of the one-dimensional density of states $\rho_0(x)$ happens to be given by the two-dimensional density of states with bandwidth $2W = 8$ (see black line). The associated picture is that the two conduction band holes move independently of each other through the lattice.

Upon increasing U , a sharp satellite emerges at the lower edge of this “band-like part” of width $2W$ and moves to higher binding energies [Cini 1977; Sawatzky 1977]. For $U \gg T$, this satellite is approximately separated by U from the barycentre of the band-like part located at $\omega = -4$. This corresponds to the formation of a stable bound doublon state. Since both the energy and momentum of an electron on a lattice are bounded from above, a decay of the bound doublon into independent holes is prohibited by energy conservation for any $U > 0$ in one spatial dimension, and for a U exceeding a critical value U_c in higher dimensions. Indeed, looking at fig. 4.1(a) one observes that the satellite consists of a δ -peak for each value of k .

The finite width of the satellite reflects the fact that the doublon is itinerant. For strong U , the propagation of a single doublon is perturbatively described by a second-order hopping process and is captured by the effective Hamiltonian (a special case of eq. (1.9))

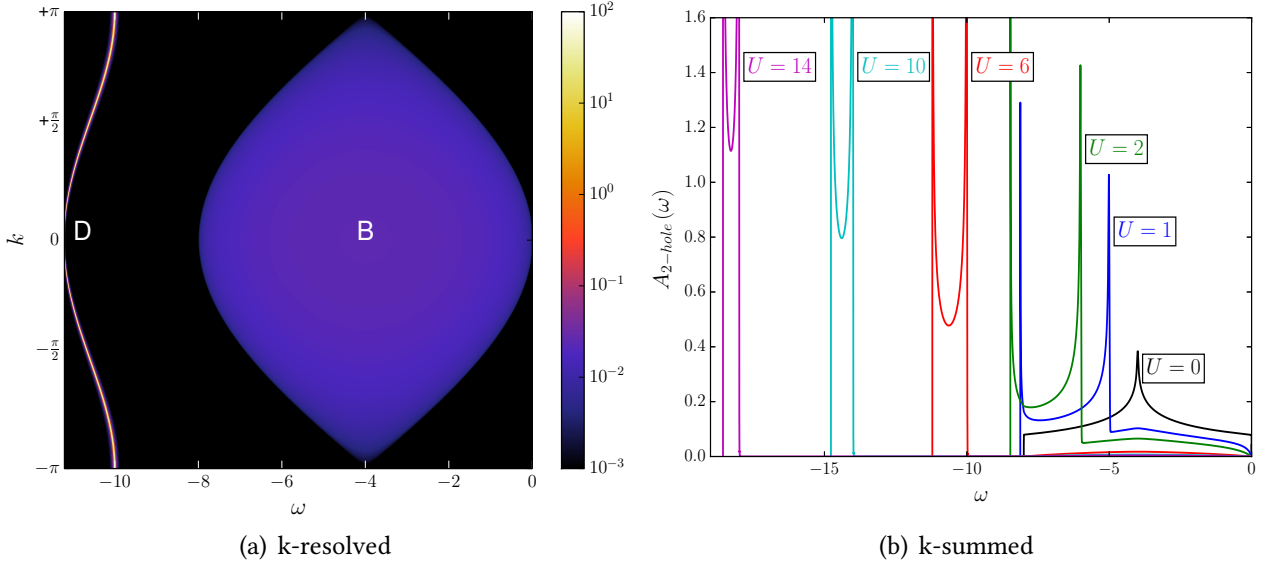


Figure 4.1.: (a) Momentum-resolved two-hole excitation spectrum of a completely filled Hubbard band ($n = 2$) for $U = 6$. Results are obtained by the Chebyshev expansion method using exact states with $L = 1000$ lattice sites and periodic boundary conditions. Energy resolution: $\delta E = 0.01$, corresponding to $M = 1134$ Chebyshev moments. Labels indicate: “D”: doublon, “B”: band-like part (cf. fig. 4.2(I)). (b) The k -summed spectrum for several values of U as indicated (same resolution, $M = 799$ to $M = 1856$).

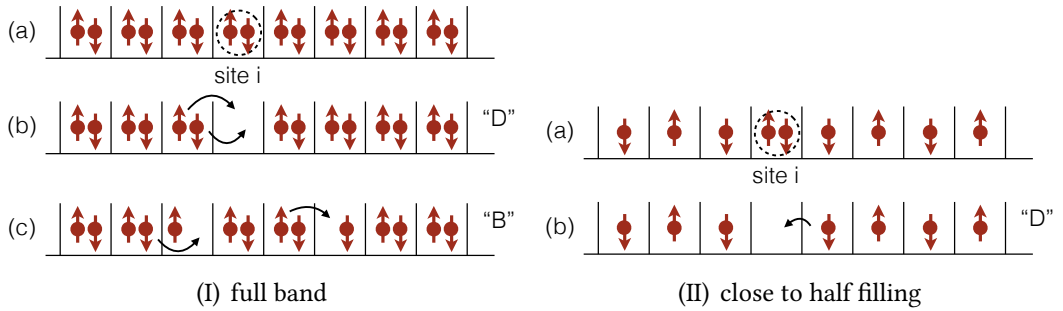


Figure 4.2.: (Ia) Ground state $|0, N\rangle$ for $N = 2L$ electrons (filling $n = 2$). The two-hole spectroscopy removes two electrons at site i (dashed line). (Ib) Configuration of an excited state $|n, N - 2\rangle$ contributing to the doublon satellite (“D”). Arrows indicate doublon propagation. (Ic) Configuration contributing to the band-like part (“B”). Arrows indicate independent motion of the two final-state holes. (IIa) Configuration with $N = L + 1$ electrons contributing to the ground state $|0, N\rangle$ close to half filling. Two electrons at site i are removed (dashed line). (IIb) Configuration contributing to an excited state $|n, N - 2\rangle$ related to the doublon satellite (“D”). The arrow indicates doublon propagation.

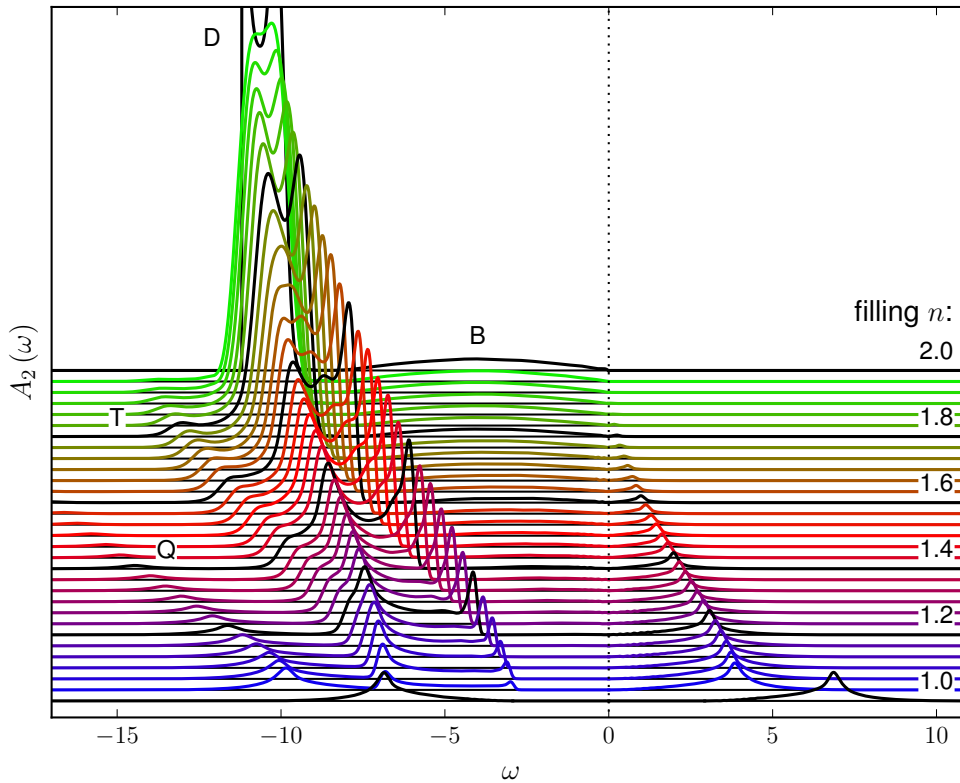


Figure 4.3.: Two-hole excitation spectrum ($\omega < 0$) and two-particle excitation spectrum ($\omega > 0$) of the one-dimensional Hubbard model at $U = 6$ for fillings n between half filling ($n = 1$) and the limit of the completely filled band ($n = 2$). The filling values indicated on the right are drawn in black. Results as obtained by DMRG for a system with $L = 60$ lattice sites and open boundary conditions at an energy resolution of $\delta E = 0.2$, corresponding to up to $M = 1149$ Chebyshev moments. The main spectral structures are labeled by “D” (doublon), “B” (band-like part), “T” (triplon) and “Q” (quadruplon) (see text).

$$H_{\text{eff}} = \frac{J}{2} \sum_{\langle ij \rangle} \left(d_i^\dagger d_j + \text{h.c.} \right) + (J + U) \sum_i n_i^d, \quad (4.9)$$

where $d_i^\dagger = c_{i\uparrow}^\dagger c_{i\downarrow}^\dagger$ is a bosonic doublon creator, $n_i^d = d_i^\dagger d_i$, and with $J = 4T^2/U$. Hence, in the strong-coupling limit the satellite has the shape of the non-interacting density of states with a rescaled bandwidth of $2J$. With increasing U , it gains more and more spectral weight at the expense of the band-like part and eventually results in a δ -peak for $U = \infty$, corresponding to a completely immobile doublon.

In the strong- U limit, the physics can be visualized to some extent by typical electronic configurations contributing to the different spectral features. Fig. 4.2(I) gives a sketch of the different configurations contributing to the doublon satellite “D” and to the band-like part “B”.

4.1.3. Partially filled band

Overview

We now turn to the case of a conduction band with a finite hole density $n < 2$. This changes the situation completely as the two additional holes placed at site i interact with a large (in principle macroscopic) amount of holes in the incompletely filled band. From the technical point of view,

the computation of the spectrum evolves into a severe many-body problem: A comprehensive and reliable study, however, is possible when tolerating a non-zero low-energy cutoff in the form of a finite spectral resolution δE . Using the Chebyshev technique combined with matrix-product states, the excitation spectra can be studied in the entire filling range $1 \leq n \leq 2$ for the Hubbard model on lattices as large as $L = 60$ at a constant energy resolution $\delta E \approx 0.2$. With $\delta E \lesssim 0.2$ one would start to resolve finite-size artifacts. Calculations have been performed for systems with open boundary conditions and choosing i as a central site in the chain (see eqs. (4.2) and (4.3)).

Fig. 4.3 provides an overview and shows the filling-dependence of the spectrum at $U = 6$, a value chosen to be larger than the bandwidth ($U = 3/2W$), so that for $n = 2$, the doublon satellite is clearly separated from the band-like part. The following observations can be made:

- The overall intensity of the two-hole spectrum in the range $\omega < 0$ is seen to decrease with decreasing filling. This is a consequence of the sum rule for the double occupancy (which is straightforwardly derived from eq. (4.2)):

$$\langle n_{i\uparrow}n_{i\downarrow} \rangle = \int d\omega A_{2\text{-hole}}(\omega), \quad (4.10)$$

and the fact that $\langle n_{i\uparrow}n_{i\downarrow} \rangle$ is decreasing with n .

- The doublon satellite (“D”) is still present with strong weight at $U = 6$, but its support broadens significantly with decreasing n . The satellite can be traced down to fillings close to half filling. Right at $n = 1$ it vanishes completely. An extended discussion is given in chapter 4.1.3.
- A continuation of the “band-like part” (“B”) of the two-hole spectrum is also clearly visible, at least down to $n \approx 1.5$. When the filling approaches half filling, however, the weight of the band-like part becomes very small, and the structure is hardly visible at low energies, say $-2 \lesssim \omega < 0$, for fillings $1 < n < 1.2$. Note, however, that there is finite spectral weight for $\omega \rightarrow 0$ at any filling $n > 1$; only at half filling, $n = 1$, is the spectrum gapped.
- As soon as $n < 2$, the spectrum exhibits an additional structure, marked as “T” in fig. 4.3. For fillings $n \rightarrow 2$ it shows up as a tiny peak at high binding energies. It gains some spectral weight upon decreasing n and moves towards $\omega = 0$, until it completely merges with the doublon satellite. At the same time, another peak can be seen emerging in the very spectral range of satellite (seen best for $n = 1.6$ at $\omega \approx -8.7$). It also moves towards $\omega = 0$ at the same rate. It turns out that both peaks are a consequence of the same effect, hence they are both labelled “T” for “triplon” an analysis will be performed in chapter 4.1.3.
- The physics close to and at half filling is complicated by the appearance of yet another structure “Q” which emerges for $n \lesssim 1.5$ at the highest binding energies and gains more and more weight as n approaches half filling. This feature will be addressed in chapter 4.1.3 and interpreted as a “quadruplon”.
- At half filling the system is a Mott insulator. The gap in the one-particle spectral function is accessible to the Bethe ansatz method [Lieb and Wu 1968] and can be computed from the exact expression [Ovchinnikov 1992]

$$\Delta = \frac{16T^2}{U} \int_1^\infty dx \frac{\sqrt{x^2 - 1}}{\sinh(2\pi x T/U)}. \quad (4.11)$$

At $U = 6$ it amounts to $\Delta = \mu_+ - \mu_- \approx 2.89$. As fig. 4.3 demonstrates, the two-particle spectral function is gapped as well, but by twice the one-particle gap $2\Delta \approx 5.86$ (the numerical value is obtained from the ground-state energies, and the slight discrepancy compared to twice of the Bethe ansatz value is due to the finite system size).

- The chemical potential jumps from $\mu = \mu_-$ for $n \nearrow 1$ to $\mu = \mu_+$ for $n \searrow 1$ and is not uniquely defined at half filling¹. The two-hole and the two-particle spectrum for $n = 1$ in fig. 4.3 have been calculated for the choice $\mu = (\mu_+ + \mu_-)/2 = U/2 = 3$, which implies a symmetric spectrum $A_2(-\omega) = A_2(\omega)$. If $\mu = \mu_+$ had been chosen, the $n = 1$ spectrum would have evolved continuously from the spectrum for $n > 1$. Hence, the single broad peak in the two-hole spectrum at $n = 1$, which takes the whole spectral weight, smoothly connects to the quadruplon peak “Q” at higher fillings.
- For fillings below half filling, $n < 1$, the two-hole spectrum is related to the two-particle spectrum for $n > 1$ via the relation eq. (4.5). As is seen for $\omega > 0$ in fig. 4.3, it consists of a single peak, smoothly connected to “Q” which just continues to lose spectral weight until it vanishes for $n \rightarrow 0$. The vanishing of the weight is related to sum rule for the two-particle spectrum (which is straightforwardly derived from eq. (4.3))

$$\langle (1 - n_{i\uparrow})(1 - n_{i\downarrow}) \rangle = \int_0^\infty d\omega A_{2\text{-particle}}(\omega), \quad (4.12)$$

and to the fact that the average number of empty sites goes to zero for $n \rightarrow 2$, i.e., the phase space for creating two additional *particles* at a site i vanishes.

- The *difference* between the total weights of the two-hole and the two-particle spectrum is given by the filling:

$$\int_{-\infty}^0 d\omega A_{2\text{-hole}}(\omega) - \int_0^\infty d\omega A_{2\text{-particle}}(\omega) = n - 1. \quad (4.13)$$

This is a direct consequence of eqs. (4.10) and (4.12).

The doublon

As soon as the filling falls below $n = 2$, the doublon starts to interact with a continuum of electron-hole excitations, such that the corresponding peak should actually be seen as a resonance with a finite lifetime rather than an exact eigenstate of the Hamiltonian (for a given wave vector). This will be discussed in detail in chapter 4.1.3.

As a consequence, the doublon peak broadens with decreasing n . Its support widens from a value slightly larger than $\Delta\omega = 2J = 4/3$, which is the perturbative result for $U \rightarrow \infty$ at $n = 2$, to $\Delta\omega \gtrsim 4$ for fillings close to, but above half filling.

To understand the main reason for this broadening, consider the spectrum for a system with $N = L + 1$ particles, i.e., for a filling slightly above $n = 1$. Fig. 4.2(II) provides a sketch.

The support of the doublon peak is given by the spectral range of the final states. As indicated in the sketch, the dominating final-state configurations are characterized by a hole moving through a lattice of half-filled sites. This is a standard many-body problem, intensively discussed, e.g., in the context of the Mott-Hubbard metal-insulator transition [Gebhard 2003]. Double occupancies are effectively suppressed at strong U , well-formed local magnetic moments emerge and develop strong antiferromagnetic correlations due to the Anderson super-exchange mechanism. While the

¹For a finite system, μ not unambiguously defined. With eq. (4.4) we use a symmetric definition, where the chemical potential for N particles is given as a difference of the total energies for $N \pm 1$ particles. This ensures that the excitation energies in the two-hole (two-particle) spectrum are strictly non-positive (non-negative). The choice implies that the two branches of the spectrum are computed with (slightly) different chemical potentials. Hence, it cannot be used for $n = 1$ where the function $\mu = \mu(n)$ is discontinuous.

effective coupling constant $J = 4T^2/U$ of the latter is derived in second-order-in- T perturbation theory and is small, the motion of the hole takes place on the large energy scale T . Neglecting J altogether, already provides the right width of about $4T$ for the doublon peak, consistent with the corresponding spectrum displayed in fig. 4.3.

Let us mention that the arguments can be formalized by considering the standard mapping of the low-energy sector of the Hubbard model for strong U onto the t - J model [Chao, Spalek, and Oleś 1978]. Close to half filling it reads ²:

$$H_{t-J} = -T \sum_{\langle ij \rangle, \sigma} \left(\tilde{c}_{i\sigma}^\dagger \tilde{c}_{j\sigma} + \text{h.c.} \right) + J \sum_{\langle ij \rangle} \mathbf{S}_i \mathbf{S}_j, \quad (4.14)$$

where $\mathbf{S}_i = \frac{1}{2} \sum_{\sigma\sigma'} c_{i\sigma}^\dagger \boldsymbol{\sigma}_{\sigma\sigma'} c_{i\sigma'}$ is the spin at site i , $\boldsymbol{\sigma}$ the vector of Pauli matrices, and where $\tilde{c}_{i\sigma}$ is the annihilator in the subspace with no double occupancies.

Neglecting J altogether yields the t -model, which has simple tight-binding character, so that the bandwidth of $4T$ becomes obvious. We thus expect a crossover from $n = 2$ where the doublon is a repulsively bound state and the satellite has a width of $2J$, to $n = 1$ where the doublon is a free particle with a width of $4T$.

The band-like part

The band-like part “B” of the two-hole spectrum results from the continuum of unbound two-hole final states. For $n = 2$ and $U = 0$, this is given by the self-convolution of the density of states $\rho_0(x)$ (see appendix A). With increasing U , it quickly loses weight in favour of the doublon satellite (see fig. 4.2(I)) and ultimately becomes an almost featureless structure whose shape still loosely resembles the self-convolution of the density of states, but without the strong van Hove singularities. Its weight is already low for $U = 6T > W$, see fig. 4.1(b).

For fillings close to half filling, this scenario still holds to a good approximation, but with the density of states replaced by its occupied part only (for a given filling). Since the occupied fraction shrinks with decreasing n , the weight of the band-like part must diminish and its spectral support narrow down, with the barycentre shifting upwards. This effect is clearly visible in fig. 4.3 for high fillings.

The barycentre of the band-like part also fixes the position of the doublon satellite, which is found at an energy of about U below. Assuming a rectangular density of states with bandwidth $W = 4$, we have $\omega_0 = -(n/2)W$ for the barycentre and $\Delta\omega = nW$ for the width of the band-like part. This simple model roughly explains the trend seen for fillings $n \gtrsim 1.6$. For example, the model predicts $\omega_0 = -3.2$ for $n = 1.6$ resulting in $\omega = -(n/2)W - U = -9.2$ for the satellite position. This should be compared with the barycentre of the satellite at $\omega \approx -8.75$ in fig. 4.3 (obtained by integrating the data).

For fillings $n \lesssim 1.5$, however, ω_0 shifts much faster with decreasing n and the model breaks down (note that there is a finite band-like part for any $n > 1$). In this filling range, one may consider the two additional holes in the final state as moving independently of each other, but strongly interacting with the high hole density in the ground state.

See also chapter 4.2 for an interpretation of the substructures within the band-like part in terms of the Bethe ansatz excitations.

²Off half filling, one has also to take three-site terms into account which describe the scattering of the holes with and without spinflip [Chao, Spalek, and Oles 1977; Ammon, Troyer, and Tsunetsugu 1995].

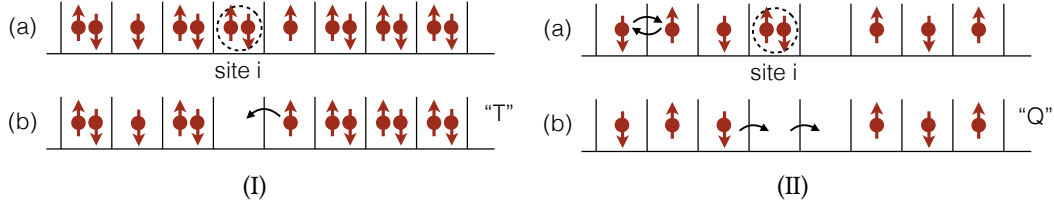


Figure 4.4.: (Ia) Ground state $|0, N\rangle$ for $N = 2L - 2$ electrons ($n < 2$, high filling). Two electrons at site i are removed (dashed line). (Ib) Configuration of an excited state $|n, N - 2\rangle$ contributing to the triplon satellite (“T”). The arrow indicates the internal degree of freedom of the triplon.

(IIa) Configuration with $N = L$ electrons (half filling $n = 1$) contributing to the ground state $|0, N\rangle$. Two electrons at site i are removed (dashed line). Arrows: virtual hopping processes of second-order perturbation theory in t . (IIb) Configuration of an excited state $|n, N - 2\rangle$ contributing to the quadruplon satellite (“Q”). Arrows indicate quadruplon propagation.

The triplon

The most apparent deviations from the standard Cini-Sawatzky theory consist in the appearance of the new structures “T” and “Q”. Let us first concentrate on “T”, which already shows up for low hole-densities $n \lesssim 2$, a limit which has been studied to some extent using the ladder approximation in the hole-hole channel [Cini 1979; Drchal and Kudrnovsky 1984].

When acting with $c_{i\uparrow}c_{i\downarrow}$ on the ground state, one may distinguish between contributions to the spectrum resulting from two different types of ground-state configurations: In the case of an excitation that takes place in a hole-free region, one expects essentially the same shape of the spectrum as in the $n = 2$ case. The closer n is to 2, the more dominant this contribution. If the excitation takes place at a site next to an already existing hole, however, a final state with three holes on nearest-neighbouring sites is created. This case is schematically illustrated on the left side of fig. 4.4(I).

Here, the question arises whether the three holes can form a new bound object, a “triplon”. This information is coded in the excited states of the Hubbard model which appear in eq. (4.2), rather than the ground state. This means that we can adjust our initial state in order to enhance the alleged triplonic contribution by giving it more spectral weight. At the same time, the initial state should be relevant for the two-hole spectral function, of course, since this is what we are ultimately interested in. If the previously described picture of creating three holes on neighbouring sites is correct, it thus stands to reason to calculate the three-hole spectral function

$$A_{3\text{-hole},\sigma}(\omega) = \sum_n |\langle n, N - 3 | c_{i\uparrow}c_{i\downarrow}c_{i+1,\sigma} | 0, N \rangle|^2 \delta\left(\omega + 3\mu - \left(E_0^{(N)} - E_n^{(N-3)}\right)\right) \quad (4.15)$$

and its k -resolved variant

$$A_{3\text{-hole},\sigma}(\omega, k) = \frac{1}{L} \sum_n \left| \langle n, N - 3 | \sum_i e^{-ikR_i} c_{i\uparrow}c_{i\downarrow}c_{i+1,\sigma} | 0, N \rangle \right|^2 \delta\left(\omega + 3\mu - \left(E_0^{(N)} - E_n^{(N-3)}\right)\right). \quad (4.16)$$

This can be studied for all fillings; however, in the same way a doublon appears already at $n = 2$ as a bound state, the triplon should do so as well, so this is the case we can first focus on. We are now left

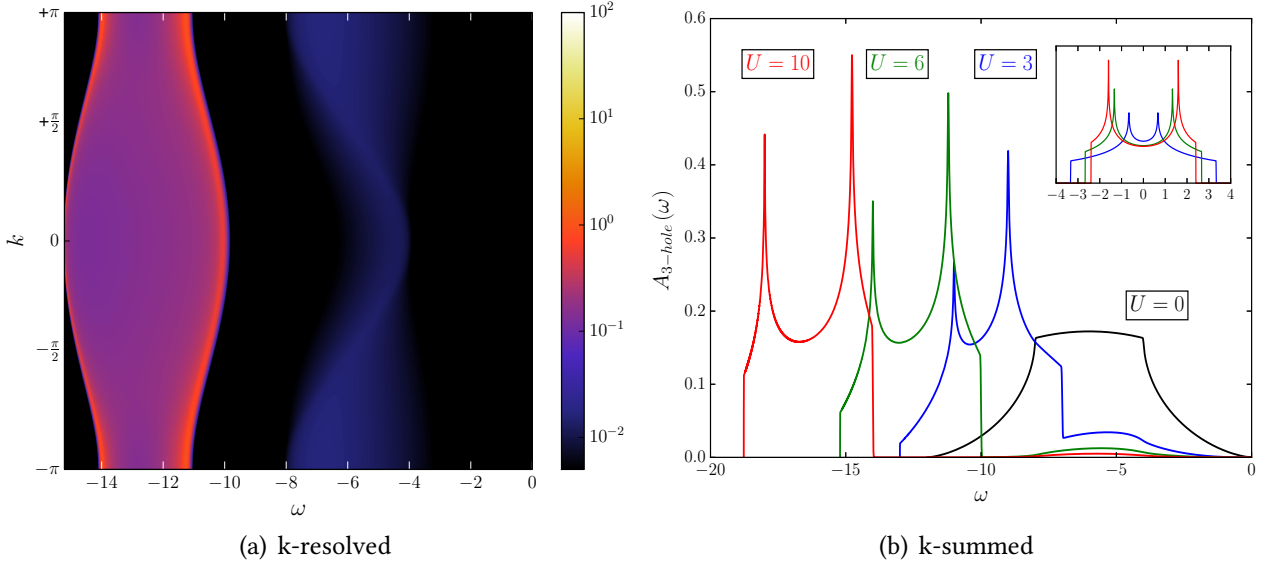


Figure 4.5.: (a) Momentum-resolved three-hole excitation spectrum for $L = 200$, $U = 6$, $n = 2$, with an energy resolution of $\delta E = 0.05$ ($M = 304$ Chebyshev moments), calculated using exact states and periodic boundary conditions.

(b) The k -summed spectrum (eq. (4.15)) for $L = 500$, $n = 2$, $\delta E = 0.01$ (up to $M = 1876$) and several values of U as indicated. The inset shows the convolutions $\int dx \rho_0(\omega - x, W) \rho_0(x, 2J)$ for the same values of U , where $\rho_0(x, W) \equiv 1/\pi \sqrt{W^2/4 - x^2}$.

with a much simpler three-body problem only. Since the Hilbert space dimension is approximately $L^3/2$, we can use the Chebyshev expansion method with exact states.

The result for $L = 500$ sites is shown in fig. 4.5(b) for several values of U , while fig. 4.5(a) shows the k -resolved spectrum for $U = 6$. One observes a similar general pattern as in the two-hole case: For $U = 0$ the spectrum consists of a three-fold self-convolution of $\rho_0(\omega)$ with a spectral width given by $3W = 12$, while for finite $U > 0$, there is a band-like part and a split-off correlation satellite.

For finite but strong U , the satellite in $A_{3\text{-hole},\sigma}(\omega)$ has a slightly asymmetric weight distribution due to the presence of the band-like part. Apart from that, its shape is in fact given by a convolution of $\rho_0(\omega)$ (the single hole, width $W = 4$) with the same density of states, but rescaled (the doublon, width $\Delta\omega = 2J = 4/3$), see the inset in fig. 4.5(b). This clearly indicates that the doublon and the hole propagate independently and do not form a bound state.

This should also hold for the two-hole spectrum (fig. 4.3): The structure “T” does not represent a stable triplon, but is rather a doublon-hole continuum superimposed on the doublon satellite. The filter-operator analysis in chapter 4.1.3 and further arguments given below indeed support this interpretation.

Compared to the three-hole spectrum, “T” in fig. 4.3 has less spectral weight, but the same shape. It should be stressed that the two peaks belonging to “T” are simply a consequence of the van Hove singularities in one dimension, separated by about $16T^2/U \approx 2.67$ for $U = 6$, and should not be mistaken for separate resonances. Hence, it is expected that they disappear for higher-dimensional lattices.

The interpretation of “T” as a doublon-hole continuum also explains that it is located at approximately U below the barycentre of the three-hole continuum. The latter is given by $\omega_0 = -6$ for $n = 2$. With decreasing filling the support of the three-hole continuum shrinks, and so does its barycentre, but it does so at a faster rate than the two-hole continuum, so that the doublon-hole

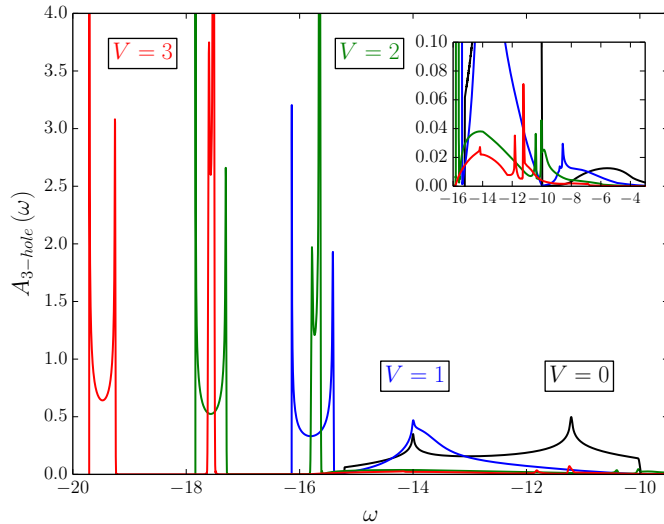


Figure 4.6.: Three-hole excitation spectrum as in fig. 4.5(b), but for different values of the nearest-neighbour interaction V and fixed $U = 6$ (up to $M = 1971$ Chebyshev moments). The inset shows a close-up view of the continua.

continuum “T” eventually merges with the doublon satellite for fillings approaching $n = 1$.

A stable, repulsively bound triplon forms in the presence of an additional repulsive nearest-neighbour Coulomb interaction V (see eq. (2.15)). This situation is shown in fig. 4.6. Starting from the doublon-hole continuum at $U = 6$ and $V = 0$, and switching on V leads to the emergence of two satellites splitting off for sufficiently strong V . Both have the same shape as the non-interacting density of states $\rho_0(x)$ and are separated by about $2V$ from the continuum. The presence of two satellites rather than one is due to the fact that a triplon has an internal degree of freedom: On two sites, the three-hole states $(1, 0)^T \equiv c_{1\uparrow}^\dagger|0\rangle$ and $(0, 1)^T \equiv c_{2\uparrow}^\dagger|0\rangle$ form two configurations. When coupled by the Hamiltonian³

$$H_{2\text{-site}} = \begin{pmatrix} U + 2V & -T \\ -T & U + 2V \end{pmatrix}, \quad (4.17)$$

they result in a pair of bonding/antibonding eigenstates at energies $E_{\pm} = U + 2V \pm T$. The energy splitting of $2T$ very well explains the energy difference between the positions of the two satellites in the spectra in fig. 4.6. Their widths are different, but become equal in the strong-coupling limit $U, V \gg T$, and are then given by $8T^2/(U + 2V)$ (which is not shown, but was checked numerically).

Fig. 4.7 shows the emergence of the two triplon satellites in the two-hole spectrum at $n = 1.8$ as obtained by DMRG. With $V > 0$, a much stronger growth of the entanglement entropy during the Chebyshev iteration is found. This is to be expected, as the model becomes nonintegrable (see chapter 3.6.5). These spectra have therefore been calculated at a moderate energy resolution $\delta E = 0.4$. For $V = 3$, for example, the MPS bond dimension at this point already exceeds 6200.

For $V = 0$, we find the dominating doublon satellite around $\omega \approx -10$ and the two peaks of the doublon-hole continuum at higher binding energies, separated by about $16T^2/U \approx 2.67$. One is located at $\omega \approx -13.1$, while the other one is next to the intense van Hove singularity of the doublon structure at $\omega \approx -10.4$, and barely distinguishable from it. It requires a high-resolution calculation to uncover this feature ($\delta E = 0.04$, the purple curve in fig. 4.7). For $V > 0$, the double-peak structure of the triplon appears, with a separation of 2 and shifting by about $2V$ with increasing V ,

³Note that with $H_{2\text{-site}}$, we count the interaction between holes rather than electrons.

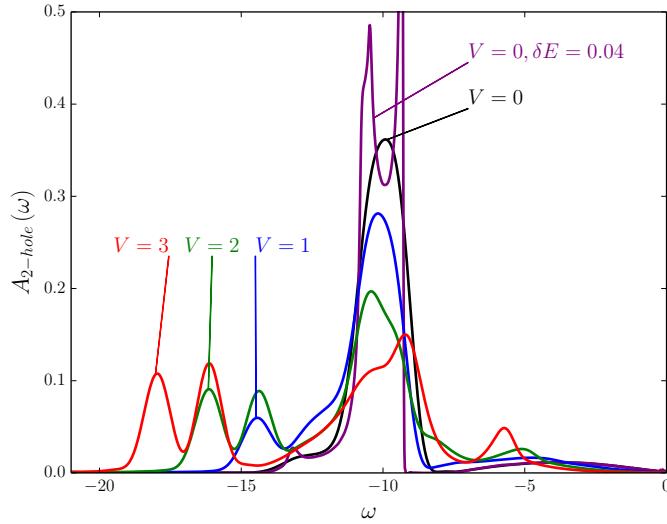


Figure 4.7.: Two-hole excitation spectrum at filling $n = 1.8$ for $U = 6$ and different V as indicated. DMRG calculations for $L = 60$ lattice sites and energy resolution $\delta E = 0.4$ (up to $M = 376$ Chebyshev moments), except for the purple line at $V = 0$ ($L = 120$, $\delta E = 0.04$, $M = 3553$).

as in the case of the three-hole spectrum (fig. 4.6). The doublon satellite, on the other hand, shows a considerable loss of spectral weight, but its position is basically unchanged when increasing V .

See chapter 4.1.4 for a discussion of this splitting and additional effects induced by V .

The quadruplon

The two-hole spectrum of the half-filled Hubbard model (see fig. 4.3, lowest panel) displays a broad peak “Q” centred around $\omega \approx -7.4$.

A two-hole excitation requires a double occupancy at a site i in the ground state $|0, N\rangle$. For strong U and $N = L$, a corresponding configuration is generated by virtual second-order hopping processes, which at the same time favour antiferromagnetic spin correlations. This is the famous Anderson super-exchange [Anderson 1959]. Starting from this initial-state configuration, the resulting configuration contributing to the $(N - 2)$ -electron final state $|n, N - 2\rangle$ must therefore contain two empty nearest-neighbouring sites, i.e., two neighbouring doublons (see the sketch given in fig. 4.4(II)). One may now ask whether these bind to form a heavier “quadruplon”.

A simple inspection of the presence of a binding energy can be done using the position of “Q”: A two-doublon continuum would be expected at twice the energetic centre of the doublon satellite, an additional binding energy would mean a shift from that position. Looking at the closest dataset to half filling ($n = 62/60$ in fig. 4.3), one cannot see such a shift within plotting accuracy, the “Q” peak at $\omega \approx 9.8$ coincides with the expected continuum centre. Going to higher fillings, however, one finds a shift that increases roughly linearly with n (from $\Delta\omega \approx 0.1$ at $n = 1.2$ to $\Delta\omega \approx 0.4$ at $n = 1.6$) towards *lower* binding energies, i.e. the doublons seem to bind *attractively* as the filling increases.

For $n \rightarrow 2$ the phase space for quadruplon formation shrinks to zero. However, we can address the quadruplon formation in the final state and carry out a similar analysis as in chapter 4.1.3 by calculating the following four-hole spectral function

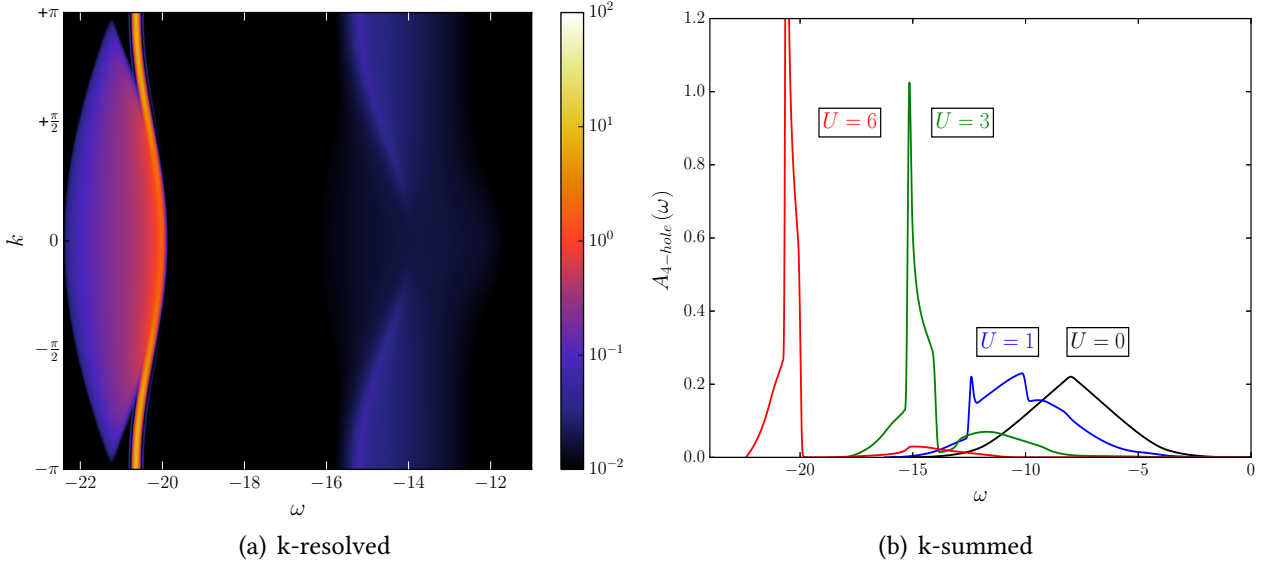


Figure 4.8.: (a) Momentum-resolved four-hole excitation spectrum (eq. (4.19)) for $L = 100$, $U = 6$, $n = 2$, with an energy resolution of $\delta E = 0.05$ ($M = 448$ Chebyshev moments), calculated using exact states and periodic boundary conditions. (b) The k -summed spectrum at the same resolution for various values of U as indicated.

$$A_{4\text{-hole}}(\omega) = \sum_n \left| \langle n, N-4 | c_{i\uparrow} c_{i\downarrow} c_{i+1\uparrow} c_{i+1\downarrow} | 0, N \rangle \right|^2 \delta \left(\omega + 4\mu - \left(E_0^{(N)} - E_n^{(N-4)} \right) \right) \quad (4.18)$$

and its k -resolved variant

$$A_{4\text{-hole}}(\omega, k) = \frac{1}{L} \sum_n \left| \langle n, N-4 | \sum_i e^{-ikR_i} c_{i\uparrow} c_{i\downarrow} c_{i+1\uparrow} c_{i+1\downarrow} | 0, N \rangle \right|^2 \times \delta \left(\omega + 4\mu - \left(E_0^{(N)} - E_n^{(N-4)} \right) \right). \quad (4.19)$$

We may continue the line of argumentation we followed for the triplon: Below a filling of $n = 1.5$, the probability to find empty sites increases and whenever a doublon is created next to such an empty site, one has created two doublons or four holes effectively, so that the initial state of $A_{4\text{-hole}}(\omega)$ should still be relevant for $A_{2\text{-hole}}(\omega)$. Again, should a quadruplon exist, it must already show up for the completely filled band. This case is shown in figs. 4.8(a) and 4.8(b).

For $U = 0$, the spectrum consists of a four-hole continuum at low binding energies; its support is given by $4W = 16$. For strong U , this continuum has extremely little spectral weight. Some of it has been transferred to an extended structure at intermediate excitation energies around $\omega = -8T - U$, which belongs to the one-doublon-two-hole continuum, though it overlaps with the four-hole continuum which stretches down to $\omega = -4W = -16$. Most of the weight, however, is taken by the correlation satellite located at $\omega \approx -8T - 2U$, which corresponds to final states with two doublons. Notably, its shape does not resemble the self-convolution of a doublon satellite (cf. fig. 4.1(b)), as one would expect for a doublon-doublon continuum.

This is in fact corroborated by the analysis of the effective doublon model (1.9). Within it, our four-particle problem reduces to a two-particle one and can be solved in much the same way as the

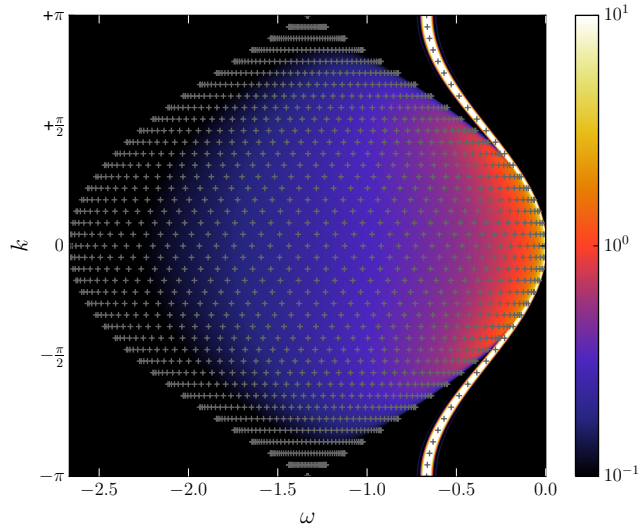


Figure 4.9.: Momentum-resolved two-doublon spectral function (eq. (4.20)) of the effective model (eq. (1.9)) calculated for $L = 1000$, $\delta E = 0.01$, $J = 2/3$ and $N_d = L$ bosons using exact states and periodic boundary conditions. The excitation energies of a smaller system with $L = 40$ sites are shown as crosses for comparison.

two-hole problem in the Cini-Sawatzky case (see [Scott, Eilbeck, and Gilhøj \(1994\)](#) and chapter 4.1.2). Separating the relative from the centre-of-mass motion, the eigenvalues can be calculated for rather large systems. One does indeed observe a split-off resonance for certain values of the wave vector k , corresponding to a bound quadruplon. However, due to the small interaction strength J , the bound state is energetically positioned within the doublon-doublon continuum.

In order to demonstrate this, rather than showing just the eigenvalues, let us calculate the k -resolved two-doublon spectral function within the effective model:

$$A_{2\text{-doublon}}(\omega, k) = \frac{1}{L} \sum_n \left| \langle n, N_d - 2 | \sum_i e^{-ikR_i} d_i d_{i+1} | 0, N_d \rangle \right|^2 \delta \left(\omega - \left(E_0^{(N_d-2)} - E_n^{(N_d-2)} \right) \right). \quad (4.20)$$

Note that the chemical potential has been omitted for simplicity, so that the lowest binding energy is at $\omega = 0$. Fig. 4.9 shows the result of a calculation for $N_d = L = 1000$ and $J = 2/3$ corresponding to filling $n = 2$ and interaction $U = 6$ in the original model. The two-doublon spectrum corresponds to the satellite around $\omega = -8t - 2U - 2J \approx -21.3$ in fig. 4.8(a). The support is given by $\Delta\omega = 8T/3 \approx 2.67$, though with very little weight on the high-binding-energy side. This is the expected value for two independent doublons: $\Delta\omega = 2 \times 4 \times J/2$.

The k -resolution uncovers that the continuum actually has very small spectral weight and that the spectrum is in fact dominated by the intense quadruplon peak. Around the Brillouin zone centre, the quadruplon is a resonance with a finite width, but still its weight dominates the whole energy range. For $|k| \gtrsim 3\pi/4$, it is fully split off from the continuum and has zero intrinsic width (the width is due to the finite δE only). One can conclude that the quadruplon excitation represents a stable compound object formed by two bound doublons when its wave vector is close to the zone boundary, while it is a well-defined resonance with finite lifetime around the zone centre.

The stability of the quadruplon can be explained by a phase-space argument: For a state from the two-doublon continuum, the hard-core constraint is not effective in the thermodynamic limit. Hence, the total energy of two doublons with wave vectors p and $k - p$ is obtained as $J \cos(p) + J \cos(k - p)$. Right at $k = \pm\pi$, this adds up to zero, so that a bound quadruplon of arbitrary energy

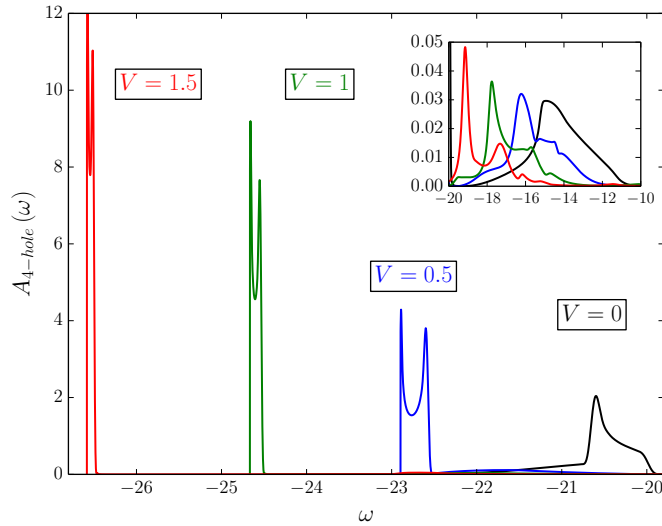


Figure 4.10.: Four-hole spectral function for $L = 100$ sites, a resolution $\delta E = 0.05$ (up to $M = 531$ Chebyshev moments) and a completely filled band ($n = 2$) for several values of V ($U = 6$) using exact states and periodic boundary conditions. The inset shows a close-up view of the continua.

$\omega \neq 0$ and wave vector $k = \pm\pi$ cannot decay. Note that the quadruplon branches split off from the continuum on the low-binding-energy side, as the quadruplon is bound by an *attractive* interaction of strength J , see eq. (1.9). Indeed, its binding energy at $k = \pm\pi$ is just given by $E_{\text{bind}} = J$ [Scott, Eilbeck, and Gilhøj 1994].

The same physics is found when considering the k -resolved four-hole spectral function (4.19) in the full model. This is shown in fig. 4.8(a) for $U = 6$. Due to the singly occupied sites, which are now allowed, and a finite U , the one-doublon-two-hole continuum around $\omega \approx \omega = -8t - U$ acquires some spectral weight. This corresponds to final states where one of the doublons has decayed. Most of the spectral weight, however, is taken by the quadruplon resonance or bound state at higher binding energies. For the quadruplon binding energy at $k = \pm\pi$, we obtain about $E_{\text{bind}} \approx 0.58 < J \approx 0.67$, probably due to the moderate strength of $U = 6$.

At this point, we briefly note that the quadruplon can be stabilized in the entire Brillouin zone by a sufficiently strong nearest-neighbour Coulomb interaction $V > 0$, very similar to the case of the triplon excitation discussed in chapter 4.1.3. Fig. 4.10 shows the (local) four-hole spectrum for $U = 6$ and different V . Here, the quadruplon satellite, with a shape approaching the shape of the free density of states for strong V , is fully split off from the (very weak) two-doublon continuum and shows up on its high-binding-energy side, since the interaction is repulsive. With increasing V , the quadruplon peak shifts with the additional binding energy $4V$.

All of this having been said, it still does not answer the question whether what is seen in the *two-hole* spectrum for $V = 0$ is the stable quadruplon as well. First, we note that the structure “Q” in $A_{2\text{-hole}}(\omega)$ (see fig. 4.3) continuously connects to the quadruplon peak analyzed with $A_{4\text{-hole}}(\omega)$. This is demonstrated in chapter 4.1.4 where the (local) four-hole spectrum is presented in the entire filling range $1 \leq n \leq 2$.

Hence, the question to be answered is the following: Do the two doublons in the final state contributing to “Q” for fillings $n < 2$ bind and form a compound object, i.e., is there an enhanced probability to find the doublons at neighbouring sites? Above an argument relying on the energy shift of “Q” with respect to the expected position of the two-doublon continuum was given. However, a more direct analysis should be possible as the numerical approach is based on the many-body wave function, which in principle contains all information about the system. One should therefore be able to

extract specific information on the final states within a given frequency range. An implementation of this idea within the Chebyshev expansion method requires a new technique which is presented in the next chapter.

Filter-operator technique

To extract specific information on the states contributing to the two-hole spectrum at a given frequency ω , let us proceed in the following way: First, we define a state $|\Psi(\omega)\rangle$ as the sum over the complete set of energy eigenstates weighted by the matrix element of the transition operator:

$$|\Psi(\omega)\rangle = \sum_m \langle m | c_{i\uparrow} c_{i\downarrow} | 0 \rangle \delta(\omega - (E_0 - E_m)) | m \rangle. \quad (4.21)$$

$|\Psi(\omega)\rangle$ is constructed to represent a typical final state contributing to the spectrum at frequency ω . Note that it is coincidentally identical to the ‘‘correction vector’’,

$$|\Psi(\omega)\rangle = -\frac{1}{\pi} \text{Im} \frac{1}{\omega + i0^+ - (E_0 - H)} c_{i\uparrow} c_{i\downarrow} | 0 \rangle, \quad (4.22)$$

which is employed within dynamical DMRG [Jeckelmann 2002] to calculate the spectral function, which in this case would be $A_{2\text{-hole}}(\omega) = \langle 0 | c_{i\downarrow}^\dagger c_{i\uparrow}^\dagger | \Psi(\omega) \rangle$.

Here, it is employed in a different way, choosing a Hermitian (but otherwise in principle arbitrary) ‘‘filter operator’’ F and calculate the following expectation value:

$$\langle \Psi(\omega) | F | \Psi(\omega) \rangle = \sum_{mn} \langle 0 | c_{i\downarrow}^\dagger c_{i\uparrow}^\dagger | m \rangle \langle m | F | n \rangle \langle n | c_{i\uparrow} c_{i\downarrow} | 0 \rangle \delta(\omega - (E_0 - E_m)) \delta(\omega - (E_0 - E_n)). \quad (4.23)$$

This constitutes a ‘‘filtered’’ two-hole spectral function which will be labelled $A_{2\text{-hole}}[F](\omega)$. The additional weight factors $\langle m | F | n \rangle$ give us some characterization of the eigenstates involved, depending on the choice of F . The normal spectrum is obviously recovered for $F = 1$. This quantity is numerically accessible as the diagonal part ($\omega = x = y$) of the two-dimensional Chebyshev expansion defined by

$$A_{2\text{-hole}}[F](x, y) = \sum_{mn} \langle 0 | c_{i\downarrow}^\dagger c_{i\uparrow}^\dagger | n \rangle \langle m | F | n \rangle \langle n | c_{i\uparrow} c_{i\downarrow} | 0 \rangle \delta(x - (x_0 - x_n)) \delta(y - (x_0 - x_m)), \quad (4.24)$$

whose calculation is described in chapter 3.3.2.

To convince ourselves that this method works, let us first consider the well-understood limit of the completely filled band $n = 2$ one more time. We can define an operator h_i which projects out states with an empty site i as

$$h_i = (1 - n_{i\uparrow})(1 - n_{i\downarrow}), \quad (4.25)$$

and an operator s_i , projecting out states with single occupancy at i :

$$s_i = (1 - n_{i\uparrow} n_{i\downarrow})(1 - h_i) = n_{i\uparrow} + n_{i\downarrow} - 2n_{i\uparrow} n_{i\downarrow}. \quad (4.26)$$

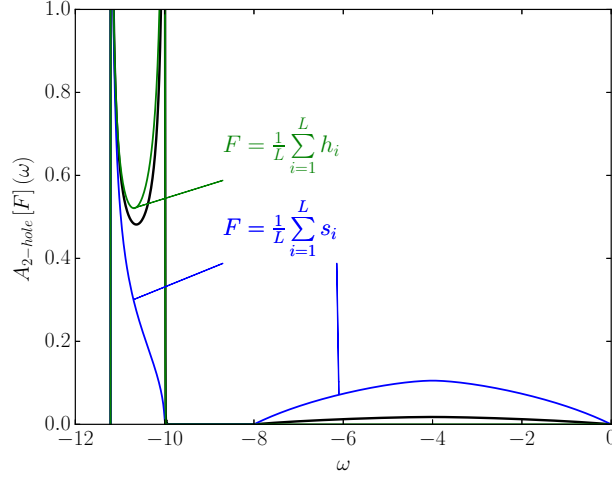


Figure 4.11.: Two-hole spectral function for $n = 2$ (thick black line) and two-hole spectra (normalized to area) using different filter operators (colored lines), calculated with exact states for $U = 6$, $L = 1000$, $\delta E = 0.01$ ($M = 1121$).

With this we can use $F = 1/L \sum_i h_i$ to filter out states characterized by doublons, and $F = 1/L \sum_i s_i$ to filter out states characterized by the absence of doublons, but the presence of single holes.

Results for $U = 6$ are shown in fig. 4.11. One does indeed observe that the spectral function obtained with the former filter has support at the doublon satellite only, while the support of the latter coincides with spectral range of both the band-like part and the satellite. This reflects the fact that singly occupied sites appear as intermediate configurations during doublon propagation.

Let us test the triplon case next. Recall that the two-hole spectral function is computed at the central site of the chain, i.e., we take $i = L/2$ for the transition operator $c_{i\uparrow}c_{i\downarrow}$. To look for triplons, we can thus choose local filters and take $F = h_{L/2}s_{L/2+\delta}$ at different distances δ . An enhanced weight at $\delta = 1$ would indicate that the doublon and the additional hole bind and form a stable triplon.

The result for $n = 1.8$ is shown in fig. 4.12(a). One does indeed see that the case $\delta = 1$ does not look any more special than $\delta = 2$, $\delta = 3$, or $\delta = L/2$. All choices roughly reproduce the shape of the two-hole spectral function and are barely distinguishable in the range of the peak at $\omega \approx -13.1$, earlier identified as the triplon structure. This corroborates the previous result that a doublon and a hole do not bind. On the other hand, it was argued that a stable triplon is formed for a nearest-neighbour interaction $V = 1$. This is indeed supported by the filter-operator technique: For $V = 1$ (see inset of fig. 4.12(a)) the case $\delta = 1$ is in fact very different as compared to $\delta \neq 1$: The weight of the filtered spectrum is strongly enhanced at frequencies around $\omega = -14.4$, where the peak of the bound triplon is located (cf. fig. 4.7).

Finally, to investigate the quadruplon, let us consider the filling $n = 62/60$ right above half filling. The quadruplon peak is located at $\omega \approx -9.8$ below the doublon structure with barycentre at $\omega \approx -6$, see fig. 4.3. The filtered spectra are now computed using $F = h_{L/2}h_{L/2+\delta}$.

The results are shown in fig. 4.12(b). In this case, a filter with $\delta = 1$ produces a strong signal at the quadruplon position even for $V = 0$, while the spectra for larger distances $\delta \neq 1$ are again close to each other and roughly coincide with the original spectral function. This is a clear indication that there is a bound quadruplon, the contribution of which dominates the two-hole spectrum $A_{2\text{-hole}}(\omega)$, as compared to the doublon-doublon continuum.

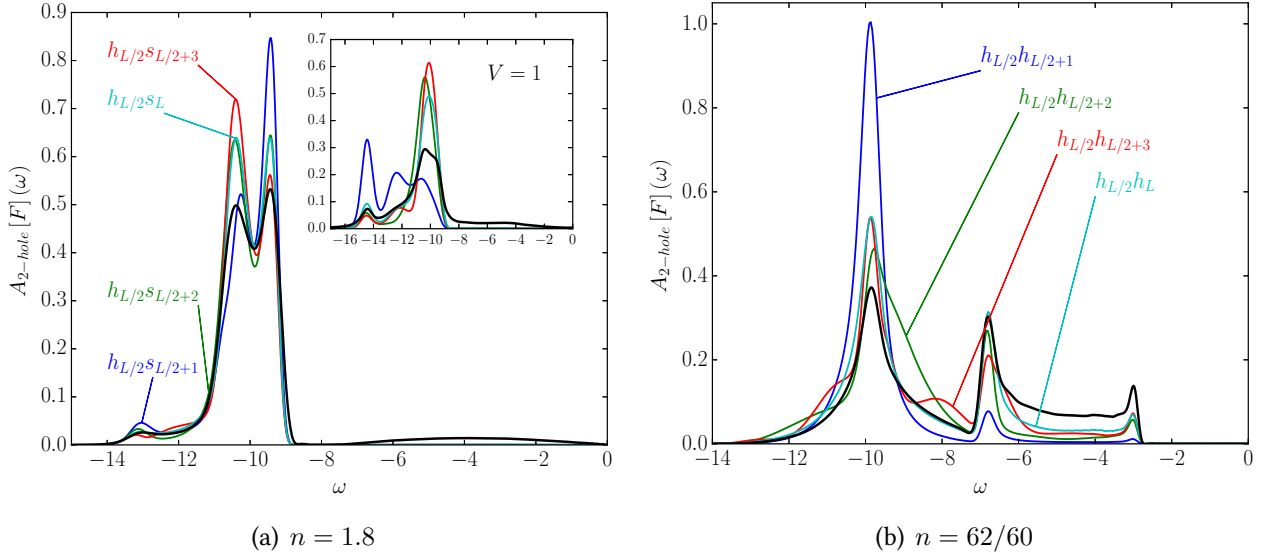


Figure 4.12.: (a) Two-hole spectral function for $n = 1.8$ (thick black line) and two-hole spectra (normalized to area) using different filter projecting out triplonic states (colored lines), calculated with DMRG for $U = 6$, $L = 60$, $\delta E = 0.2$ ($M = 380$). Inset: results for finite nearest-neighbour interaction $V = 1$, at $\delta E = 0.4$ ($M = 239$). (b) The same for $n = 62/60 \approx 1.03$, $\delta E = 0.3$ ($M = 766$), with filter operators now chosen to project out quadruplonic states.

Infinite doublon lifetime for $k = \pi$

Let us return to the doublon. As has been discussed in chapter 4.1.3, a stable excitation with infinite lifetime is found in the simple $n = 2$ limit and explained as a repulsively bound pair of holes. This interpretation breaks down for fillings close to half filling, where the two-hole excitation propagates through a background of singly occupied sites with antiferromagnetic correlations. We are thus left with the question whether there is a stable doublon for fillings $n < 2$, and close to half filling in particular.

The U -dependence of the doublon lifetime has been addressed in a number of previous theoretical as well as experimental studies [Strohmaier et al. 2010; Lenarčič and Prelovšek 2013; Chudnovskiy, Gangardt, and Kamenev 2012; Petrosyan et al. 2007; Hofmann and Pothoff 2012; Rosch et al. 2008; Hansen, Perepelitsky, and Shastry 2011], starting from the concept of repulsive binding. The k -resolution of the local two-hole excitation adds a new view on this problem.

With $A_{2\text{-hole}}(\omega, k)$, one actually decomposes the local two-hole excitation into a coherent linear superposition of k -dependent two-hole excitations:

$$c_{i\uparrow}c_{i\downarrow}|0, N\rangle = \sum_k d_k|0, N\rangle, \quad (4.27)$$

where $d_k = 1/L \sum_i e^{-ikR_i} c_{i\uparrow}c_{i\downarrow} = 1/L \sum_p c_{p\uparrow}c_{k-p\downarrow}$ with $c_{k\sigma} = 1/\sqrt{L} \sum_i e^{-ikR_i} c_{i\sigma}$. The important observation is that the state $d_k|0, N\rangle$ has a strongly k -dependent lifetime. At the zone boundary $k = \pi$, the lifetime is even infinite, which can be verified numerically and understood analytically.

Let us first discuss the numerical results. Eq. (4.6) can be used to approximate the two-hole spectrum with a calculation for a system with open boundaries. In this case, the k -summation of $A_{2\text{-hole}}(\omega, k)$ (eq. (4.7)) yields the local spectrum, but averaged over all sites, rather than the local spectral function

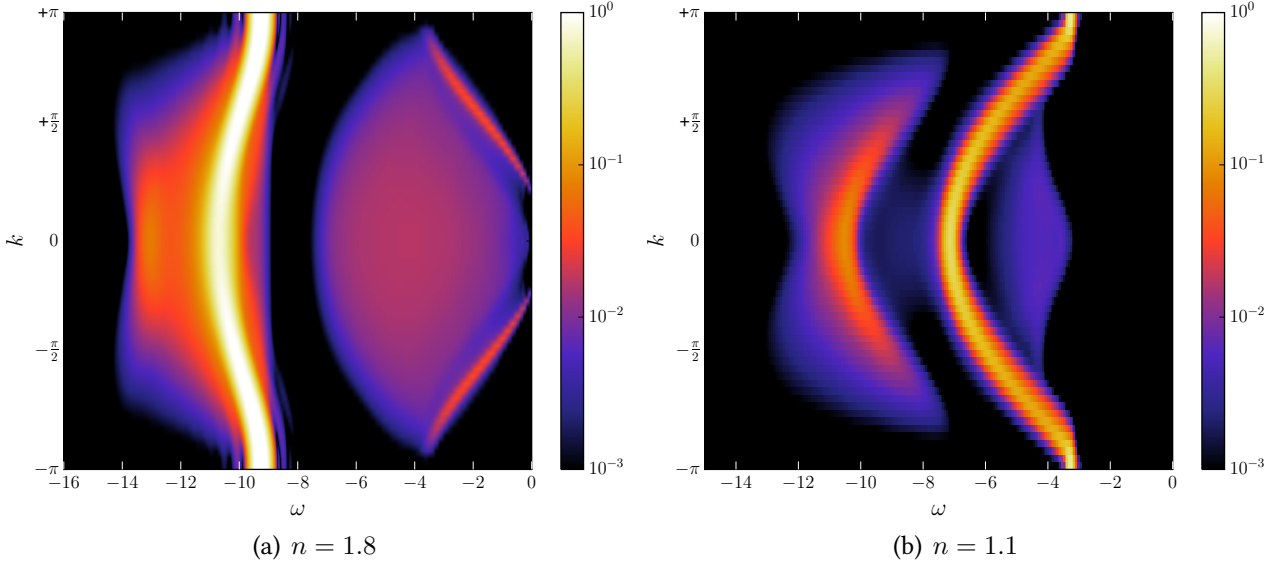


Figure 4.13.: (a) Momentum-resolved two-hole spectral function for $n = 1.8$ and $U = 6$. DMRG calculations for $L = 60$ sites, $\delta E = 0.2$ ($M = 380$). Note that the spectral weight is plotted on a logarithmic scale. (b) The same for $n = 1.1$ ($M = 1118$).

at the central site i , as defined in eq. (4.2). For a system with size $L = 60$, however, the approximation is already excellent. Note that this can also be thought of as carrying out a Fourier transform with two momenta, $A_{2\text{-hole}}(\omega, k, k')$, but then only looking at the diagonal component with $k = k'$: $A_{2\text{-hole}}(\omega, k) \equiv A_{2\text{-hole}}(\omega, k, k)$.

Fig. 4.13(a) shows the k -resolved spectrum for $n = 1.8$ and $U = 6$. The band-like part extends from $\omega = 0$ to $\omega \approx -8$ with most of the spectral weight at low binding energies and a ridge-like structure around $k = 0$. Its overall spectral weight, however, is very small compared to the weight of the doublon satellite, which is centred around $\omega \approx -10$. Interestingly, one finds that the doublon satellite is not broadened at all for $k = \pm\pi$. In fact, the structure at $k = \pm\pi$ should be interpreted as a δ -peak at frequency $\omega = \omega_0(\pi) \approx -9.25$. Note that on the logarithmic scale, there are seemingly sidebands visible close to $\omega_0(\pi)$ and $k = \pm\pi$. These are, however, simply the numerical artefact of Gibbs oscillations. As shown below, the position of the δ -peak is precisely given by $\omega_0(\pi) = U - 2\mu \approx -9.25$, where the value of μ is obtained from the ground-state calculation (eq. (4.4)). When $|k| < \pi$, the satellite acquires some finite width, i.e., the doublon changes from a stable bound object into a resonance, meaning that there are continuum states right on top of it. Its width is largest around $k = 0$, so that the lifetime is shortest. This is opposed to the simple $n = 2$ limit, where the doublon, if created with the appropriate value of k , is stable in the entire Brillouin zone.

The situation at a filling of $n = 1.1$ is very similar. The results are shown fig. 4.13(b). Here, the k -resolved two-hole spectrum consists of an intense doublon satellite (centred around $\omega \approx -5$) and the quadruplon structure (around $\omega \approx -10$), as well as a band-like part with non-zero, but extremely low weight close to $\omega = 0$, which is not visible in the figure. Referring to the results obtained by means of the filter-operator technique in chapter 4.1.3, we interpret the quadruplon structure as an object composed of two doublons on top of a continuum, i.e., a resonance. Most of its weight is located close to $k = 0$. It is tempting to assume that the quadruplon is entirely stable at $k = \pi$, similar to the four-hole spectrum case (fig. 4.8(a)), but the whole spectral weight at the zone boundary is instead taken by the doublon. We have already seen a similar effect in the case of the triplon: In the three-hole spectral function for $n = 2$ (fig. 4.6), it clearly has a different dispersion

from the two-hole spectral function for $n < 2$ (the inset of fig. 4.7), while the energetic positions follow the same rules.

Turning to the doublon in fig. 4.13(b), we observe that it has infinite lifetime at $k = \pm\pi$ again, but now also displays a distinct “shadow” around $k = 0$. For $n = 1.1$, we find $2\mu = 9.25$, and thus expect the doublon at energy $\omega_0(\pi) = U - 2\mu \approx -3.25$. This perfectly fits with the position that can be read off from fig. 4.13(b).

The stability of the doublon at the zone edges can be understood analytically by referring to the “hidden” charge-SU(2) symmetry of the Hubbard model, described in chapter 2.1.2.

At half filling, the ground state $|0, N\rangle$ is a non-degenerate total spin singlet. This implies immediately that $|0, N\rangle$ is a total isospin singlet as well. Hence, we have $\eta|0, N = L\rangle = 0$. Since $d_{k=\pi} = \eta/L$ for $k = \pi$, the transition operator in the Lehmann representation of the k -resolved two-hole spectral function, eq. (4.6), is just proportional to η , which for half filling implies

$$A_{2\text{-hole}}(\omega, k = \pi) = 0 \quad (4.28)$$

for all excitation energies ω . This is consistent with the DMRG calculations which predict the doublon satellite to vanish for $n = 1$, even in the entire Brillouin zone (see fig. 4.3).

Off half filling, the chemical potential $\mu \neq U/2$ explicitly breaks the charge-SU(2) symmetry and produces a gapped collective mode showing up as a single δ -peak in the two-hole spectrum at wave vector $k = \pi$ (or $k = -\pi$). This can be inferred from eq. (2.11). Namely, it is easy to see that, for arbitrary N , the state $\eta|0, N\rangle$ is an *exact* eigenstate of H with energy $E_0^{(N)} - U$. Inserting this into eq. (4.6), yields

$$A_{2\text{-hole}}(\omega, k = \pi) = \alpha \delta(\omega + 2\mu - U) \quad (4.29)$$

and explains the observed position $\omega_0(\pi) = U - 2\mu$.

Integrating the k -resolved spectrum, eq. (4.6), over ω yields the total weight at a given k :

$$\alpha(k) = \frac{1}{L} \sum_{ij} e^{-ik(R_i - R_j)} \langle 0, N | c_{j\downarrow}^\dagger c_{j\uparrow}^\dagger c_{i\uparrow} c_{i\downarrow} | 0, N \rangle. \quad (4.30)$$

This gives $\sum_k \alpha(k) = \sum_i \langle n_{i\uparrow} n_{i\downarrow} \rangle$, consistent with the global sum rule eq. (4.10). At $k = \pi$, as expressed by eq. (4.29), the whole spectral weight condenses to $\alpha(\pi)$ at the frequency $\omega = U - 2\mu$. The weight of the mode at the zone boundary is then given by $\alpha = 1/L \langle 0, N | \eta^\dagger \eta | 0, N \rangle$, see eqs. (2.10) and (4.30), and can be expressed in terms of the isospin as follows:

$$\alpha = \frac{1}{L} \langle 0, N | (\mathbf{T}^2 - T_z(T_z + 1)) | 0, N \rangle. \quad (4.31)$$

The chemical potential acts like an external field leading to a state with the isospin pointing into the negative- z direction above half-filling, i.e., $M_T = -T$. With $M_T = (L - N)/2$, this leads to:

$$\alpha = -2M_T/L = (N - L)/L = n - 1. \quad (4.32)$$

This means that the weight of the mode linearly increases from zero at half filling to unity at $n = 2$ and explains the strong difference in the weights seen in the DMRG results (figs. 4.13(a) and 4.13(b)).

The same analysis can be done for the k -resolved *two-particle* spectrum and fillings $n > 1$. Here, however, the exact eigenstate $\eta^\dagger|0, N\rangle$ would lead to a δ -peak at *negative* frequency $\omega = \omega_0(\pi) = U - 2\mu < 0$ for $n > 1$ (which would contradict eqs. (4.3) and (4.4)), but the weight $\alpha = 1/L \langle \eta \eta^\dagger \rangle = 1/L \langle (\mathbf{T}^2 - T_z(T_z - 1)) \rangle$ vanishes exactly since $M_T = -T$. For fillings $n < 1$, the δ -peak in the two-particle spectrum shows up on the $\omega > 0$ side with a non-zero weight since $M_T = +T$ in this case – analogous to the two-hole spectrum for $n > 1$ and related to the latter by particle-hole transformation.

Physically, the collective mode describes a *coherent* doublon with energy $U - 2\mu$ which is not scattered, i.e., the final state with wave vector $k = \pi$ in the two-hole spectroscopy has infinite lifetime. Note that it does not propagate through the lattice, since the dispersion flattens out at this point and the velocity becomes zero. The stability is enforced by the remaining isospin-rotation symmetry around the z -axis which protects this “ η -mode” at the zone edge from decay. Note further that the η -mode only shows up off half filling and is not bound to off-diagonal long-range order as has been discussed previously [Yang 1989; Zhang 1990]. For bipartite lattices of higher dimensions, it is predicted to be found at the Brillouin-zone edges $\mathbf{k} = (\pm\pi, \pm\pi, \dots)$.

4.1.4. Additional points

One-hole spectra: the doublon in photoemission

Fig. 4.14 shows the (local) one-hole excitation spectrum,

$$A_{1\text{-hole},\sigma}(\omega) = \sum_n |\langle n, N-1 | c_{i\sigma} | 0, N \rangle|^2 \delta(\omega + \mu - (E_0^{(N)} - E_n^{(N-1)})) \quad (4.33)$$

and the one-particle excitation spectrum,

$$A_{1\text{-particle},\sigma}(\omega) = \sum_n |\langle n, N+1 | c_{i\sigma}^\dagger | 0, N \rangle|^2 \delta(\omega + \mu - (E_n^{(N+1)} - E_0^{(N)})). \quad (4.34)$$

These correspond to photoemission (one-hole spectrum) and inverse photoemission (one-particle spectrum).

For $n = 2$, the unrenormalized density of states is recovered: $A_{1\text{-particle},\sigma}(\omega) = \rho_0(\omega + \mu)$. The van Hove singularities at $\omega = 0$ and $\omega = -4$ are somewhat broadened due to the finite resolution of $\delta E = 0.2$.

For fillings $n < 2$, the spectrum consists of the upper Hubbard band (UHB) at low binding energies and the lower Hubbard band (LHB) showing up at higher binding energies, approximately at U below the UHB (labeled “D” in the figure). Since the LHB for particles corresponds to the UHB for holes, these states are characterized by two holes on the same lattice site, and thus to the propagation of a doublon. This means that a doublon resonance appears in the one-hole spectrum in much the same way higher resonances appear in the two-hole spectrum.

The substructure of the LHB and UHB can be analyzed and understood in terms of collective spinon and holon excitations, see [Benthien, Gebhard, and Jeckelmann \(2004\)](#); [Feiguin and Huse \(2009\)](#); [Kohn \(2010\)](#) and fig. 3.7.

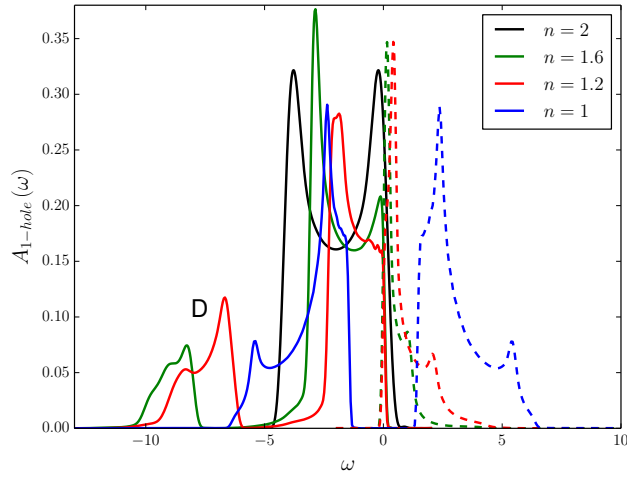


Figure 4.14.: One-hole excitation spectrum (4.33) for $\omega < 0$ (solid line) and one-particle spectrum (4.34) for $\omega > 0$ (dashed line) for selected fillings n . Parameters as in fig. 4.3.

Two-hole spectra: additional effects of V

Due to strong increase in entanglement entropy, the resolution that could be achieved in the DMRG calculations with $V > 0$ was not sufficient to analyze the fine-structure of the triplon peaks. A common technique to deal with such a problem is *linear prediction* [Ganahl et al. 2014; Wolf et al. 2014]. There, one divides a series of datapoints in two halves and makes the ansatz that the second half can be written as a linear combination of the first half. One can use this newly obtained functional dependence in order to “predict” more datapoints in the series. If applied to the first Chebyshev moments of the spectral function, which are still identical to the infinite system, one hopes that linear prediction yields the decaying spectral moments of the infinite system before finite-size effects kick in. As one can imagine, however, this post-processing is not without problems. Ideally, the moments have to decay exponentially, which is not the case at zero temperature (finite temperature serves as a natural broadener). Furthermore, the continuous application of a matrix to the data requires all eigenvalues to be smaller than unity in magnitude for stability; but in practice, eigenvalues larger than unity will usually appear and there is no general prescription of how to deal with them. In the given case, linear prediction was attempted did not enhance the frequency resolution far enough to reveal the triplon fine-structure. It would seem that this information is just not yet contained in the first Chebyshev moments that are numerically accessible.

Therefore, a different path is pursued: One can go to an even higher filling, $n = 1.98$, where an exact calculation is still feasible for a fairly large system. The result for $L = 100$ and $\delta E = 0.01$ is shown in fig. 4.15. We observe that while the first of the triplon peaks appears right away, the second one only rises above the continuum when V exceeds a critical value of $V_c \approx 1.3$.

Note that the shape of the former markedly differs from the free density of states, indicating that in contrast to the three-hole spectral function (fig. 4.6), the triplon in $A_{2\text{-hole},\sigma}(\omega)$ does not become stable in the whole Brillouin zone.

This is further explored in the k -resolved spectra shown in figs. 4.16(a) and 4.16(b). We see that the first peak occurs close to the Γ -point, while the second appears near the zone edges. In addition, we observe another resonance emerging out of the band-like part, separated by V from its barycentre (this can be read off easily at the zone edge), which we can identify as two neighbouring holes repulsively bound by V as a “dimeron”. The deformation of the band-like part due to such dimerons can also be seen at $n = 1.8$ in fig. 4.7.

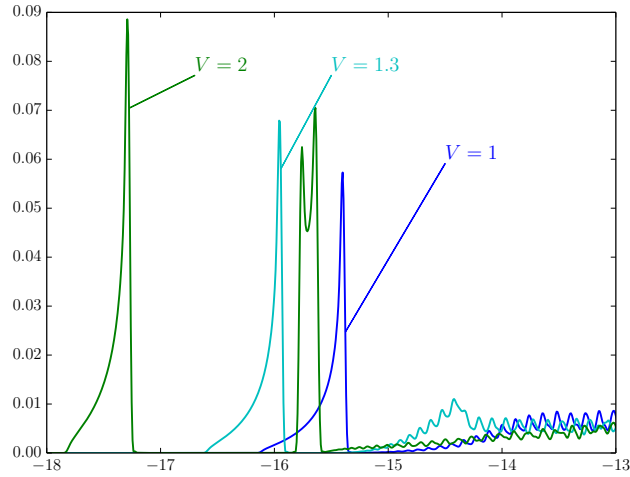


Figure 4.15.: Two-hole excitation spectrum at high binding energies for $L = 100$ and $n = 1.98$, $\delta E = 0.01$ (up to $M = 2852$) and several values of V as indicated, calculated using exact states and periodic boundary conditions.

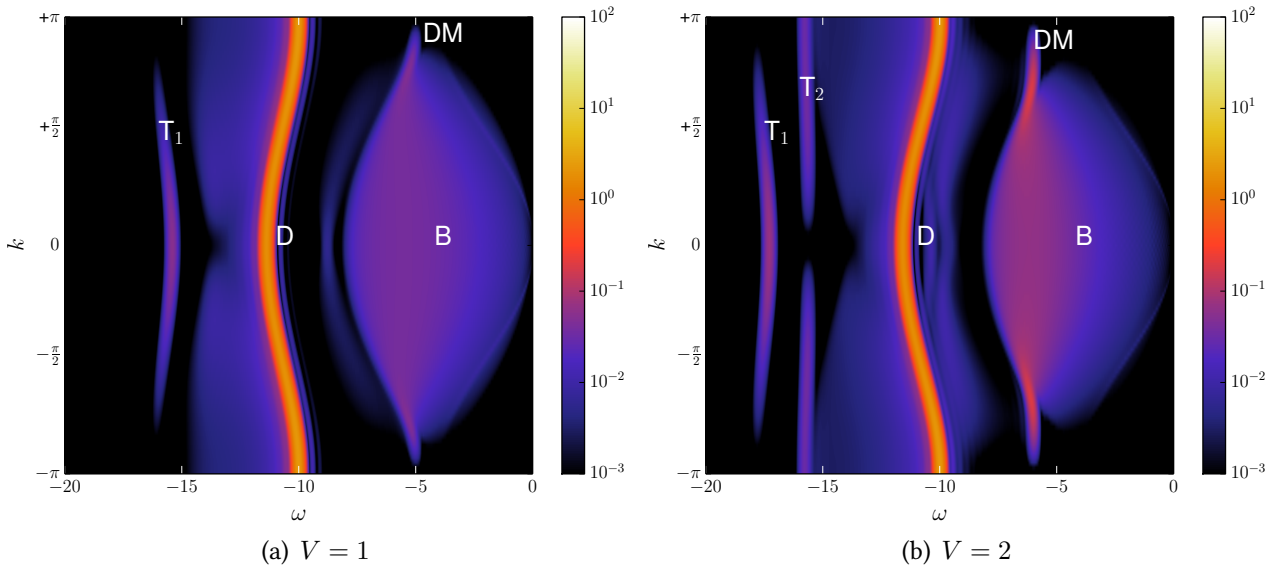


Figure 4.16.: (a) Momentum-resolved two-hole excitation spectrum for $U = 6$, $V = 1$, $L = 100$, $n = 1.98$, $\delta E = 0.1$ ($M = 246$), calculated using exact states and periodic boundary conditions.

(b) The same for $V = 2$ ($M = 285$).

Labels indicate: “D”: doublon, “B”: band-like part, “ T_1 ”, “ T_2 ”: triplon, “DM”: dimeron

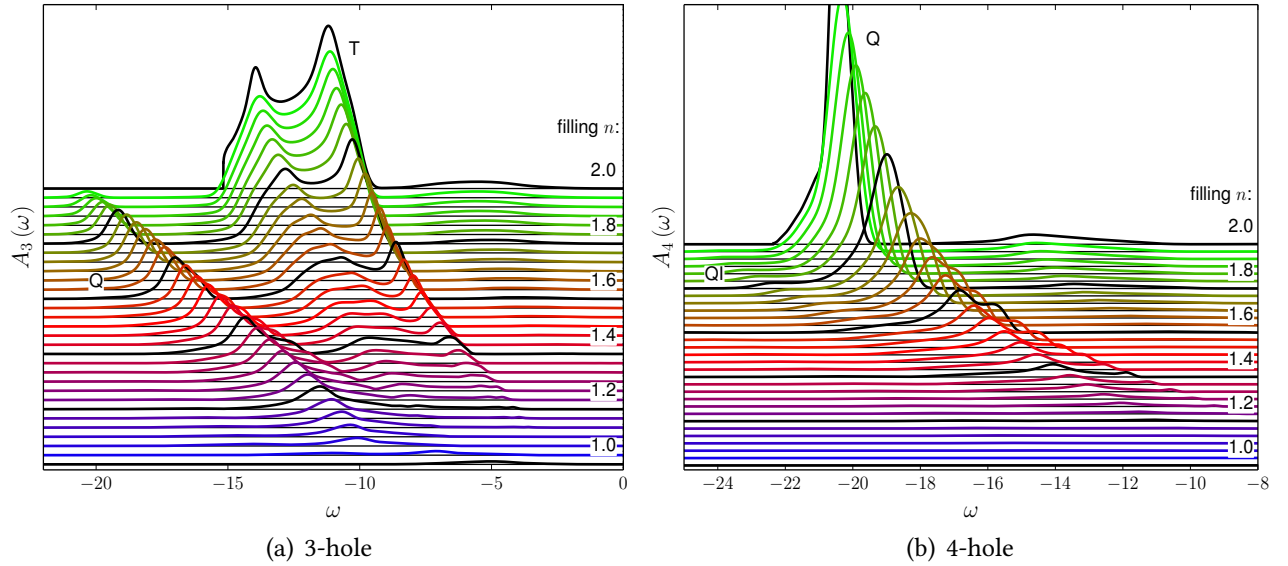


Figure 4.17.: (a) Three-hole excitation spectrum (4.15) for various fillings as indicated, calculated with DMRG. The filling values indicated on the right are drawn in black. Parameters as in fig. 4.3.
 (b) The same for the four-hole excitation spectrum (4.18).

Three-hole spectra: filling dependence

For the sake of completeness, the three-hole spectra are shown for all fillings in fig. 4.17(a). One observes an immediate appearance of the quadruplon satellite as the filling is reduced. It occupies the same energetic position from $\omega \approx -20$ (close to $n = 2$) to $\omega \approx -10$ (close to $n = 1$) as in the two-hole (fig. 4.3) and the four-hole spectral function (fig. 4.17(b)).

Interestingly, the spectral weight of the quadruplon even exceeds the triplonic (doublon-hole) contribution below $n \approx 1.4$.

Four-hole spectra: filling dependence

Fig. 4.17(b) shows the filling-dependence of the four-hole excitation spectrum in the range of the quadruplon excitation energies. Again, the position of the main peak in fig. 4.17(b) approximately coincides with the position of “Q” in the two-hole spectrum, if the same final subspaces are compared (for example, at $\omega \approx -14.5$ in $A_{2\text{-hole}}(\omega)$ for $n = 84/60 = 1.4$ compared to $\omega \approx -14.6$ in $A_{4\text{-hole}}(\omega)$ for $n = 86/60 \approx 1.43$). For $n \rightarrow 2$, the main peak evolves into the quadruplon excitation that has been analyzed in chapter 4.1.3.

The spectrum also uncovers the existence of a “quintuplon”, i.e., a final state composed of two neighbouring doublons plus an additional neighbouring hole. This is visible as the additional structure on the high-binding-energy side of the quadruplon in fig. 4.17(b) (labeled “QI”). As in the triplon case, we suspect that the quintuplon can be stabilized as a truly bound state with infinite lifetime when switching on a nearest-neighbour Coulomb interaction. For $V = 0$, however, it is not stable and should correspond to a hole-quadruplon continuum of final states.

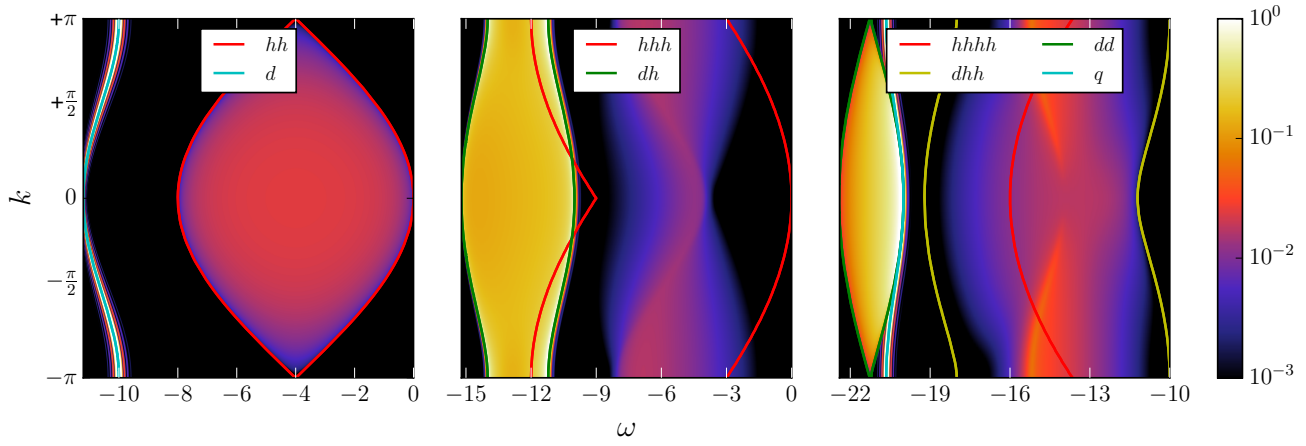


Figure 4.18.: Two- (left), three- (middle) and four-hole (right) spectral function for the full band with overlaid borders of the Bethe ansatz continua and dispersions as coloured lines. The same shorthand notations are used as in fig. 3.6.

4.2. Bethe Ansatz analysis of the multi-hole spectra

4.2.1. The full band for various spectroscopies

We have seen in chapter 1.1 that the Schrödinger eigenvalue problem of the Hubbard model, restricted to the subspace of two holes in the full valence band, is easily solvable and the eigenstates can be classified either as "scattering states" or as "bound states" (repulsively bound for $U > 0$, attractively for $U < 0$). The two-hole spectral function adds weights to them and in spectroscopic terms we call the former "band-like part" and the latter "(correlation) satellite". In the Bethe ansatz, the scattering states appear as a continuum of two electron holes. Although an electron hole is composed out of a holon and a spinon, the phase space for spinons vanishes for $n = 2$, so that the scattering states coincide with the 2-holon continuum (hh). The bound state of a doublon corresponds to the k - Λ -string of length 1 (for brevity, let us use the label d). This is shown in the left plot of fig. 4.18. We can also understand the higher spectroscopies for $n = 2$ in the same way:

The satellite of the three-hole spectrum (central plot in fig. 4.18) exactly coincides with the 1-string-1-hole continuum (dh), corroborating the fact that there is no repulsively bound triplon for $V = 0$ (see 4.1.3). The support of the band-like part lies within the 3-holon continuum (hhh), although now it does not coincide with it fully.

The satellite of the four-hole spectrum coincides with the 2-string continuum (dd), corresponding to independent doublons in the effective model 1.9 and a k - Λ -string of length 2, corresponding to the quadruplon bound state (q). The band-like part within the frequency range from $\omega \approx -18.3$ to $\omega \approx -11.2$ has its support within the 1-string-2-holon continuum (dhh) and almost completely coincides with it. The 4-hole continuum ($hhhh$) is very broad and also harbours some spectral weight at low energies (not shown in the plot).

4.2.2. The band-like part for $n < 2$

Fig. 4.19 shows a close-up of the band-like part of the two-hole spectral function for various fillings, previously shown in fig. 4.13(a) and 4.13(b). We can interpret these eigenstates as the decay products of the local doublon excitation created in the initial state.

The whole support of the band-like part is expected to fall within the 2-holon-2-spinon continuum

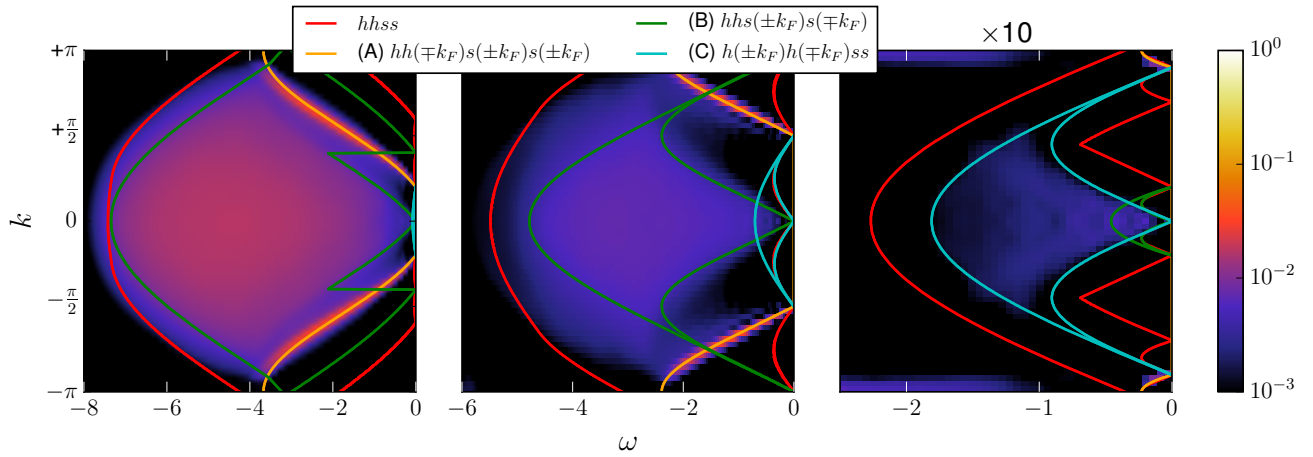


Figure 4.19.: Band-like parts of the two-hole spectral function for the fillings $n = 1.8$ (left), $n = 1.5$ (middle), $n = 1.1$ (right) with overlaid borders of the Bethe ansatz continua as coloured lines (see explanation in the text). The spectrum at $n = 1.1$ is multiplied by a factor of 10 to maintain a common scale.

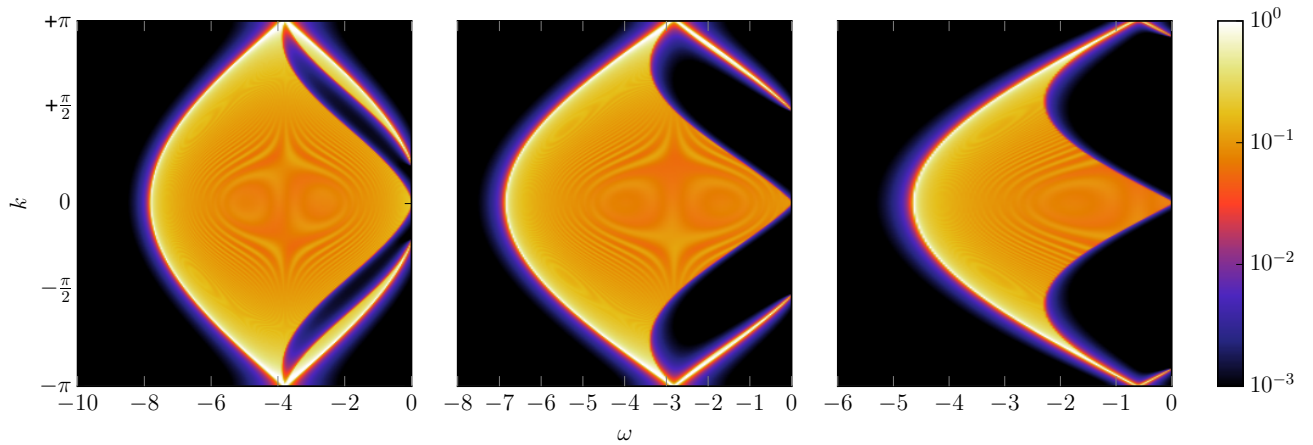


Figure 4.20.: Exact noninteracting two-hole spectral function for $L = 600$ as a sum of Lorentzians broadened with $\eta = 0.01$, for the fillings $n = 1.8$ (left), $n = 1.5$ (middle), $n = 1.1$ (right).

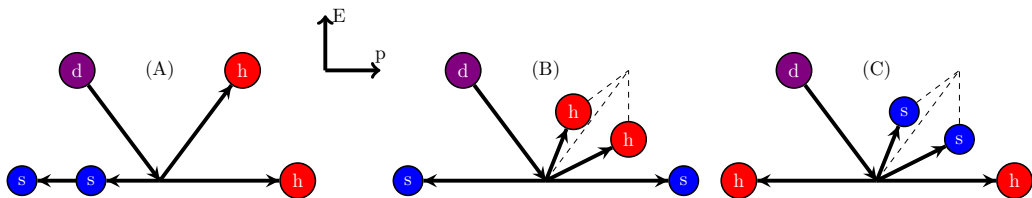


Figure 4.21.: Sketches of the decay processes (4.35) and (4.36) determined from the band-like part in fig. 4.19. The x-axis shows the magnitude and direction of the involved momenta, the y-axis the magnitude of the involved energies (such that a flat line corresponds to the Fermi energy $E = 0$). Purple circles: doublons, red circles: holons and blue circles: spinons.

(*hhs*) and this is indeed the case, though notably there are areas without any spectral weight at all, moreso toward half filling.

At $n = 1.8$, there is a notable ridge-like structure at which the spectral weight suddenly drops off (orange line). For $n = 1.8$, it starts at $k = \pm 0.2\pi \approx 0.628$ and $\omega = 0$, shifts towards the zone edge with decreasing filling, and can only be faintly seen at $n = 1.1$ as two speckles of spectral weight at $k = \pm 0.9\pi \approx 2.827$. This structure can be identified as the decay channel

$$(A) d \rightarrow h(k) h(\pm k_F^h) s(\mp k_F^s) s(\mp k_F^s), \quad (4.35)$$

namely a final state where a single holon is fixed to its Fermi momentum k_F^h , while both of the spinons are also fixed to their respective Fermi momenta k_F^s , but with signs opposite to k_F^h . Since it holds that $k_F^s = k_F^h/2$ for any filling, these three momenta cancel each other, so that one is effectively left with a single dispersing holon $h(k)$. This is sketched in fig. 4.21 (A).

The other two relevant decay channels are found to be

$$\begin{aligned} (B) d &\rightarrow h(k_1) h(k_2) s(\pm k_F^s) s(\mp k_F^s), \\ (C) d &\rightarrow h(\pm k_F^h) h(\mp k_F^h) s(k_1) s(k_2), \end{aligned} \quad (4.36)$$

namely, situations where either the two holons or the two spinons are pinned to their Fermi momenta with opposite sign (cyan and green boundary lines, respectively). In these cases, these fixed momenta also cancel each other, while the remaining two dispersive particles form a continuum. See also fig. 4.21 (B), (C) for a sketch.

Since spinons only start to become relevant towards half filling, the area of (C) is vanishingly small at $n = 1.8$, becomes noticeable at $n = 1.5$, but does not seem to coincide with a specific part of the spectrum. At $n = 1.1$, however, its shape coincides with the whole support of the band-like part apart from the speckles of (A) at $k = \pm 0.9\pi$ mentioned above. We can thus conclude that (C) becomes the dominant decay channel at half filling.

On the other hand, holon excitations disappear toward half filling, so that while (B) has a large support at $n = 1.8$ and $n = 1.5$, it becomes rather small at $n = 1.1$. One observes that its lower border reproduces the onset of the spectral weight close to the Γ -point rather well, while its upper border does not seem to delimit anything specific.

Finally, fig. 4.20 shows the noninteracting k -resolved two-hole spectral function for comparison. It shares several features with the interacting one due to the fact that some properties of the system remain unchanged with interaction: The spinon and holon dispersions (3.5) are still cosine-shaped as the free dispersion, though renormalized. Due to the Luttinger theorem, the Fermi momentum $k_F = n\pi/2$ remains unchanged with interaction and is incommensurate except for the cases $n = 0, 1, 2$. Thus the sum of the dispersions, when folded back into the first Brillouin zone, results in pockets without any spectral weight in both cases. Furthermore, we have the same soft modes at $k = 0$ and $k = \pm n\pi \pmod{\pi}$. However, the major differences are that the interacting bandwidth is much smaller in the interacting case, that the spectral weight is not as evenly distributed and can vanish in large regions, and that the overall spectral weight is diminished in favour of the satellite.

4.2.3. The satellites for $n < 2$

Let us finally turn to the high-binding-energy parts of the two-hole spectral function for open bands. Fig. 4.22 gives an overview. It turns out that the Bethe ansatz is only of very limited assistance in this case.

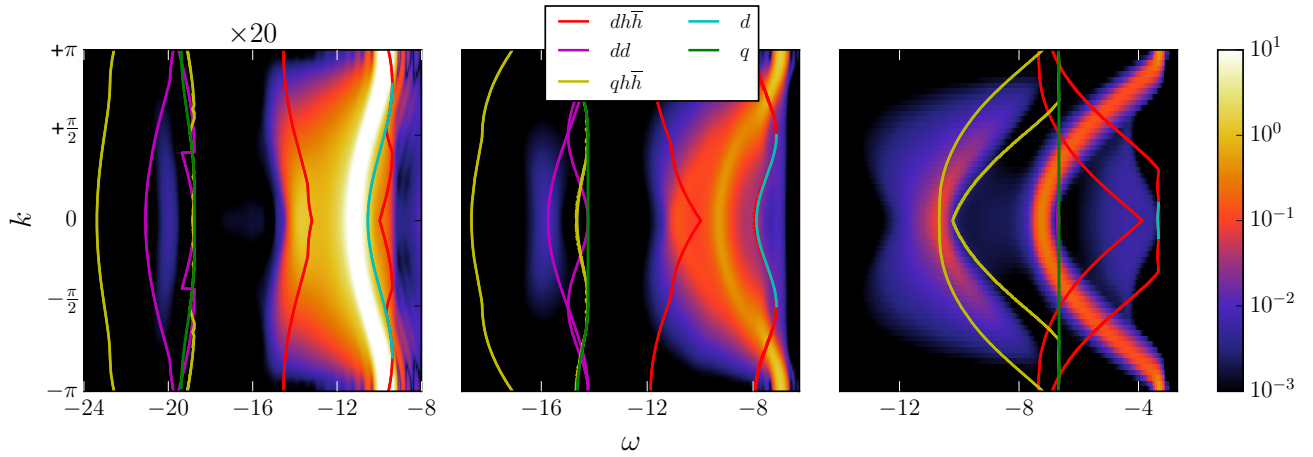


Figure 4.22.: High-binding-energy parts of the two-hole spectral function for the fillings $n = 1.8$ (left), $n = 1.5$ (middle), $n = 1.1$ (right) with overlaid borders of the Bethe ansatz continua and dispersions as coloured lines. The same shorthand notations are used as in fig. 3.6, with \bar{h} denoting an antiholon. The spectrum at $n = 1.8$ is multiplied by a factor of 20 to enhance the quadruplon contribution.

While the agreement of the satellite with the k - Λ -string for the full band (fig. 4.18) is perfect, the spectral weight in fig. 4.22 shifts more and more away from the string as the filling is decreased. This is consistent with the picture of a crossover from a perfect repulsively bound state at $n = 2$ to a freely dispersive particle at $n = 1$ (see the discussion in chapter 4.1.3). Interestingly, the string solution only fills out the whole Brillouin zone for $n = 2$ and becomes centred around the Γ -point as the filling is decreased, while the spectral weight is always distributed in the whole Brillouin zone for any filling and continuously connects to the η -eigenstate (see chapter 4.1.3)⁴ at the zone edge. The red boundaries in fig. 4.22 show the continuum of one k - Λ -string and a single holon-antiholon pair ($dh\bar{h}$). It reproduces the doublon spectral weight at $n = 1.8$ only roughly and completely fails to do so at $n = 1.1$. Note, however, that it is possible to excite any number of holon-antiholon pairs together with one string, with the support in the (ω, k) -plane growing with the amount of such pairs. Apart from that, some of the momenta could be pinned to certain values as in the case of the band-like part, which increases the amount of possibilities even more.

A similar situation is found in the case of the quadruplon: While the k - Λ -string of length 2 stretches over the whole Brillouin zone, the spectral weight is only centred around the Γ -point and the position shifts away from the Bethe ansatz prediction the further one goes away from the full band. In this case, however, the support more or less lies within the continuum of a k - Λ -string of length 2 with a holon-antiholon pair ($qh\bar{h}$), even at $n = 1.1$.

Overall, it would appear that the spectra at higher binding energies simply defy an easy interpretation in terms of Bethe ansatz states. The same problem actually already appears in the one-hole spectral function [Benthien 2005]. And in fact, there is actually no reason to expect that simple Bethe ansatz states should be excited, there is always the possibility that the spectral weight comes from a number of different eigenstates which share a given (ω, k) -region.

⁴Note that the η -eigenstate is not among the Bethe ansatz solutions per se and must be obtained by an additional construction, eqs. (3.179) and (3.180).

4.3. Two dimensions

4.3.1. Ladder geometry

A first step of extending one-dimensional physics into two dimensions is to consider a ladder, that is a finite number of chains (“legs”) stacked in the y -direction and coupled by tight-binding hopping:

$$H = -t \sum_{y=1}^{N_{\text{legs}}} \sum_{x\sigma} \left(c_{(x+1)y\sigma}^\dagger c_{xy\sigma} + c_{x(y+1)\sigma}^\dagger c_{xy\sigma} + \text{h.c.} \right) + U \sum_{y=1}^{N_{\text{legs}}} \sum_x n_{xy\uparrow} n_{xy\downarrow}, \quad (4.37)$$

where x and y independently enumerate the lattice sites in the corresponding axis directions.

While one-dimensional systems are generally Tomonaga-Luttinger liquids (TLL), exhibiting in particular the phenomenon of spin-charge separation, this picture has to be revised already for the two-leg ladder: If an electron is removed from the antiferromagnetic ground state and the resulting hole is allowed to propagate along a leg of the ladder, decaying into a spinon and a holon, it creates magnetically frustrated interactions with the second leg. This results in a “string potential” which increases linearly with the separation of the holon and spinon, creating a force that brings them back together. This situation is similar to the confinement of quarks in quantum chromodynamics. A very illustrative limit is the anisotropic t - J model on a two-leg ladder, where the nearest-neighbour exchange within a rung J_\perp is much larger than the exchange along the legs J_\parallel : $J_\perp \gg J_\parallel$. In this case, it is energetically favourable for two holes off half filling to remain on the same rung, while the other rungs form spin singlets. The bound pair of holes then propagates in the background of these singlets like a composite boson. The effective description of the model is thus a linear chain of repulsively interacting bosons. Furthermore, spin and charge switch their roles: Before, we had a tendency to an antiferromagnet with gapped charge excitations, while the above case has a tendency towards a charge density wave with gapped spin excitations, which is called *Luther-Emery liquid* (LEL). Finally, the system shows superconducting instabilities.

The isotropic case ($J_\perp = J_\parallel$ or $t_\perp = t_\parallel$), which we are dealing with here, and which is also relevant for the physics of cuprates, is most difficult to understand and it is believed that the TLL phase coexists with the LEL phase. See [Kagan \(2013\)](#) for a more detailed overview.

Collecting the x -dependence of the two-hole spectral function into one term,

$$A_{xy,x'y'}(\omega) := \langle 0 | c_{xy\downarrow}^\dagger c_{xy\uparrow}^\dagger \delta \left(\omega - E_0^{(N-2)} + H \right) c_{xy\uparrow} c_{xy\downarrow} | 0 \rangle e^{-ik_x(\mathbf{R}_x - \mathbf{R}'_x)}, \quad (4.38)$$

we can carry out the sum over $y = 1, 2$:

$$\begin{aligned} A_{2\text{-hole}}(\omega, k_x, k_y) &= \frac{1}{L_x L_y} \sum_{xyx'y'} A_{xy,x'y'}(\omega) e^{-ik_y(\mathbf{R}_y - \mathbf{R}'_y)} \\ &= \frac{1}{L_x L_y} \sum_{xx'} \left(A_{x1,x'1}(\omega) + A_{x2,x'2}(\omega) + A_{x1,x'2}(\omega) e^{ik_y} + A_{x2,x'1}(\omega) e^{-ik_y} \right). \end{aligned} \quad (4.39)$$

An convenient advantage of the two-leg ladder is that there is no difference between open and periodic boundary conditions in y -direction. Thus, there are two well-defined values of the lattice momentum $k_{y,n} = 2\pi n/L_y$, namely $k_y = 0$ and $k_y = \pi$ for $n = 0, 1$ respectively. With this, we obtain two spectra for each of the momentum values:

$$\begin{aligned}
A_{2\text{-hole}}(\omega, k_x, k_y = 0) &= \frac{1}{L_x} \sum_{xx'} (A_{x1,x'1}(\omega) + A_{x1,x'2}(\omega)), \\
A_{2\text{-hole}}(\omega, k_x, k_y = \pi) &= \frac{1}{L_x} \sum_{xx'} (A_{x1,x'1}(\omega) - A_{x1,x'2}(\omega)).
\end{aligned} \tag{4.40}$$

This is very reminiscent of bonding and antibonding orbitals of the hydrogen atom problem. For $U = 0$ and a tight-binding dispersion, the “bonding” part ($k_y = 0$) of the two-hole spectral function consists out of two football-shaped continua, each with a width of $8T$. The “antibonding” ($k_y = \pi$) part has just one football-shaped continuum centred around $\omega = -8T$ and thus gapped by $4T$ (see figs. 4.23(c) and 4.23(d)).

The density of states is readily computed for a ladder:

$$\begin{aligned}
\rho(\epsilon) &= \frac{1}{L_x L_y} \sum_{k_x k_y} \delta(\epsilon - 2T \cos k_x - 2T \cos k_y) \\
&= \frac{1}{2L_x} \sum_{k_x} (\delta(\epsilon - 2T \cos k_x - 2T) + \delta(\epsilon - 2T \cos k_x + 2T)).
\end{aligned} \tag{4.41}$$

We have thus two copies of the chain density of states shifted by $\pm 2T$, altogether giving a bandwidth of $W = 8T$. Staying faithful to the choice $U = 1.5W$, one should now set $U/T = 12$.

Figs. 4.23(a) and 4.23(b) show the two-hole spectral function of a 40×2 ladder calculated with DMRG, compared to the $U = 0$ case in figs. 4.23(c) and 4.23(d), both at a filling of $n = 1.8$. As expected, the main dichotomy of a band-like part and a satellite is preserved from the simple chain. One observes that while the width of the noninteracting band-like part for $k_y = 0$ is about 15.5, it is strongly reduced in the interacting case to about 10.5. The satellite is positioned at about U below its barycentre, namely at $\omega = -17 \sim -17.8$.

For $k_y = 0$, the band-like part shows a lot of substructure: We see an asymmetric shift of spectral weight towards the satellite, increased intensity at $k_x = \pm\pi$ and a small gap at $k_x = 0$, possibly corresponding to the touching pseudogap of the “footballs” in the $U = 0$ case. This hints at highly specific decay channels which might still be interpreted in terms of spinons and holons, albeit in a modified form. At $k_y = \pi$, however, the band-like part looks just the same as in the $U = 0$ case (except for the renormalization of the width), indicating no spin-charge separation at such a small y -extension. At $k_x = k_y = \pi$, the whole spectral weight is concentrated in the satellite, as we would expect it from general considerations of the η -eigenstate (see chapter 4.1.3). Consequently, the spectral weight at the cusps of the “football” at $k_y = \pi$ goes to zero.

Figs. 4.24(a) and 4.24(b) show a lower filling of $n = 1.5$. At $k_y = 0$, the band-like part loses all of its intensity at $k_x = \pm\pi$, indicating that the corresponding decay process is now absent. At $k_y = \pi$, slightly more spectral weight in the band-like part is now gained for $k_x = \pm\pi/2$.

Furthermore, the quadruplon now appears, separated by an energy of U from the doublon satellite. At $k_y = 0$, it is mostly dispersionless, with slightly more weight at the Γ -point. For $k_y = \pi$ we know that its weight must go to zero at the η -point $k_x = \pm\pi$, but it is already negligible for $|k_x| > \pm\pi/2$.

Thus, all the basic features of the spectral function, including the doublon and quadruplon peaks as well as the η -mode, survive when going from the chain to the ladder. We can thus expect them to survive in higher dimensions as well. The main change concerns the physics at the Fermi edge where the decay products of the doublon are now different and more difficult to analyse, since the Bethe ansatz cannot be employed anymore. Hence, this must remain a problem for the future.

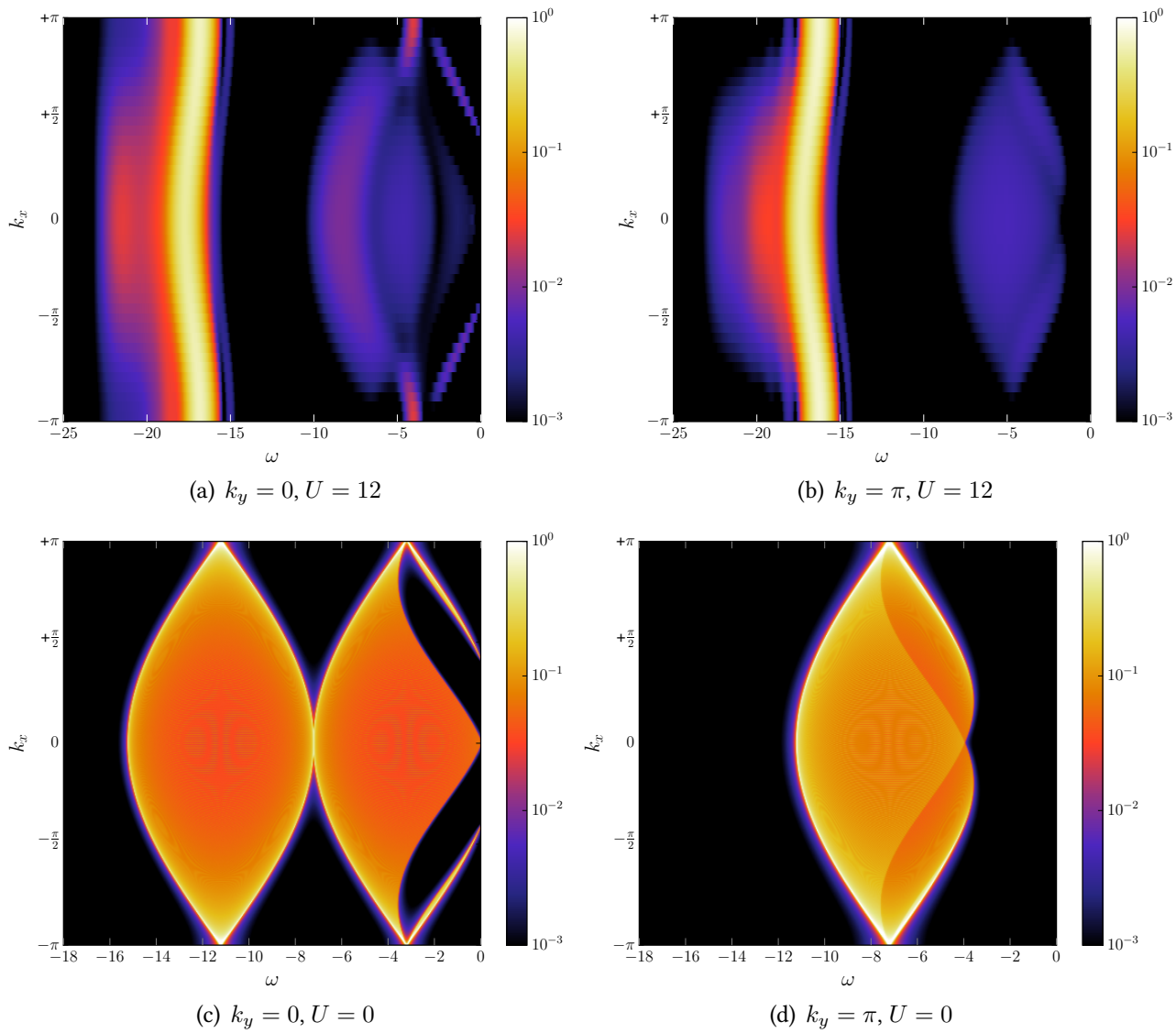


Figure 4.23.: Upper panels: Momentum-resolved two-hole spectral function for a 40×2 Hubbard ladder with $U = 12$ and $n = 1.8$, calculated with DMRG at an energy resolution of $\delta E = 0.5$, corresponding to $M = 327$ Chebyshev moments. Lower panels: The same calculated exactly for $U = 0$, $L = 600$ and periodic boundary conditions, with a Lorentzian broadening of $\eta = 0.01$.

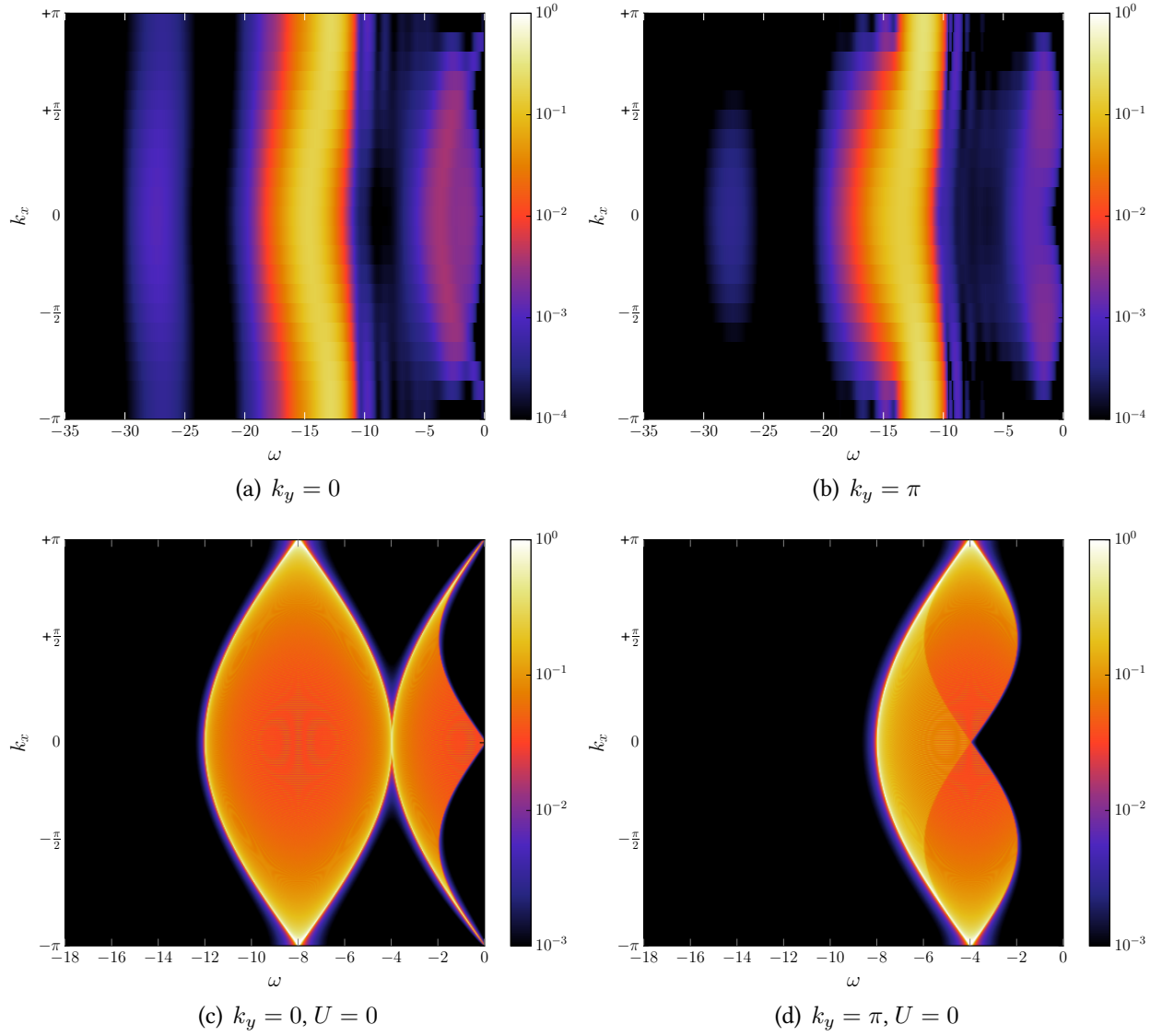


Figure 4.24.: Upper panels: The same as in figs. 4.23(a) and 4.23(b), but for a filling of $n = 1.5$ and a 20×2 ladder at a resolution of $\delta E = 1$, corresponding to $M = 175$ Chebyshev moments.

Lower panels: The same calculated exactly for $U = 0$, $L = 600$ and periodic boundary conditions, with a Lorentzian broadening of $\eta = 0.01$.

5. Dynamics

5.1. Doublon dynamics

5.1.1. Introduction

Apart from their appearance in Auger spectra, bound doublon states can also be directly observed in ultracold atom experiments. This is straightforward for the two-electron case with only one doublon: It can be trapped on a central site of the lattice and will expand into it once the trapping potential is switched off. It partly decays on a short time scale, while the surviving part propagates in a light-cone-like fashion. This can be nicely modelled using exact diagonalization and the emerging phenomenology has been investigated theoretically for both fermions [[Kajala, Massel, and Törmä 2011](#); [Hofmann and Potthoff 2012](#)] and bosons [[Boschi et al. 2014](#)].

When one proceeds to the many-body case, more setups are possible. One could just put many doublons into the centre of a lattice and let this conglomerate expand, which can be again experimentally realized with trapping potentials. Such setups have also been investigated theoretically for fermions [[Langer et al. 2012](#)] and bosons [[Vidmar et al. 2013](#); [Hauschild, Pollmann, and Heidrich-Meisner 2015](#)] using DMRG. The procedure could be termed “geometrical quench”, since it is equivalent to the preparation of lattice segments with different occupancy numbers in their respective ground states¹ and then joining them by switching on the hopping. While the simplest setup is to join a filled segment with an empty one, one can also join a filled segment (which is a product state) with an entangled many-body state [[Paula et al. 2017](#); [Ganahl et al. 2012](#)].

In a different approach, one can apply a creation or annihilation operator to the ground state, removing or shifting the particles suddenly, and then observe the real-time evolution of this perturbation. This has been investigated by removing a single boson at unit filling for the Bose-Hubbard model [[Andraschko and Sirker 2015](#)] and, for fermions, by creating a nearest-neighbour particle-hole excitation in the half-filled ground state [[Al-Hassanieh et al. 2008](#)].

Yet another setup consists in preparing a Gaussian wave packet, where a compromise is struck between localization in real and momentum space. This idea has been pursued in particular in order to study spin-charge separation in one spatial dimension within the Hubbard and t - J models [[Ulbricht and Schmitteckert 2009](#); [Al-Hassanieh et al. 2013](#); [Moreno, Muramatsu, and Carmelo 2013](#)].

In this work, the sudden annihilation approach is chosen. We are interested in the dynamics following a sudden doublon creation at a site i_0 using DMRG. One thus starts from the normalized state

$$|\Psi_{i_0}\rangle = \frac{1}{\sqrt{\mathcal{N}}} c_{i_0\uparrow} c_{i_0\downarrow} |0, N\rangle. \quad (5.1)$$

Compared to a geometrical quench, this has the disadvantage of having somewhat less control over the initial occupancies, since the doublon excitation will be slightly spread over several lattice sites due to the entanglement in the ground state. The advantage is, however, that the initial state is the

¹This can be done for spin systems as well, in this case with different magnetizations. In particular, one can create a domain wall.

same as in eq. (4.2) and we are dealing with information extracted from the same wave function as in the two-hole spectral function (cf. the Fourier transform representation (1.12)).

This information is extracted by way of calculating time-dependent expectation values $\langle O_j \rangle(t) = \langle \Psi(t) | O_j | \Psi(t) \rangle$ of suitable local observables O_j . Obvious choices for O_j include the charge density $n_j = n_{j\uparrow} + n_{j\downarrow}$ or observables resulting from the decomposition $1 = n_j^d + n_j^h + n_j^s$, which allows us to specifically look at

- doubly occupied sites:

$$n_j^d = n_{j\uparrow}n_{j\downarrow}, \quad (5.2)$$

- empty sites:

$$n_j^h = n_j^d - n_j + 1, \quad (5.3)$$

- singly occupied sites:

$$n_j^s = 1 - n_j^d - n_j^h = n_j - 2n_{j\uparrow}n_{j\downarrow}. \quad (5.4)$$

For the given problem, n_j^h is most useful, revealing both the decay and the propagation of the doublon excitation.

5.1.2. Decay

Let us first concentrate on doublon decay. Rather than analysing the contributing eigenstates, as was done in chapter 4.2.3, the object of interest is now the *total* hole density as a function of time:

$$n_{\text{tot}}^h(t) = \sum_j \langle n_j^h \rangle(t). \quad (5.5)$$

Going away from the limiting case of the full band, one expects two effects to compete: On the one hand, the finite hole density provides phase space for the doublons to decay, as the bound state is now positioned within many continua of various particles (for example, arbitrarily many holon-antiholon excitations). On the other hand, movement along the background of singly occupied sites does not cost an energy U and should rather stabilize the doublon. It is therefore interesting to see how these two effects establish themselves and which one wins out.

Fig. 5.1(a) shows $n_{\text{tot}}^h(t)$ (normalized to $n_{\text{tot}}^h(0)$) for different fillings. Its shape is a typical sharp dip for very short times and a subsequent “relaxation” to an intermediate value with weak superimposed oscillations. The many-body case with $n < 2$ looks very similar to the overall behaviour previously seen for the two-particle case (here corresponding to $n = 2$) [Hofmann and Potthoff 2012]. The position of the first minimum t_{min} can be interpreted as the characteristic “decay time” and results from the uncertainty principle. The drop to the emerging constant value indicates the decayed fraction of doublons r_{decay} .

Similarly to what has been observed in the two-particle case, the decay time t_{min} is rather short, below one inverse hopping at $U = 6$, and only slightly increases with decreasing filling. Its U -dependence is also instructive and is shown in fig. 5.1(b). As a simple estimate, one would expect that a transition to a state separated by an energy of ΔE should be possible within a time $t \sim 1/\Delta E$, even if it is prohibited by energy conservation, thus in our case $t_{\text{min}} \sim 1/U$.

However, one can do it more rigorously and employ an exactly solvable two-site Hubbard model, since on the very short decay time scale, only the neighbouring site can be explored by the doublon. Furthermore, the initial state of a two-site model is actually locally the same as in the $n = 2$ case, consisting out of an empty site with an adjacent doubly occupied one in the former case, and a

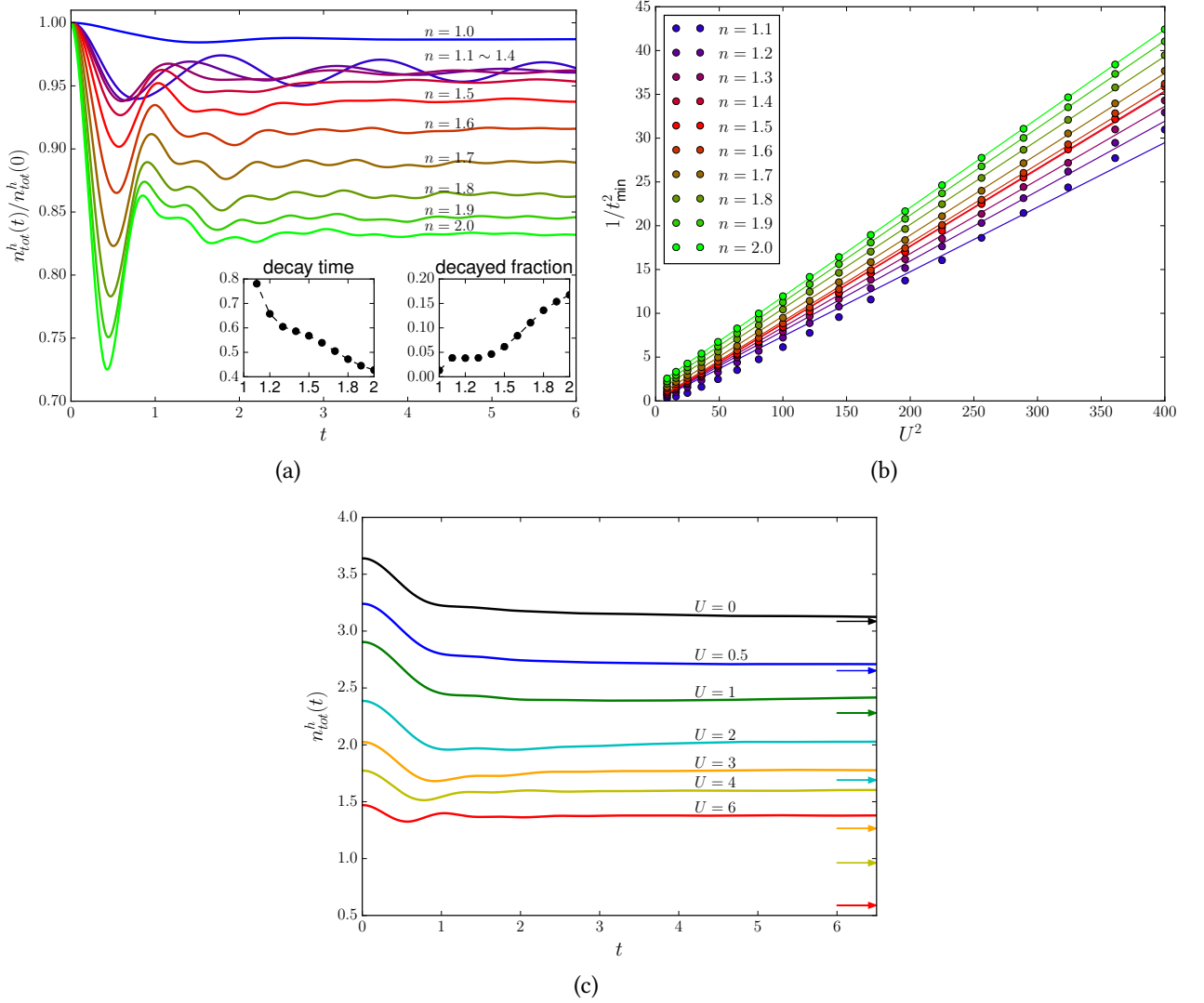


Figure 5.1.: (a) Total hole density $n_{\text{tot}}^h(t)$, normalized to $n_{\text{tot}}^h(0)$, for various fillings as indicated. Time-dependent DMRG calculation at $U = 6$ for $L = 40$. Left inset: characteristic decay time t_{min} , defined as the location of the first minimum, as a function of filling. Right inset: decayed fraction of doublons, defined as the time average $1 - \overline{n_{\text{tot}}^h(t)/n_{\text{tot}}^h(0)}$ between $t = 4$ and the maximal propagation time, as a function of filling. (b) Inverse square of the decay time t_{min} , where $n_{\text{tot}}^h(t)$ exhibits its first pronounced minimum, as a function of U^2 for different fillings. Lines: linear fits of the DMRG data based on the result of the two-site model (5.6), see text. (c) Comparison of the unnormalized hole density with the expected relaxed ground-state expectation value (indicated by arrows of the same colour) for various values of U at a filling of $n = 1.5$.

whole doubly occupied lattice in the latter case. The two-site calculation predicts a collapse-and-revival frequency $\omega_0 = \sqrt{U^2 + 16T^2}$ [Kajala, Massel, and Törmä 2011]. Indeed, the data for the first minimum at $n = 2$, which is expected to be at $\omega_0 t_{\min} = \pi$ for a cosine, are nicely fitted by

$$1/t_{\min}^2 \approx (U^2 + 16T^2) / \pi^2. \quad (5.6)$$

Obviously, the simpler proportionality $t_{\min} \sim 1/U$ emerges for $U \gg T$.

For $n < 2$ down to $n \approx 1.4$, we find that there is still a U^2 dependence of $1/t_{\min}^2$ (shown by the linear fits in fig. 5.1(b)), reflecting the fact that the doublon decay is more and more suppressed with increasing U . However, discrepancies with respect to the fit grow in the range $1 < n \lesssim 1.4$.

On the intermediate time scale up to the maximum propagation time the main effect of the decreasing filling seems to consist in the decrease of the decayed fraction of doublons r_{decay} , see the left inset in fig. 5.1(a). This indicates that the doublon is actually stabilized by the presence of more and more singly occupied sites. This argument also consistently explains the dramatic overall loss of spectral weight in the band-like part of the two-hole spectral function with decreasing n (see fig. 4.3, for example).

At half filling the doublon is most stable. At the same time, the *creation* of a doublon is most unlikely in this case, since the double occupancy is strongly reduced. In the two-hole spectral function this results in the overall decrease of total spectral weight with filling (including the doublon satellite). Note that this effect cannot be seen in fig. 5.1(a) since it is compensated by the normalization constant $n_{\text{tot}}^h(0)$, which becomes small at (and close to) $n = 1$.

After the initial decay on the time scale t_{\min} , one observes oscillations of $n_{\text{tot}}^h(t)$ in fig. 5.1(a) resulting from repeated decay-and-recombination processes. The corresponding frequency is of the order of U . These oscillations die out and the decay process is essentially completed within a few inverse hoppings. However, the filling regime $1 < n \lesssim 1.4$ is again somewhat exceptional. Here, the decayed fraction is seen to reach a plateau at a value of about 0.05 (see right inset). Furthermore, the dip of $n_{\text{tot}}^h(t)$ at t_{\min} is so shallow that the “decay time” defined via its position does not seem to be very meaningful anymore. Instead, $n_{\text{tot}}^h(t)$ shows several oscillations of comparable magnitude and the decay process does yet not seem to be completed.

One can summarize: The (more or less) constant value of $n_{\text{tot}}^h(t)$ on the intermediate time scale is the result of the kinematic constraints becoming active, while an initial decay is possible on the short time scale $t_{\min} \sim 1/U$ via low-order scattering processes. Note that the “relaxed” values of $n_{\text{tot}}^h(t)$ that can be read off as time averages from the DMRG data for the different fillings in fig. 5.1(a) do not coincide with the respective ground-state expectation values $\langle 0, N - 2 | n_{\text{tot}}^h | 0, N - 2 \rangle$ in the subspace with $N - 2$ electrons. The latter is expected to be reached for $t \rightarrow \infty$, probably on a time scale exponentially long in U , on which higher-order scattering processes are activated. One would also expect an increase in temperature, which should be, however, negligible in our case of a local excitation.

One can also check that the “relaxed” value of n_{tot}^h more and more approaches the ground-state expectation value $\langle 0, N - 2 | n_{\text{tot}}^h | 0, N - 2 \rangle$ when decreasing U . This is shown in fig. 5.1(c) for $n = 1.5$. It is noticeable that even small values of U have the consequence that the relaxed value is not completely reached within the accessible time scale, indeed suggesting a behaviour which is exponential in U . The hole density actually seems to go *away* from the relaxed value for some U , which is probably the result of an overlaid long-time oscillation, possibly with a frequency of the order of J .

5.1.3. Propagation

Let us now take a look at the spatiotemporal evolution of the doublon excitation itself. The result of a corresponding time-dependent DMRG calculation is shown in fig. 5.2(a) for a high filling of $n = 1.8$ and in fig. 5.2(b) for $n = 1.2$.

In order to analyse the emerging light-cone dynamics, two models can be employed: a ballistic and a diffusive one. Broadly speaking, the former is a signature of a freely propagating excitation as in a noninteracting system, while scattering induced by interactions is essential for the latter. Although integrable one-dimensional systems with many conserved quantities, such as the Hubbard chain, are expected to behave ballistically as noninteracting ones, ballistic and diffusive transport have also been shown to coexist [Sirker, Pereira, and Affleck 2009; Andraschko and Sirker 2015]. The following presentation is based preceding work [Dunlap and Kenkre 1986; Langer et al. 2009; Vidmar et al. 2013; Andraschko and Sirker 2015] in establishing the two models.

Given some density distribution $\langle \rho_j \rangle (t)$ localized at time t around the centre of excitation i_0 , one can introduce a time-dependent radius $R(t)$ via

$$R^2(t) [\langle \rho \rangle] = \sum_j (j - i_0)^2 \langle \rho_j \rangle (t). \quad (5.7)$$

With this, the ballistic and diffusive case can be distinguished.

Let us first consider the former and compute the radius for noninteracting particles with a dispersion $\epsilon(k) = \pm v \cos(k)$ on an infinite lattice. The time-dependent density is given by:

$$\langle n_j(t) \rangle = \langle 0 | c_{i_0} e^{iHt} c_j^\dagger c_j e^{-iHt} c_{i_0}^\dagger | 0 \rangle. \quad (5.8)$$

Using the Fourier transform $c_j = 1/\sqrt{L} \sum_k e^{-ikR_j} c_k$ and time evolution of the operators in reciprocal space, $c_k(t) = e^{-i\epsilon(k)t} c_k(0)$, one obtains:

$$\begin{aligned} \langle n_j(t) \rangle &= \frac{1}{L^2} \sum_{kk'pp'} \langle 0 | c_p c_k^\dagger c_{k'} c_{p'}^\dagger | 0 \rangle e^{iR_{i_0}(p'-p)} e^{-iR_j(k'-k)} e^{-i(\epsilon(k')-\epsilon(k))t} \\ &= \frac{1}{L^2} \sum_{kk'} e^{i(k-k')(R_j-R_{i_0})} e^{-i(\epsilon(k')-\epsilon(k))t} \\ &= \left(\frac{1}{L} \sum_k e^{i[k(R_j-R_{i_0})+\epsilon(k)t]} \right) \left(\frac{1}{L} \sum_k e^{i[k(R_{i_0}-R_j)-\epsilon(k)t]} \right). \end{aligned} \quad (5.9)$$

Plugging in the dispersion $\epsilon(k) = v \cos(k)$ and converting the k -sums into integrals $1/L \sum_k \rightarrow 1/2\pi \int_{-\pi}^{\pi} dk$, we can use the definition of the n -th Bessel function of the first kind

$$i^n \mathcal{J}_n(x) = \frac{1}{2\pi} \int_{-\pi}^{\pi} dk e^{ix \cos(k)} e^{ink} \quad (5.10)$$

to obtain:

$$\begin{aligned} \langle n_j(t) \rangle &= \mathcal{J}_{j-i_0}(vt) \mathcal{J}_{i_0-j}(-vt) \\ &= \mathcal{J}_{j-i_0}^2(vt). \end{aligned} \quad (5.11)$$

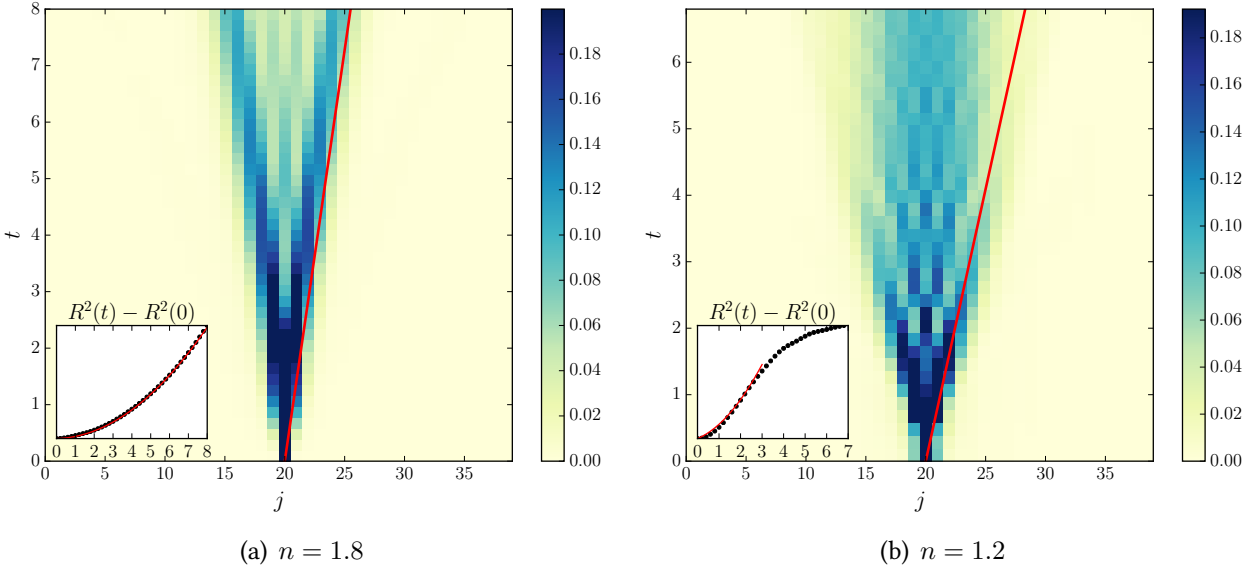


Figure 5.2.: (a) Space-time plot of $\langle \tilde{n}_j^h \rangle(t)$ $n = 1.8$. DMRG calculation at $U = 6$ for $L = 40$. The inset shows $R^2(t)$ (after subtracting the initial value) with the fit according to eq. (5.16). The red line in the main plot indicates vt with the velocity extracted from the fit. (b) Space-time plot of $\langle \tilde{n}_j^h \rangle(t)$ for $n = 1.2$ and other parameters as in fig. 5.2(a). The fit is limited to $t = 3$.

Note that the sign of the velocity v does not matter and the density is normalized to unity: $\sum_j \langle n_j(t) \rangle = 1$. Plugging (5.11) back into (5.7) leads to a known identity for Bessel functions, which results in:

$$R^2(t) [\langle n \rangle] = \frac{1}{2} v^2 t^2. \quad (5.12)$$

In our case, we consider the doublon density $\rho_j(t) = \langle n_j^h \rangle(t)$, and the above relation should be fulfilled for large U in the two limiting cases: On the one side we have $n = 2$, where the effective doublon model (1.9) describes a free particle with $\epsilon(k) = J \cos(k)$. On the other side, we have $n = 1$, where the effective model is the t - J model [Chao, Spałek, and Oleś 1978] with negligible J (i.e., the t model), so that an empty site $\tilde{}$ corresponds to a hole in the singly-occupied antiferromagnetic background and similarly moves like a free particle with $\epsilon(k) = -2T \cos(k)$.

Let us now turn to the diffusive model [Langer et al. 2009; Vidmar et al. 2013; Andraschko and Sirker 2015]. A solution of the continuous diffusion equation

$$\frac{\partial \rho}{\partial t} - \mathcal{D} \frac{\partial^2 \rho}{\partial x^2} = 0, \quad (5.13)$$

where \mathcal{D} is the diffusion constant, with the boundary condition $\rho(x, t=0) = \delta(x)$ and with normalization $\int_{-\infty}^{\infty} dx \rho(x, t) = 1$ is given by:

$$\rho(x, t) = \frac{1}{\sqrt{2\pi\mathcal{D}t}} e^{-\frac{x^2}{4\mathcal{D}t}}. \quad (5.14)$$

In this case, $R^2(t)$ is just the second moment of the Gaussian distribution (5.14), given by the square of the standard deviation

$$R^2(t) [\rho] = 2\mathcal{D}t, \quad (5.15)$$

so that the spread is slower and scales with t rather than with t^2 .

Thus, the following composite ansatz can be made for the doublon problem:

$$R^2(t) [\langle n^h \rangle] = \frac{1}{2}v^2t^2 + 2\mathcal{D}t, \quad (5.16)$$

and the calculated $R^2(t) [\langle n^h \rangle]$ can be fitted to obtain the corresponding velocity v and diffusion constant \mathcal{D} . To neutralize Friedel oscillations originating from open boundary conditions in the DMRG calculation, the ground-state expectation value is subtracted, so that

$$\langle \tilde{n}_j^h \rangle(t) \equiv \langle \Psi(t) | n_j^h | \Psi(t) \rangle - \langle N, 0 | n_j^h | N, 0 \rangle \quad (5.17)$$

will be the quantity to work with. The fits are shown in the insets of figs. 5.2(a) and 5.2(b), and the corresponding wavefronts $j(t) = i_0 + vt$ with v determined by the fit, are indicated by red lines in the space-time plots. It turns out that at $n = 1.2$, the fit only gives meaningful values up to a time of $t \sim 3$; thereafter the dynamics changes noticeably. The fit is therefore limited to $t \leq 3$ in this case and it will be discussed further below.

Fig. 5.3 displays the filling dependence of the velocity v (red circles) and of the diffusion constant \mathcal{D} (yellow circles) as obtained from the fit (5.16). The regime where eq. (5.16) is only valid up to $t \sim 3$ is found to lie between $n = 1$ and $n \sim 1.4$, and the corresponding restricted fit results for v and \mathcal{D} are displayed as white circles.

For an interpretation of the obtained velocities, a comparison with the predictions of the Bethe ansatz is once more required. To this end the time-dependent expectation value of n_j^h can be first brought into a form similar to the Lehmann representation of a Green's function [Ganahl et al. 2012]. Introducing the momentum operator P to shift O_j to the point of reference, $O_j = e^{-iP(R_j - R_{i_0})} O_{i_0} e^{+iP(R_j - R_{i_0})}$, and writing the initial state as a linear combination of Bethe ansatz states, which are eigenstates of both the momentum operator $\exp(iPx) |k_n\rangle = \exp(ik_n x) |k_n\rangle$ and the Hamiltonian $H |k_n\rangle = E_n(k) |k_n\rangle$, one obtains:

$$\begin{aligned} \langle n_j^h \rangle(t) &= \frac{1}{\mathcal{N}} \sum_{p_m k_n} \langle 0 | d_{i_0}^\dagger | p_m \rangle \langle k_n | d_{i_0} | 0 \rangle \times \\ &\quad \times \langle p_m | e^{ipR_{i_0}} e^{iHt} e^{-iP(R_j - R_{i_0})} O_{i_0} e^{+iP(R_j - R_{i_0})} e^{-iHt} e^{-ikR_{i_0}} | k_n \rangle \\ &= \frac{1}{\mathcal{N}} \sum_{p_m k_n} \langle 0 | d_{i_0}^\dagger | p_m \rangle \langle p_m | O_{i_0} | k_n \rangle \langle k_n | d_{i_0} | 0 \rangle e^{i\phi_{mn}(p,k)}, \end{aligned} \quad (5.18)$$

where $\phi_{mn}(p, k)$ is a plane-wave-like phase:

$$\phi_{mn}(p, k) = (k - p)(R_j - R_{i_0}) - (E_n(k) - E_m(p))t. \quad (5.19)$$

A stationary phase requires $\partial\phi_{mn}(p, k)/\partial k = 0$. This implies that the wave with wave vector k travels the distance $|R_j - R_{i_0}| = \frac{\partial E_n(k)}{\partial k} t$ within the time t . Taking the maximum with respect to k^2 , the wavefront propagates according to

$$R_j^{\max} - R_{i_0} = \max_k \frac{\partial E_n(k)}{\partial k} t = v_{n,\max} t. \quad (5.20)$$

²The same expression results when taking the derivative with respect to p , of course.

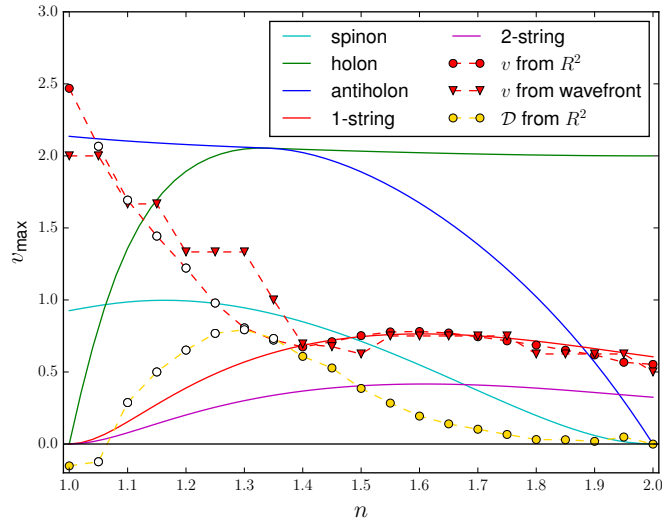


Figure 5.3.: *Symbols*: velocity v of the holon wavefront extracted from the fit of $R^2(t)$ via eq. (5.16) (red circles) and directly from the DMRG data (red triangles). Yellow circles show the diffusion constant \mathcal{D} from the same fit. White circles indicate where the fitting procedure for v and \mathcal{D} was restricted to times $t \leq 3$ (see text). *Lines*: maximal velocities obtained via eq. (5.20) from different Bethe ansatz eigenstates as functions of the filling.

Apparently, this estimate only yields the ballistic component, while a diffusive component should arise from the dephasing within the linear combination of eigenstates. This means that if velocities are to be compared with $R(t)$ from DMRG data, a potentially appearing diffusive component has to be filtered out according to eq. (5.16). Hence, the procedure is to calculate the maximal velocity $v_{n,\max}$ from the Bethe ansatz and identify it with the velocity v obtained from eq. (5.16), expecting a match for a suitable excitation n .

Fig. 5.3 shows $v_{n,\max}$ from various Bethe ansatz excitations displayed as solid lines. From $n = 2$ down to $n \approx 1.4$, one finds an almost perfect matching of the velocity of the wavefront with the k - Λ string (of length 1). In this range, the doublon propagates nearly ballistically, and it appears that the effective doublon Hamiltonian eq. (1.9) is still approximately valid, the main effect of its interaction term just being a renormalization of the doublon hopping amplitude. With decreasing filling, however, the presence of more and more singly occupied sites progressively invalidates the effective model, so that the scattering of doublons from single occupancies becomes an interaction process with increasing relevance. This is reflected in the increase of the diffusion constant \mathcal{D} .

As already mentioned, while the additional scattering at intermediate fillings might be expected to contribute to a stronger doublon decay and to hinder doublon propagation, singly occupied sites can also “accelerate” a doublon by providing a background on which the propagation does not require a virtual process costing an energy of the order of U . Indeed, the analysis suggests that scattering at first merely adds a diffusive component to the dynamics, while the ballistic part continues to propagate with the velocity of the bound state. It starts to increase and deviate from the velocity of the k - Λ string below $n \sim 1.4$ (see Fig. 5.3).

As mentioned above, we expect a crossover between *two* ballistic regimes: a bound state at $n = 2$ (with $v = J$) and a free particle at $n = 1$ (with $v = 2T$), so that the actual doublon velocity should interpolate between the two cases, requiring an “acceleration” toward half filling. This effect is obviously not peculiar to one-dimensional systems and has also been observed using nonequilibrium dynamical mean-field theory [Eckstein and Werner 2014].

However, for times larger than $t \sim 3$ in the filling range $1 < n \lesssim 1.4$, the mixed ballistic/diffusive model breaks down. Evidently, the many-body character of the problem becomes so severe as to

disallow an interpretation of the excitation in terms of a single spreading particle. The initial wavefront dies out and the dynamics becomes much slower (see fig. 5.2(b)), so that the exact scaling of $R^2(t)$ with t is difficult to read off on the accessible time scale (see the inset of fig. 5.2(b)). A possible explanation could be that quadruplons (k - Λ strings of length 2) begin to contribute significantly to the final states. This is evidenced by the two-hole spectral function, where the quadruplon peak becomes visible below a filling of $n \approx 1.5$ (see chapter 4.1.3). In this filling range, the velocity of the quadruplons is very low (see the “2-string” line in fig. 5.3), so that they may stay behind as a very slowly expanding core after the doublons have moved away or decayed. The total double occupancy (Fig. 5.1(a)) does not discriminate between empty doublonic and quadruplonic sites, so that this separation can only be seen in the spatially resolved plot.

Note that for $n = 1$, the fit of $R^2(t)$ yields a too large velocity of $v \approx 2.5T$ and \mathcal{D} becomes negative (see fig. 5.3). This is due to the fact that the hole density in the initial state after the application of d_i is spread out across several lattice sites, so that the boundary condition of a strictly localized hole, needed to derive eq. (5.14), is no longer perfectly fulfilled. Alternatively, one can extract the wavefront directly from the data by looking for the point when $|\langle \tilde{n}_j^h \rangle(t)| > \epsilon$, where the cutoff is set at $\epsilon = 0.05$. The respective results for v are displayed in fig. 5.3 by red triangles and indeed yield a velocity close to the expected value $2T$ at half filling. Similarly, without this artefact, we would expect the diffusion constant to go to zero at $n = 1$.

5.1.4. Summary

Let us now summarize what can be learned from the real-time doublon dynamics. There are two limits which can be understood in terms of the propagation and partial decay of a single particle: For $n = 2$, the initial doublon excitation is a linear combination of a bound state, which propagates with the velocity $v = J$; and scattering states with two independent electrons. For $n = 1$, it consists out of two holes on an antiferromagnetic background, moving with the Fermi velocity $v = 2T$ upon propagation. For intermediate values of n , two competing effects could be expected beforehand: On the one hand, an opening up of decay channels and increased scattering due to singly occupied sites, on the other hand a stabilization in the form of a background where doublon propagation does not require a virtual process.

It turns out that there are two regimes as a function of the filling: Above $n = 1.4$ (for the given choice of $U = 6$), the dichotomy between a bound state and scattering states is kept. However, both now have to be understood in terms of Bethe ansatz eigenstates: The bound state propagates with the velocity of a k - Λ string, while the scattering states involve two spinons and two holons (see chapter 4.2.3). The additional scattering of doublons only leads to an additional diffusive component \mathcal{D} , but the maximal velocity is not lowered, so that a ballistic component remains and the dynamics is therefore mixed ballistic/diffusive. Furthermore, the decayed fraction of doublons actually decreases, indicating that the stabilization effect of singly occupied sites wins out.

The regime below $n = 1.4$ is more complicated to understand. It is marked by an increased deviation of the decay time from the relation $1/t_{\min}^2 \sim U^2$, a qualitatively different behaviour of n_{tot}^h involving long-time oscillations rather than a dip and a plateau. The maximal velocity now deviates from the velocity of the k - Λ string, since the doublon becomes increasingly unbound and we have a crossover to the $n = 1$ case where it is a free particle. At the same time, the mixed ballistic/diffusive model only remains valid for short times $t \lesssim 3$, after which it breaks down and $R(t)$ shows a qualitatively different dependence. This might be connected with slow quadruplons which are seen in the two-hole spectrum in this filling range. Note that the initial conditions of both the ballistic and the diffusive model involve a single localized particle. However, it would seem that the problem now attains a many-body character which is impossible to understand in such a simple picture.

5.2. Spin dynamics

5.2.1. Introduction

This chapter presents the results of the work on spin dynamics using DMRG and compared to other methods. The common link to doublon dynamics has been outlined in chapter 1.4. Since spin dynamics has not been the main focus of this work, no in-depth description will be attempted here and just the two relevant publications are presented instead.

If the magnetic energy of an impurity spin coupled to a substrate exceeds the bandwidth of the substrate, the spin cannot relax by getting rid of this energy and remains stationary at an intermediate value. This is basically the same mechanism which stabilizes doublons on an intermediate time scale, where the excess energy is given by U . Compare in particular fig. 2 of the following paper, displaying the components of the spin as a function of time, with fig. 5.1(a) displaying the double occupancy in the latter case.

In the second work, the spin quantum number S of the impurity spin is increased in order to get closer to the classical limit $S \rightarrow \infty$. However, if no rescaling of the spin is done, this also increases the magnetic energy BS and a bound state emerges at the impurity site. It is only weakly coupled to the rest of the chain due to the separation in energy, so that the dynamics of the impurity spin can be described by an effective two-spin model.

Relaxation of a Classical Spin Coupled to a Strongly Correlated Electron System

Mohammad Sayad, Roman Rausch, and Michael Potthoff

I. Institute for Theoretical Physics, University of Hamburg, Jungiusstraße 9, D-20355 Hamburg, Germany

(Received 23 February 2016; revised manuscript received 15 August 2016; published 13 September 2016)

A classical spin which is antiferromagnetically coupled to a system of strongly correlated conduction electrons is shown to exhibit unconventional real-time dynamics which cannot be described by Gilbert damping. Depending on the strength of the local Coulomb interaction U , the two main electronic dissipation channels, namely transport of excitations via correlated hopping and via excitations of correlation-induced magnetic moments, become active on largely different time scales. We demonstrate that correlations can lead to a strongly suppressed relaxation which so far has been observed in purely electronic systems only and which is governed here by proximity to the divergent magnetic time scale in the infinite- U limit.

DOI: 10.1103/PhysRevLett.117.127201

Motivation.—A classical spin in an external magnetic field shows a precessional motion but when exchange coupled to a conduction-electron system the spin additionally relaxes and finally aligns to the field direction. This is successfully described on a phenomenological level by the Landau-Lifschitz-Gilbert (LLG) equation [1] and extensions of this concept [2,3]. The Gilbert damping constant α is often taken as a phenomenological parameter but can also be computed *ab initio* for real materials [4–6] within a framework of effectively independent electrons using band theory [7] and then serves as an important input for atomistic spin-dynamics calculations [8].

Electron correlations are expected to have an important effect on the spin dynamics. This has been demonstrated in a few pioneering studies [9–11]—within different models and using various approximations—but only indirectly by computing the effect of the Coulomb interaction on the Gilbert damping. One hallmark of strong correlations, however, is the emergence and the separation of energy (and time) scales—with the correlation-induced Mott insulator [12] as a paradigmatic example.

With the present study we address correlation effects beyond an LLG-type approach and keep the full temporal memory effect. It is demonstrated that correlation-induced time-scale separation has profound and qualitatively new consequences for the spin dynamics. These are important, e.g., for the microscopic understanding of the emerging relaxation time scales in modern nanospintronics devices involving various transition metals and compounds [13–15].

Concretely, we consider a generic model with a classical spin S that is antiferromagnetically exchange coupled ($J > 0$) to a Hubbard system and study the spin dynamics as a function of the Hubbard U . To tackle this quantum-classical hybrid problem, we develop a novel combination of linear-response theory [6,16,17] for the spin dynamics with time-dependent density-matrix renormalization group (t-DMRG) [18–20] for the correlated electron system.

For technical reasons we consider a chain geometry but concentrate on generic effects which are not bound to the one-dimensionality of the model.

In the metallic phase at quarter filling, a complex phenomenology is found where two different channels for energy and spin dissipation, namely dissipation via correlated hopping and via excitations of local magnetic moments, become active on characteristic time scales, depending on U . While magnetic excitations give the by far dominating contribution to the Gilbert damping in the strong-coupling limit, they contribute to the spin dynamics to a much lesser extent and on later and later time scales when U is increased.

It is demonstrated that electron correlations can have extreme consequences: At half-filling and strong U , the spin relaxation is incomplete on intermediate time scales. This represents a novel effect in a quantum-classical hybrid model which is reminiscent of prethermalization [21–24] or metastability of excitations due to the lack of phase space for decay [25–28], i.e., physics which so far has been observed in purely electronic quantum systems only.

Gilbert damping.—We consider the Hubbard model for N electrons on an open chain of length L as a prototypical model of correlated conduction electrons:

$$H_e = -T \sum_{i < j}^{\text{NN}} \sum_{\sigma} (c_{i\sigma}^{\dagger} c_{j\sigma} + \text{H.c.}) + U \sum_{i=1}^L n_{i\uparrow} n_{i\downarrow}. \quad (1)$$

The nearest-neighbor (NN) hopping $T = 1$ sets the energy and time scale ($\hbar = 1$). Using standard arguments [16,17], the Gilbert damping parameter α can be computed as

$$\alpha = -J^2 \int_0^{\infty} dt t \chi_{\text{loc}}(t) \quad (2)$$

and depends on the Hubbard interaction U via the local (diagonal and isotropic) retarded spin susceptibility

$$\chi_{\text{loc}}(t) = -i\Theta(t)\langle 0|[s_{i_0z}(t), s_{i_0z}(0)]|0\rangle \quad (3)$$

at the site i_0 where the classical spin is coupled to. J is the strength of the exchange interaction [see Eq. (4) below]. Furthermore, $|0\rangle$ is the ground state of H_e , $s_{iz}(t) = e^{iH_e t} s_{iz} e^{-iH_e t}$, and s_{iz} is the z component of the local conduction-electron spin $s_i = \sum_{\sigma\sigma'} c_{i\sigma}^\dagger \boldsymbol{\tau}_{\sigma\sigma'} c_{i\sigma'}/2$, with the vector of Pauli matrices $\boldsymbol{\tau}$ and with $\sigma, \sigma' = \uparrow, \downarrow$.

We choose $i_0 = 1$ for two reasons: (i) As compared to the symmetric choice $i_0 = L/2$, this allows us to double the accessible time scale (before finite-size effects set in). (ii) The time integral in (2) is sensitive to the long-time behavior of $\chi_{\text{loc}}(t)$ which, at least for $U = 0$, is related to the strength of the van Hove singularities in the local density of states [17]. At the edge of the open chain, those are weak and characteristic for a three-dimensional system.

Local-spin correlations at quarter filling.—To compute $\chi_{\text{loc}}(t)$, we apply t-DMRG and the framework of matrix-product states [18] for systems with $L = 80$ –120 sites. Concretely, we use the two-site version of the algorithm suggested in Refs. [19,20] which is based on the time-dependent variational principle.

Electron correlations are expected to speed up the relaxation of the classical spin since electron scattering facilitates the transport of energy and spin density from i_0 to the bulk of the system. An increasingly efficient dissipation implies an increase of α with U . This can be nicely seen in $\chi_{\text{loc}}(t)$, which determines α via Eq. (2) and which is shown in Fig. 1 (upper panel) for quarter filling $n \equiv N/L = 0.5$ where we have a (correlated) metal in the entire U range. In fact, the absolute value of the integral weight $\int dt \chi_{\text{loc}}(t)$ grows with increasing U .

Note that via the fluctuation-dissipation theorem, the total weight $\int dt \chi_{\text{loc}}(t)$ is given by the negative local static spin susceptibility. This explains that $\chi_{\text{loc}}(t)$ is mainly negative.

Separation of time scales.—A central observation is that $\chi_{\text{loc}}(t)$ develops a pronounced two-peak structure for strong U . For $U = 0$ and in the weak-coupling regime, there is essentially a single (negative) peak around $t \sim 1$ only. This corresponds to fast correlated-hopping processes on a scale set by the inverse hopping $1/T$. As is seen in the figure, the contribution of these processes to the Gilbert damping grows with increasing U .

The second (negative) peak is clearly present for $U \gtrsim 8$. The almost linear shift of its position with U hints towards a time scale set by an effective magnetic interaction $J_H \sim 1/U$ between local magnetic moments formed by strong correlations in the conduction-electron system. Even for $U \rightarrow \infty$, however, local-moment formation is not perfect at quarter filling: We have $\langle s_i^2 \rangle = \frac{3}{4}n = \frac{3}{8} < s(s+1)$ with $s = 1/2$ for the size of the correlated local moment [12]. This explains the residual contributions from correlated-hopping processes (first peak).

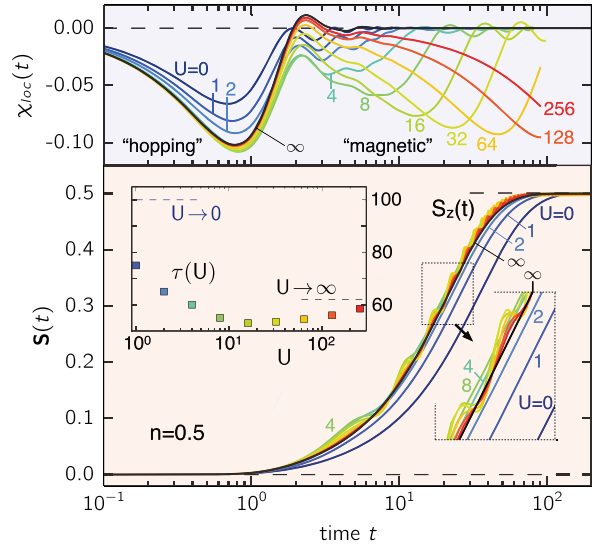


FIG. 1. Upper panel: Local-spin correlation $\chi_{\text{loc}}(t)$ at $i_0 = 1$ for an open Hubbard chain with $L = 80$ sites as obtained by t-DMRG for quarter filling and different U as indicated. ($U \geq 32$: t - J model with three-site terms [29], $L = 100$ sites; $U = \infty$: $L = 120$). Energy and time scales are fixed by the NN hopping $T = 1$. Lower panel: Resulting real-time dynamics of a classical spin $S(t)$ (with $|S(t)| = \frac{1}{2}$, only S_z is shown) coupled at i_0 to the local conduction-electron spin as obtained from Eq. (5) for $J = 1$ and different U . The spin dynamics is initiated by switching the local magnetic field in Eq. (5) at time $t = 0$ from the x to the z direction ($B_{\text{fin}} = 1$). Inset: U dependence of the relaxation time τ , defined as $S_z(\tau) = 0.98|S|$.

For strong U the Gilbert damping is dominated by magnetic processes: Because of the extra factor t under the integral in Eq. (2), the contribution of the second peak in $\chi_{\text{loc}}(t)$ by far exceeds the hopping contribution (note the logarithmic scale in Fig. 1). Clearly, α strongly increases with U though a precise value cannot be given due to limitations of the t-DMRG in accessing the long-time limit.

Spin-dynamics model.—The simple LLG equation for a classical spin, i.e., $\dot{\mathbf{S}} = \mathbf{S} \times \mathbf{B} - \alpha \mathbf{S} \times \dot{\mathbf{S}}$, can only provide an overall picture of the spin dynamics and in fact ignores the electronic time-scale separation. We therefore apply a refined approach which explicitly accounts for the conduction-electron degrees of freedom in a model H which, besides H_e , Eq. (1), includes the local and isotropic coupling between s_{i_0} and the classical spin S ($|S| = 1/2$):

$$H = H_e + H_{e\text{-spin}} = H_e + J s_{i_0} \mathbf{S} - \mathbf{B} S. \quad (4)$$

We have also added a local magnetic field \mathbf{B} which, at time $t = 0$, is suddenly switched from $\mathbf{B} = B_{\text{ini}} \hat{x}$, forcing the spin to point in the x direction, to $\mathbf{B} = B_{\text{fin}} \hat{z}$ with $B_{\text{fin}} = 1$ to initiate the spin dynamics. Complete relaxation is achieved if $S(t) \rightarrow \frac{1}{2} \hat{z}$ for $t \rightarrow \infty$.

The Hamiltonian (4) represents a semiclassical Kondo-impurity model with finite Hubbard U . For a strong local field B_{fin} , the dynamical Kondo effect [30] that would show up in the case of a quantum-spin $S = \frac{1}{2}$ is suppressed—this justifies the classical-spin approximation. The quantum-classical hybrid (4) is also obtained in the limit of large spin quantum numbers S [31] of a correlated quantum-spin Kondo impurity model [32].

$\mathbf{S}(t)$ satisfies the classical equation of motion $\dot{\mathbf{S}}(t) = \mathbf{S}(t) \times \mathbf{B} - J\mathbf{S}(t) \times \langle \mathbf{s}_{i_0} \rangle_t$ [33]. Applying lowest-order perturbation theory in J , the Kubo formula yields $\langle \mathbf{s}_{i_0} \rangle_t = J \int_0^t dt' \chi_{\text{loc}}(t-t')\mathbf{S}(t')$, where the retarded local-spin correlation $\chi_{\text{loc}}(t)$ now plays the role of the linear-response function. As has been demonstrated in Ref. [17] for $U = 0$, this approach is perfectly reliable even for fairly strong couplings J and up to the time scale necessary for complete spin relaxation. Here, we choose $J = 1$ to generate relaxation times accessible to the t-DMRG approach.

The resulting effective integro-differential equation of motion [6,16] (see also Refs. [34,35]),

$$\dot{\mathbf{S}}(t) = \mathbf{S}(t) \times \mathbf{B} - J^2 \mathbf{S}(t) \times \int_0^t dt' \chi_{\text{loc}}(t-t')\mathbf{S}(t'), \quad (5)$$

is numerically solved using high-order Runge-Kutta [36] and quadrature techniques.

Correlation effects in the spin dynamics.—The resulting spin dynamics (Fig. 1, lower panel) is characterized by precessional motion [$S_x(t), S_y(t)$ not shown] with Larmor frequency $\omega_L \propto B$ around the \hat{z} axis, and by relaxation driven by dissipation of energy and spin into the bulk of the electronic system. In the final state there is complete alignment, $\mathbf{S}(t) \uparrow \uparrow \mathbf{B}$.

Comparing the results for the different U , we find the following. (i) Significant relaxation starts at times $t \sim 1/T$, i.e., on the time scale for dissipation through the correlated-hopping process. (ii) Correlation effects lead to a considerably shorter relaxation time, e.g., by about a factor 2 when comparing the results for $U = 0$ and $U = 16$ (see inset). (iii) To some extent this is due to an additional damping mechanism, namely via excitations of *correlation-induced* magnetic moments—at least for moderate U . (iv) For strong U , however, the relaxation time *increases* again. This is counterintuitive but readily explained: Since the second, “magnetic” peak in $\chi_{\text{loc}}(t)$ shifts with increasing U to later and later times, relaxation is already completed before dissipation through spin-flip processes can become active. This is most obvious for $U \rightarrow \infty$ where magnetic damping is *never* activated, and where a renormalized band picture may apply. (v) At intermediate U , however, the picture is different. Here, spin-flip processes do contribute to the relaxation but more than an order of magnitude later ($t \gtrsim U/T^2$) than the hopping time scale. Despite their dominating contribution to α , their effect is

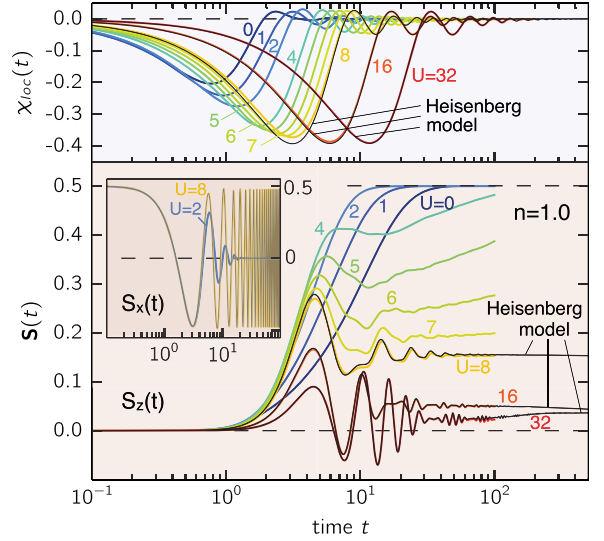


FIG. 2. The same as Fig. 1 but for $n = 1$ ($L = 60$). Thin black lines: Heisenberg model with $J_H = 4T^2/U$ ($L = 400$) and, for improved accuracy at $U = 8$, with NN and NNN couplings $J_H = 4T^2/U - 16T^4/U^3$ and $J'_H = 4T^4/U^3$ [38] ($L = 300$).

weaker as compared to the correlated-hopping processes. Still, spin flips leave clear characteristics in $S_z(t)$: their additional torque produces oscillations (with a period largely independent of U) which superimpose the monotonic relaxation dynamics. The onset of these magnetic oscillations linearly grows with U . Note that the interpretation of these (and the following) findings does not rely on the one-dimensionality of the model.

Gilbert damping of a Mott insulator.—Dissipation through correlated hopping is impeded or even suppressed at half filling where the system is a Mott insulator for all $U > 0$. Figure 2 (upper panel) shows the t-DMRG data for $\chi_{\text{loc}}(t)$ at $n = 1$ and different U . Its time dependence is dominated by a single (negative) structure which grows with increasing U up to, say, $U \approx 8$. In the weak-coupling regime, $U \lesssim 4$, the local magnetic moments are not yet well formed since the charge gap $\Delta \sim e^{-1/U}$ (as obtained from the Bethe ansatz [37] for $U \rightarrow 0$) is small as compared to T . Hence, residual hopping processes still contribute significantly.

In the strong-coupling limit, on the other hand, spin-flip processes dominate. Here, we observe scaling behavior, $\chi_{\text{loc}}(t) = F(4tT^2/U)$ with a universal function $F(x)$. Indeed, due to the suppression of charge fluctuations, the long-time, low-energy dynamics is captured by a Heisenberg chain $H_{\text{Heis}} = J_H \sum_i s_i s_{i+1}$ with antiferromagnetic interaction $J_H = 4T^2/U$ between rigid $s = 1/2$ spins. As J_H is the only energy scale remaining, $F(tJ_H)$ is the retarded local susceptibility of the Heisenberg chain. With $F(x)$ obtained numerically by means of t-DMRG applied to H_{Heis} at $J_H = 1$, the t-DMRG data for strong U are fitted perfectly (see Fig. 2). Significant deviations from the

scaling behavior can be seen in Fig. 2 for $U = 8$ and $t \approx 3$, for instance.

Scaling can be exploited to determine the U dependence of the Gilbert damping for a Mott insulator. From Eq. (2) we get

$$\alpha = \frac{J^2}{J_H^2} \int_0^\infty dx xF(x) = \frac{J^2}{J_H^2} \alpha_0 = \frac{J^2 U^2}{16T^4} \alpha_0, \quad (6)$$

and thus, for fixed J and T , we have $\alpha \propto U^2$. For the universal dimensionless Gilbert damping constant α_0 we find

$$\alpha_0 \approx 4.8. \quad (7)$$

For a correlated Mott insulator, Eqs. (6) and (7) completely describe the U dependence of the classical-spin dynamics in the weak- J , weak- B limit where the t dependence of $S(t)$ is so slow, as compared to the typical memory time τ_{mem} characterizing $\chi_{\text{loc}}(t)$, that the Taylor expansion $S(t') \approx S(t) + \dot{S}(t)(t' - t)$ can be cut at the linear order under the t' integral in Eq. (5), such that the LLG equation is obtained as a Redfield equation [39].

Incomplete spin relaxation.—As demonstrated with Fig. 2 (lower panel), there is an anomalous U dependence of the spin dynamics at $n = 1$. Only in the weak-coupling regime, $U \lesssim 2$, do damping effects increase and lead to a decrease of the relaxation time with increasing U . For $U = 4$, however, the relaxation time *increases* again. This behavior is clearly beyond the LLG theory and is attributed to the fact that the memory time, $\tau_{\text{mem}} \propto 1/J_H \propto U$ for strong U , becomes comparable to and finally exceeds the precession time scale $\tau_B = 2\pi/B$ (see the Supplemental Material [40]).

In addition, as for $n = 0.5$, we note a nonmonotonic behavior of $S_z(t)$ with superimposed oscillations (see $U = 6$, for example). With increasing U these oscillations die out, and from a “critical” interaction $U_c \sim 8$ onwards the relaxation time seems to diverge. Namely, the z component of $S(t)$ approaches a nearly constant value which decreases with increasing U while S_x (and S_y) still precess around \mathbf{B} (see inset). Hence, on the accessible time scale, U_c marks a transition or crossover to an incompletely relaxed but “stationary” state.

The same type of dynamical transition is also seen for a classical spin coupled to a Heisenberg chain for which much larger system sizes ($L = 400$) and thus about an order of magnitude longer time scales are accessible to t-DMRG. Here, the crossover coupling is $J_{H,c} \sim 0.5$. However, these calculations as well as analytical arguments clearly indicate that a state with $S_z = \text{const} \neq 1/2$ is unstable and that finally, for $t \rightarrow \infty$, the fully relaxed state with $S(t) \uparrow \mathbf{B}$ must be reached (see [40] for details).

The “stationary state” on an intermediate time scale originates when the bandwidth of magnetic excitations gets smaller than the field—as can be studied in detail already for $U = 0$ (and very strong B). On the time axis, the missing relaxation results from a strong memory effect

which, in the strong- U limit, shows up for $J_H \lesssim B$. Here, $\tau_{\text{mem}} \gtrsim \tau_B$, which implies that the z component of the spin torque on $S(t)$ averages to zero [40].

The incomplete spin relaxation can also be understood as a transient “phase” similar to the concept of a prethermalized state. The latter is known for purely electronic systems [21–24] which, in close parametric distance to integrability, do not thermalize directly but are trapped for some time in a prethermalized state. Here, for the quantum-classical hybrid, the analogue of an “integrable” point is given by the $U \rightarrow \infty$ limit where, for every *finite* t , the integral kernel $\chi_{\text{loc}}(t) \equiv 0$, and Eq. (5) reduces to the simple (linear) Landau-Lifschitz equation [1].

The situation is also reminiscent of *quantum* excitations which are metastable on an exponentially long time scale due to a small phase space for decay. An example is given by doublons in the Hubbard model which, for U much larger than the bandwidth and due to energy conservation, can only decay in a high-order scattering process [25–28]. The relaxation time diverges in the $U \rightarrow \infty$ limit where the doublon number is conserved. Here, for a *classical* spin, one would expect that relaxation via dissipation of (arbitrarily) small amounts of energy is still possible. Our results show, however, that this would happen on a longer time scale not accessible to the linear-response approach while the stationary state on the intermediate time scale is well captured [40].

Outlook.—Correlation-induced time-scale separation and incomplete relaxation represent phenomena with further general implications. While slow correlation-induced magnetic scales dominate the Gilbert damping α , their *activation* has been found to depend on microscopic details. This calls for novel correlated spin-dynamics approaches. The combination of t-DMRG with non-Markovian classical-spin dynamics is an example of how to link the fields of strongly correlated electron systems and spin dynamics, but further work is necessary. Combination with dynamical mean-field theory [41] is another promising option. Also spin dynamics based on LLG-type approaches combined with *ab initio* band theory could be successful in the case of very strong U where due to the absence of magnetic damping a renormalized band picture may be adequate. Further progress is even needed for the very theory of a consistent hybrid-system dynamics [33,42]. Generally, hybrid systems are not well understood and call for a merger of known quantum and classical concepts, such as eigenstate thermalization, prethermalization, (non)integrability, etc. [43]. However, also concrete practical studies with classical spins coupled to conduction electrons [17] are needed, as those hold the key for the microscopic understanding of nanospintronics devices [15] or Skyrmion dynamics [44,45].

We thank F. Hofmann for instructive discussions. Support of this work by the DFG within the SFB 668 (project B3) and within the SFB 925 (project B5) is gratefully acknowledged.

- [1] L. D. Landau and E. M. Lifshitz, *Phys. Z. Sowjetunion* **8**, 153 (1935); T. Gilbert, *Phys. Rev.* **100**, 1243 (1955); *IEEE Trans. Magn.* **40**, 3443 (2004).
- [2] G. Tataru, H. Kohno, and J. Shibata, *Phys. Rep.* **468**, 213 (2008).
- [3] G. Bertotti, I. D. Mayergoyz, and C. Serpico, *Nonlinear Magnetization Dynamics in Nanosystems* (Elsevier, Amsterdam, 2009).
- [4] K. Gilmore, Y. U. Idzerda, and M. D. Stiles, *Phys. Rev. Lett.* **99**, 027204 (2007).
- [5] H. Ebert, S. Mankovsky, D. Ködderitzsch, and P. J. Kelly, *Phys. Rev. Lett.* **107**, 066603 (2011).
- [6] A. Sakuma, *J. Phys. Soc. Jpn.* **81**, 084701 (2012).
- [7] M. Fähnle and C. Illg, *J. Phys. Condens. Matter* **23**, 493201 (2011).
- [8] B. Skubic, J. Hellsvik, L. Nordström, and O. Eriksson, *J. Phys. Condens. Matter* **20**, 315203 (2008).
- [9] E. M. Hankiewicz, G. Vignale, and Y. Tserkovnyak, *Phys. Rev. B* **78**, 020404(R) (2008).
- [10] I. Garate and A. MacDonald, *Phys. Rev. B* **79**, 064404 (2009).
- [11] K. M. D. Hals, K. Flensberg, and M. S. Rudner, *Phys. Rev. B* **92**, 094403 (2015).
- [12] F. Gebhard, *The Mott Metal-Insulator Transition* (Springer, Berlin, 1997).
- [13] M. Morgenstern, *Science* **329**, 1609 (2010).
- [14] S. Loth, M. Etzkorn, C. P. Lutz, D. M. Eigler, and A. J. Heinrich, *Science* **329**, 1628 (2010).
- [15] A. A. Khajetoorians, J. Wiebe, B. Chilian, and R. Wiesendanger, *Science* **332**, 1062 (2011).
- [16] S. Bhattacharjee, L. Nordström, and J. Fransson, *Phys. Rev. Lett.* **108**, 057204 (2012).
- [17] M. Sayad and M. Potthoff, *New J. Phys.* **17**, 113058 (2015).
- [18] U. Schollwöck, *Ann. Phys. (Amsterdam)* **326**, 96 (2011).
- [19] J. Haegeman, J. I. Cirac, T. J. Osborne, I. Pižorn, H. Verschelde, and F. Verstraete, *Phys. Rev. Lett.* **107**, 070601 (2011).
- [20] J. Haegeman, C. Lubich, I. Oseledets, B. Vandereycken, and F. Verstraete, *arXiv:1408.5056*.
- [21] M. Moeckel and S. Kehrein, *Phys. Rev. Lett.* **100**, 175702 (2008).
- [22] M. Moeckel and S. Kehrein, *New J. Phys.* **12**, 055016 (2010).
- [23] M. Kollar, F. A. Wolf, and M. Eckstein, *Phys. Rev. B* **84**, 054304 (2011).
- [24] M. Marcuzzi, J. Marino, A. Gambassi, and A. Silva, *Phys. Rev. Lett.* **111**, 197203 (2013).
- [25] A. Rosch, D. Rasch, B. Binz, and M. Vojta, *Phys. Rev. Lett.* **101**, 265301 (2008).
- [26] N. Strohmaier, D. Greif, R. Jördens, L. Tarruell, H. Moritz, T. Esslinger, R. Sensarma, D. Pekker, E. Altman, and E. Demler, *Phys. Rev. Lett.* **104**, 080401 (2010).
- [27] F. Hofmann and M. Potthoff, *Phys. Rev. B* **85**, 205127 (2012).
- [28] R. Rausch and M. Potthoff, *New J. Phys.* **18**, 023033 (2016).
- [29] B. Ammon, M. Troyer, and H. Tsunetsugu, *Phys. Rev. B* **52**, 629 (1995).
- [30] M. Nuss, M. Ganahl, E. Arrigoni, W. von der Linden, and H. G. Evertz, *Phys. Rev. B* **91**, 085127 (2015).
- [31] D. A. Garanin, *Phys. Rev. B* **78**, 144413 (2008).
- [32] M. Sayad, R. Rausch, and M. Potthoff (to be published).
- [33] H. Elze, *Phys. Rev. A* **85**, 052109 (2012).
- [34] T. Bose and S. Trimper, *Phys. Rev. B* **83**, 134434 (2011).
- [35] D. Thonig, J. Henk, and O. Eriksson, *Phys. Rev. B* **92**, 104403 (2015).
- [36] J. H. Verner, *Numerical Algorithms* **53**, 383 (2010).
- [37] A. A. Ovchinnikov, *Zh. Eksp. Teor. Fiz.* **57**, 2137 (1969).
- [38] L. N. Buleavskii, *Sov. J. Exp. Theor. Phys.* **24**, 154 (1967).
- [39] H. P. Breuer and F. Petruccione, *The Theory of Open Quantum Systems* (Oxford University Press, New York, 2002).
- [40] See Supplemental Material at <http://link.aps.org/supplemental/10.1103/PhysRevLett.117.127201> for the validity of the linear-response theory, the mechanism of incomplete relaxation, results for the Heisenberg chain and for an explanation of short-time oscillations.
- [41] A. Georges, G. Kotliar, W. Krauth, and M. J. Rozenberg, *Rev. Mod. Phys.* **68**, 13 (1996).
- [42] L. L. Salcedo, *Phys. Rev. A* **85**, 022127 (2012).
- [43] M. Rigol, V. Dunjko, and M. Olshanii, *Nature (London)* **452**, 854 (2008).
- [44] A. Fert, V. Cros, and J. Sampaio, *Nat. Nanotechnol.* **8**, 152 (2013).
- [45] J. Iwasaki, M. Mochizuki, and N. Nagaosa, *Nat. Nanotechnol.* **8**, 742 (2013).

Relaxation of a classical spin coupled to a strongly correlated electron system: Supplementary material

Mohammad Sayad, Roman Rausch and Michael Potthoff

I. Institute for Theoretical Physics, University of Hamburg, Jungiusstraße 9, D-20355 Hamburg, Germany

Validity of linear-response theory.

The reliability of the linear-response approach (see Eq. (5) of the main text) can be tested by comparing with the results of the full (non-perturbative) quantum-classical hybrid dynamics for the model given by Eq. (4) of the main text. This is easily accessible for the case $U = 0$ (see Ref. [1] for details). Fig. 1 displays the time dependence of the z -component of the classical spin for $J = 1$, for a half-filled system ($n = 1$) of non-interacting conduction electrons ($U = 0$) and for different strengths of the field B after switching from x - to z -direction.

While there are some discrepancies visible, as expected, the figure demonstrates that the agreement on a qualitative level is in fact excellent for weak as well as for strong fields. Both approaches also predict a crossover from complete to incomplete spin relaxation at $B = B_c \approx 4$. We conclude that the linear-response approach provides reliable results for the classical spin dynamics.

This can be explained by the observation that $|\langle \mathbf{s}_{i_0} \rangle_t|$ is small and that the classical spin $\mathbf{S}(t)$ and the conduction-electron moment $\langle \mathbf{s}_{i_0} \rangle_t$ are nearly collinear at any instant of time (see Ref. [1] for a detailed and systematic discussion). Hence, even for moderately strong couplings J , the linear-response contribution $J^2 \mathbf{S}(t) \times \langle \mathbf{s}_{i_0} \rangle_t$ to the equation of motion for $\mathbf{S}(t)$ is small (and the quadratic and higher-order corrections are expected to be even smaller).

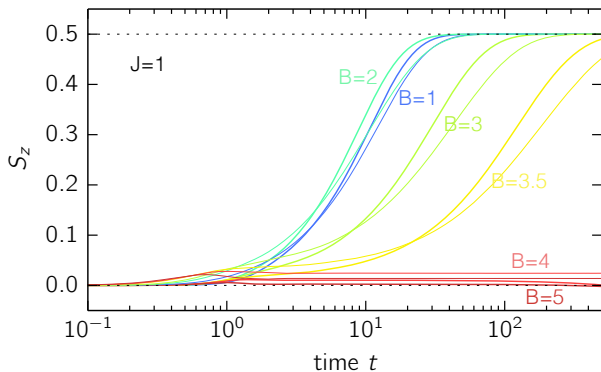


FIG. 1: Time dependence of the z -component of the classical spin for $J = 1$, $n = 1$, $U = 0$ and different values of the field B as indicated. Calculations based on the linear-response approach (fat solid lines) are compared to the results of the full quantum-classical hybrid theory (thin solid lines) for $L = 500$.

Mechanism for incomplete relaxation.

Fig. 1 shows that the relaxation of the classical spin becomes incomplete for strong B . On the basis of the linear-response theory this can be explained as follows: The x and y components of the linear response

$$\langle \mathbf{s}_{i_0} \rangle_t = \int_0^t d\tau \chi_{\text{loc}}(\tau) \mathbf{S}(t - \tau), \quad (1)$$

tend to zero if the characteristic memory time τ_{mem} of the kernel $\chi_{\text{loc}}(\tau)$ is much larger than the precession time scale $\tau_B = 2\pi/B$ since the integral produces a vanishing average in this case. This means that the corresponding torque, $-J^2 \mathbf{S}(t) \times \langle \mathbf{s}_{i_0} \rangle_t$, is perpendicular to the field direction and hence there is no relaxation of the spin.

The same argument can also be formulated after transformation to frequency space: After some transient effect, we have $\langle \mathbf{s}_{i_0} \rangle_\omega = \chi_{\text{loc}}(\omega) \mathbf{S}(\omega)$, and thus the x, y -components of the linear response will vanish if $\chi_{\text{loc}}(\omega = B) = 0$, i.e., if B is stronger than the bandwidth of the magnetic excitations (here: $B_c \approx 4$). Note that this requires an unrealistically strong field in case of non-interacting conduction electrons.

In the case of correlated conduction electrons, $|\mathbf{S}(t) \times \langle \mathbf{s}_{i_0} \rangle_t|$ remains small (of the order of 0.1 or smaller), for weak and for strong B , as has been checked numerically. We therefore expect the linear-response approach to provide qualitatively correct results for $U > 0$ as well.

At half-filling and for strong U , the memory time $\tau_{\text{mem}} \propto J_H^{-1} \propto U$, i.e., τ_{mem} can easily become large as compared to τ_B , and thus incomplete spin relaxation can occur at comparatively weak and physically meaningful field strengths. For example, from the Bethe ansatz [2] we have

$$W_{\text{spinon}} = 2 \int_0^\infty dx \frac{J_1(x)}{x \cosh(Ux/4)} \rightarrow \frac{\pi}{2} J_H \quad \text{for } U \rightarrow \infty \quad (2)$$

for the spinon bandwidth W_{spinon} where $J_1(x)$ is the first Bessel function. Hence, for strong Hubbard interaction, $B_c \approx 2W_{\text{spinon}} = \pi J_H$.

Classical spin coupled to a Heisenberg model.

At half-filling and in the limit $U \rightarrow \infty$ the low-energy physics of the Hubbard model is captured by an antifer-

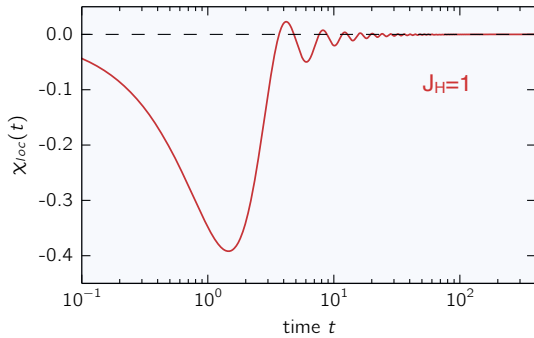


FIG. 2: Local susceptibility at the edge of an open Heisenberg chain ($J_H = 1$).

romagnetic Heisenberg model,

$$H_s = \sum_i (J_H \mathbf{s}_i \mathbf{s}_{i+1} + J'_H \mathbf{s}_i \mathbf{s}_{i+2}), \quad (3)$$

where up to order $\mathcal{O}(T^2/U)$ the nearest-neighbor and the next-nearest-neighbor couplings [3] are $J_H = 4T^2/U$ and $J'_H = 0$, and up to order $\mathcal{O}(T^4/U^3)$,

$$J_H = \frac{4T^2}{U} - \frac{16T^4}{U^3}, \quad J'_H = \frac{4T^4}{U^3}. \quad (4)$$

Analytically, by perturbation theory in $x = 4tT^2/U = tJ_H$, one verifies the linear short-time behavior

$$\chi_{\text{loc}}(t) = \Theta(t) t \frac{2}{3} (J_H \langle \mathbf{s}_{i_0} \mathbf{s}_{i_0+1} \rangle + J'_H \langle \mathbf{s}_{i_0} \mathbf{s}_{i_0+2} \rangle) + \mathcal{O}(x^2), \quad (5)$$

valid to leading order for both, the Hubbard and the effective Heisenberg model. However, as can be seen in Fig. 2 of the main text, the Heisenberg dynamics also applies to intermediate times; the effective model with coupling constants (4) almost perfectly reproduces the results of the Hubbard model for $U \geq 8$.

Here, we treat the Heisenberg model with n.n. coupling as an independent system. Fig. 2 shows the corresponding local spin susceptibility for $J_H = 1$ as obtained by t-DMRG calculations with $L = 400$ Heisenberg spins. Since J_H is the only energy scale, we have $\chi_{\text{loc}}(t) = F(t J_H)$ for arbitrary J_H where $F(x)$ is a function independent of J_H . This implies that the dominant (negative) peak of $\chi_{\text{loc}}(t)$ shifts to later and later times as J_H decreases.

Fig. 3 displays the spin dynamics resulting from the full model

$$H = H_s + H_{s-\text{spin}} = H_s + J \mathbf{s}_{i_0} \mathbf{S} - \mathbf{B} \mathbf{S}, \quad (6)$$

as obtained by the linear-response approach. One clearly notes that for $J \lesssim J_c \sim 0.5$ (corresponding to $U_c \sim 8$) the time dependence of S_z develops a prethermalization-like plateau on an intermediate time scale $t \sim 100$ (in units of $1/J_H$).

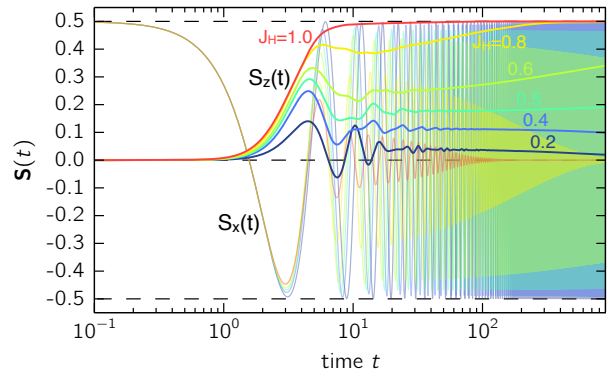


FIG. 3: Classical spin dynamics for $J = 1$ and different J_H .

For the Heisenberg model, using the scaling property of $\chi_{\text{loc}}(t)$, it is easily possible to perform calculations up to $t = 1000$. On this longer time scale, it is clearly visible (see Fig. 3) that S_z does *not* approach a constant value asymptotically. For $J_H = 0.4$ and $J_H = 0.2$ the z -component of $\mathbf{S}(t)$ is even found to decrease and appears to approach the trivial solution $S_z(t) \equiv 0$.

However, it is straightforwardly seen that a “stationary state” of the form

$$\mathbf{S}(t) = S_z \hat{z} + S_\perp \cos(\omega t + \varphi) \hat{x} + S_\perp \sin(\omega t + \varphi) \hat{y} \quad (7)$$

with arbitrary parameters S_\perp, ω, φ and with constant (time-independent) S_z does not solve the integro-differential equation (5) of the main text for $t \rightarrow \infty$. There is one exception only, namely the trivial case where $\chi_{\text{loc}}(t) \equiv 0$ which can be realized, up to arbitrarily long times, in the limit $J_H \rightarrow 0$.

For small but finite $J_H > 0$, we therefore expect that the classical spin develops a dynamics on an extremely long time scale $t \gg 10^3$, the onset of which is already seen in Fig. 3, which finally terminates in the fully relaxed state with $\mathbf{S}(t) \rightarrow \mathbf{S}_0 \uparrow \uparrow \mathbf{B}$.

It is in fact easy to see from the integro-differential equation that, if there is spin relaxation to a time-independent constant, $\mathbf{S}(t) \rightarrow \mathbf{S}_0$ for $t \rightarrow \infty$, the relaxed state has $\mathbf{S}_0 = 0.5 \hat{z}$. This implies that if there is complete relaxation at all, the spin relaxes to the equilibrium direction.

Oscillations at short times.

As can be seen in Fig. 3 for weak J_H , the z -component of the spin develops oscillations at short times, which can also be seen for the case of the Hubbard model (cf. Fig. 2 of the main text). These oscillations can be understood in the following way: Inserting the expression (5) with $J'_H = 0$ for the behavior of $\chi_{\text{loc}}(t)$ at short times into Eq.

(5) of the main text,

$$\begin{aligned} \dot{\mathbf{S}}(t) &= \mathbf{S}(t) \times \mathbf{B} - \frac{2}{3} J^2 J_{\text{H}} \langle \mathbf{s}_{i_0} \mathbf{s}_{i_0+1} \rangle \mathbf{S}(t) \\ &\times \int_0^t dt' (t-t') \mathbf{S}(t') + \mathcal{O}(t^3 J^4), \end{aligned} \quad (8)$$

and approximating $\mathbf{S}(t)$ by the $J = 0$ result $\mathbf{S}_0(t) = S(\cos \omega t, \sin \omega t, 0)$ (with $\mathbf{B} = B\hat{z}$, $\omega = B$, $S = 1/2$) in the second term on the right-hand side, a straightforward calculation yields:

$$\begin{aligned} S_z(t) &= \frac{2}{3} J^2 J_{\text{H}} \langle \mathbf{s}_{i_0} \mathbf{s}_{i_0+1} \rangle S^2 \frac{\omega t \sin \omega t + 2 \cos \omega t - 2}{\omega^3} \\ &+ \mathcal{O}(t^4 J^2 J_{\text{H}}^2). \end{aligned} \quad (9)$$

This is found to perfectly describe the short-time oscillations for weak J_{H} in Fig. 3 and for strong U in Fig. 2 in the main text. For longer times the oscillations are damped and eventually die out.

-
- [1] M. Sayad and M. Potthoff, *New J. Phys.* **17**, 113058 (2015).
 - [2] F. H. L. Essler, H. Frahm, F. Göhmann, A. Klümper, and V. Korepin, *The One-Dimensional Hubbard Model* (Cambridge University Press, Cambridge, 2005).
 - [3] L. N. Buleavskii, *Soviet Journal of Experimental and Theoretical Physics* **24**, 154 (1967).

Inertia effects in the real-time dynamics of a quantum spin coupled to a Fermi sea

MOHAMMAD SAYAD, ROMAN RAUSCH and MICHAEL POTTHOFF

I. Institut für Theoretische Physik, Universität Hamburg - Jungiusstraße 9, 20355 Hamburg, Germany

received 22 September 2016; accepted 19 October 2016

published online 28 October 2016

PACS 75.20.Hr – Local moment in compounds and alloys; Kondo effect, valence fluctuations, heavy fermions

PACS 75.78.Jp – Ultrafast magnetization dynamics and switching

PACS 03.65.Sq – Semi-classical theories and applications

Abstract – Spin dynamics in the Kondo impurity model, initiated by suddenly switching the direction of a local magnetic field, is studied by means of the time-dependent density-matrix renormalization group. Quantum effects are identified by systematic computations for different spin quantum numbers S and by comparing with tight-binding spin-dynamics theory for the classical-spin Kondo model. We demonstrate that, besides the conventional precessional motion and relaxation, the quantum-spin dynamics shows nutation, similar to a spinning top. Opposed to semiclassical theory, however, the nutation is efficiently damped on an extremely short time scale. The effect is explained in the large- S limit as quantum dephasing of the eigenmodes in an emergent two-spin model that is weakly entangled with the bulk of the system. We argue that, apart from the Kondo effect, the damping of nutational motion is essentially the only characteristics of the quantum nature of the spin. Qualitative agreement between quantum and semiclassical spin dynamics is found down to $S = 1/2$.

Copyright © EPLA, 2016

Introduction. – The paradigmatic system to study the real-time dynamics of a spin-(1/2) coupled to a Fermi sea is the Kondo model [1]. It is mainly considered as a generic model for the famous Kondo effect [2], namely screening of the impurity spin by a mesoscopically large number of electrons in a thermal state with temperature below the Kondo temperature $T_K \sim \exp(-1/J\rho)$, where J is the strength of the exchange coupling and ρ is the density of states. The Kondo effect is a true *quantum* effect which originates from the two-fold spin degeneracy and is protected by time-reversal symmetry. Longitudinal spin dynamics, such as the time-dependent Kondo screening, has been studied recently [3,4] by starting from an initial state with a fully polarized spin, which can be prepared with the help of local magnetic field. The longitudinal dynamics is initiated by suddenly switching off the field.

Transversal spin dynamics, on the other hand, appears as a more *classical* phenomenon: It can be induced, for example, by suddenly tilting a strong field $B \gg T_K$ from, say, the \hat{x} - to the \hat{z} -direction. In first place this induces a precession of the spin around the new field direction with Larmor frequency $\omega_L \propto B$. For $J = 0$, the equation of motion for the expectation value of the spin, $(d/dt)\langle \mathbf{S} \rangle_t = \langle \mathbf{S} \rangle_t \times \mathbf{B}$ with $\mathbf{B} = B\hat{z}$ has the same form

as the Landau-Lifschitz equation for a classical spin [5]. When coupling the spin to the Fermi sea with a finite J , energy can be transferred to the electronic system and dissipated into the bulk. Hence, the spin must relax and align to the new field direction as is nicely seen in numerical studies of the Kondo model out of equilibrium [6]. For $B \gg T_K$ the spin precession and relaxation is qualitatively well described by semiclassical tight-binding spin dynamics (TB-SD) (cf., *e.g.* ref. [7]) where the spin is assumed to be a classical dynamical observable. In many cases, even the simple Landau-Lifschitz-Gilbert (LLG) equation [8,9] including a non-conserving damping term, proportional to the first time derivative of the spin, seems to capture the essential (classical) physics.

A major purpose of the present study is to check if there are quantum effects which are overlooked by the semiclassical approach to transversal spin dynamics (*i.e.*, apart from the Kondo effect). To this end we compare numerical results from exact quantum-classical hybrid theory [10,11], *i.e.*, the TB-SD [7,12], with those of exact quantum theory, computed with time-dependent density-matrix renormalization group (t-DMRG) [13,14], for different spin quantum numbers S . It turns out that even for $S = 1/2$ there is a surprisingly good qualitative agreement of quantum

with semiclassical dynamics. However, we also identify a physical phenomenon, namely nutational motion, where remarkable differences are found:

Classical and quantum nutation. – Besides precession and damping, inertia effects are well known in classical spin dynamics [15,16] and can be described by an additional term to the LLG equation with second-order time derivative of the spin. The resulting nutation of the spin motion has been introduced and studied phenomenologically [17,18] or with realistic parameters taken from first-principles calculations [19] but can also be derived on a microscopic level [20–22] within the general framework of semiclassical spin dynamics [23–25].

In case of a quantum spin, inertia effects have not yet been studied. As compared to spin precession and damping, nutation is a higher-order effect [21], so that it is not *a priori* clear whether or not spin nutation is suppressed by quantum fluctuations. Here, by applying the t-DMRG to the spin- S Kondo impurity model in a magnetic field, we are able to show for the first time that nutation also shows up in the full quantum spin dynamics. Remarkably, however, *quantum nutation* turns out to be strongly damped and shows up on a much shorter time scale as compared to the relaxation time. On a fundamental level, this pinpoints an unconventional new quantum effect in transversal spin dynamics but is also relevant for experimental studies suggesting, *e.g.*, inertia-driven spin switching [26,27] opposed to standard precessional switching [28,29].

Model. – Using standard notations, the Hamiltonian of the Kondo impurity model reads

$$H = -T \sum_{i < j}^{n.n.} \sum_{\sigma=\uparrow,\downarrow} (c_{i\sigma}^\dagger c_{j\sigma} + \text{H.c.}) + J \mathbf{s}_{i_0} \mathbf{S} - \mathbf{B} \mathbf{S}. \quad (1)$$

Here, $c_{i\sigma}$ is the annihilator of an electron with spin projection $\sigma = \uparrow, \downarrow$ at site $i = 1, \dots, L$ of an open one-dimensional chain of length L . The hopping $T = 1$ between nearest-neighbor (n.n.) sites defines the energy and the time scale ($\hbar \equiv 1$). We assume a half-filled band with $N = L$ conduction electrons. The impurity spin \mathbf{S} is coupled antiferromagnetically with exchange coupling constant J to the local spin \mathbf{s}_{i_0} of the itinerant conduction-electron system at the first site of the chain, $i_0 = 1$. With the vector of Pauli matrices $\boldsymbol{\tau}$, we have $\mathbf{s}_i = \sum_{\sigma\sigma'} c_{i\sigma}^\dagger \boldsymbol{\tau}_{\sigma\sigma'} c_{i\sigma'}/2$.

\mathbf{S} is a quantum spin characterized by quantum number $S = \frac{1}{2}, 1, \frac{3}{2}, \dots$, and for $S > 1/2$, eq. (1) is the underscreened Kondo model. Alternatively, \mathbf{S} is considered as a classical spin with fixed length $|\mathbf{S}| = S_{\text{cl.}}$, where $S_{\text{cl.}} = \sqrt{S(S+1)}$ for a meaningful comparison with results for a quantum spin.

Real-time dynamics. – To initiate spin dynamics we consider a local magnetic field \mathbf{B} which, at time $t = 0$, is suddenly switched from $\mathbf{B} = B_{\text{ini}} \hat{x}$, forcing the spin to point in the \hat{x} -direction, to $\mathbf{B} = B_{\text{fin}} \hat{z}$. This addresses,

e.g., spin-resolved scanning-tunneling microscope experiments [30–34]. We choose $B_{\text{ini}} = \infty$ to initially fully polarize the impurity spin. Note that the conduction-electron spin \mathbf{s}_{i_0} in the initial state is also polarized, but typically much weaker, depending on the internal Weiss field $\mathbf{B}_{\text{eff}} \equiv J \mathbf{S}$ produced by the exchange interaction and the impurity spin. The dynamics is (predominantly) transversal if $B_{\text{fin}} \gg T_K$ which ensures that the Kondo singlet remains broken and that there are no (significant) longitudinal spin fluctuations.

For $t \rightarrow \infty$ we expect complete relaxation. This is achieved if the classical spin $\mathbf{S}(t)$ or, in the quantum case, $\mathbf{S}(t) \equiv \langle \mathbf{S} \rangle_t = \langle \Psi(t) | \mathbf{S} | \Psi(t) \rangle$ fully aligns with the \hat{z} -axis. Likewise the expectation value $\mathbf{s}_{i_0}(t) \equiv \langle \mathbf{s}_{i_0} \rangle_t$ of the local conduction-electron spin at i_0 is expected to orient itself antiparallel to $\mathbf{S}(t)$ for $t \rightarrow \infty$.

Time-dependent DMRG. – To study the (quantum) time-evolution of $\mathbf{S}(t)$ and $\mathbf{s}_{i_0}(t)$ after the sudden switch of the field, we employ the time-dependent density-matrix renormalization-group technique (t-DMRG) in the framework of matrix-product states and operators [13]. The implementation of a quantum spin with arbitrary S is straightforward. For an impurity model with the spin attached to the first site of the chain, the numerical effort is essentially independent of S as only the dimension of the local Hilbert space at i_0 scales with $2S + 1$. Due to the global $U(1) \times U(1)$ symmetry of H , the total particle number and the z -component of the total spin are conserved. For a sudden field switch from the \hat{x} - to the \hat{z} -direction, however, only particle-number conservation can be exploited in the t-DMRG calculation. As compared to a purely longitudinal dynamics, this implies an increased computational effort. The time evolution of matrix-product states is computed using the two-site version of the algorithm as suggested in refs. [14,35] which is based on the time-dependent variational principle. The maximum bond dimension reached during the propagation is about 2000.

Quantum-spin dynamics. – We start the discussion with the t-DMRG results, see the red lines in fig. 1. The calculations have been performed for a chain with $L = 80$ sites. For a quantum spin $S = 1/2$ (fig. 1, top panel), and for $J = 1$ and $B_{\text{fin}} = 2$, the dynamics is sufficiently fast, *i.e.*, the main physical effects take place on a time scale shorter than the time where finite-size artifacts show up. In the bulk of the non-interacting conduction-electron system, wave packets typically propagate with group velocity $v_F = d\varepsilon(k)/dk = \pm 2T$ at the Fermi wave vectors $k = k_F = \pm \pi/2$ for half filling. This roughly determines the maximum speed of the excitations and defines a “light cone” [36,37]. Hence, a local perturbation at $i_0 = 1$ starts to show artificial interference with its reflection from the opposite boundary at $i = L$ after a time of about $t_{\text{inter}} = 2L/v_g = L/T$, *i.e.*, after about 80 inverse hoppings – which is well beyond the time scale covered by fig. 1.

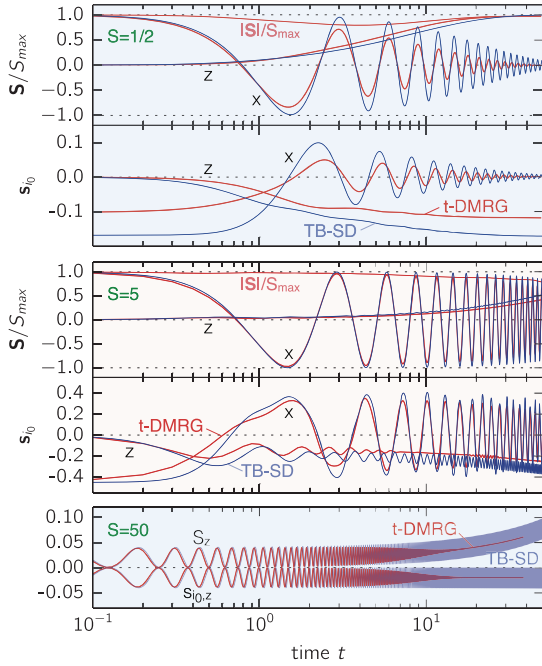


Fig. 1: (Colour online) Top panel, upper part: dynamics of $\mathbf{S}(t)/S_{\max}$ for the Kondo impurity model, eq. (1), for $J = 1$ and $\mathbf{B} = B_{\text{fin}}\hat{z}$ with $B_{\text{fin}} = 2$. Only x and z components are shown. At $t = 0$, the system is prepared with $\mathbf{S}(0)/|\mathbf{S}(0)| = \hat{x}$. Time units are fixed by the inverse hopping $1/T \equiv 1$. Red lines: t-DMRG calculations for a quantum spin, $\mathbf{S}(t) \equiv \langle \Psi(t) | \mathbf{S} | \Psi(t) \rangle$, and $S = 1/2$ ($S_{\max} = S$). Blue lines: semiclassical dynamics (TB-SD) with a classical spin $\mathbf{S}(t)$ of length $S_{\text{cl.}} = \sqrt{S(S+1)} = \sqrt{3}/2$ ($S_{\max} = S_{\text{cl.}}$). Top panel, lower part: local conduction-electron moment $\mathbf{s}_{i_0}(t) \equiv \langle \mathbf{s}_{i_0} \rangle_t$. Middle panel: the same for $S = 5$. Bottom panel: z -components of $\mathbf{S}(t)$ and $\mathbf{s}_{i_0}(t)$ for $S = 50$.

The most obvious effect in the time dependence of $\mathbf{S}(t)$ (see upper part of the top panel) is the precessional motion around the \hat{z} -axis: $S_x(t)$ (and likewise of $S_y(t)$ which is not shown in the figure) oscillate with Larmor frequency $\omega_L \approx B_{\text{fin}}$. Note that $|\mathbf{S}(t)| = |\langle \Psi(t) | \mathbf{S} | \Psi(t) \rangle|$ is nearly constant, *i.e.*, there are no substantial longitudinal fluctuations or Kondo screening.

In addition to the spin precession, there is damping: The spin relaxes to its new equilibrium direction $\propto \hat{z}$ on the relaxation time scale $\tau_{\text{rel}} \approx 50$. Despite the fact that the total energy and the z -component of the total spin are conserved (as is also checked numerically), this is the expected result: At $t = 0$ the system is locally in an excited state; for large t , spin relaxation is achieved by dissipation of energy into the bulk of the chain. The dynamics does not stop until the excitation energy $\sim SB_{\text{fin}}$ is fully dissipated into the bulk, and the system is —locally, close to i_0 — in its ground state.

Conduction-electron dynamics. — In the ground state of the system at time $t = 0$, the local conduction-electron spin at i_0 is partially polarized in the

$-\hat{x}$ -direction, *i.e.*, antiparallel to $\mathbf{S}(t = 0)$ due to the internal magnetic field $J\mathbf{S}(0)$ (see top panel of fig. 1, lower part). For $t > 0$ we find that $\mathbf{s}_{i_0}(t)$ follows the dynamics of the impurity spin $\mathbf{S}(t)$ *almost* adiabatically, *i.e.*, at a given instant of time t it is slightly behind the (instantaneous) ground-state expectation value $\langle \mathbf{s}_{i_0} \rangle_{\text{g.s.}} \uparrow \downarrow \mathbf{S}(t)$ for the conduction-electron system with a “given” Weiss field $J\mathbf{S}(t)$. This slight retardation effect is clearly visible in fig. 1 (compare the location of the first minimum of $S_x(t)$ with the first maximum of $s_{i_0,x}(t)$, for instance). In the semiclassical picture retardation has been identified to drive the relaxation of $\mathbf{S}(t)$ [7].

Quantum nutation. — In addition to the expected precessional motion and relaxation of $\mathbf{s}_{i_0}(t)$, there is a weak additional superimposed oscillation visible in $s_{i_0,z}(t)$. For $S = 1/2$ the frequency is close to the precession frequency. However, the results for higher spin quantum numbers (see lower part of the middle panel, $S = 5$) show that these oscillations have a characteristic frequency ω_N and hence a physical cause which may require but is independent of the precessional motion.

The z -component of the impurity spin actually shows oscillations with the same frequency and almost the same amplitude (which can hardly be seen in the first two panels of fig. 1 due to the rescaling of $\mathbf{S}(t)$ by S_{\max}) but becomes obvious in the bottom panel (no rescaling, $S = 50$). By comparing with the semiclassical spin dynamics, we will argue that this is in fact nutation of the quantum spin.

Tight-binding spin dynamics. — Most (but not all) features of the transversal quantum dynamics are qualitatively captured by the numerically much cheaper “tight-binding spin dynamics” (TB-SD) [7,12], *i.e.*, quantum-classical hybrid or Ehrenfest dynamics. TB-SD originates from the Hamiltonian eq. (1) by treating the impurity spin $\mathbf{S}(t)$ as a classical dynamical observable which couples to the (quantum) system of conduction electrons. Its equation of motion is derived from the canonical equation $\dot{\mathbf{S}} = \{\mathbf{S}, \langle H \rangle_t\}$ (see refs. [7,10] for the Poisson bracket of spin systems), which has the form of a Landau-Lifschitz equation,

$$\dot{\mathbf{S}}(t) = \mathbf{S}(t) \times \mathbf{B} - J\mathbf{S}(t) \times \mathbf{s}_{i_0}(t). \quad (2)$$

To also get $\mathbf{s}_{i_0}(t) = \frac{1}{2} \text{tr}_{2 \times 2} \rho_{i_0 i_0}(t) \boldsymbol{\tau}$, it must be complemented, however, by a von Neumann equation, $i \frac{d}{dt} \rho(t) = [\mathbf{T}(t), \rho(t)]$, for the reduced one-particle density matrix $\rho(t)$ of the electron system whose elements are defined as $\rho_{i i', \sigma \sigma'}(t) \equiv \langle c_{i' \sigma'}^\dagger c_{i \sigma} \rangle_t$. Here, the elements of the effective hopping matrix are $T_{i i', \sigma \sigma'}(t) = -T \delta_{\langle i i' \rangle} \delta_{\sigma \sigma'} + \delta_{i i_0} \delta_{i' i_0} \frac{J}{2} (\mathbf{S}(t) \boldsymbol{\tau})_{\sigma \sigma'}$. The numerical solution using a high-order Runge-Kutta method is straightforward [38].

Results of the semiclassical approach. — TB-SD results are shown by light blue lines in fig. 1. To make contact with the t-DMRG data, we again consider $L = 80$ sites although much larger systems could be treated

numerically (see, for instance, ref. [7]). Overall, the semiclassical theory produces qualitatively very similar results as compared to the quantum dynamics. This concerns the precessional motion, the relaxation time scale and also the occurrence of nutation and the nutation frequency and amplitude.

However, we can identify basically three quantum effects which are different or even absent in the TB-SD:

- i) Initially the local conduction-electron spin at i_0 is less polarized in the quantum case, and this has some quantitative consequences for the subsequent spin dynamics. The reason is that with $S_{\text{cl.}} = \sqrt{S(S+1)}$ the classical Weiss field is stronger: $JS_{\text{cl.}} = J\sqrt{3}/2 > J/2 = JS$.
- ii) Opposed to the classical-spin case, which exclusively comprises transversal dynamics, we find $|\mathbf{S}(t)| \neq \text{const}$ in the quantum case, *i.e.*, there are residual longitudinal fluctuations (see top panel, upper part). Due to the suppression of the Kondo effect by the magnetic field, these are moderate, such that the deviations from the TB-SD are small. One should note, however, that nevertheless (weak) longitudinal fluctuations are *essential* for true quantum-spin dynamics: Assuming the complete absence of longitudinal fluctuations, we would have $\langle \mathbf{S} \rangle_t = S \hat{n}(t)$ with some unit vector $\hat{n}(t)$. Aligning the momentary quantization axis to $\hat{n}(t)$, the quantum state at time t is a product state with zero impurity-bath entanglement. For the impurity-spin equation of motion, $d\langle \mathbf{S} \rangle_t/dt = \langle \mathbf{S} \rangle_t \times \mathbf{B} - J\langle \mathbf{S} \times \mathbf{s}_{i_0} \rangle_t$, this implies the factorization $\langle \mathbf{S} \times \mathbf{s}_{i_0} \rangle_t = \mathbf{S}(t) \times \mathbf{s}_{i_0}(t)$, resulting in eq. (2). With the analogous factorization in the equations of motion for the conduction-electron degrees of freedom, this implies classical spin behavior. Hence, longitudinal fluctuations produce entanglement and quantum effects.
- iii) The nutational motion is strongly damped in the quantum-spin case. Oscillations of $S_z(t)$ and of $s_{i_0,z}(t)$ with frequency ω_N decay on a finite time scale τ_N while there is no visible damping of the nutation for a classical spin on the scale displayed in fig. 1. This is most obvious for $S = 50$ (bottom panel), but also for $S = 5$ (middle panel, lower part).

S dependence. – For large spin quantum numbers, one expects that the quantum-spin dynamics becomes equivalent with that of a classical spin of length $S_{\text{cl.}} = \sqrt{S(S+1)}$ [39–43]. Indeed, the agreement constantly improves with increasing S , see fig. 1. The common trends found with increasing S are the following:

- i) There is a stronger and stronger initial polarization of the local conduction-electron spin at i_0 due to the increasing magnitude of the Weiss field $\mathbf{B}_{\text{eff}} \equiv J\mathbf{S}$ coupling to \mathbf{s}_{i_0} . For $S = 5$ it is more than 80% polarized.

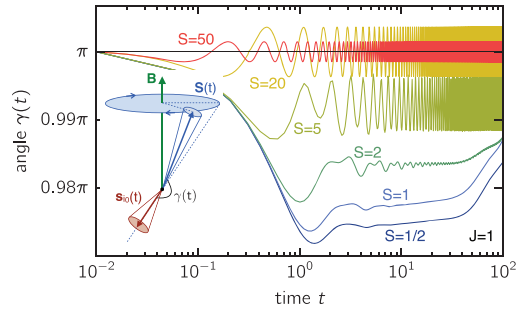


Fig. 2: (Colour online) Angle $\gamma(t)$ between $\mathbf{S}(t)$ and $\mathbf{s}_{i_0}(t)$ in the spin dynamics after the sudden switch of the field from the \hat{x} - to the \hat{z} -direction. TB-SD results for $J = 1$, $B_{\text{fin}} = 0.1$ and different $S_{\text{cl.}} = \sqrt{S(S+1)}$ as indicated. Inset: schematic illustration of the nutational motion, see text.

- ii) The relaxation time τ_{rel} increases with increasing S . For $S = 5$ (see fig. 1, middle panel) $S_z(t)$ has reached only 50% of its final saturation value, and for $S = 50$ (bottom panel) there is hardly any damping visible on the time scale accessible to the t-DMRG computations. Within weak- J perturbation theory and assuming that the spin dynamics is slow as compared to the electronic time scales, we expect $\tau_{\text{rel}} \propto S$ in the large- S limit, as is detailed in ref. [44]. However, for both the semiclassical and the quantum theory, we find $\tau_{\text{rel}} \propto S^2$ from the data. This is at variance with LLG theory and can be traced back to the breakdown of the Markov approximation (see ref. [44]).
- iii) For the nutation frequency we find $\omega_N \propto S$ in the large- S limit (see also the discussion below). The amplitude of the nutation vanishes for $S \rightarrow \infty$ in both, the quantum- and the classical-spin case. In this way quantum- and classical-spin dynamics become equivalent in the large- S limit despite the absence of damping of the nutational motion in the classical case.
- iv) We finally note that $|\mathbf{S}(t)|/S_{\text{max}}$ becomes constant in the quantum case as $S \rightarrow \infty$.

Microscopic cause of nutation. – The nutational motion can be understood easily within the semiclassical approach (except for damping): Recall that the impurity spin precession with frequency $\omega_L \approx B_{\text{fin}}$ is mainly caused by the torque due to the magnetic field and note that the second term on the right-hand side of eq. (2) is small if $\mathbf{s}_{i_0}(t)$ and $\mathbf{S}(t)$ are nearly collinear. In fact, in the instantaneous ground state at time t , the conduction-electron local moment $\mathbf{s}_{i_0}(t)$ would be perfectly aligned antiparallel to $\mathbf{S}(t)$ due to the antiferromagnetic exchange coupling J such that $\mathbf{s}_{i_0}(t)$ exhibits a precessional motion with the same frequency $\omega_L \approx B_{\text{fin}}$. Figure 2 demonstrates that the stronger the effective field JS , the smaller is the deviation of the angle $\gamma(t)$ between $\mathbf{S}(t)$ and $\mathbf{s}_{i_0}(t)$ from $\gamma = \pi$. Generally, however, $\gamma(t) < \pi$ (for all t) since, due to the damping, it takes a finite time for $\mathbf{s}_{i_0}(t)$ to react to the new position of $\mathbf{S}(t)$ (see the inset of fig. 2). Note that for

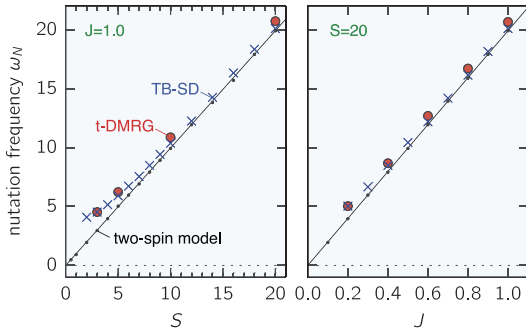


Fig. 3: (Colour online) Nutation frequency ω_N as a function of S for $J = 1$ (left) and as a function of J for $S = 20$ (right). Dynamics initiated by a switch of the field from the \hat{x} - to the \hat{z} -direction with $B_{\text{fin}} = 0.1$. Results for different $S_{\text{cl.}}$ or S , respectively, as obtained by TB-SD (crosses) and t-DMRG (circles) in comparison with the classical two-spin model (filled dots).

very large S only the time average $\overline{\gamma(t)}$ is smaller than π (for instance, see $S \geq 20$ in fig. 2). This retardation effect results in a finite (average) torque $J\mathbf{S}(t) \times \mathbf{s}_{i_0}(t)$ acting on $\mathbf{s}_{i_0}(t)$, as can be seen from its equation of motion:

$$\frac{d}{dt}\mathbf{s}_{i_0}(t) = J\mathbf{S}(t) \times \mathbf{s}_{i_0}(t) + T \text{Im} \sum_{\sigma\sigma'} \langle c_{i_0\sigma}^\dagger \boldsymbol{\tau}_{\sigma\sigma'} c_{i_0+1\sigma'} \rangle_t. \quad (3)$$

The second term on the right-hand side is important for energy and spin dissipation into the bulk of the system and causes the usual damping of the precession of $\mathbf{s}_{i_0}(t)$ (and of $\mathbf{S}(t)$) around \mathbf{B} . The first term, however, leads to nutational motion.

This is most easily understood if there is a separation of time scales, *i.e.*, if the nutation frequency ω_N is large compared to the Larmor frequency $\omega_L \approx B_{\text{fin}}$. In this limit, eq. (3) implies that $\mathbf{s}_{i_0}(t)$ precesses with frequency $\omega_N \approx JS_{\text{cl.}}$ approximately around the momentary direction of $\mathbf{S}(t)$ (which itself slowly precesses around the field direction). Actually, however, due to the retardation, \mathbf{s}_{i_0} precesses around an axis which is slightly tilted as compared to the momentary direction of $\mathbf{S}(t)$. This is nicely demonstrated by the oscillations of $\gamma(t)$ with time-average $\overline{\gamma(t)} < \pi$ as displayed in fig. 2. Furthermore, the equations of motion, eq. (2) and eq. (3), with the second term disregarded, imply that $S_z(t) + s_{i_0z}(t) = \text{const}$ and, therefore, the impurity spin shows the same nutational motion, but with opposite amplitude.

In the middle panel of fig. 1 we in fact observe a fast oscillation of $\mathbf{s}_{i_0}(t)$ with a frequency almost perfectly given by $JS_{\text{cl.}}$ (with $J = 1$ and $S = 5$). Note that the nutation of $\mathbf{S}(t)$ is hardly visible due to the rescaling with $S_{\text{max.}}$. The third panel for $S = 50$ nicely demonstrates the nutational motion of both, $\mathbf{s}_{i_0}(t)$ and $\mathbf{S}(t)$, with opposite amplitudes and common frequency $\omega_N \gg \omega_L$.

Figure 3 displays the results of systematic TB-SD calculations which demonstrate the linear dependence of ω_N on J and S for large JS . These calculations have been

performed for a much weaker field $B_{\text{fin}} = 0.1$ resulting in a much slower precession of $\mathbf{S}(t)$ around \mathbf{B} . Note the nearly perfect agreement between classical- and quantum-spin calculations also for smaller JS where there is a significant deviation from a linear behavior.

The mechanism described above also explains that the amplitudes of the nutational oscillations vanish in the limit $S \rightarrow \infty$: An increasing internal Weiss field JS more and more aligns $\mathbf{s}_{i_0}(t)$ to $\mathbf{S}(t)$, *i.e.*, $\gamma(t) \rightarrow \pi$. Consequently, the torque $J\mathbf{S}(t) \times \mathbf{s}_{i_0}(t)$ acting on $\mathbf{s}_{i_0}(t)$ vanishes in the large- S limit.

Two-spin model. – Figure 3 additionally presents the results for ω_N as obtained by a semiclassical two-spin model:

$$H_{2\text{-spin}} = J\mathbf{s}\mathbf{S} - \mathbf{B}\mathbf{S}. \quad (4)$$

This model disregards the coupling of the site i_0 to the bulk of the conduction-electron system and thus cannot describe the damping of the precessional motion. Due to the absence of damping, the time-averaged angle is $\overline{\gamma(t)} = \pi$.

From the numerical solution of eq. (4) we also learn that it does not predict any damping of the nutational motion. The nutational oscillations themselves, however, are qualitatively captured by $H_{2\text{-spin}}$ and, in fact, the whole line of reasoning explaining the inertia effect also applies to this model. The nutation frequencies as computed from $H_{2\text{-spin}}$ fit the TB-SD and t-DMRG results rather well for strong effective fields $B_{\text{eff}} \equiv JS \gg T = 1$; stronger deviations are found for $JS \rightarrow 2$ (see fig. 3). For $JS < 2$, there are clear nutational oscillations in the spin dynamics of the full model (1), as is seen in the top panel of fig. 1, but ω_N cannot be defined accurately.

Bound states. – $B_{\text{eff, cr}} = 2$ is actually the critical value of the local effective field $B_{\text{eff}} \equiv JS$ which couples to the local conduction-electron spin at i_0 . For $B_{\text{eff}} > B_{\text{eff, cr}}$ there are two one-particle eigenenergies of the Hamiltonian (1) corresponding to bound states which symmetrically split off the continuum at the lower and at the upper band edge, respectively. Note that $B_{\text{eff, cr}}$ vanishes for a site i_0 in the bulk of an infinite chain as is well known for one-dimensional systems. Contrary, at the edge ($i_0 = 1$) there is a finite critical field, as is reminiscent of the physics in higher dimensions.

The sudden switch of the field excites the system locally at i_0 . Consequently, if $JS > B_{\text{eff, cr}}$, the subsequent dynamics is predominantly local since the excitation is mainly carried by a state whose amplitude is exponentially suppressed with increasing distance from i_0 . The dynamics should be understood in this case as a weak perturbation of the dynamics of the two-spin model eq. (4).

That this also applies to the quantum-spin case is demonstrated with fig. 4 which shows the entanglement entropy \mathcal{S}_{i_0} of the subsystem consisting of the quantum impurity spin and the conduction-electron site i_0 . In the ground state at $t = 0$, the entropy decreases with

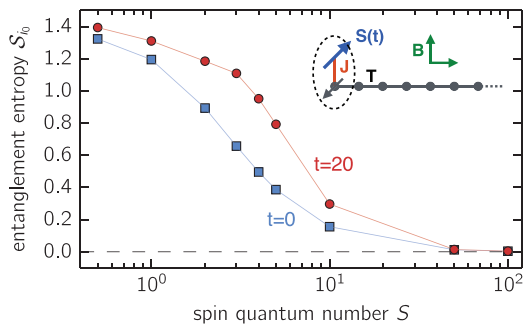


Fig. 4: (Colour online) Entanglement entropy of the two-spin subsystem (impurity spin and site $i_0 = 1$, see dashed ellipse inset) in the environment ($i = 2, \dots, L$) as a function of S for $J = 1$ and at different times $t = 0$ and $t = 20$. t-DMRG results for $B_{\text{fin}} = 2$ and $L = 50$.

increasing effective field JS . For $JS = 50$ it nearly vanishes which implies that ground-state expectation values of local observables at i_0 are almost perfectly described with the (quantum version of the) two-spin model eq. (4). With increasing time t , the entropy generally increases, while for strong effective fields JS is stays close to zero, *i.e.*, the two-spin model also well captures the dynamics of local observables in this case.

Damping of quantum nutation. – To explain the efficient damping of the nutational motion on a very short time scale τ_N in the quantum-spin case, we first consider the quantum variant of the two-spin model eq. (4), *i.e.*, both, \mathbf{S} and \mathbf{s} , are considered as quantum spins with spin quantum numbers S and $1/2$, respectively. The time-dependent expectation value $S_z(t)$ after the sudden switch of the field is readily computed and shows oscillations with frequency ω_N . Already in the two-spin model those are damped on a time scale τ_N which agrees with that seen in the results of the full model in fig. 1 for $S \geq 5$. Writing $S_z(t) = \langle S_z \rangle_t = \sum_{m,n} c_{m,n} \exp(i(E_m - E_n)t)$ with energy eigenstates m and n of $H_{2\text{-spin}}$ and coefficients $c_{m,n}$ depending on the preparation of the initial state, it becomes obvious that this damping results from the dephasing of oscillations with the excitation energies $E_m - E_n$ of the system.

Due to the small Hilbert-space dimension of the two-spin model, however, there are strong revivals of the oscillations occurring at finite revival times. In fact, for $S = 5$, the first revival of nutational oscillations of $s_{i_0z}(t)$ can be seen in the t-DMRG result around $t = 20$ (fig. 1, middle panel, lower part). With increasing S and thus with increasing Hilbert space, however, the revival times quickly exceed the time scale accessible to t-DMRG in the full model. Furthermore, as the example for $S = 5$ in fig. 1 shows, the revivals themselves are strongly damped in the full theory, opposed to the nearly perfect revivals in the two-spin-model dynamics. As this (secondary) damping of nutation is caused by the residual effective coupling of the two-spin model to the bulk of the system, it becomes

less and less efficient with increasing S , while at the same time the revival time strongly increases and the amplitude of the oscillations decreases.

Conclusions. – Inertia effects in spin dynamics have been discussed intensively in the recent years, mainly in the context of applications for magnetic devices [15–27]. The most fundamental system which covers the essentials of spin dynamics, however, namely a single spin coupled to a Fermi sea has not yet been addressed in this respect. Applying exact quantum and semiclassical numerical techniques to the Kondo impurity model, we could demonstrate that the real-time dynamics, initiated by switching the direction of a magnetic field coupled to the spin, not only exhibits spin precession and spin relaxation but also nutational motion known from a gyroscope. The effect not only shows up in the impurity-spin dynamics but also in the dynamics of the conduction-electron local magnetic moments. It is very robust and found in a large regime of coupling constants using tight-binding spin dynamics and treating the spin as a classical observable. We find that nutation amplitudes are small as compared to amplitudes in precessional motion. The frequency is, in the strong-coupling limit, linear in J and S_{cl} .

Our study has demonstrated that nutational motion is not restricted to classical-spin systems but is robust against quantum fluctuations. Despite the fundamental differences between semiclassical and quantum dynamics, quantum-spin nutation is found to be very similar to the classical-spin case in many respects. There is a qualitative, and with increasing spin-quantum numbers also quantitative agreement between quantum and semiclassical dynamics. Kondo screening of the impurity spin represents an important exception which, however, in the present study plays a minor role only as Kondo-singlet formation is inhibited by the external field.

The main effect of the quantum nature of the spin is a very efficient damping of the nutational motion on a very short (femtosecond) time scale which is basically independent of the relaxation time scale for the precessional motion. In the strong-coupling ($JS \rightarrow \infty$) limit, the spin dynamics is essentially local and captured by an emergent two-spin model which has served to understand the physical origin of the damping of quantum nutation, namely dephasing of local spin excitations with revivals suppressed by the coupling to the bulk of the system.

An important implication of our study is that direct observation of nutational motion, *e.g.*, of magnetic nanoparticles with a (quantum) macrospin S coupled to the conduction-electron band of a nonmagnetic metallic surface, requires a sub-picosecond time resolution. On the other hand, inertia-driven spin switching in antiferromagnets [26,27] has already been demonstrated successfully.

We would like to thank CHRISTOPHER STAHL for instructive discussions. Support of this work by the

Deutsche Forschungsgemeinschaft within the SFB 668 (project B3), within the SFB 925 (project B5), and by the excellence cluster “The Hamburg Centre for Ultrafast Imaging - Structure, Dynamics and Control of Matter at the Atomic Scale” is gratefully acknowledged. Numerical calculations were performed on the PHYSnet HPC cluster at the University of Hamburg.

REFERENCES

- [1] KONDO J., *Prog. Theor. Phys.*, **32** (1964) 37.
- [2] HEWSON A. C., *The Kondo Problem to Heavy Fermions* (Cambridge University Press, Cambridge) 1993.
- [3] MEDVEDYEVA M., HOFFMANN A. and KEHREIN S., *Phys. Rev. B*, **88** (2013) 094306.
- [4] NUSS M., GANAHL M., ARRIGONI E., VON DER LINDEN W. and EVERTZ H. G., *Phys. Rev. B*, **91** (2015) 085127.
- [5] LANDAU L. D. and LIFSHITZ E. M., *Phys. Z. Sowjetunion*, **8** (1935) 153.
- [6] ANDERS F. B. and SCHILLER A., *Phys. Rev. B*, **74** (2006) 245113.
- [7] SAYAD M. and POTTHOFF M., *New J. Phys.*, **17** (2015) 113058.
- [8] GILBERT T., *Phys. Rev.*, **100** (1955) 1243.
- [9] GILBERT T., *IEEE Trans. Magn.*, **40** (2004) 3443.
- [10] ELZE H. T., *Phys. Rev. A*, **85** (2012) 052109.
- [11] SALCEDO L. L., *Phys. Rev. A*, **85** (2012) 022127.
- [12] SAYAD M., RAUSCH R. and POTTHOFF M., *Phys. Rev. Lett.*, **117** (2016) 127201.
- [13] SCHOLLWÖCK U., *Ann. Phys. (N.Y.)*, **326** (2011) 96.
- [14] HAEGEMAN J., CIRAC J. I., OSBORNE T. J., PIŻORN I., VERSCHELDE H. and VERSTRAETE F., *Phys. Rev. Lett.*, **107** (2011) 070601.
- [15] BUTIKOV E., *Eur. J. Phys.*, **27** (2006) 1071.
- [16] WEGROWE J.-E. and CIORNEI M.-C., *Am. J. Phys.*, **80** (2012) 607.
- [17] CIORNEI M.-C., RUBÍ J. M. and WEGROWE J.-E., *Phys. Rev. B*, **83** (2011) 020410.
- [18] OLIVE E., LANSAC Y. and WEGROWE J.-E., *Appl. Phys. Lett.*, **100** (2012) 192407.
- [19] BÖTTCHER D. and HENK J., *Phys. Rev. B*, **86** (2012) 020404(R).
- [20] FÄHNLE M., STEIAUF D. and ILLG C., *Phys. Rev. B*, **84** (2011) 172403.
- [21] BHATTACHARJEE S., NORDSTRÖM L. and FRANSSON J., *Phys. Rev. Lett.*, **108** (2012) 057204.
- [22] KIKUCHI T. and TATARA G., *Phys. Rev. B*, **92** (2015) 184410.
- [23] TATARA G., KOHNO H. and SHIBATA J., *Phys. Rep.*, **468** (2008) 213.
- [24] FÄHNLE M. and ILLG C., *J. Phys.: Condens. Matter*, **23** (2011) 493201.
- [25] EVANS R. F. L., FAN W. J., CHUREEMART P., OSTLER T. A., ELLIS M. O. A. and CHANTRELL R. W., *J. Phys.: Condens. Matter*, **26** (2014) 103202.
- [26] KIMEL A. V., IVANOV B. A., PISAREV R. V., USACHEV P. A., KIRILYUK A. and RASING T., *Nat. Phys.*, **5** (2009) 727.
- [27] KIRILYUK A., KIMEL A. V. and RASING T., *Rev. Mod. Phys.*, **82** (2010) 2731.
- [28] GERRITS T., VAN DEN BERG H. A. M., HOHLFELD J., BÄR L. and RASING T., *Nature (London)*, **418** (2002) 509.
- [29] TUDOSA I., STAMM C., KASHUBA A. B., KING F., SIEGMANN H. C., STÖHR J., JU G., LU B. and WELLER D., *Nature (London)*, **428** (2004) 831.
- [30] WIESENDANGER R., *Rev. Mod. Phys.*, **81** (2009) 1495.
- [31] NUNES G. and FREEMAN M. R., *Science*, **262** (1993) 1029.
- [32] MORGENSTERN M., *Science*, **329** (2010) 1609.
- [33] LOTH S., ETZKORN M., LUTZ C. P., EIGLER D. M. and HEINRICH A. J., *Science*, **329** (2010) 1628.
- [34] YAN S., CHOI D.-J., BURGESS J. A. J., ROLF-PISSARCZYK S. and LOTH S., *Nat. Nanotechnol.*, **10** (2015) 40.
- [35] HAEGEMAN J., LUBICH C., OSELEDETS I., VANDEREYCKEN B. and VERSTRAETE F., *Phys. Rev. B*, **94** (2016) 165116.
- [36] LIEB E. H. and ROBINSON D. W., *Commun. Math. Phys.*, **28** (1972) 251.
- [37] BRAVYI S., HASTINGS M. B. and VERSTRAETE F., *Phys. Rev. Lett.*, **97** (2006) 050401.
- [38] VERNER J. H., *Numer. Algorithms*, **53** (2010) 383.
- [39] LIEB E. H., *Commun. Math. Phys.*, **31** (1973) 327.
- [40] KLADKO K., FULDE P. and GARANIN D. A., *Europhys. Lett.*, **46** (1999) 425.
- [41] GARANIN D. A., KLADKO K. and FULDE P., *Eur. Phys. J. B*, **14** (2000) 293.
- [42] GARANIN D. A., *Phys. Rev. B*, **78** (2008) 144413.
- [43] SAYAD M., GÜTERSLOH D. and POTTHOFF M., *Euro. Phys. J. B*, **85** (2012) 125.
- [44] See Supplemental Material at URL <http://arxiv.org/abs/1609.05526>.

6. Pump-probe spectra

6.1. Introduction

Auger electron spectroscopy has recently received a further surge of attention with the advent of attosecond physics, allowing experimentalists to steer and control electron dynamics on a very short time scale by varying pump-probe delay times and pulse intensities. The pioneering experiments [[Drescher et al. 2002](#); [Cavalieri et al. 2007](#)] and theoretical studies [[Smirnova, Yakovlev, and Scrinzi 2003](#); [Kazansky, Sazhina, and Kabachnik 2009](#)] have been so far performed for atoms in the gas phase, but upcoming experiments for condensed-matter systems are anticipated. Hence, the present work attempts to make some first predictions of what to expect of a pump-probe spectrum for strongly correlated solids and what kind of setups may be of interest.

The Hubbard system is excited by a laser pump pulse of strength \mathcal{E}_0 and colour Ω , described by a harmonic cosine term which is damped by a Gaussian envelope of width σ_t :

$$\mathcal{E}(t) = \mathcal{E}_0 \cos [\Omega(t - t_0)] \exp \left[-\frac{1}{2} \left(\frac{t - t_0}{\sigma_t} \right)^2 \right]. \quad (6.1)$$

The corresponding vector potential is given by the integral

$$A(t) = - \int_{-\infty}^t dt' \mathcal{E}(t'), \quad (6.2)$$

which can be expressed in terms of the complex error function. The latter can be calculated numerically in an efficient manner using the Faddeeva package [[Johnson 2013](#)]. The vector potential enters the Hubbard system via the Peierls substitution (see chapter 2.1.5).

After a certain delay time Δt , the system is hit by a probe pulse of the same general shape, but with a high frequency inducing the transition $a_{\sigma}^{\dagger}(\epsilon) f_{i\sigma}$ which removes an electron from a deep-lying core state. Following this, the Auger process is free to happen and the number of Auger electrons in a given range of the kinetic energy is measured.

6.2. Computational details

The computational setup for the pump-probe spectra is somewhat elaborate and requires some explanation. It is in fact most convenient to use formula (2.59), even though it is nonperturbative. In order to maintain continuity with the previous results for the two-hole spectral function based on perturbation theory, the Coulomb matrix element is simply set to a value much smaller than any other energy scale of the system, $U_A = 0.001$. The system is then propagated through the pump pulse using the CFET technique combined with a Lanczos propagator in order to calculate the matrix exponentials (see chapter 3.4).

The scattering continuum is coupled as a semi-infinite chain which is cut at the far end (see appendix

C). One has to take care that the wavepacket of the Auger electron which moves through the chain does not hit this cutoff (which would lead to unphysical results), i.e. the chain must be long enough so that the occupancy number at the last site remains negligibly small.

Finally, the integral in eq. (2.59) has to be taken care of. This can be done efficiently by realizing that for a very high frequency of the probe¹, its fast oscillations cannot be felt by the much slower system (this is similar to the *rotating wave approximation* common to optics), so that only the envelope $s^2(t)$ remains. Since this is a Gaussian, it is positive definite and can be regarded as a weight function for the integral. Hence, it is possible to create adapted Gaussian integration weights for it using the Golub-Welsch algorithm [Golub and Welsch 1969]. It turns out that it is quite sufficient to work with only three integration points. This is of great help, as each point necessitates a time propagation.

6.3. Pump-probe spectra

At first one needs to make a choice about the pump parameters. In the following calculations, $\sigma_t = 1$ is always kept. Furthermore, we shall always work at half filling, where one has the largest phase space for the increase of the double occupancy d_{tot} . Fig. 6.1(a) shows the value of d_{tot} which settles in after a pump with various \mathcal{E}_0 and Ω . Since it becomes nearly constant after the pulse is over, the values are averaged over the remaining time interval.

In order to excite electrons across the charge gap, the frequency must be at least as large as the gap itself, which for $U = 6$ is found to be $\Delta = 1.446$ from the Bethe ansatz. For transitions from the barycentre of the lower Hubbard band to the barycentre of the upper Hubbard band, it should be around $W/2 + W/2 + \Delta \approx 5.4$. Indeed, one finds that the largest value of the double occupancy is achieved with $\Omega \approx 4$, which is the right order of magnitude. The optimal field strength turns out to be $\mathcal{E}_0 \approx 8$. Note that too small a frequency is not well defined due to the finite duration of the pump pulse which cuts off the oscillations prematurely. Furthermore, the double occupancy shows higher fluctuations in this case.

With the naive pump-probe setup described above, a problem comes up immediately: While the pump pulse will put energy into the system, allowing electrons to bridge the Hubbard gap, thereby increasing the double occupancy, due to the high stability of doublons, the double occupancy will not relax on a short to intermediate time scale (as we have seen in chapter 5.1.2). This means that the resulting spectrum will be dependent on the parameters of the pump pulse, but there will be no dependence on the pump-probe delay Δt in this range and thus no additional time resolution. To demonstrate this, a series of pump-probe spectra is shown in fig. 6.1(b) and the double occupancy as a function of time is displayed in the inset of fig. 6.1(a).

This means that the pure Hubbard-like physics does not really lend itself to pump-probe Auger experiments and one has to make the setup more sophisticated. For example, the pump could be made rather slow, allowing the double occupancy to vary over a prolonged time interval, so that the probe hits the system while the pump is still active. Another idea is to reverse the order of the pump and probe. This is possible since the core hole has a finite lifetime, so that the final states it decays into can be modified at the beginning or at the end of it; and a dependence on the delay will be achieved. Finally, one may seek out systems which go beyond the physics of the Hubbard model and are described by an extended variant of it. Such a system will be presented in the next chapter.

¹It must necessarily be high in order to be able to bridge the gap between the deep core state and a high-energy scattering state

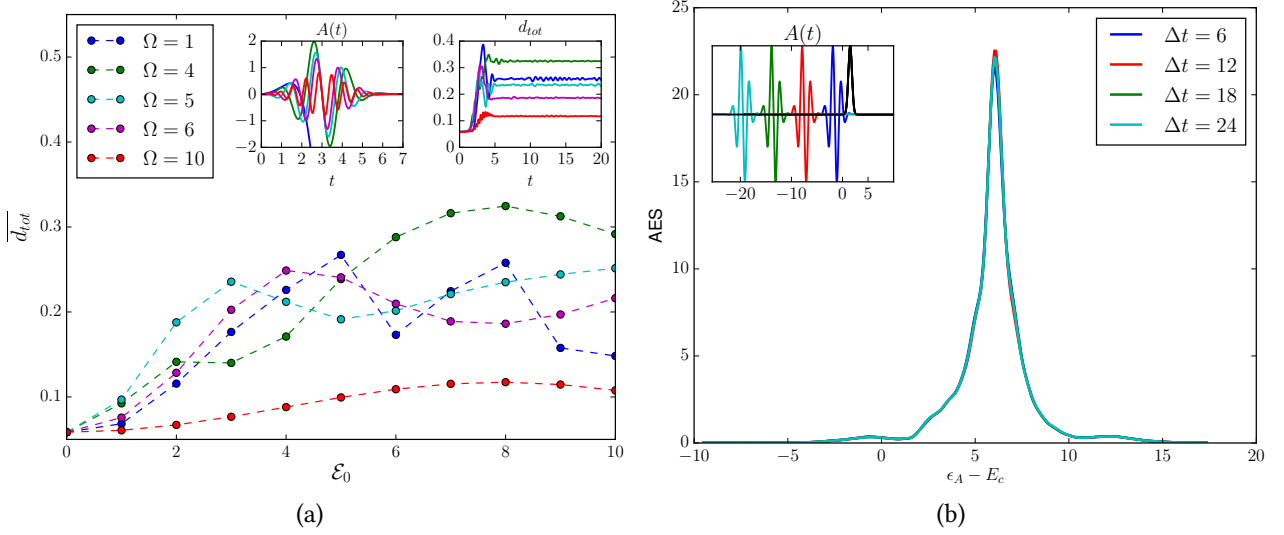


Figure 6.1.: (a) Double occupancy after a pump pulse $\overline{d_{tot}}$, averaged between $t = 7$ and $t = 20$ as a function of the electric field strength \mathcal{E}_0 for various frequencies Ω of the light field. ED calculations for $L = 12$, $U = 6$, $n = 1$ with periodic boundary conditions. The left inset shows the pump pulse, the right inset shows the double occupancy as a function of time, both for $\mathcal{E}_0 = 8$. (b) Pump-probe Auger spectra for the same system parameters as in (a) with $\mathcal{E}_0 = 8$ and $\Omega = 4$.

6.4. The dynamic Hubbard model

A plausible ansatz to achieve a relaxation of double occupancy is to couple the Hubbard system to phonons or, in general, bosonic degrees of freedom. The simplest way to approach this is to treat them classically. The Hamiltonian now has the following form:

$$H = H_{el} + H_{lat} + H_{int}, \quad (6.3)$$

where the lattice part just consists out of classical harmonic oscillators at each site:

$$H_{lat} = \frac{1}{2m} \sum_i p_i^2 + \frac{m\omega_0^2}{2} \sum_i q_i^2. \quad (6.4)$$

Each oscillator displacement is coupled to an operator A_i of the system, which will be specified later:

$$H_{int} = \lambda \sum_i q_i A_i, \quad (6.5)$$

where λ is the coupling strength. To derive the classical equation of motion, one has to assume that the classical Hamilton function is given by the expectation value of the Hamiltonian:

$$H_{class} = \langle H \rangle. \quad (6.6)$$

The Hamiltonian equations of motion read:

$$\begin{aligned}\dot{q}_i &= \frac{\partial H_{\text{class}}}{\partial p_i} = \frac{p_i}{m}, \\ \dot{p}_i &= -\frac{\partial H_{\text{class}}}{\partial q_i} = -(m\omega_0^2 q_i + \lambda \langle A_i \rangle_t).\end{aligned}\tag{6.7}$$

Eliminating the momentum gives a closed equation of motion for the oscillator displacements:

$$m\ddot{q}_i + m\omega_0^2 q_i + \lambda \langle A_i \rangle_t = 0.\tag{6.8}$$

One can see that the expectation value $\langle A_i \rangle_t$ acts like a time-dependent force on the classical system. At this point it is convenient to introduce a rescaled interaction k and coordinate u_i :

$$\begin{aligned}k &:= \frac{\lambda}{\sqrt{m\omega_0^2}}, \\ u_i &:= \sqrt{m\omega_0^2} q_i.\end{aligned}\tag{6.9}$$

Thus the interaction term just becomes:

$$H_{\text{int}} = k \sum_i u_i A_i.\tag{6.10}$$

Note that if A is dimensionless, k and u have the dimension of \sqrt{E} . The transformed equation of motion for u_i becomes:

$$\frac{1}{\omega_0^2} \ddot{u}_i + u_i + k \langle A_i \rangle_t = 0.\tag{6.11}$$

We assume that the system is in its ground state at $t = t_0$, for which the subscript “g” shall be used: $\langle \cdot \rangle_{t=t_0} = \langle \cdot \rangle_g$. The equilibrium position of the oscillators $u_i^{(0)}$ is then found by setting $\dot{u}_i^{(0)} = 0$ and one obtains:

$$u_i^{(0)} = -k \langle A_i \rangle_g.\tag{6.12}$$

This can be found numerically by a self-consistent computation, updating $\langle A_i \rangle_g$ after each ground-state calculation until convergence is reached. Note that the equilibrium solution does not depend on the oscillator frequency ω_0 , as it is in rest. The interaction term during the self-consistent loop in fact shows similarity to a mean-field decoupled Hamiltonian:

$$H_{\text{int}} = -k^2 \sum_i \langle A_i \rangle_g A_i.\tag{6.13}$$

The full, time-dependent solution is found to be:

$$u_i(t) = -k \langle A_i \rangle_g \cos(\omega_0(t - t_0)) + k\omega_0 \left[\int_{t_0}^t dt' [\cos(\omega_0 t) \sin(\omega_0 t') - \sin(\omega_0 t) \cos(\omega_0 t')] \langle A_i \rangle_{t'} \right],\tag{6.14}$$

with the initial conditions $u_i(t_0) = u_i^{(0)}$ and $\dot{u}_i(t_0) = 0$. The total energy is conserved as long as $H_{\text{el}} \neq H_{\text{el}}(t)$ and reads in the rescaled units:

$$\begin{aligned} E_{\text{tot}} &= E_{\text{el}} + E_{\text{int}} + E_{\text{lat,kin}} + E_{\text{lat,pot}} \\ &= \langle H_{\text{el}} \rangle + k \sum_i u_i \langle A_i \rangle + \frac{1}{2\omega_0^2} \sum_i \dot{u}_i^2 + \frac{1}{2} \sum_i u_i^2. \end{aligned} \quad (6.15)$$

Numerically, after propagating the electronic system over a small time step δt , the oscillator displacements in eq. (6.14) can be updated and $\partial E_{\text{tot}}/\partial t \approx 0$ as well as $\ddot{u}_i/\omega_0^2 + u_i + k\langle A_i \rangle_t \approx 0$ can be taken as error estimates.

Several choices for A_i are possible:

- A coupling to the particle density, $A_i = n_i$, defines the semiclassical Holstein model [Kalosakas, Aubry, and Tsironis 1998].
- A coupling to the hopping term, $H_{\text{int}} = k \sum_{i\sigma} (u_{i+1} - u_i) (c_{i+1,\sigma}^\dagger c_{i\sigma} + \text{h.c.})$, defines the Su-Schrieffer-Heeger model [Su, Schrieffer, and Heeger 1979], which was originally introduced to describe polyacetylene, but has seen a resurgence in the last years as a demonstration model for topological insulators (without interaction)².
- A coupling to the double occupancy $A_i = d_i = n_{i\uparrow}n_{i\downarrow}$ defines a particular *dynamic Hubbard model* [Hirsch 2001; Werner and Eckstein 2016]. The motivation behind this ansatz is that a doubly occupied orbital will spatially expand to reduce the Coulomb interaction between the electrons, so that there is no particle-hole symmetry between empty and doubly occupied sites any longer. The oscillators now cause an effective Coulomb interaction $U_{i,\text{eff}} := U + ku_i$. This class of models owes its name to this very fact: The Hubbard interaction is not just a fixed parameter anymore. This “dynamic” modification can be done in various ways, however – for example by a coupling to auxiliary spins [Bach, Hirsch, and Marsiglio 2010] or quantum bosons [Marsiglio, Teshima, and Hirsch 2003] rather than classical oscillators. Note also that a mean-field decoupling of the Hubbard term produces a Holstein-like coupling.

In the following chapter, the dynamic Hubbard model will be investigated using Auger electron spectroscopy. It stands to reason that this kind of physics with an asymmetry between empty and doubly occupied sites (or between the lower and upper Hubbard band) is well-suited to be probed by AES where the doublon creators and annihilators bridge this gap.

Before looking at the spectra, let us take a brief look at the equilibrium properties. It turns out that there are two phases: As long as k is small, one finds a slight reduction of the Coulomb interaction $U_{\text{eff}} < U$. Accordingly, the double occupancy increases slightly. As soon as k exceeds a critical value, however, the energy gain due to the oscillators is so large that U becomes negative and the double occupancy is maximized. In order to optimize the kinetic energy as well, the system goes into a charge density wave (CDW) phase, where empty and doubly occupied sites alternate. This is also the ground state one would find for a static $U < 0$. The resulting phase diagram is shown in fig. 6.2. For small values of U , one finds a crossover region where $\langle d_i \rangle$ does not exactly alternate between 0 and 1, for larger values of U the phase transition is remarkably sharp for a finite system.

²The coupling breaks translational invariance, leading to two sublattices and thus two subbands with a gap. Depending on the ratio of the two effective hoppings, there can be a topologically non-trivial phase with localized edge states for open boundary conditions; and in the bulk, a non-zero winding number of the mapping $S^1 \rightarrow S^1$ inherent to the Hamiltonian in k -space in the basis of Pauli matrices $H(k) = \mathbf{d}(k) \cdot \boldsymbol{\sigma}$.

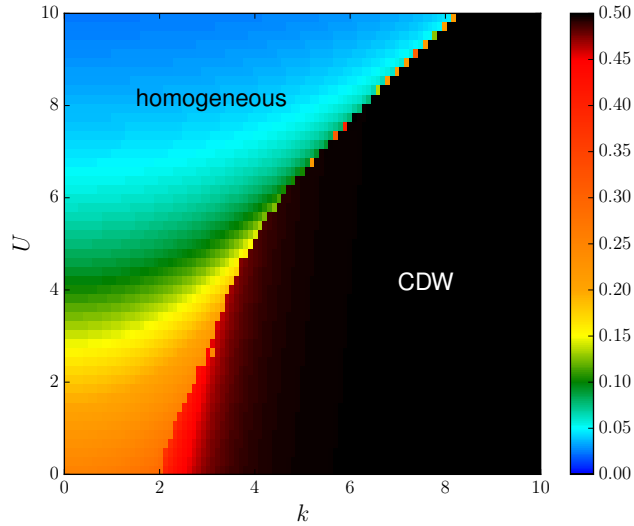


Figure 6.2.: Phase diagram of the dynamic Hubbard model as a function of the electron-oscillator coupling k and Hubbard interaction U for $L = 10$ sites at half filling with periodic boundary conditions. The total double occupancy d_{tot} is colour-coded. In the charge density wave phase (CDW), the local double occupancy $\langle d_i \rangle$ alternates between 0 and 1 (within numerical errors), leading to $d_{\text{tot}} = 0.5$.

For $U = 6$, the critical value is found to be $k_c \approx 4.6$. Note that for large U , the phase boundary is given by $k \lesssim U$, meaning that the phase transition takes place when k becomes comparable to U . The Auger spectra discussed in the following chapter will be all calculated for the homogeneous phase.

6.4.1. Pump-probe AES spectra

Fig. 6.3 shows pump-probe AES spectra for the dynamic Hubbard model³. One can distinguish the cases of weak and strong coupling to the oscillators ($k = 2$ on the left and $k = 4$ on the right) as well as the adiabatic and nonadiabatic regimes ($\omega_0 = 0.1$ on top and $\omega_0 = 1$ on the bottom)⁴.

Let us look at first at the weakly coupled adiabatic case: Contrary to what might have been expected, the double occupancy does not decay after the pulse is over, even in the presence of the oscillators, but still remains nearly constant. Nevertheless, U_{eff} changes and in fact starts to oscillate with the frequency ω_0 (upper inset) and a period $\tau = 2\pi/\omega_0 \approx 62.8$, much larger than the pump-probe delay in this case. The particular value of the double occupancy after the pump gives the Auger spectrum its shape, but there is an additional energetic shift which depends on the value and variation of U_{eff} within the core hole lifetime. Since the coupling is weak, U_{eff} drops only slightly and oscillates around an average value of $\overline{U_{\text{eff}}} \sim 5$, so that the spectrum shifts only slightly as well. Furthermore, since U_{eff} oscillates with the frequency ω_0 , one expects the spectrum to behave accordingly and shift back once U_{eff} has increased again after a long time.

The strongly coupled adiabatic case is very similar except for the fact that due to the higher value of k , $U_{\text{eff}}(t)$ goes down further and even becomes negative, oscillating around a much smaller value. As

³The calculations have been performed with exact diagonalization for a fairly small system for simplicity (as the surrounding formalism is fairly sophisticated), but should be extendable to DMRG as well, so that larger systems can be treated. In the latter case, it is probably more sensible to couple a spin-1/2 to the double occupancy operator [Bach, Hirsch, and Marsiglio 2010] rather than a classical oscillator and thus work within the Hilbert space of the Kondo model. The disadvantage of a semiclassical system is that the simple strategy of successive subsystem updates requires very small time steps, which would in turn greatly increase the compression error of DMRG.

⁴In the extreme case $\omega_0 \rightarrow \infty$, one reaches the far antiadiabatic limit.

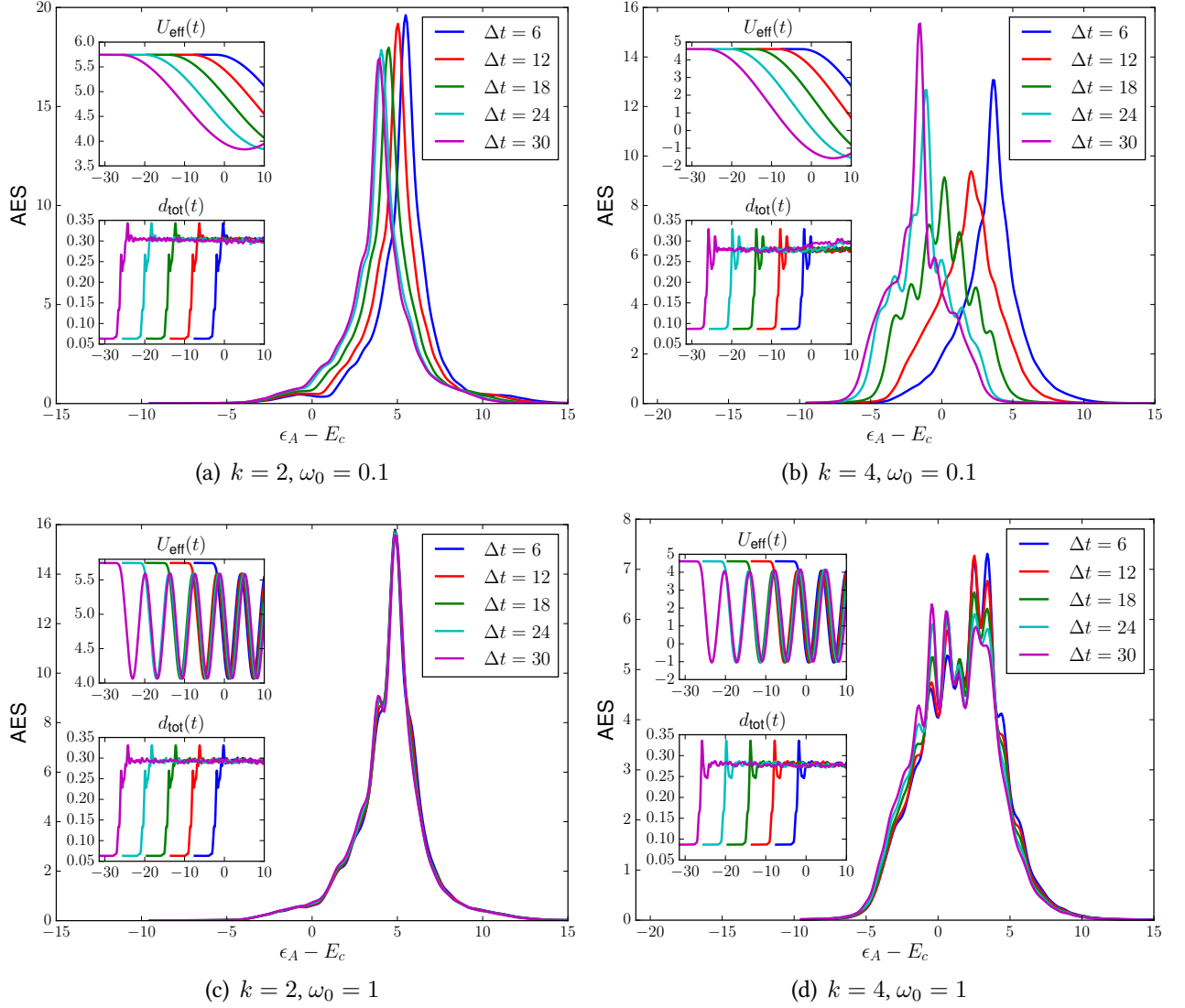


Figure 6.3.: Pump-probe Auger spectra of the dynamic Hubbard model calculated for $L = 10$ sites at half filling with periodic boundary conditions, $U = 6$ and a pump pulse with $\mathcal{E}_0 = 8$ and $\Omega = 4$ for various values of the electron-oscillator coupling k and oscillator frequency ω_0 . The upper insets show the effective Coulomb interaction $U + ku$ (where u is the dimensionless displacement), the lower insets show the double occupancy as a function of time. Note that the probe (core hole emission followed by the Auger process) starts at $t = 0$.

soon as it switches sign, the double occupancy can actually be observed to further increase beyond the value achieved by the pump, though the effect is very small. The spectrum is now also shifted towards higher binding energies and in addition shows stronger distortion.

For the nonadiabatic case, the time scale on which $U_{\text{eff}}(t)$ oscillates is comparable to the pump-probe delay or smaller. Furthermore, the delay time is actually approximately an integer multiple of the oscillation period, $\Delta t \sim n \cdot 2\pi/\omega_0$ ($n \in \mathbb{N}$). Due to the two being in sync and the absence of damping on the given time scale, the dependency on the delay time for both weak and strong electron-oscillator coupling disappears (except for some finite-size noise). Also, an averaging effect sets in, whereby $U_{\text{eff}}(t)$ seems to oscillate too strongly for the double occupancy to react, so that it remains at a constant value, even as $U_{\text{eff}}(t)$ switches sign for $k = 4$.

Summarizing the findings one can say that an electric pulse hitting an electron system described by the dynamic Hubbard model allows electrons to bridge the charge gap, increasing the double occupancy d_{tot} . Still, d_{tot} does not relax at the intermediate time scale, but remains constant. At the same time, the oscillators are tipped off and start to vibrate with their frequency ω_0 , inducing a corresponding oscillation in $U_{\text{eff}}(t)$. The near-independent behaviour of the two quantities is a distinct feature of the nonequilibrium state, as we would expect d_{tot} to change significantly with varying U in equilibrium.

The Auger spectrum allows one to deduce the value of the electron-oscillator coupling k : The larger the energetic shift as a function of Δt , the higher the amplitude of $U_{\text{eff}}(t)$ and the stronger the coupling k . Furthermore, the oscillator frequency ω_0 can be measured with the help of AES by varying the pump-probe delay time Δt : The spectrum looks the same if $2\pi/\Delta t$ is a harmonic of ω_0 . In this way, Auger electron spectroscopy remains an investigative tool of the Coulomb interaction, which for the given model is a time-dependent effective quantity $U_{\text{eff}}(t)$.

The above calculations should be seen as only the first step and further work into pump-probe spectroscopies must be continued [[Rausch and Potthoff n.d.](#)], preferably in close collaboration with the experiment. AES is not the only spectroscopy that can be extended in this way, one can think about pump-probe setups of RIXS and double photoemission (see chapter [2.2.7](#)) as well.

7. Summary and outlook

In this work, the physics of doublons, which are repulsively bound states of two electrons within the Hubbard model, has been investigated from three points of view: (1) the two-hole spectral function, accessible within high-resolution CVV Auger electron spectroscopy, (2) real-time dynamics of the double occupancy, measurable in ultracold atom experiments and (3) pump-probe AES setups, which have yet to be realized experimentally. A side-project consisted in the calculation of spin dynamics and emerging effect of bound states there.

Two-particle spectral function

While the limiting case of two interacting holes has been understood a long time ago, no reliable calculation yet existed for the case of general filling, where one has to deal with a true many-body problem. Such a calculation has become possible, however, with the advent of the DMRG, yielding numerically exact calculations. It has been demonstrated that away from $n = 2$, the doublon satellite blends with a doublon-hole continuum, which can be turned into a bound state of three electrons (“triplon”) with a nearest-neighbour Coulomb interaction V ; that a new bound state of four electrons (“quadruplon”) appears below a filling of $n = 1.5$; and that the doublon lifetime becomes infinite at the Brillouin zone edge in any spatial dimension for a bipartite lattice. The results were also extended to a two-leg Hubbard ladder, where the same general features appear.

It would be interesting to truly extend the results to higher dimensions. A common ansatz used in the case of photoemission spectra in this case is *cluster perturbation theory* (CPT) [Yang and Feiguin 2016], where the Green’s function on an infinite (or very large) lattice is interpolated from a cluster which can be solved exactly. However, since a two-particle Green’s function is governed by the more complicated Bethe-Salpeter equation rather than the Dyson equation, extending this concept to two-particle Green’s functions is not easily done. An ansatz used by several other authors [Brehm et al. 2010; Imriška, Gull, and Troyer 2016] is to make the approximation $\underline{\Gamma}(\omega) = \underline{G}'^{(0)}(\omega)^{-1} - \underline{G}'(\omega)^{-1}$, where the prime index indicates that the quantities belong to the cluster and underlining indicates a matrix in the cluster indices. $\underline{\Gamma}(\omega)$ is then used in the same way as a one-particle self-energy. This has been tried out by the author, but the results were not satisfactory, the application of the two approximations does not seem to yield reliable results. In particular, the high weighting of the noninteracting Green’s function in the CPT formula always leads to a band-like part of the width of $2W$, while one expects a strong renormalization away from $n = 2$.

Hence, in order to calculate Auger spectra in two dimensions, one either needs a modification of CPT or has indeed to solve the very costly Bethe-Salpeter equation. Recent advances in the *dynamical mean field theory* (DMFT) and related methods also seem promising in that the calculation of a two-particle Green’s function becomes feasible [Loon et al. 2016].

Of course, other extensions, as for instance to finite temperatures or disordered systems can also be contemplated.

Another prospect is to actually observe the predicted features, in particular the quadruplon peak, in the experiment. For this, a strongly correlated material slightly above half filling and high resolution away from the Fermi edge are the things that are required. An alternative route could be to

manufacture a Hubbard model on an ultracold lattice and perform an Auger measurement there. A persistent problem in such experiments is the cooling of the lattice.

Using the Bethe ansatz, the band-like part of the spectral function has been analysed to reveal the decay products of the doublon into spinons and holons. It has been shown that decay channels usually involve a pinning of either of them to the Fermi energy, where they have a lot of momentum, but no energy. The multiplonic bound states can be identified with the string solutions of the Bethe ansatz. This is the only part of the work which manifestly contains one-dimensional physics and the band-like part is expected to change significantly in higher dimensions. However, the multiplons are expected to exist in any spatial dimension.

Doublon dynamics

In the real-time dynamics of an initially localized doublon it has been observed that the decayed fraction of doublons increases with decreasing filling, indicating a stabilization. The double occupancy does not relax to the ground state, but still becomes constant at a different value, up to an intermediate time scale. At the same time, the increased phase space for the decay manifests itself in a diffusive behaviour of the doublon cloud, leading to a mixed diffusive/ballistic propagation. Below a certain filling, this picture is only valid for a short time, however, after which such simple models break down.

For this problem, it would be of course very interesting to observe a longer time scale in order to see how the double occupancy eventually relaxes to the ground state after high-order scattering processes of doublons, which one believes to happen. Such time scales are well beyond the numerical methods which exist today, however.

Pump-probe Auger spectroscopy

For the pump-probe AES setup (pumping the system into a nonequilibrium state before probing it with AES) it has been demonstrated that due to the high stability of doublons, no dependence on the pump-probe delay is observed. Several modifications of the setup (slow pump, reversed order of pump and probe) have been suggested and can be implemented in the future. Instead, it has been demonstrated how pump-probe AES could provide one with a measurement of the parameters of the dynamic Hubbard model. But most importantly, an elaborate formalism has been developed, so that such spectra can be calculated at all, involving the mapping of the continuum of scattering states onto a semi-infinite chain. It has been implemented with exact states and small systems, but can be combined with DMRG as well. The same formalism can be used to calculate pump-probe spectra for other multi-particle spectroscopies, as RIXS and double photoemission.

Spin dynamics

It has been demonstrated that bound states strongly influence the magnetization dynamics of impurities coupled to fermionic substrates. Thus, a thinking in such concepts offers insight into understanding the ongoings of such systems. In particular, one needs to be familiar with the concept of an excess energy that cannot be absorbed by the substrate (which is also the reason for the stability of doublons) and of bound states resulting from strong local perturbations that decouple from the rest of the system. Both can severely hinder a complete relaxation of the system up to rather long times.

An extension of the work to more than one spin, introducing RKKY-interaction between them, can be contemplated. Furthermore, it may be useful to implement a generic and efficient quantum-classical propagation algorithm, where the quantum system is described by DMRG, in order to study classical spins coupled to a substrate; and possibly other problems, as the dynamic Hubbard model with classical oscillators.

Appendix

A. Noninteracting two-hole spectral function

The calculation of the two-hole spectral function for a non-interacting system is presented here. The first step is to rewrite it as a time integral:

$$\begin{aligned}
 G_{ij}^{(0)}(\omega) &= \langle 0 | c_{i\downarrow}^\dagger c_{i\uparrow}^\dagger \frac{1}{\omega + i0^+ - E_0^{(N-2)} + H} c_{j\uparrow} c_{j\downarrow} | 0 \rangle \\
 &= \int_0^\infty dt \langle 0 | c_{i\downarrow}^\dagger c_{i\uparrow}^\dagger e^{-i(\omega + i0^+ - E_0^{(N-2)} + H_0)t} c_{j\uparrow} c_{j\downarrow} | 0 \rangle \\
 &= \int_0^\infty dt \langle 0 | c_{i\downarrow}^\dagger(t) c_{i\uparrow}^\dagger(t) c_{j\uparrow}(0) c_{j\downarrow}(0) | 0 \rangle e^{-i(\omega + i0^+)t} e^{-i(E_0^{(N)} - E_0^{(N-2)})t}.
 \end{aligned} \tag{A.1}$$

Now one can insert the Fourier-transformed creation and annihilation operators

$$\begin{aligned}
 c_{\mathbf{k}\sigma} &= \frac{1}{\sqrt{L}} \sum_i e^{-i\mathbf{k}\mathbf{R}_i} c_{i\sigma}, \\
 c_{i\sigma} &= \frac{1}{\sqrt{L}} \sum_{\mathbf{k}} e^{i\mathbf{k}\mathbf{R}_i} c_{\mathbf{k}\sigma},
 \end{aligned} \tag{A.2}$$

exploiting the fact that the time evolution is known in \mathbf{k} -space:

$$c_{\mathbf{k}\sigma}(t) = e^{-i\epsilon(\mathbf{k})t} c_{\mathbf{k}\sigma}(0). \tag{A.3}$$

Carrying out the lattice summations and the time integral, one obtains:

$$G_{ij}^{(0)}(\omega) = \frac{1}{L^2} \sum_{\mathbf{k}_1 \mathbf{k}_2} \frac{\langle n_{\mathbf{k}_1} \rangle \langle n_{\mathbf{k}_2} \rangle e^{i(\mathbf{k}_1 + \mathbf{k}_2)(\mathbf{R}_i - \mathbf{R}_j)}}{\omega + i0^+ + E_0^{(N)} - E_0^{(N-2)} - \epsilon(\mathbf{k}_1) - \epsilon(\mathbf{k}_2)}. \tag{A.4}$$

For free fermions at $T = 0$, the occupancy numbers are given by the Fermi function:

$$\langle n_{\mathbf{k}} \rangle = 1 - \theta(|\mathbf{k}| - k_F), \tag{A.5}$$

which restricts the sum:

$$G_{ij}^{(0)}(\omega) = \frac{1}{L^2} \sum_{|\mathbf{k}_1| < k_F} \sum_{|\mathbf{k}_2| < k_F} \frac{e^{i(\mathbf{k}_1 + \mathbf{k}_2)(\mathbf{R}_i - \mathbf{R}_j)}}{\omega + i0^+ + E_0^{(N)} - E_0^{(N-2)} - \epsilon(\mathbf{k}_1) - \epsilon(\mathbf{k}_2)}. \tag{A.6}$$

Introducing the occupied density of states,

$$\rho^{\text{occ}}(\epsilon) := \frac{1}{L} \sum_{|\mathbf{k}| < k_F} \delta(\epsilon - \epsilon(\mathbf{k})), \quad (\text{A.7})$$

one finally obtains the self-convolution formula:

$$-\frac{1}{\pi} \text{Im} G_{ii}^{(0)}(\omega) = \int d\epsilon \rho^{\text{occ}}(\epsilon) \rho^{\text{occ}}(\omega + E_0^{(N)} - E_0^{(N-2)} - \epsilon). \quad (\text{A.8})$$

B. Time-dependent perturbation theory

B.1. General

We are faced with the general problem of a differential equation, where the differential operator D can be decomposed into a “free” operator D_0 , which poses no problems, and an “interacting” part D_{int} , which complicates things:

$$Du = D_0u + D_{\text{int}}u. \quad (\text{B.1})$$

Then one can formally introduce a dimensionless coupling strength $\lambda \in [0, 1]$:

$$Du = D_0u + \lambda D_{\text{int}}u \quad (\text{B.2})$$

One assumes that the solution can be written as a power series in the interaction strength λ :

$$u = \sum_{k=0}^{\infty} \lambda^k u_k. \quad (\text{B.3})$$

Plugging this into the differential equation yields:

$$\begin{aligned} 0 &= D_0u_0 + D_0 \sum_{k=1}^{\infty} \lambda^k u_k + D_{\text{int}} \sum_{k=0}^{\infty} \lambda^{k+1} u_k \\ &= D_0u_0 + D_0 \sum_{k=0}^{\infty} \lambda^{k+1} u_{k+1} + D_{\text{int}} \sum_{k=0}^{\infty} \lambda^{k+1} u_k \\ &= \sum_{k=0}^{\infty} \lambda^{k+1} (D_0u_{k+1} + D_{\text{int}}u_k) + D_0u_0. \end{aligned} \quad (\text{B.4})$$

This gives an iterative solution scheme: By calculating u_{k+1} from a previous u_k via setting

$$D_0u_{k+1} + D_{\text{int}}u_k = 0 \quad (\text{B.5})$$

one obtains the solution to the order $k + 1$. At each step, the calculation of u_{k+1} involves solving an inhomogeneous problem where the inhomogeneity $D_{\text{int}}u_k$ is known from the previous step. The starting point of the iteration is obtained from the free solution $D_0u_0 = 0$.

B.2. Time domain

For the Schrödinger equation with the Hamiltonian of the type $H(t) = H_c + s(t) V_p$ (see chapter 2.2.2), we now identify:

$$\begin{aligned} D_0 &= i \frac{\partial}{\partial t} - H_c, \\ D_{\text{int}} &= -s(t) V_p. \end{aligned} \quad (\text{B.6})$$

Thus, the free part (zeroth order) is given by:

$$i \frac{\partial}{\partial t} |\Psi^{(0)}(t)\rangle = H_c |\Psi^{(0)}(t)\rangle, \quad (\text{B.7})$$

and the solution reads:

$$|\Psi^{(0)}(t)\rangle = e^{-iH_c t} |\Psi(0)\rangle. \quad (\text{B.8})$$

In first order, we get:

$$i \frac{\partial}{\partial t} |\Psi^{(1)}(t)\rangle = H_c |\Psi^{(1)}(t)\rangle + s(t) V_p e^{-iH_c t} |\Psi(0)\rangle. \quad (\text{B.9})$$

This can be solved by introducing an integrating factor $U_c^\dagger(t)$ with the following property:

$$-i \frac{\partial}{\partial t} U_c^\dagger(t) = U_c^\dagger(t) H_c. \quad (\text{B.10})$$

Namely, differentiating the product $U_c^\dagger(t) |\Psi^{(1)}(t)\rangle$ one obtains:

$$\begin{aligned} i \frac{\partial}{\partial t} (U_c^\dagger(t) |\Psi^{(1)}(t)\rangle) &= -U_c^\dagger(t) H_c |\Psi^{(1)}(t)\rangle + i U_c^\dagger(t) \frac{\partial}{\partial t} |\Psi^{(1)}(t)\rangle \\ &= U_c^\dagger(t) s(t) V_p e^{-iH_c t} |\Psi(0)\rangle. \end{aligned} \quad (\text{B.11})$$

Now a solution by integration is possible:

$$|\Psi^{(1)}(t)\rangle = -i (U_c^\dagger)^{-1}(t) \int_0^t dt' U_c^\dagger(t') s(t') V_p e^{-iH_c t'} |\Psi(0)\rangle + (U_c^\dagger)^{-1}(t) |\Psi(0)\rangle. \quad (\text{B.12})$$

To this we need to add the differential equation for the integrating factor, which is just the Schrödinger equation for $\langle \Psi^{(0)}(t) | = \langle \Psi^{(0)}(0) | U_c^\dagger(t)$. The corresponding equation for $|\Psi^{(0)}(t)\rangle = U_c(t) |\Psi^{(0)}(0)\rangle$ is found by taking the adjoint (and acting on $|\Psi^{(0)}(0)\rangle$):

$$i \frac{\partial}{\partial t} U_c(t) = H_c U_c(t). \quad (\text{B.13})$$

We need to impose the boundary condition

$$U_c(0) = U_c^\dagger(0) = \mathbb{1}. \quad (\text{B.14})$$

Hence the solution reads:

$$\begin{aligned} U_c^\dagger(t) &= e^{iH_c t}, \\ (U_c^\dagger)^{-1}(t) &= U_c(t) = e^{-iH_c t}. \end{aligned} \quad (\text{B.15})$$

Finally, the first-order result reads:

$$|\Psi^{(1)}(t)\rangle = e^{-iH_c t} |\Psi(0)\rangle - i e^{-iH_c t} \int_0^t dt' s(t') e^{iH_c t'} V_p e^{-iH_c t'} |\Psi(0)\rangle. \quad (\text{B.16})$$

B.3. The Laplace transform

For time-homogeneous spectroscopies it is often more convenient to work directly in the energy domain by Laplace-transforming the Schrödinger equation¹. Let us therefore briefly summarize the main facts about the Laplace transform. It is defined via:

$$\mathcal{L}[f(t)](p) = \bar{f}(p) = \int_0^\infty dt e^{-pt} f(t), \quad \text{Re } p > 0. \quad (\text{B.17})$$

For the inverse transform, one has to solve the Bromwich integral in the complex plane:

$$f(t) = \frac{1}{2\pi i} \lim_{T \rightarrow \infty} \int_{c-iT}^{c+iT} dp e^{pt} \bar{f}(p). \quad (\text{B.18})$$

The integration path is a parallel line $\text{Re } p = c$ to the imaginary axis and c is chosen such that it is greater than the real part of all singularities of $\bar{f}(p)$.

For physical applications, it is more convenient to apply a Wick rotation $p = -iz$:

$$\mathcal{L}[f(t)](z) = \bar{f}(z) = \int_0^\infty dt e^{izt} f(t), \quad z \in \mathbb{C}, \quad (\text{B.19})$$

so that:

$$\mathcal{L}^{-1}[\bar{f}(z)](t) = f(t) = \lim_{T \rightarrow \infty} \frac{-1}{2\pi} \int_{ic+T}^{ic-T} dz e^{-izt} \bar{f}(z). \quad (\text{B.20})$$

Now, ic has to be *above* all poles of the function.

The Laplace transform has the following useful properties:

- A derivative in the time domain becomes a multiplication with z in the Laplace domain:

$$\mathcal{L}\left[i \frac{\partial f}{\partial t}\right](z) = z \bar{f}(z) - i f(0). \quad (\text{B.21})$$

¹Often misnamed “Fourier transform” in the literature, but a one-sided Fourier transform to complex arguments is a Laplace transform.

- An exponential function in the time domain becomes a resolvent in the Laplace domain:

$$\mathcal{L}[e^{-iat}](z) = \frac{i}{z - a}. \quad (\text{B.22})$$

- Multiplication with a phase factor in the time domain becomes a frequency shift in the Laplace domain:

$$\mathcal{L}[e^{-i\omega t} f(t)](z) = \mathcal{L}[f(t)](z - \omega). \quad (\text{B.23})$$

- A convolution integral from 0 to t in the time domain becomes a product in the Laplace domain:

$$\mathcal{L}\left[\int_0^t dt' f(t-t') g(t')\right](z) = \mathcal{L}[f(t)](z) \cdot \mathcal{L}[g(t)](z). \quad (\text{B.24})$$

B.4. Laplace domain

We now derive the wavefunction correction within first-order perturbation theory in the Laplace domain. Using the Fourier transform of the pump pulse envelope $s(t)$,

$$\begin{aligned} s(t) &= \int_{-\infty}^{\infty} d\tilde{\omega} s(\tilde{\omega}) e^{-i\tilde{\omega}t}, \\ \mathcal{F}[s(t)](\tilde{\omega}) \equiv s(\tilde{\omega}) &= \frac{1}{2\pi} \int_{-\infty}^{\infty} dt s(t) e^{i\tilde{\omega}t} \end{aligned} \quad (\text{B.25})$$

one can make use of the property (B.23) and Laplace-transform the Schrödinger equation

$$i \frac{\partial}{\partial t} |\Psi(t)\rangle = (H_c + s(t) V_p) |\Psi(t)\rangle \quad (\text{B.26})$$

to get

$$(z - H_c) |\Psi(z)\rangle = i |\Psi(0)\rangle + V_p \int_{-\infty}^{\infty} d\tilde{\omega} s(\tilde{\omega}) |\Psi(z - \tilde{\omega})\rangle. \quad (\text{B.27})$$

Setting

$$\begin{aligned} D_0 |\Psi(z)\rangle &= (z - H_c) |\Psi(z)\rangle - i |\Psi(0)\rangle, \\ D_{\text{int}} |\Psi(z)\rangle &= -V_p \int_{-\infty}^{\infty} d\tilde{\omega} s(\tilde{\omega}) |\Psi(z - \tilde{\omega})\rangle \end{aligned} \quad (\text{B.28})$$

one obtains with the previous procedure:

$$\begin{aligned} |\Psi(z)\rangle_{V_p^0} &= \frac{i}{z - H_c} |\Psi(0)\rangle, \\ |\Psi(z)\rangle_{V_p^1} &= \frac{i}{z - H_c} |\Psi(0)\rangle + i \int_{-\infty}^{\infty} d\tilde{\omega} s(\tilde{\omega}) \frac{1}{z - H_c} V_p \frac{1}{z - \tilde{\omega} - H_c} |\Psi(0)\rangle. \end{aligned} \quad (\text{B.29})$$

Of course, if $s(t) \equiv 1$, then $s(\tilde{\omega}) = \delta(\tilde{\omega})$ and the integral is eliminated.

C. Orthogonal Polynomial Mapping

Many problems fall into the general class of system-bath models, where the Hamiltonian of a given correlated system H_{sys} is coupled to a continuous, non-interacting bath H_{bath} via a coupling term H_{sb} . For example, within dynamical mean-field theory (DMFT) the Hubbard lattice is mapped onto the Anderson impurity model, where a single correlated site is coupled to a bath [Georges et al. 1996]. Bosonic baths are used to describe relaxation processes in open systems [Breuer and Petruccione 2002]. Finally, in the description of spectroscopies, the continuum of scattering states can also be regarded as a bath.

In order for the continuous bath to become manageable numerically, it needs to be discretized. The method used in this work has been introduced by Chin et al. [Chin et al. 2010] and employs orthogonal polynomials to map the bath onto a semi-infinite chain. The mapping is exact as long as the far end of the chain remains infinite. If the chain is cut at the end, it still remains exact as long as a perturbation entering the bath does not hit the edge². The procedure is quite similar to the ‘‘Wilson chain’’, a mapping of a continuum on a chain within the *numerical renormalization group* (NRG) [Wilson 1975]. The latter is, however, not an exact mapping, but employs a logarithmic discretization to favour small energies, leading to a drop-off of the chain hopping, so that it can eventually be cut with negligible error.

The general Hamiltonian reads

$$H = H_{\text{sys}} + H_{\text{bath}} + H_{sb}, \quad (\text{C.1})$$

where the environment is described by a density of states $\rho(\epsilon) = 1/L \sum_{\mathbf{k}} \delta(\epsilon - \epsilon(\mathbf{k}))$ (2.24), the bath Hamiltonian has the form (2.22)

$$H_{\text{scat}} = \int d\epsilon \rho(\epsilon) \epsilon a_{\sigma}^{\dagger}(\epsilon) a_{\sigma}(\epsilon), \quad (\text{C.2})$$

and we assume a convention where the bath creation and annihilation operators are dimensionless, so that a factor of $1/\rho(\epsilon)$ appears in the commutator (2.25):

$$\{a_{\sigma}^{\dagger}(\epsilon), a_{\sigma'}(\epsilon')\} = \frac{1}{\rho(\epsilon)} \delta_{\sigma\sigma'} \delta(\epsilon - \epsilon'). \quad (\text{C.3})$$

Electrons can hop in and out of the bath, coupling to an arbitrary operator of the system $A_{i\sigma}$ with a hybridization strength $V_i(\epsilon)$:

$$H_{sb} = \sum_{i\sigma} \int d\epsilon \rho(\epsilon) \left(V_i(\epsilon) a_{\sigma}^{\dagger}(\epsilon) A_{i\sigma} + V_i(\epsilon)^* A_{i\sigma}^{\dagger} a_{\sigma}(\epsilon) \right). \quad (\text{C.4})$$

We will assume that the hybridization is site-independent: $V_i(\epsilon) \approx V(\epsilon)$.

Let us now take $\rho(\epsilon) |V(\epsilon)|^2 d\epsilon$ as a weight function defining a class of orthonormal polynomials $p_n(\epsilon)$ [Gautschi 2004]:

$$\langle p_n, p_m \rangle := \int \rho(\epsilon) |V(\epsilon)|^2 d\epsilon p_n(\epsilon) p_m(\epsilon) = \delta_{nm}. \quad (\text{C.5})$$

²It is always assumed that the bath is empty initially, otherwise the initial ground state will depend on the chain length as well.

We can now transform the bath operators $a_\sigma^\dagger(\epsilon)$ onto new discrete operators $b_{n\sigma}^\dagger$

$$b_{n\sigma}^\dagger := \int \rho(\epsilon) V(\epsilon) d\epsilon p_n(\epsilon) a_\sigma^\dagger(\epsilon). \quad (\text{C.6})$$

Due to the orthogonality of the polynomials, the inverse transformation is given by:

$$a_\sigma^\dagger(\epsilon) = \sum_{n=0}^{\infty} V^*(\epsilon) p_n(\epsilon) b_{n\sigma}^\dagger, \quad (\text{C.7})$$

and it holds that the new operators are also fermionic (and dimensionless):

$$\{b_{n\sigma}, b_{n'\sigma'}^\dagger\} = \delta_{nn'} \delta_{\sigma\sigma'}. \quad (\text{C.8})$$

The system-environment interaction becomes:

$$H_{sb} = \sum_{i\sigma} \int \rho(\epsilon) |V(\epsilon)|^2 d\epsilon \sum_n p_n(\epsilon) [b_{n\sigma}^\dagger A_{i\sigma} + A_{i\sigma}^\dagger b_{n\sigma}]. \quad (\text{C.9})$$

All orthogonal polynomials start with a constant, and to maintain the orthonormality (C.5), it has to be given by:

$$p_0 = \frac{1}{\sqrt{\int \rho(\epsilon) |V(\epsilon)|^2 d\epsilon}} =: \frac{1}{|\pi_0|}. \quad (\text{C.10})$$

Thus, the interaction term (C.9) actually contains a product of p_n and p_0 :

$$p_n = p_n p_0 |\pi_0|, \quad (\text{C.11})$$

so that due to orthogonality, only the first term of the sum survives:

$$H_{sb} = |\pi_0| \sum_{i\sigma} \left(b_{0\sigma}^\dagger A_{i\sigma} + A_{i\sigma}^\dagger b_{0\sigma} \right). \quad (\text{C.12})$$

The kinetic energy of the bath becomes:

$$H_{\text{bath}} = \sum_{nm} \sum_{\sigma} \int \rho(\epsilon) |V(\epsilon)|^2 d\epsilon \epsilon p_n(\epsilon) p_m(\epsilon) b_{n\sigma}^\dagger b_{m\sigma}. \quad (\text{C.13})$$

Using the recurrence relation of orthogonal polynomials [Gautschi 2004],

$$p_{n+1}(x) = (C_n x - A_n) p_n(x) - B_n p_{n-1}(x), \quad (\text{C.14})$$

and once more exploiting orthogonality, (C.13) becomes:

$$\begin{aligned}
H_{\text{bath}} &= \sum_{nm} \sum_{\sigma} \int \rho(\epsilon) |V(\epsilon)|^2 d\epsilon \frac{p_{n+1}(\epsilon) + A_n p_n(\epsilon) + B_n p(\epsilon)}{C_n} p_m(\epsilon) b_{n\sigma}^{\dagger} b_{m\sigma} \\
&= \sum_{n\sigma} \frac{A_n}{C_n} b_{n\sigma}^{\dagger} b_{n\sigma} + \sum_{n\sigma} \left(\frac{1}{C_n} b_{n\sigma}^{\dagger} b_{n+1,\sigma} + \frac{B_{n+1}}{C_{n+1}} b_{n+1,\sigma}^{\dagger} b_{n\sigma} \right) \\
&= \sum_{n\sigma} \alpha_n b_{n\sigma}^{\dagger} b_{n\sigma} + \sum_{n\sigma} \sqrt{\beta_{n+1}} (b_{n\sigma}^{\dagger} b_{n+1,\sigma} + b_{n+1,\sigma} b_{n\sigma}^{\dagger}),
\end{aligned} \tag{C.15}$$

where the newly introduced α_n and β_n are the corresponding recurrence coefficients of the monic polynomials π_n ³, which are related to the original ones (C.14) via

$$\begin{aligned}
A_n &= \frac{\alpha_n}{\sqrt{\beta_{n+1}}}, \\
B_n &= \sqrt{\frac{\beta_n}{\beta_{n+1}}}, \\
C_n &= \frac{1}{\sqrt{\beta_{n+1}}}.
\end{aligned} \tag{C.16}$$

For a given weight function, the recurrence coefficients can be computed by the Gander-Karp algorithm [Gander and Karp 2001; Gautschi 2004; Gautschi 1982]. For the common case of a constant density of states (between ϵ_{\min} and ϵ_{\max}) and constant hybridization, the generated orthogonal polynomials are the (shifted) Legendre polynomials:

$$\begin{aligned}
\alpha_n &= b, \\
\beta_n &= \frac{a^2}{4 - n^2}, \quad n \geq 1,
\end{aligned} \tag{C.17}$$

where $a = \frac{1}{2}(\epsilon_{\max} - \epsilon_{\min})$ and $b = \frac{1}{2}(\epsilon_{\max} + \epsilon_{\min})$.

The interpretation of the transformed terms (C.12) and (C.15) is quite obvious: Particles from the system can hop onto the first site of the chain and then proceed to move along it. Each site is associated with progressively higher polynomial order. Since in spectroscopy, one essentially measures $\langle a^{\dagger}(\epsilon) a(\epsilon) \rangle$, one is able to resolve finer structures with more available maxima and minima from a linear combination of high-order polynomials at long propagation times. This is, of course, just a manifestation of the uncertainty principle: The longer the time of propagation within the chain, the smaller the energy uncertainty and the better the energy resolution.

C.1. Test case: The Friedrichs-Lee model

As a simple test case for the mapping, let us take a look at the dynamic Friedrichs-Lee model [Friedrichs 1948; Lee 1954; Horwitz and Levitan 1991], where a single atomic level (without spin),

$$H_{\text{sys}} = \epsilon_0 f^{\dagger} f, \tag{C.18}$$

³A monic polynomial $\pi_n = c_n x^n + c_{n-1} x^{n-1} + \dots + c_0$ is scaled such that the leading coefficient is $c_n = 1$.

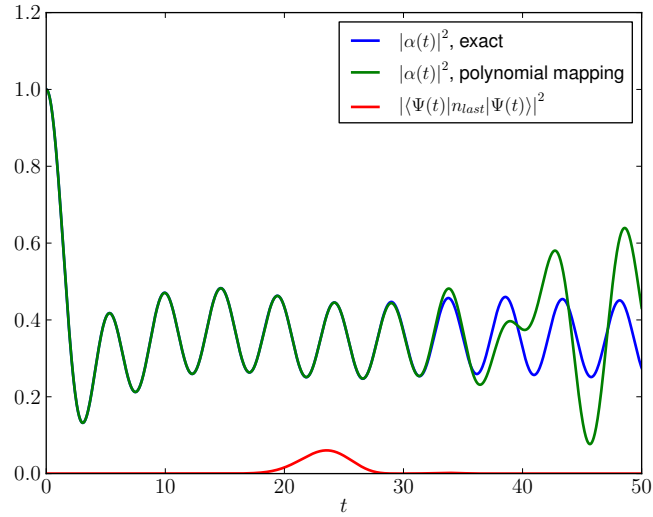


Figure C.1.: Population of the atomic level $|\alpha(t)|^2$ for the dynamic Friedrichs-Lee model. Comparison of the exact solution (except for the RWA approximation) with the orthogonal polynomial mapping (also with the RWA applied). Parameters: $L_{\text{chain}} = 10$, $\rho(\epsilon) \equiv 1$ on $[0, 1]$, $V(\epsilon) = 1$, $\Omega + \epsilon_0 = 0.9$. Shown in red is the occupancy of the last site of the chain.

is coupled to a continuum via a harmonic laser field

$$V(\epsilon, t) = V(\epsilon) \cos(\Omega t), \quad (\text{C.19})$$

so that $A_{i\sigma} = f$.

This model has the advantage of being exactly solvable. The wavefunction can be written as a superposition of states where the electron is within the atomic level with amplitude $\alpha(t)$, and states where it is within the continuum having an energy ϵ with the amplitude $\beta(\epsilon, t)$:

$$|\Psi(t)\rangle = e^{-i\epsilon_0 t} \alpha(t) f^\dagger |0\rangle + \int \rho(\epsilon) d\epsilon e^{-i\epsilon t} \beta(\epsilon, t) a^\dagger(\epsilon) |0\rangle. \quad (\text{C.20})$$

Plugging this into the Schrödinger equation and eliminating $\beta(\epsilon, t)$ and its time-derivative in favour of $\alpha(t)$, we obtain the following integro-differential equation:

$$\dot{\alpha}(t) = - \int_0^t dt' \alpha(t') \int \rho(\epsilon) d\epsilon e^{-i(\epsilon - \epsilon_0)(t - t')} V^*(\epsilon, t) V(\epsilon, t'). \quad (\text{C.21})$$

A very reasonable approximation to apply now, which does not distort the result too much is the *rotating-wave approximation* (RWA), which only leaves the resonant parts from the $\cos(\Omega t)$ term in (C.19) and neglects the rapid short-time dynamics. This leads to:

$$\dot{\alpha}(t) \approx -\frac{1}{4} \int_0^t dt' \alpha(t') \int \rho(\epsilon) |V(\epsilon)|^2 d\epsilon e^{i(\Omega + \epsilon_0 - \epsilon)(t - t')}. \quad (\text{C.22})$$

Fig. C.1 compares the exact result with the orthogonal polynomial mapping for 10 chain sites and the initial state $|\Psi(0)\rangle = f^\dagger |0\rangle$. One can see that a particle entering the chain reaches the end at $t \approx 20$ (the unit of time is now the continuum bandwidth, set to 1), so that the average velocity is

about $v \approx 0.5$. It is then reflected and goes back into the system where it influences the system properties just before $t \approx 40$ and leads to deviations from the exact result.

D. List of publications and preprints

The following publications have a substantial overlap with the present work:

Doublons and the two-hole spectral function

- R. Rausch and M. Potthoff (2016). “Multiplons in the two-hole excitation spectra of the one-dimensional Hubbard model”. *New Journal of Physics* 18.2, p. 023033
- R. Rausch and M. Potthoff (2017). “Filling-dependent doublon dynamics in the one-dimensional Hubbard model”. *Phys. Rev. B* 95 (4), p. 045152
- R. Rausch and M. Potthoff. “Pump-probe Auger electron spectroscopy”. *in preparation*

The side-project of using DMRG for spin dynamics involves the following publications:

Spin dynamics

- M. Sayad, R. Rausch, and M. Potthoff (2016a). “Relaxation of a Classical Spin Coupled to a Strongly Correlated Electron System”. *Phys. Rev. Lett.* 117 (12), p. 127201
- M. Sayad, R. Rausch, and M. Potthoff (2016b). “Inertia effects in the real-time dynamics of a quantum spin coupled to a Fermi sea”. *EPL (Europhysics Letters)* 116.1, p. 17001

Another side-project to this work involved the development of a code for the calculation of *ab initio* pump-probe photoemission. The author has not been involved in the code development itself, but rather participated in the establishing the theoretical framework in terms of Green’s functions and the presentation of the results in a clear fashion. This involves the following publications:

Ab initio photoemission

- J. Braun, R. Rausch, M. Potthoff, J. Minár, and H. Ebert (2015). “One-step theory of pump-probe photoemission”. *Phys. Rev. B* 91 (3), p. 035119
- J. Braun, R. Rausch, M. Potthoff, and H. Ebert (2016). “One-step theory of two-photon photoemission”. *Phys. Rev. B* 94 (12), p. 125128

Bibliography

1. Abraham-Ibrahim, S., B. Caroli, C. Caroli, and B. Roulet (1978). “Deep-hole interferences in photon-induced Auger emission from solids”. *Phys. Rev. B* 18 (12), pp. 6702–6712.
2. Affleck, I., T. Kennedy, E. H. Lieb, and H. Tasaki (1987). “Rigorous results on valence-bond ground states in antiferromagnets”. *Phys. Rev. Lett.* 59 (7), pp. 799–802.
3. Almladh, C.-O. (1985). “On the Theory of Photoemission”. *Physica Scripta* 32.4, p. 341.
4. Alvermann, A. and H. Fehske (2011). “High-order commutator-free exponential time-propagation of driven quantum systems”. *Journal of Computational Physics* 230.15, pp. 5930–5956.
5. Alvermann, A., H. Fehske, and P. B. Littlewood (2012). “Numerical time propagation of quantum systems in radiation fields”. *New Journal of Physics* 14.10, p. 105008.
6. Ammon, B., M. Troyer, and H. Tsunetsugu (1995). “Effect of the three-site hopping term on the t - J model”. *Phys. Rev. B* 52 (1), pp. 629–636.
7. Anderson, P. W. (1959). “New Approach to the Theory of Superexchange Interactions”. *Phys. Rev.* 115 (1), pp. 2–13.
8. Andraschko, F. and J. Sirker (2015). “Propagation of a single-hole defect in the one-dimensional Bose-Hubbard model”. *Phys. Rev. B* 91 (23), p. 235132.
9. Auerbach, A. (2012). *Interacting Electrons and Quantum Magnetism*. Graduate Texts in Contemporary Physics. Springer New York.
10. Avdeev, L. V. and B. -D. Dörfel (1987). “Solutions of the Bethe ansatz equations for XXX antiferromagnet of arbitrary spin in the case of a finite number of sites”. *Theoretical and Mathematical Physics* 71.2, pp. 528–542.
11. Bach, G. H., J. E. Hirsch, and F. Marsiglio (2010). “Two-site dynamical mean field theory for the dynamic Hubbard model”. *Phys. Rev. B* 82 (15), p. 155122.
12. Benthien, H., F. Gebhard, and E. Jeckelmann (2004). “Spectral Function of the One-Dimensional Hubbard Model away from Half Filling”. *Phys. Rev. Lett.* 92 (25), p. 256401.
13. Benthien, H. (2005). “Dynamical properties of quasi one-dimensional correlated electron systems”. PhD thesis. Philipps-Universität Marburg.
14. Berakdar, J. (1998). “Emission of correlated electron pairs following single-photon absorption by solids and surfaces”. *Phys. Rev. B* 58 (15), pp. 9808–9816.
15. Blanes, S., F. Casas, and A. Murua (2008). “Splitting and composition methods in the numerical integration of differential equations”. *ArXiv e-prints*. arXiv: [0812.0377 \[math.NA\]](https://arxiv.org/abs/0812.0377).
16. Blanes, S., F. Casas, J. Oteo, and J. Ros (2009). “The Magnus expansion and some of its applications”. *Physics Reports* 470.5–6, pp. 151–238.
17. Boschi, C. D. E., E. Ercolessi, L. Ferrari, P. Naldesi, F. Ortolani, and L. Taddia (2014). “Bound states and expansion dynamics of interacting bosons on a one-dimensional lattice”. *Phys. Rev. A* 90 (4), p. 043606.

18. Braun, J., R. Rausch, M. Potthoff, and H. Ebert (2016). “One-step theory of two-photon photoemission”. *Phys. Rev. B* 94 (12), p. 125128.
19. Braun, J., R. Rausch, M. Potthoff, J. Minár, and H. Ebert (2015). “One-step theory of pump-probe photoemission”. *Phys. Rev. B* 91 (3), p. 035119.
20. Brehm, S., E. Arrigoni, M. Aichhorn, and W. Hanke (2010). “Theory of two-particle excitations and the magnetic susceptibility in high-T_c cuprate superconductors”. *EPL (Europhysics Letters)* 89.2, p. 27005.
21. Breuer, H. and F. Petruccione (2002). *The Theory of Open Quantum Systems*. Oxford University Press.
22. Calabrese, P. and J. Cardy (2005). “Evolution of entanglement entropy in one-dimensional systems”. *Journal of Statistical Mechanics: Theory and Experiment* 2005.04, P04010.
23. Cavalieri, A. L., N. Müller, T. Uphues, V. S. Yakovlev, A. Baltuška, B. Horvath, B. Schmidt, L. Blümel, R. Holzwarth, S. Hendel, et al. (2007). “Attosecond spectroscopy in condensed matter”. *Nature* 449.7165, pp. 1029–1032.
24. Chao, K. A., J. Spalek, and A. M. Oles (1977). “Kinetic exchange interaction in a narrow S-band”. *Journal of Physics C: Solid State Physics* 10.10, p. L271.
25. Chao, K. A., J. Spalek, and A. M. Oleś (1978). “Canonical perturbation expansion of the Hubbard model”. *Phys. Rev. B* 18 (7), pp. 3453–3464.
26. Chin, A. W., Á. Rivas, S. F. Huelga, and M. B. Plenio (2010). “Exact mapping between system-reservoir quantum models and semi-infinite discrete chains using orthogonal polynomials”. *Journal of Mathematical Physics* 51.9, 092109.
27. Chudnovskiy, A. L., D. M. Gangardt, and A. Kamenev (2012). “Doublon Relaxation in the Bose-Hubbard Model”. *Phys. Rev. Lett.* 108 (8), p. 085302.
28. Cini, M. (1977). “Two hole resonances in the XVV Auger spectra of solids”. *Solid State Communications* 24.9, pp. 681–684.
29. Cini, M. (1979). “Theory of Auger XVV spectra of solids: Many body effects in incompletely filled bands”. *Surface Science* 87.2, pp. 483–500.
30. Claessen, R., J. Schäfer, and M. Sing (2007). “Photoemission on Quasi-One-Dimensional Solids: Peierls, Luttinger & Co.” *Very High Resolution Photoelectron Spectroscopy*. Ed. by S. Hüfner. Berlin, Heidelberg: Springer Berlin Heidelberg, pp. 115–146.
31. Claessen, R., M. Sing, U. Schwingenschlögl, P. Blaha, M. Dressel, and C. S. Jacobsen (2002). “Spectroscopic Signatures of Spin-Charge Separation in the Quasi-One-Dimensional Organic Conductor TTF-TCNQ”. *Phys. Rev. Lett.* 88 (9), p. 096402.
32. Czekster, R. M., P. Fernandes, J.-M. Vincent, and T. Webber (2007). “Split: A Flexible and Efficient Algorithm to Vector-descriptor Product”. *Proceedings of the 2Nd International Conference on Performance Evaluation Methodologies and Tools*. ValueTools '07. Nantes, France: ICST (Institute for Computer Sciences, Social-Informatics and Telecommunications Engineering), 83:1–83:8.
33. Davio, M. (1981). “Kronecker Products and Shuffle Algebra”. *IEEE Trans. Comput.* 30.2, pp. 116–125.
34. Deguchi, T., F. Essler, F. Göhmann, A. Klümper, V. Korepin, and K. Kusakabe (2000). “Thermodynamics and excitations of the one-dimensional Hubbard model”. *Physics Reports* 331.5, pp. 197–281.

35. Dirac, P. A. M. (1930). “Note on Exchange Phenomena in the Thomas Atom”. *Mathematical Proceedings of the Cambridge Philosophical Society* 26 (03), pp. 376–385.
36. Dolfi, M., B. Bauer, S. Keller, A. Kosenkov, T. Ewart, A. Kantian, T. Giamarchi, and M. Troyer (2014). “Matrix product state applications for the {ALPS} project”. *Computer Physics Communications* 185.12, pp. 3430–3440.
37. Drchal, V. and J. Kudrnovsky (1984). “The Auger spectra of metals: effect of electron correlations in partially filled narrow bands”. *Journal of Physics F: Metal Physics* 14.10, p. 2443.
38. Drescher, M., M. Hentschel, R. Kienberger, M. Uiberacker, V. Yakovlev, A. Scrinzi, T. Westerwalbesloh, U. Kleineberg, U. Heinzmann, and F. Krausz (2002). “Time-resolved atomic inner-shell spectroscopy”. *Nature* 419.6909, pp. 803–807.
39. Dunlap, D. H. and V. M. Kenkre (1986). “Dynamic localization of a charged particle moving under the influence of an electric field”. *Phys. Rev. B* 34 (6), pp. 3625–3633.
40. Eckardt, A. (2016). “Atomic quantum gases in periodically driven optical lattices”. *ArXiv e-prints*. arXiv: [1606.08041](https://arxiv.org/abs/1606.08041) [cond-mat.quant-gas].
41. Eckstein, M. and P. Werner (2014). “Ultrafast Separation of Photodoped Carriers in Mott Antiferromagnets”. *Phys. Rev. Lett.* 113 (7), p. 076405.
42. Essler, F., H. Frahm, F. Göhmann, A. Klümper, and V. Korepin (2005). *The One-Dimensional Hubbard Model*. Cambridge University Press.
43. Fazekas, P. (1999). *Lecture Notes on Electron Correlation and Magnetism*. Series in Modern Condensed Matter Physics. World Scientific.
44. Feiguin, A. E. and D. A. Huse (2009). “Spectral properties of a partially spin-polarized one-dimensional Hubbard/Luttinger superfluid”. *Phys. Rev. B* 79 (10), p. 100507.
45. Fernandes, P., B. Plateau, and W. J. Stewart (1998). “Efficient Descriptor-vector Multiplications in Stochastic Automata Networks”. *J. ACM* 45.3, pp. 381–414.
46. Freericks, J. K., H. R. Krishnamurthy, and T. Pruschke (2009). “Theoretical Description of Time-Resolved Photoemission Spectroscopy: Application to Pump-Probe Experiments”. *Phys. Rev. Lett.* 102 (13), p. 136401.
47. Friedrichs, K. O. (1948). “On the perturbation of continuous spectra”. *Communications on Pure and Applied Mathematics* 1.4, pp. 361–406.
48. Frigo, M. and S. G. Johnson (1998). “FFTW: An adaptive software architecture for the FFT”. *Acoustics, Speech and Signal Processing, 1998. Proceedings of the 1998 IEEE International Conference on*. Vol. 3. IEEE, pp. 1381–1384.
49. Fröwis, F., V. Nebendahl, and W. Dür (2010). “Tensor operators: Constructions and applications for long-range interaction systems”. *Phys. Rev. A* 81 (6), p. 062337.
50. Ganahl, M., E. Rabel, F. H. L. Essler, and H. G. Evertz (2012). “Observation of Complex Bound States in the Spin-1/2 Heisenberg XXZ Chain Using Local Quantum Quenches”. *Phys. Rev. Lett.* 108 (7), p. 077206.
51. Ganahl, M., P. Thunström, F. Verstraete, K. Held, and H. G. Evertz (2014). “Chebyshev expansion for impurity models using matrix product states”. *Phys. Rev. B* 90 (4), p. 045144.
52. Gander, M. J. and A. H. Karp (2001). “Stable computation of high order Gauss quadrature rules using discretization for measures in radiation transfer”. *Journal of Quantitative Spectroscopy and Radiative Transfer* 68.2, pp. 213–223.

53. Gautschi, W. (1982). “On Generating Orthogonal Polynomials”. *SIAM Journal on Scientific and Statistical Computing* 3.3, pp. 289–317.
54. — (2004). *Orthogonal polynomials: computation and approximation*. Oxford University Press on Demand.
55. Gebhard, F. (2003). *The Mott metal-insulator transition: models and methods*. Vol. 137. Springer.
56. Georges, A., G. Kotliar, W. Krauth, and M. J. Rozenberg (1996). “Dynamical mean-field theory of strongly correlated fermion systems and the limit of infinite dimensions”. *Rev. Mod. Phys.* 68 (1), pp. 13–125.
57. Golub, G. H. and J. H. Welsch (1969). “Calculation of Gauss quadrature rules”. *Mathematics of computation* 23.106, pp. 221–230.
58. Grcar, J. F. (1981). “Analyses of the Lanczos algorithm and of the approximation problem in Richardson’s method”. PhD thesis. University of Illinois at Urbana-Champaign.
59. Gunnarsson, O. and K. Schönhammer (1980). “Dynamical theory of Auger processes”. *Phys. Rev. B* 22 (8), pp. 3710–3733.
60. Gutzwiller, M. C. (1963). “Effect of Correlation on the Ferromagnetism of Transition Metals”. *Phys. Rev. Lett.* 10 (5), pp. 159–162.
61. Haak, H. W., G. A. Sawatzky, and T. D. Thomas (1978). “Auger-Photoelectron Coincidence Measurements in Copper”. *Phys. Rev. Lett.* 41 (26), pp. 1825–1827.
62. Haegeman, J., J. I. Cirac, T. J. Osborne, I. Pižorn, H. Verschelde, and F. Verstraete (2011). “Time-Dependent Variational Principle for Quantum Lattices”. *Phys. Rev. Lett.* 107 (7), p. 070601.
63. Haegeman, J., C. Lubich, I. Oseledets, B. Vandereycken, and F. Verstraete (2016). “Unifying time evolution and optimization with matrix product states”. *Phys. Rev. B* 94 (16), p. 165116.
64. Hansen, D., E. Perepelitsky, and B. S. Shastry (2011). “Split Hubbard bands at low densities”. *Phys. Rev. B* 83 (20), p. 205134.
65. Hartmann, M. J., J. Prior, S. R. Clark, and M. B. Plenio (2009). “Density Matrix Renormalization Group in the Heisenberg Picture”. *Phys. Rev. Lett.* 102 (5), p. 057202.
66. Al-Hassanieh, K. A., F. A. Reboledo, A. E. Feiguin, I. González, and E. Dagotto (2008). “Excitons in the One-Dimensional Hubbard Model: A Real-Time Study”. *Phys. Rev. Lett.* 100 (16), p. 166403.
67. Al-Hassanieh, K. A., J. Rincón, E. Dagotto, and G. Alvarez (2013). “Wave-packet dynamics in the one-dimensional extended Hubbard model”. *Phys. Rev. B* 88 (4), p. 045107.
68. Hauschild, J., F. Pollmann, and F. Heidrich-Meisner (2015). “Sudden expansion and domain-wall melting of strongly interacting bosons in two-dimensional optical lattices and on multileg ladders”. *Phys. Rev. A* 92 (5), p. 053629.
69. Haverkort, M. W., M. Zwierzycki, and O. K. Andersen (2012). “Multiplet ligand-field theory using Wannier orbitals”. *Phys. Rev. B* 85 (16), p. 165113.
70. Hecker Denschlag, J. and A. J. Daley (2006). “Exotic atom pairs: Repulsively bound states in an optical lattice”. *eprint arXiv:cond-mat/0610393*. eprint: [cond-mat/0610393](https://arxiv.org/abs/cond-mat/0610393).
71. Hirsch, J. E. (2001). “Dynamic Hubbard Model”. *Phys. Rev. Lett.* 87 (20), p. 206402.
72. Hofmann, F. and M. Potthoff (2012). “Doublon dynamics in the extended Fermi-Hubbard model”. *Phys. Rev. B* 85 (20), p. 205127.

73. Horwitz, L. and J. Levitan (1991). “A soluble model for time dependent perturbations of an unstable quantum system”. *Physics Letters A* 153.8, pp. 413–419.
74. Hubbard, J. (1963). “Electron correlations in narrow energy bands”. *Proceedings of the royal society of london a: mathematical, physical and engineering sciences*. Vol. 276. 1365. The Royal Society, pp. 238–257.
75. Hubig, C., I. P. McCulloch, and U. Schollwöck (2017). “Generic construction of efficient matrix product operators”. *Phys. Rev. B* 95 (3), p. 035129.
76. Hubig, C., I. P. McCulloch, U. Schollwöck, and F. A. Wolf (2015). “Strictly single-site DMRG algorithm with subspace expansion”. *Phys. Rev. B* 91 (15), p. 155115.
77. Imriška, J., E. Gull, and M. Troyer (2016). “Thermodynamics of the Hubbard model on stacked honeycomb and square lattices”. *The European Physical Journal B* 89.8, pp. 1–11.
78. Jeckelmann, E. (2002). “Ground-State Phase Diagram of a Half-Filled One-Dimensional Extended Hubbard Model”. *Phys. Rev. Lett.* 89 (23), p. 236401.
79. Johnson, S. (2013). *Faddeeva Package—AbInitio*.
80. Jordan, P. and E. P. Wigner (1993). “über das Paulische Äquivalenzverbot”. *The Collected Works of Eugene Paul Wigner: Part A: The Scientific Papers*. Ed. by A. S. Wightman. Berlin, Heidelberg: Springer Berlin Heidelberg, pp. 109–129.
81. Jorgensen, P. E. T. (2006). “The road to reality: a complete guide to the laws of the universe”. *The Mathematical Intelligencer* 28.3, pp. 59–61.
82. Kagan, M. Y. (2013). “Spin-Charge Separation and Confinement in Ladder Systems and in High- T_c Superconductors”. *Modern trends in Superconductivity and Superfluidity*. Dordrecht: Springer Netherlands, pp. 397–427.
83. Kajala, J., F. Massel, and P. Törmä (2011). “Expansion Dynamics in the One-Dimensional Fermi-Hubbard Model”. *Phys. Rev. Lett.* 106 (20), p. 206401.
84. Kalosakas, G., S. Aubry, and G. P. Tsironis (1998). “Polaron solutions and normal-mode analysis in the semiclassical Holstein model”. *Phys. Rev. B* 58 (6), pp. 3094–3104.
85. Kanamori, J. (1963). “Electron Correlation and Ferromagnetism of Transition Metals”. *Progress of Theoretical Physics* 30.3, pp. 275–289.
86. Kazansky, A. K., I. P. Sazhina, and N. M. Kabachnik (2009). “Time-dependent theory of Auger decay induced by ultra-short pulses in a strong laser field”. *Journal of Physics B: Atomic, Molecular and Optical Physics* 42.24, p. 245601.
87. Kohno, M. (2010). “Spectral Properties near the Mott Transition in the One-Dimensional Hubbard Model”. *Phys. Rev. Lett.* 105 (10), p. 106402.
88. Lander, J. J. (1953). “Auger Peaks in the Energy Spectra of Secondary Electrons from Various Materials”. *Phys. Rev.* 91 (6), pp. 1382–1387.
89. Langer, S., F. Heidrich-Meisner, J. Gemmer, I. P. McCulloch, and U. Schollwöck (2009). “Real-time study of diffusive and ballistic transport in spin- $\frac{1}{2}$ chains using the adaptive time-dependent density matrix renormalization group method”. *Phys. Rev. B* 79 (21), p. 214409.
90. Langer, S., M. J. A. Schuetz, I. P. McCulloch, U. Schollwöck, and F. Heidrich-Meisner (2012). “Expansion velocity of a one-dimensional, two-component Fermi gas during the sudden expansion in the ballistic regime”. *Phys. Rev. A* 85 (4), p. 043618.
91. Lee, T. D. (1954). “Some Special Examples in Renormalizable Field Theory”. *Phys. Rev.* 95 (5), pp. 1329–1334.

92. Lenarčič, Z. and P. Prelovšek (2013). “Ultrafast Charge Recombination in a Photoexcited Mott-Hubbard Insulator”. *Phys. Rev. Lett.* 111 (1), p. 016401.
93. — (2014). “Charge recombination in undoped cuprates”. *Phys. Rev. B* 90 (23), p. 235136.
94. Lieb, E. H. and F. Y. Wu (1968). “Absence of Mott Transition in an Exact Solution of the Short-Range, One-Band Model in One Dimension”. *Phys. Rev. Lett.* 20 (25), pp. 1445–1448.
95. Loon, E. G. C. P. van, F. Krien, H. Hafermann, E. A. Stepanov, A. I. Lichtenstein, and M. I. Katsnelson (2016). “Double occupancy in dynamical mean-field theory and the dual boson approach”. *Phys. Rev. B* 93 (15), p. 155162.
96. Lubich, C. (2008). *From quantum to classical molecular dynamics: reduced models and numerical analysis*. European Mathematical Society.
97. Magnus, W. (1954). “On the exponential solution of differential equations for a linear operator”. *Communications on Pure and Applied Mathematics* 7.4, pp. 649–673.
98. Marsiglio, F., R. Teshima, and J. E. Hirsch (2003). “Dynamic Hubbard model: Effect of finite boson frequency”. *Phys. Rev. B* 68 (22), p. 224507.
99. McLachlan, R. I. (1995). “On the Numerical Integration of Ordinary Differential Equations by Symmetric Composition Methods”. *SIAM Journal on Scientific Computing* 16.1, pp. 151–168.
100. Melzer, E. (1995). “On the scaling limit of the 1D Hubbard model at half-filling”. *Nuclear Physics B* 443.3, pp. 553–564.
101. Moreno, A., A. Muramatsu, and J. M. P. Carmelo (2013). “Charge and spin fractionalization beyond the Luttinger-liquid paradigm”. *Phys. Rev. B* 87 (7), p. 075101.
102. Muth, D., R. G. Unanyan, and M. Fleischhauer (2011). “Dynamical Simulation of Integrable and Nonintegrable Models in the Heisenberg Picture”. *Phys. Rev. Lett.* 106 (7), p. 077202.
103. Nolting, W. (1990). “Influence of electron correlations on Auger electron —and appearance potential — spectra of solids”. *Zeitschrift für Physik B Condensed Matter* 80.1, pp. 73–86.
104. Ovchinnikov, A. (1992). “Excitation spectrum in the one-dimensional Hubbard model”. *The Hubbard Model: A Reprint Volume* 30.6, p. 58.
105. Paula, A. L. de, H. Bragança, R. G. Pereira, R. C. Drumond, and M. C. O. Aguiar (2017). “Spinon and bound-state excitation light cones in Heisenberg XXZ chains”. *Phys. Rev. B* 95 (4), p. 045125.
106. Pavlyukh, Y., M. Schüler, and J. Berakdar (2015). “Single- or double-electron emission within the Keldysh nonequilibrium Green’s function and Feshbach projection operator techniques”. *Phys. Rev. B* 91 (15), p. 155116.
107. Petrosyan, D., B. Schmidt, J. R. Anglin, and M. Fleischhauer (2007). “Quantum liquid of repulsively bound pairs of particles in a lattice”. *Phys. Rev. A* 76 (3), p. 033606.
108. Potthoff, M., J. Braun, G. Borstel, and W. Nolting (1993a). “Theory of Auger electron and appearance-potential spectroscopy from solids with partially filled valence bands: Effects of valence-band-core interaction”. *Phys. Rev. B* 47 (19), pp. 12480–12497.
109. Potthoff, M., J. Braun, W. Nolting, and G. Borstel (1993b). “VV and CV correlation effects in CVV Auger-electron and appearance-potential spectroscopy: exact results for limiting cases”. *Journal of Physics: Condensed Matter* 5.37, p. 6879.
110. Potthoff, M., J. Braun, W. Nolting, and G. Borstel (1994). “Effects of electron correlations on Auger-electron and appearance-potential spectra of solid surfaces”. *Surface Science* 307, pp. 942–946.

111. Potthoff, M., T. Wegner, W. Nolting, T. Schlathölter, M. Vonbank, K. Ertl, J. Braun, and M. Donath (2001). “Electron-correlation effects in appearance-potential spectra of Ni”. *Phys. Rev. B* 63 (16), p. 165118.
112. Press, W. (2007). *Numerical Recipes 3rd Edition: The Art of Scientific Computing*. Cambridge University Press.
113. Prosen, T. and M. Žnidarič (2007). “Is the efficiency of classical simulations of quantum dynamics related to integrability?” *Phys. Rev. E* 75 (1), p. 015202.
114. Qin, X., Y. Ke, X. Guan, Z. Li, N. Andrei, and C. Lee (2014). “Statistics-dependent quantum co-walking of two particles in one-dimensional lattices with nearest-neighbor interactions”. *Phys. Rev. A* 90 (6), p. 062301.
115. Rausch, R. and M. Potthoff. “Pump-probe Auger electron spectroscopy”. *in preparation*.
116. — (2016). “Multiplons in the two-hole excitation spectra of the one-dimensional Hubbard model”. *New Journal of Physics* 18.2, p. 023033.
117. — (2017). “Filling-dependent doublon dynamics in the one-dimensional Hubbard model”. *Phys. Rev. B* 95 (4), p. 045152.
118. Regnault, N. (2017). “Entanglement spectroscopy and its application to the quantum Hall effects”. *Topological Aspects of Condensed Matter Physics: Lecture Notes of the Les Houches Summer School: Volume 103, August 2014* 103, p. 165.
119. Riessen, G. van, Z. Wei, R. S. Dhaka, C. Winkler, F. O. Schumann, and J. Kirschner (2010). “Direct and core-resonant double photoemission from Cu(001)”. *Journal of Physics: Condensed Matter* 22.9, p. 092201.
120. Rosch, A., D. Rasch, B. Binz, and M. Vojta (2008). “Metastable Superfluidity of Repulsive Fermionic Atoms in Optical Lattices”. *Phys. Rev. Lett.* 101 (26), p. 265301.
121. Ruskey, F. (2003). “Combinatorial generation”. *Preliminary working draft. University of Victoria, Victoria, BC, Canada* 11, p. 20.
122. Rzązewski, K. and R. W. Boyd (2004). “Equivalence of interaction Hamiltonians in the electric dipole approximation”. *Journal of Modern Optics* 51.8, pp. 1137–1147.
123. Savasta, S. and R. Girlanda (1995). “The particle-photon interaction in systems described by model Hamiltonians in second quantization”. *Solid State Communications* 96.7, pp. 517–522.
124. Sawatzky, G. A. (1977). “Quasiatomic Auger Spectra in Narrow-Band Metals”. *Phys. Rev. Lett.* 39 (8), pp. 504–507.
125. Sawatzky, G. A. and A. Lenselink (1980). “Auger line shape in narrow-band metals”. *Phys. Rev. B* 21 (5), pp. 1790–1796.
126. Sayad, M., R. Rausch, and M. Potthoff (2016a). “Relaxation of a Classical Spin Coupled to a Strongly Correlated Electron System”. *Phys. Rev. Lett.* 117 (12), p. 127201.
127. — (2016b). “Inertia effects in the real-time dynamics of a quantum spin coupled to a Fermi sea”. *EPL (Europhysics Letters)* 116.1, p. 17001.
128. Schaich, W. and N. Ashcroft (1970). “Theory of photoemission”. *Solid State Communications* 8.23, pp. 1959–1963.
129. Schollwöck, U. (2005). “The density-matrix renormalization group”. *Rev. Mod. Phys.* 77 (1), pp. 259–315.
130. Schollwöck, U. (2011). “The density-matrix renormalization group in the age of matrix product states”. *Annals of Physics* 326.1. January 2011 Special Issue, pp. 96–192.

131. Schulz, H. J. (1993). “Interacting fermions in one dimension: from weak to strong correlation”. *eprint arXiv:cond-mat/9302006*. eprint: [cond-mat/9302006](https://arxiv.org/abs/cond-mat/9302006).
132. Schütte, B., S. Bauch, U. Fröhling, M. Wieland, M. Gensch, E. Plönjes, T. Gaumnitz, A. Azima, M. Bonitz, and M. Drescher (2012). “Evidence for Chirped Auger-Electron Emission”. *Phys. Rev. Lett.* 108 (25), p. 253003.
133. Schwabe, A. (2015). personal communication.
134. Scott, A., J. Eilbeck, and H. Gilhøj (1994). “Quantum lattice solitons”. *Physica D: Nonlinear Phenomena* 78.3, pp. 194–213.
135. Scully, M. and M. Zubairy (1997). *Quantum Optics*. Cambridge University Press.
136. Silver, R. N. and H. Röder (1997). “Calculation of densities of states and spectral functions by Chebyshev recursion and maximum entropy”. *Phys. Rev. E* 56 (4), pp. 4822–4829.
137. Silver, R. and H. Röder (1994). “Densities of states of mega-dimensional Hamiltonian matrices”. *International Journal of Modern Physics C* 05.04, pp. 735–753.
138. Simon, H. D. (1984). “Analysis of the symmetric Lanczos algorithm with reorthogonalization methods”. *Linear Algebra and its Applications* 61, pp. 101–131.
139. Sirker, J., R. G. Pereira, and I. Affleck (2009). “Diffusion and Ballistic Transport in One-Dimensional Quantum Systems”. *Phys. Rev. Lett.* 103 (21), p. 216602.
140. Smirnova, O., V. S. Yakovlev, and A. Scrinzi (2003). “Quantum Coherence in the Time-Resolved Auger Measurement”. *Phys. Rev. Lett.* 91 (25), p. 253001.
141. Smith, N. V. (1988). “Inverse photoemission”. *Reports on Progress in Physics* 51.9, p. 1227.
142. Sólyom, J. (2010). *Fundamentals of the Physics of Solids: Volume 3 - Normal, Broken-Symmetry, and Correlated Systems*. Theoretical Solid State Physics: Interaction Among Electrons. Springer Berlin Heidelberg.
143. Strohmaier, N., D. Greif, R. Jördens, L. Tarruell, H. Moritz, T. Esslinger, R. Sensarma, D. Pekker, E. Altman, and E. Demler (2010). “Observation of Elastic Doublon Decay in the Fermi-Hubbard Model”. *Phys. Rev. Lett.* 104 (8), p. 080401.
144. Su, W. P., J. R. Schrieffer, and A. J. Heeger (1979). “Solitons in Polyacetylene”. *Phys. Rev. Lett.* 42 (25), pp. 1698–1701.
145. Takahashi, M. (1971). “One-Dimensional Electron Gas with Delta-Function Interaction at Finite Temperature”. *Progress of Theoretical Physics* 46.5, pp. 1388–1406.
146. Tal-Ezer, H. and R. Kosloff (1984). “An accurate and efficient scheme for propagating the time dependent Schrödinger equation”. *The Journal of Chemical Physics* 81.9, pp. 3967–3971.
147. Ulbricht, T. and P. Schmitteckert (2009). “Is spin-charge separation observable in a transport experiment?” *EPL (Europhysics Letters)* 86.5, p. 57006.
148. Valiente, M. and D. Petrosyan (2008). “Two-particle states in the Hubbard model”. *Journal of Physics B: Atomic, Molecular and Optical Physics* 41.16, p. 161002.
149. — (2009). “Scattering resonances and two-particle bound states of the extended Hubbard model”. *Journal of Physics B: Atomic, Molecular and Optical Physics* 42.12, p. 121001.
150. Vidmar, L., S. Langer, I. P. McCulloch, U. Schneider, U. Schollwöck, and F. Heidrich-Meisner (2013). “Sudden expansion of Mott insulators in one dimension”. *Phys. Rev. B* 88 (23), p. 235117.
151. Wang, L.-W. (1994). “Calculating the density of states and optical-absorption spectra of large quantum systems by the plane-wave moments method”. *Phys. Rev. B* 49 (15), pp. 10154–10158.

152. Weiße, A. and H. Fehske (2008). “Chebyshev expansion techniques”. *Computational many-particle physics*. Springer, pp. 545–577.
153. Weiße, A., G. Wellein, A. Alvermann, and H. Fehske (2006). “The kernel polynomial method”. *Rev. Mod. Phys.* 78 (1), pp. 275–306.
154. Werner, P. and M. Eckstein (2016). “Effective doublon and hole temperatures in the photo-doped dynamic Hubbard model”. *Structural Dynamics* 3.2, 023603.
155. White, S. R. (2005). “Density matrix renormalization group algorithms with a single center site”. *Phys. Rev. B* 72 (18), p. 180403.
156. Wilson, K. G. (1975). “The renormalization group: Critical phenomena and the Kondo problem”. *Rev. Mod. Phys.* 47 (4), pp. 773–840.
157. Wolf, F. A., I. P. McCulloch, O. Parcollet, and U. Schollwöck (2014). “Chebyshev matrix product state impurity solver for dynamical mean-field theory”. *Phys. Rev. B* 90 (11), p. 115124.
158. Woynarovich, F. (1996). “Massive particles in the relativistic limit of the non-half-filled 1D attractive Hubbard model”. *Journal of Physics A: Mathematical and General* 29.2, p. L37.
159. Yang, C. N. and C. P. Yang (1969). “Thermodynamics of a One-Dimensional System of Bosons with Repulsive Delta-Function Interaction”. *Journal of Mathematical Physics* 10.7, pp. 1115–1122.
160. Yang, C. N. (1989). “ η pairing and off-diagonal long-range order in a Hubbard model”. *Phys. Rev. Lett.* 63 (19), pp. 2144–2147.
161. Yang, C. and A. E. Feiguin (2016). “Spectral function of the two-dimensional Hubbard model: A density matrix renormalization group plus cluster perturbation theory study”. *Phys. Rev. B* 93 (8), p. 081107.
162. Yang, Q., J. Ellis, K. Mamakani, and F. Ruskey (2013). “In-place permuting and perfect shuffling using involutions”. *Information Processing Letters* 113.10, pp. 386–391.
163. Zhang, S. (1990). “Pseudospin symmetry and new collective modes of the Hubbard model”. *Phys. Rev. Lett.* 65 (1), pp. 120–122.

Declaration on oath

I hereby declare, on oath, that I have written the present dissertation by my own and have not used other than the acknowledged resources and aids.

Eidesstattliche Versicherung

Hiermit erkläre ich an Eides statt, dass ich die vorliegende Dissertationsschrift selbst verfasst und keine anderen als die angegebenen Quellen und Hilfsmittel benutzt habe.

Hamburg, 24. November 2016

Danksagung

Hiermit möchte ich all denjenigen danken, die direkt oder indirekt zum Abschluss dieser Arbeit beigetragen haben.

Zuallerst Michael, der für einen immer Zeit aufgebracht hat, keine Frage unbeantwortet und kein Problem ungelöst ließ.

Andrej und Matthias für ihre Unterstützung beim Schreiben des DMRG-Codes.

Mohammad für die fabulös erfolgreiche Kollaboration.

Felix für den Austausch vieler Informationen über die Jahre.

Lena für die freundschaftliche und angenehme Atmosphäre im Büro.

Und natürlich auch (por último, si bien no menos importante) Silke für ihre Geduld beim Diamantenschleifen.